

# Exfoliation and characterisation of naturally occurring misfit layer chalcogenides by cross sectional scanning transmission electron microscopy

A thesis submitted to The University of Manchester for the degree of Doctor of  
Philosophy in the Faculty of Science and Engineering

2018

Alexander M Rakowski

School of Materials

BLANK PAGE

# Contents

Contents .....	3
Abbreviations .....	5
List of Figures .....	6
Abstract .....	9
Declaration .....	10
Copyright statement .....	10
Acknowledgements.....	11
Publications .....	12
1. Introduction .....	13
1.1. Aims .....	13
1.2. Thesis structure .....	13
2. Literature review .....	15
2.1. Electron microscopy .....	15
2.1.1. The transmission electron microscope (TEM) .....	16
2.1.3. The scanning electron microscope (SEM) .....	38
2.1.4. The focused ion beam (FIB) .....	42
2.1.5. References.....	46
2.2. 2D and van der Waals (vdW) materials.....	57
2.2.1. References.....	61
2.3. Misfit layer chalcogenides (MLCs).....	65
2.3.1. Introduction .....	65
2.3.2. Structure.....	66
2.3.3. Interlayer interactions.....	69
2.3.4. Properties.....	71
2.3.5. Formation.....	74
2.3.6. Intercalation .....	77
2.3.7. Allotropes and cleavage .....	78
2.3.8. Characterisation .....	80
2.3.9. References:.....	82
3. Experimental Methods .....	91
3.1. Chemicals.....	91

3.2.	Minerals.....	91
3.3.	Plan view sample preparation by dry stamp transfer .....	91
3.4.	Plan view TEM sample preparation by drop casting.....	91
3.5.	Cross section STEM lamellae preparation by focused ion beam .....	92
3.6.	STEM imaging .....	93
3.7.	Raman spectroscopy .....	93
3.8.	AFM .....	93
3.9.	References.....	94
4.	Paper 1 – Exfoliation of natural van der Waals heterostructures to a single unit cell thickness.....	95
4.1.	Supplementary information .....	123
5.	Paper 2 – Isolation of 2D cylindrite as a naturally occurring van der Waals heterostructure.....	151
5.1.	Supplementary information .....	173
6.	Paper 3 – <i>In-situ</i> thickness determination of TEM lamellae prepared by focused ion beam .....	185
7.	Summary and future work.....	207
7.1.	Summary of thesis .....	207
7.2.	Future work .....	209
7.2.1.	Expanding the library of 2D misfit layer chalcogenides.....	209
7.2.2.	Exfoliation of non-layered crystals.....	211
7.2.3.	Integration of <i>in-situ</i> thickness measurements with native FIB python interface.....	213
7.3.	References.....	213

**Word Count:** 48066



## Abbreviations

Abbreviation	Meaning
0D	Zero dimensional
1D	One dimensional
2D	Two dimensional
3D	Three dimensional
ADF	Annular dark field
AFM	Atomic force microscope
ARPES	Angle-resolved photoelectron spectroscopy
BF	Bright field
BSE	Backscattered electron microscope/microscopy
CDW	Charge density wave
CTEM	Conventional transmission electron microscope/microscopy
CVD	Chemical vapour deposition
CVT	Chemical vapour transport
DI water	Deionised water
EBSD	Electron backscattered diffraction
EDX	Energy dispersive X-ray
EELS	Electron energy loss spectroscopy
FEG	Field emission gun
FIB	Focused ion beam
FWHM	Full width half maximum
GIS	Gas injection system
HAADF	High angle annular dark field
h-BN	Hexagonal boron nitride
ICE	Ion conversion electron
IPA	Propan-2-ol
LMS	Liquid metal source
MBE	Molecular beam epitaxy
MFP	Mean free path
MLC	Misfit layer chalcogenide
OTF	Optical transfer function
PCTF	Phase contrast transfer function
PMGI	Polydimethylglutarimide
PMMA	Polymethylmethacrylate
SE	Secondary electron
SEM	Scanning electron microscope/microscopy
SNR	Signal to noise ratio
STEM	Scanning transmission electron microscope/microscopy
STM	Scanning tunnelling microscope/microscopy
TDS	Thermal diffuse scattering
TEM	Transmission electron microscope/microscopy
TLD	Through lens detector
TMDC	Transition metal dichalcogenide
XPS	X-ray photoemission spectroscopy
XRD	X-ray diffraction
ZLP	Zero loss peak

## List of Figures

Figure 2-1 - Summary of electron specimen interactions and the signals generated....	16
Figure 2-2 - Beam diagrams for transmission electron microscopy .....	17
Figure 2-3 - Illustration of spherical aberrations effect on focussing of electrons.....	22
Figure 2-4 - Simulated electron probes under different conditions.....	23
Figure 2-5 - Example EELS spectrum.....	30
Figure 2-6- Example EDX spectrum of cylindrite .....	34
Figure 2-7 - Illustration of secondary electron (SE) generation in a bulk specimen.....	41
Figure 2-8 Illustrations of the typical stacking types in TMDCs .....	58
Figure 2-9 – Illustration of layer types and stacking sequences in MLCs .....	67
Figure 2-10 – Illustrative model of misfit layer chalcogen T and H layers.....	67
Figure 2-11 –Reciprocal lattice of orthorhombic MLC with a modulation along the a axis .....	68
Figure 4-1 - SEM and TEM-EDXS characterisation of franckeite.....	100
Figure 4-2 - HAADF-STEM imaging of franckeite .....	102
Figure 4-3 - XPS characterisation of franckeite surface.....	105
Figure 4-4 - Optical microscopy, AFM, and Raman spectroscopy identification of thin franckeite .....	106
Figure 4-5 - Electrochemical characterisation and liquid-phase exfoliation of franckeite .....	109
Figure 4-6 - Transport characterisation of franckeite.....	111
Figure 4-7 - DFT calculations of franckeite's electronic band structure .....	113
SI Figure 4-8 - SEM images and TEM-EDXS mapping of franckeite.....	123
SI Figure 4-9 - TEM imaging of franckeite viewed along the [001] direction .....	124
SI Figure 4-10 - Cross-sectional HAADF-STEM imaging of franckeite along the [100] direction .....	125
SI Figure 4-11 - XPS of the aged and freshly cleaved franckeite surface.....	126
SI Figure 4-12 - High-resolution XPS spectra of the impurity elements .....	127
SI Figure 4-13 - AFM characterisation of franckeite with a sub-monolayer thickness.	127
SI Figure 4-14 - Optical and AFM characterisation of thin franckeite crystals .....	128
SI Figure 4-15 -Raman spectra of monolayer franckeite, bulk franckeite, and SiO <sub>2</sub> /Si substrate .....	129

SI Figure 4-16 - PL measurement of monolayer and bulk franckeite .....	130
SI Figure 4-17 - Laser-induced degradation of franckeite.....	131
SI Figure 4-18 - Laser ablation of franckeite surface .....	132
SI Figure 4-19 - Capacitance, electron transfer, and hydrogen evolution measurements .....	132
SI Figure 4-20 - Voltammetry under varied illumination intensity .....	133
SI Figure 4-21 -Device fabrication and characterisation .....	134
SI Figure 4-22 - Transport characterisation of a 4-layer franckeite crystal .....	135
SI Figure 4-23 - Electrostatic force microscopy measurements .....	135
Figure 5-1 – HAADF STEM images of cylindrite cross sections prepared by FIB .....	153
Figure 5-2 – Illustration of new FIB lamella preparation method .....	153
Figure 5-3 - Atomic models illustrating misfit layer compounds layering .....	157
Figure 5-4 – Optical, AFM and Raman spectra of exfoliated a cylindrite flake .....	160
Figure 5-5 – Plan view characterisation of crushed and exfoliated cylindrite flakes. STEM characterisation along the [001] direction .....	162
Figure 5-6 – Cross sectional characterisation of exfoliated cylindrite flakes .....	165
Figure 5-7 – Characterisation of scrolled cylindrite flake .....	167
Figure 5-8 – Characterisation of kink band in exfoliated cylindrite flake .....	168
Figure 5-9 - Electrical transport measurements of cylindrite .....	170
SI Figure 5-10 - Effects of the cylindrical shape of the cylindrite on its exfoliation.....	173
SI Figure 5-11 – Processed and raw Processed height and raw adhesion and deformation AFM maps of exfoliated cylindrite flake .....	174
SI Figure 5-12 –AFM and HAADF STEM images of cracks and voids in exfoliated cylindrite flakes .....	174
SI Figure 5-13 – Optical images and AFM height map of cylindrite flake used in Raman spectroscopy characterisation .....	175
SI Figure 5-14 - Demonstration of laser induced damage of exfoliated bulk cylindrite flake .....	175
SI Figure 5-15 - Atomic model of the pseudo tetragonal (T) PbS layer tilted off the [001] axis resulting in the appearance of a hexagonal lattice.....	177
SI Figure 5-16 - HAADF STEM images of an exfoliated cylindrite flake viewed along the [001] direction.....	177

SI Figure 5-17 – Investigation of Pb-Pb interatomic distances for cylindrite flake with low curvature .....	178
SI Figure 5-18 – EDX line scan taken along [010] direction .....	178
SI Figure 5-19 – Illustration of Transverse modulation along semi commensurate [010] direction .....	179
SI Figure 5-20 - Incommensurate relationship along the [100] direction of exfoliated cylindrite flake.....	179
SI Figure 5-21 - Illustrative examples of crystal tilts observed in cylindrite crystals ....	180
SI Figure 5-22 - Optical and AFM images of failed cylindrite devices.....	180
SI Figure 5-23 - Optical image of electrical transport device and corresponding Raman spectrum showing the presence of graphene contacts. Scale bar is $20\ \mu\text{m}$ . ....	181
Figure 6-1–Calculated inelastic mean free path for an incident electron traversing a solid for a range of common materials and beam energies .....	187
Figure 6-2 – Overview of electron generation in the FIB.....	192
Figure 6-3– Alignment of SEM images (TLD and ICE detectors) to the STEM-EELS thickness map .....	195
Figure 6-4 – Detector signals and associated errors in thickness estimation .....	198
Figure 6-5- Probability and cumulative distribution functions for BSE generation, electron implantation and transmission in silicon.....	201
Figure 6-6 – Comparison of experimental and modelled detector responses .....	202
Figure 6-7 – Flowchart for the new proposed FIB thinning workflow.....	203
Figure 7-1 – Demonstration of the exfoliation of an MLC provided as ‘coiraité’ .....	211
Figure 7-2 - Demonstration of the exfoliation of mineral ‘vrbaite’ .....	212

## Abstract

# Exfoliation and characterisation of naturally occurring misfit layer chalcogenides by cross sectional scanning transmission electron microscopy

A thesis submitted to The University of Manchester for the degree of Doctor of Philosophy in the Faculty of Science and Engineering

Alexander M Rakowski,

School of Materials, The University of Manchester, 2018

The aim of this thesis is to exfoliate and characterise misfit layer chalcogenides (MLCs). There is a focus on the application of analytical scanning transmission electron microscopy (STEM), in particular viewed in cross section. The cross section specimens are prepared by focused ion beam (FIB), as such novel methods for the optimisation of this technique for preparation of specimens suitable for high quality STEM analysis are proposed.

Misfit layer chalcogenides are a group of compounds formed from alternating layers of pseudo-tetragonal (T) PbS like, and pseudo-hexagonal (H) transition metal dichalcogenide like layers. They demonstrate remarkable flexibility in incorporating different elements into the layers allowing for the creation of crystals with a broad range of properties. Previously, MLCs  $[(\text{PbS})][(\text{NbS}_2)_2]$  and  $[(\text{SmS})][(\text{NbS}_2)_2]$  have been successfully exfoliated to single unit cell thickness. However, these compounds possess a stacking sequence ( $n=1$ ,  $m=2$ , where  $n$  and  $m$  refer to the stacking sequence of T and H layers respectively) which contains a van der Waals (vdW) gap. Here we explore the exfoliation of two naturally occurring MLCs, franckeite ( $n=2$ ,  $m=1$ ) and cylindrite ( $n$ ,  $m=1$ ), which do not possess a vdW gap. The successful exfoliation of these crystals demonstrates that exfoliation is invariant to stacking sequence. As such all MLCs can be considered as realistic targets as 2D materials. Furthermore we demonstrate the power of cross sectional analytical STEM for the characterisation and analysis of MLCs, and directly observe features within the individual layers, which are inaccessible through other characterisation techniques. Including elemental ordering and structural features previously not described in literature, which have allowed for a better understanding of the macroscopic structures of franckeite and cylindrite. Specimen preparation by FIB is optimised for cylindrite specimens, yielding a new procedure for the preparation of these samples. Finally, two novel methods for the *in-situ* thickness measurements of TEM lamellae prepared by FIB are proposed. The first method describes the accurate calibration of a FIB instrument, and the second allows for accurate thickness estimation without the need for prior calibration, through the use of Monte Carlo modelling. The Monte Carlo method allows for high quality lamella from new materials to be milled to a predetermined thickness with outstanding accuracy. Furthermore a workflow for the automation of TEM lamellae preparation is presented, which utilises this accurate modelling.

## Declaration

No portion of the work referred to in the thesis has been submitted in support of an application for another degree or qualification of this or any other university or other institute of learning

## Copyright statement

- i. The author of this thesis (including any appendices and/or schedules to this thesis) owns certain copyright or related rights in it (the “Copyright”) and s/he has given The University of Manchester certain rights to use such Copyright, including for administrative purposes.
- ii. Copies of this thesis, either in full or in extracts and whether in hard or electronic copy, may be made **only** in accordance with the Copyright, Designs and Patents Act 1988 (as amended) and regulations issued under it or, where appropriate, in accordance with licensing agreements which the University has from time to time. This page must form part of any such copies made.
- iii. The ownership of certain Copyright, patents, designs, trademarks and other intellectual property (the “Intellectual Property”) and any reproductions of copyright works in the thesis, for example graphs and tables (“Reproductions”), which may be described in this thesis, may not be owned by the author and may be owned by third parties. Such Intellectual Property and Reproductions cannot and must not be made available for use without the prior written permission of the owner(s) of the relevant Intellectual Property and/or Reproductions.
- iv. Further information on the conditions under which disclosure, publication and commercialisation of this thesis, the Copyright and any Intellectual Property and/or Reproductions described in it may take place is available in the University IP Policy (see <http://documents.manchester.ac.uk/DocuInfo.aspx?DocID=24420>), in any relevant Thesis restriction declarations deposited in the University Library, The University Library’s regulations (see <http://www.library.manchester.ac.uk/about/regulations/>) and in The University’s policy on Presentation of Theses

## Acknowledgements

I would first like to thank Prof. Sarah Haigh whose training, advice and mentorship have made this PhD project possible. I would also like to thank all the members of the Haigh group who have been of great assistance in the duration of my PhD. Special thanks go to Dr. Aidan Rooney whose advice on all things STEM, FIB and coding have made an invaluable contribution to this project. Furthermore I would like to thank the staff members of the electron microscopy centre at the University of Manchester; particular thanks is owed to Matthew Smith for his tuition on all things TEM. I would also like to thank Dr. David Lewis for offering keen insight and positivity during this project.

The fabrication of samples would not have been possible without assistance and training from all the 'tape monkeys'. Particular thanks goes to Dr. Nicholas Clarke, Dr. Greg Auton, Dr. David Perello, Dr. Lee Hague, Matthew Holwill, Matthew Hamer, John Birkbeck, Daniel Terry and James Howarth. I would also like to thank Adrian Cereantfio.

I would like to thank the students and staff of the Graphene NowNano CDT program and in particular the 2018 Cohort, whose assistance and friendships have not only helped with this project but made it a pleasure.

I have been fortunate enough to be able to rely on the support of a great many people outside of the academic environment. Firstly I would like to thank all my flatmates who I have been lucky enough to spend the last 2 years with. Thanks goes to my family whose love and constant support have been greatly appreciated throughout the duration of my PhD. A special mention goes to Imogen Nevard, without whom this would not have been possible.

## Publications

---

**(Submitted) Synthetic 2-D Lead Tin Sulfide Nanosheets With Tuneable Optoelectronic Properties From a Potentially Scalable Reaction Pathway,**

K Norton, J Kunstmann, L Ping, [A Rakowski](#), C Wang, A Marsden, G Murtaza, N Zeng, S McAdams, M Bissett, S Haigh, B Derby, G Seifert & D Lewis; Journal of the American Chemical Society, 2018

---

**Infrared-to-violet tunable optical activity in atomic films of GaSe, InSe, and their heterostructures,**

D Terry, V Zolyomi, M Hamer, A Tyurnina, D Hopkinson, [A Rakowski](#), S Magorrian, N Clark, Y Andreev, O Kazakova, K Novoselov, S Haigh, V Fal'ko & R Gorbachev; 2D Materials, 2018

---

**Transport of hydrogen isotopes through interlayer spacing in van der Waals crystals,**  
S Hu, K Gopinadhan, [A Rakowski](#), M Neek-Amal, T Heine, IV Grigorieva, SJ Haigh, FM Peeters, AK Geim & M Lozada-Hidalgo; Nature nanotechnology, 2018

---

**Nanometer Resolution Elemental Mapping in Graphene-Based TEM Liquid Cells,**

D Kelly, M Zhou, N Clark, M Hamer, E Lewis, [A Rakowski](#), S Haigh & R Gorbachev; Nano letters, 2018

---

**Magnetoresistance of vertical Co-graphene-NiFe junctions controlled by charge transfer and proximity-induced spin splitting in graphene,**

P Asshoff, J Sambricio, A Rooney, S Slizovskiy, A Mishchenko, [A Rakowski](#), E Hill, A Geim, S Haigh, V Fal'ko, I Vera-Marun & I Grigorieva; 2D Materials, 2017

---

**Exfoliation of natural van der Waals heterostructures to a single unit cell thickness,**

M Velický, P Toth, [A Rakowski](#), A Rooney, A Kozikov, C Woods, A Mishchenko, L Fumagalli, J Yin, V Zolyomi, T Georgiou, S Haigh, K Novoselov & R Dryfe; Nature Communications, 2017

---

**Asymmetric MoS<sub>2</sub>/Graphene/Metal Sandwiches: Preparation, Characterization, and Application,**

P Toth, M Velický, M Bissett, T Slater, N Savjani, A Rabiú, [A Rakowski](#), J Brent, S Haigh, P O'Brien & R Dryfe; Advanced Materials, 2016

---

**Preparation of low-dimensional carbon material-based metal nanocomposites using a polarizable organic/water interface,**

P Toth, S Haigh, A Rabiú, A Rodgers, [A Rakowski](#) & R Dryfe; Journal of Materials Research, 2015

---



# **1. Introduction**

## **1.1. Aims**

The aims of the project were three fold:

- i. To exfoliate the misfit layer chalcogenides (MLCs) cylindrite and franckeite, demonstrating that the exfoliation of MLCs is invariant to stacking sequence.
- ii. Characterise the exfoliated MLCs flakes with a number of analytical techniques with a focus on cross sectional scanning transmission electron microscopy (STEM).
- iii. Optimise the preparation of cross section lamellae by focused ion beam (FIB).

To achieve these objectives required the development of skills in a number of areas including: mechanical exfoliation and nanofabrication techniques, preparation of high quality cross section samples by FIB suitable for analytical STEM characterisation, operation of aberration corrected analytical STEM, utilisation of other materials characterisation techniques, Monte Carlo modelling, and data processing.

## **1.2. Thesis structure**

This thesis covers work carried out over a three and half year period at the School of Materials, University of Manchester, UK, utilising the STEM and FIB instruments based in the electron microscopy centre, and the cleanroom facilities based in the national graphene institute. Chapters 4, 5 and 6 are composed of papers in their entirety, which have been published, submitted or will be submitted shortly to peer reviewed journals. These manuscripts contain collaborative work, as such the contributions are noted in the introduction of each chapter.

A literature review is presented in chapter 2, overviewing electron microscopy, two dimensional materials, and MLCs. Within the electron microscopy section, the TEM is introduced with a focus on aberration corrected analytical STEM. The challenges of specimen preparation are discussed, followed by an introduction to the scanning electron microscope with an emphasis on signal generation. Finally the FIB instrument and its application for TEM lamellae preparation is reviewed. After this a brief introduction to 2D materials with an emphasis on the variety of electronic properties

of transition metal dichalcogenides. Finally MLCs are discussed with reference to structure, properties, formation, cleavage and characterisation.

Chapter 3 provides the experimental methods used in the exfoliation of MLCs and the preparation of MLCs samples for STEM analysis and other characterisation techniques.

Chapters 4 and 5 contain two papers, *Exfoliation of natural van der Waals heterostructures to a single unit cell thickness*, and *Isolation of 2D Cylindrite as a naturally occurring van der Waals heterostructure*, in which the exfoliation of MLCs franckeite and cylindrite to single unit cell thickness are reported. In both papers, analytical STEM imaging, in particular cross sectional STEM imaging, was central to the identification of and subsequent characterisation of these materials. A number of complimentary characterisation techniques are utilised in addition to analytical STEM.

These two chapters demonstrate the advantages of cross sectional analytical STEM characterisation in the investigation of MLCs; they also highlight the difficulties associated with the preparation of high quality samples by FIB. The final paper (Chapter 6), *In-situ thickness determination of TEM lamellae prepared by focused ion beam*, addresses these issues through the development of novel *in-situ* thickness measurement methods. Two methods are presented, the first of which allows for calibration of an individual FIB instrument; the second utilises Monte Carlo simulations to model electron detector responses allowing for the accurate *in-situ* thickness measurements, without the requirement of calibration.

The final chapter (7) summarises the presented work and discusses future research avenues building upon this project. Sections 7.2.1 and 7.2.2 consider the impact of chapters 4 and 5 and present next steps for two dimensional MLCs research, discussing the possibility of future exfoliation of non-layered crystals. Section 7.2.3 builds upon chapter 6, and discusses a route for the integration of *in-situ* measurement in commercial FIB instruments.

## 2. Literature review

The following three sections outline current literature surrounding electron microscopy, 2D materials and misfit layer chalcogenides. There is a focus on analytical scanning transmission electron microscopy, scanning electron microscopy, and focused ion beam technology and its application for sample preparation. A brief introduction to 2D materials focused on transition metal chalcogenides is presented. The chapter concludes with an overview of misfit layer chalcogenides.

### 2.1. Electron microscopy

The ability to resolve atoms and assign elemental identity is extremely powerful, and has allowed for a fuller understanding of atomic structure, defects, and elemental composition on nanometre to micrometre length scales.<sup>1</sup> This requires Ångstrom resolution and probe specimen interaction, allowing for chemical identification. Abbe's diffraction limit shows the ultimate resolution of classical light microscopes (wavelengths between 400 and 600 nm) to be  $\approx 200$  nm.<sup>2</sup> While super-resolution techniques have demonstrated resolutions beyond this, they are still insufficient to obtain atomic resolution.<sup>3</sup> While X-rays have a sufficiently small wavelength to resolve atomic features, they have a very weak interaction with matter.<sup>4</sup> Conversely, electrons are an ideal analytical probe due to their small wavelength, strong matter interaction and ability to form high quality beams. When an electron impacts on a specimen it may interact in a number of different ways. These interactions will generate a range of useful signals which can be collected to generate an image, summarised in Figure 2-1.

The two most common methods utilising an electron probe are transmission electron microscopy (TEM) and scanning electron microscopy (SEM). TEM examines very thin samples, collecting the transmitted electrons to form the image. SEM however, is typically a bulk technique, forming an image from backscattered (BSE) and/or secondary electrons (SE). Both techniques may utilise the additional signals generated by electron specimen interactions to obtain spectroscopic data. Focused ion beam (FIB) is similar to SEM, differing by scanning a probe of charged ions ( $\text{Ga}^+$  in this work) on to the sample, rather than electrons. All three techniques are central components of the work presented, as such these techniques are explored in greater detail beginning with transmission electron microscopy (Section 2.1.1), following on with

scanning electron microscopy (Section 2.1.3) and concluding with the focused ion beam (Section 2.1.4).

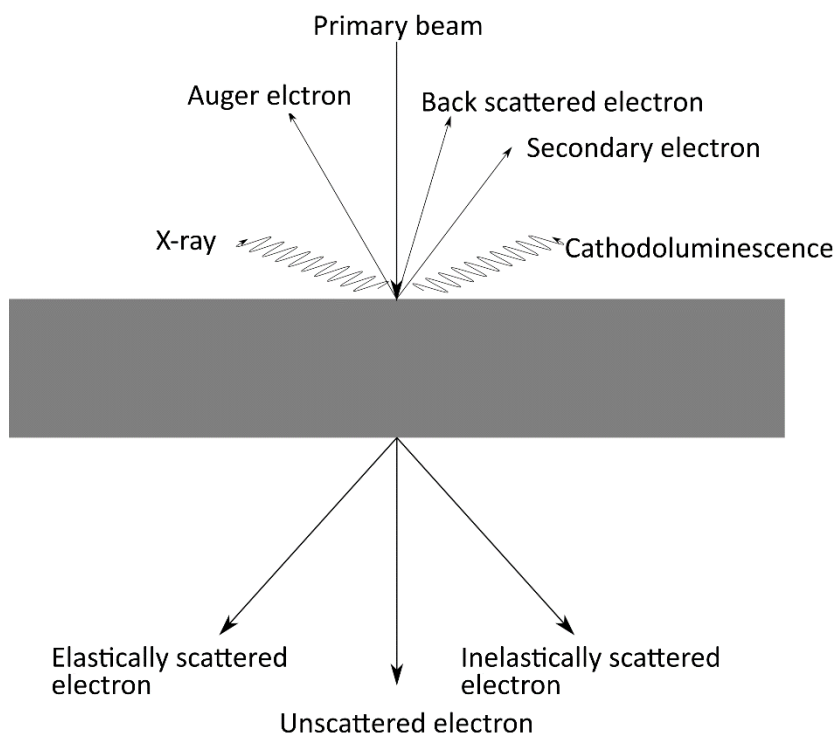


Figure 2-1 - Summary of electron specimen interactions and the signals generated

### 2.1.1. The transmission electron microscope (TEM)

TEM was first demonstrated in 1932 by Ruska and Knoll<sup>5,6</sup>. Due to decades of intensive research, TEM is now able to collect ultrahigh resolution ( $< 1 \text{ \AA}$ ) images with the simultaneous collection of spectroscopic information.<sup>1</sup> This ability to image individual atoms and identify elemental composition has seen TEM become a vital pillar in a broad range of research areas including nanoscience<sup>7</sup>, materials science<sup>8</sup> and biology<sup>9</sup>.

The wavelengths for electrons with energies typically used in TEM (60 – 300 keV) are of the order  $1 \times 10^{-12} \text{ m}$ .<sup>10</sup> It would seem trivial to obtain atomic resolution images, based on the diffraction limit alone. However, due to a number of inherent aberrations in electron lenses, the resolution is severely reduced.<sup>11,12</sup> There has been a concerted effort for 70 years to reduce the magnitudes of these aberrations, as well as to improve electron sources and microscope stability, with the aim of increasing the resolution of TEM.<sup>13</sup>

TEM can be broadly categorised into two principle techniques, conventional TEM (CTEM) and scanning TEM (STEM). CTEM illuminates the specimen with a broad beam, collecting information from a relatively large area simultaneously. Conversely, STEM uses a finely focused electron probe which is rastered across the specimen to build up the image a single pixel at a time. Both techniques are summarised in Figure 2-2. While STEM and CTEM differ in the manner in which the sample is addressed, many similarities can be drawn between the two techniques, and both are underpinned by the reciprocity principle.<sup>14</sup> Both techniques use an electron 'gun' in which electrons are first emitted from a source and subsequently accelerated across a high potential. The electron sources are either a sharp tungsten pin or an orientated LaB<sub>6</sub> crystal. These sources are either heated or subjected to an electric field, for thermionic and field emission guns (FEGs) respectively. Schottky FEGs are a hybrid of the two, in which both heat and electron field are simultaneously applied.<sup>15</sup> Simple thermionic guns are the least technically complicated, and inexpensive, but cold FEGs produce higher quality beams, having the smallest source size, highest brightness and largest temporal and spatial coherence lengths.<sup>15</sup>

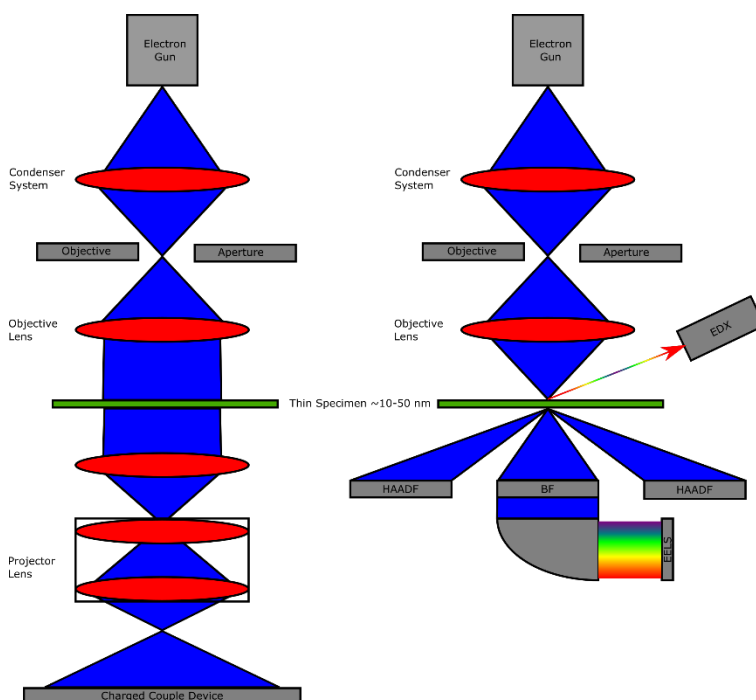


Figure 2-2 - Beam diagrams for transmission electron microscopy (TEM), left) conventional and right) scanning mode. Conventional TEM impinges a broad near parallel beam on the sample, which is projected through multiple lenses and onto a CCD camera. The data is collected in near-parallel. Scanning TEM uses highly convergent focused beam which is subsequently rastered across the sample. The signal is then collected serially by multiple detectors. (Adapted from<sup>16</sup>)

Irrespective of the choice of electron source, highly energetic electrons exit the gun at relativistic velocities. These electrons are a rare example of a system in which relativity and quantum mechanics overlap, as the electrons exhibit wave particle duality whilst undergoing relativistic contraction. The choice of accelerating voltage dictates an ultimate diffraction limited resolution of the microscope, with a higher potential allowing higher resolutions. Upon exiting the electron gun, the electrons will enter the condenser system which consists of several apertures and electron lenses. The condenser system is responsible for producing a refined, de-magnified image of the source. CTEM and STEM differ in the way electrons address the sample. In STEM the beam is focused to a fine point by the objective lens and is scanned across the sample.<sup>17,18</sup> The electrons interact and transmit through the specimen and are collected by a range of detectors simultaneously. The detectors discriminate by scattering angle. Typical detectors used are bright field (BF) (collecting lowly scattered) and high angle annular dark field (HAADF)<sup>19</sup> (collecting highly scattered) (Figure 2-2). The detector signal is output to a computer which records the intensity for each detector at each pixel to build up the images, in a serial fashion. The detectors form images from different scattering processes yielding distinct images. In contrast, CTEM collects the data in parallel, by using a broad beam to illuminate the specimen, the wave front interacts and transmits through the specimen.<sup>20</sup> After this the altered wave front enters the objective lens, collecting and magnifying all transmitted electrons. Electrons then travel through the intermediate lens and projector system, which further magnifies the image and projects it on to a phosphor screen or camera. STEM however, is able to simultaneously generate multiple images formed by different contrast mechanisms, in comparison to the single image collected by CTEM. Furthermore the serial collection of data used in STEM allows for the collection of spectroscopic data at each pixel, producing a spectrum image.

One of the reasons for the improvement in TEM resolution has been in the development of aberration correctors for spherical and other geometric aberrations.<sup>21,22</sup> More recent efforts in the correction of chromatic aberrations have been successful either by directly correcting the chromatic aberration or through the use of monochromators to minimise its effect.<sup>23,24</sup> Due to differences in how the electron beams address the specimen, the approach used in correcting aberrations

differs in CTEM and STEM. In STEM, the resolution of the microscope is dictated by the probe size and aberration correction must be ‘probe side’ i.e. reduction in aberrations originating in the probe forming objective lens. CTEM however, requires correction in the image forming objective lens. Correction of CTEM aberrations is more complex than in that of STEM. This combined with the other advantages offered by STEM, has led to the more widespread adoption of aberration corrected STEM compared to CTEM, despite the similar ultimate resolutions.<sup>25</sup>

While TEM is a key resource in investigating materials and nanoscale phenomena, it does have limitations. Possibly the most significant is the small sampling size. While materials may be studied at atomic resolution, only a very small region of the total specimen size may be investigated. As of 2009 it was estimated that only  $10^3 \text{ mm}^3$  has been investigated since the development of the technique.<sup>26</sup> As such, when compared to other commonly used bulk characterisation techniques, TEM requires more planning to ensure the sample is representative. In addition, the sample must be able to withstand the high vacuum conditions required for TEM, and be robust to the electron beam.<sup>27</sup> The high vacuum levels in TEM are unlikely to be representative of the material’s native environment, which may alter the properties of the sample.<sup>28,29</sup> This can be of particular concern for biological and catalytic active samples.<sup>30,31</sup> The development of environmental TEMS<sup>32</sup> and specialised holders, have allowed for the creation of more realistic environments and applications of different stimuli.<sup>30,33,34</sup> Further constraints include lateral size and thickness of the TEM sample, which are discussed in detail in section 2.1.2.4.

### 2.1.2. STEM imaging theory

The size and intensity of the probe ultimately dictates the highest achievable resolution of the instrument for incoherent imaging. The probe is formed by the objective lens which focuses the beam to form a crossover, forming the probe which intersects the specimen. The probe size impinging on the sample,  $d_{STEM}$ , can be approximated as:

$$d_{STEM} = \sqrt{d_s^2 + d_a^2 + d_{sa}^2 + d_c^2 + d_f^2} \quad 2.1$$

where the components contributing to the probe size are,  $d_s$ , the finite source size,  $d_d$  the diffraction limit contribution,  $d_{sa}$  the size of the probe due to spherical aberration,  $d_c$  due to chromatic aberration and  $d_f$  the size of the probe resulting from incorrect focusing.<sup>15</sup> FEGs are almost always used for STEMs, giving a source size of approximately 5 nm<sup>35</sup>, as such it must be sufficiently demagnified so as to produce an atomic sized probe. This is achieved by the condenser and objective lenses. The objective lens is the final focusing lens before the sample, producing the largest demagnification. Consequently the aberrations of this lens have the most impact on the probe size.<sup>36</sup> Spherical aberration is the over focusing of electrons entering the lens at higher angles, relative to those entering along the optic axis (Figure 2-3).<sup>11</sup> This leads to the distribution of focal planes, resulting in broadening of the probe. The smallest probe diameter is formed at the plane of least confusion, which is above the Gaussian plane. The contribution of spherical aberration may be reduced by the use of an aperture, to limit the angular distribution of electrons entering the objective lens. Whilst the aperture reduces the effect of spherical aberration, it necessarily induces a diffraction limited minimum probe size, and limits the maximum beam current available. Alternatively a spherical aberration corrector may be used to directly compensate for the geometric aberrations of the objective lens.<sup>37</sup> This is achieved through the breaking of rotational symmetry, through the incorporation of a combination of quad/sextu/octopoles, which allows for the manipulation of the probe wave front and correction of spherical aberration and higher order geometrical aberrations.<sup>13,21,22,38</sup> The direct reduction in spherical aberration allows for the use of larger apertures, resulting in smaller probes with higher currents available. Similar broadening is induced by chromatic aberration, in which electrons of different energies are unequally focused.<sup>39</sup> The correction of chromatic aberration may be achieved through either filtering the beam to reduce the energy spread<sup>40-44</sup> or direct correction.<sup>45,46</sup> Monochromators have proven the most popular route for STEM, offering additional advantages in spectroscopic data collection, with direct correction only used for CTEM.<sup>23</sup> Assuming  $C_s$  is the largest aberration, the optimal defocus,  $Z_{defocus}$ , is given in equation 2.2. In order to ensure the smallest probe the beam must be accurately defocused from the sample by this amount.<sup>35</sup>



$$z_{defocus} = -0.71\lambda^{1/2}C_s^{1/2} \quad 2.2$$

$$d_{80\%} = 0.4\lambda^{3/4}C_s^{1/4} \quad 2.3$$

The size of the probe for an un-corrected microscope containing eighty percent of the intensity can be approximated using equation 2.3.<sup>15</sup> For  $C_s$  corrected microscopes, where the spherical aberration is minimised, the equation may be adapted to include the contribution of higher order aberrations, such as  $C_5$  (equation 2.4).<sup>37</sup>

$$d_{80\%} = 0.4\lambda^{5/6}C_5^{1/6} \quad 2.4$$

The effects of aberrations on the electron probe at the sample are described in the electron probe function  $P(r)$ , which is expressed in equation 2.5. It is composed of the aperture function  $A(K)$  and the complex reciprocal space wavevector  $K$  (equation 2.6).<sup>35</sup> The aperture function describes the transmission of electrons through the aperture and accounts for the aberrations present in the microscope. The effect of these aberrations on probe size, shape and intensity is demonstrated in Figure 2-4.

$$P(r) = \int A(K) \exp(-i2\pi K \cdot r) dK \quad 2.5$$

$$K = \frac{2\pi}{\lambda} \quad 2.6$$

To understand the various imaging modes available in STEM, we first need to consider the way in which probe electrons interact with the specimen. For an electron beam impinging upon the specimen, there are two outcomes: the electron may transmit unaffected by the sample, or alternatively it may interact with the specimen's nuclei or electron cloud and be scattered to some angle.<sup>47</sup> Those scattering events can be categorised into two distinct classes, elastic and inelastic. Elastic interactions are those in which no energy is transferred to the specimen. Inelastic scattering interactions are those in which an appreciable amount of energy is transferred from the probe to the specimen.<sup>47</sup> It is the inelastic interactions which are utilised for the collection of spectroscopic data, and will be explored in section 2.1.2.2. We will first consider elastic scattering events.

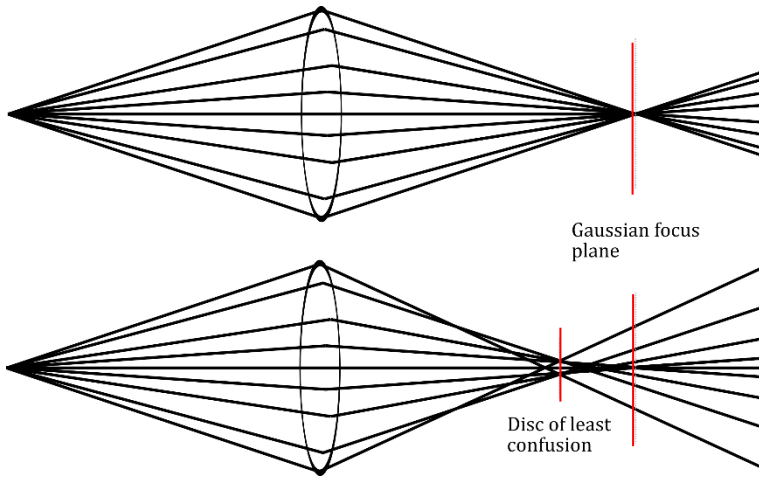


Figure 2-3 - Illustration of spherical aberrations effect on focussing of electrons. Top) a perfect lens with no aberration. Bottom) an imperfect lens with spherical aberration. The minimum probe size is at the disc of least confusion, rather than the Gaussian focus plane. (Recreated with permission from<sup>48</sup> © 2004 Elsevier Ltd)

### 2.1.2.1. Elastic scattering

An elastic scattering event can be categorised as either coherent or incoherent.

Coherent scattering occurs when only a small phase shift occurs, typically through a small angle. Specimens which are sufficiently thin and do not strongly scatter can be treated as ‘weak phase objects’.<sup>49</sup> The weak phase approximation assumes scattering produces only a small phase shift with an insignificant change in amplitude. Under this assumption, the transmission function,  $\psi(r)$ , (Equation 2.7) for an electron passing through the sample may be written as the complex function of the potential of the sample,  $V(r)$ , and the interaction constant,  $\sigma$  (Equation 2.8), where both  $m$ , the electron mass and  $\lambda$ , the electron wave length, are relativistic.<sup>35</sup>

$$\psi(r) = 1 + i\sigma V(r) \quad 2.7$$

$$\sigma = \frac{2\pi m e \lambda}{h^2} \quad 2.8$$

It can then be shown that the intensity of signal from coherent scattering,  $I_{coh}$ , at a probe position,  $r$ , can be described as the square of the convolution of the transmission function,  $\psi(r)$ , and the probe function,  $P(r)$  (Equation 2.5).<sup>35</sup>

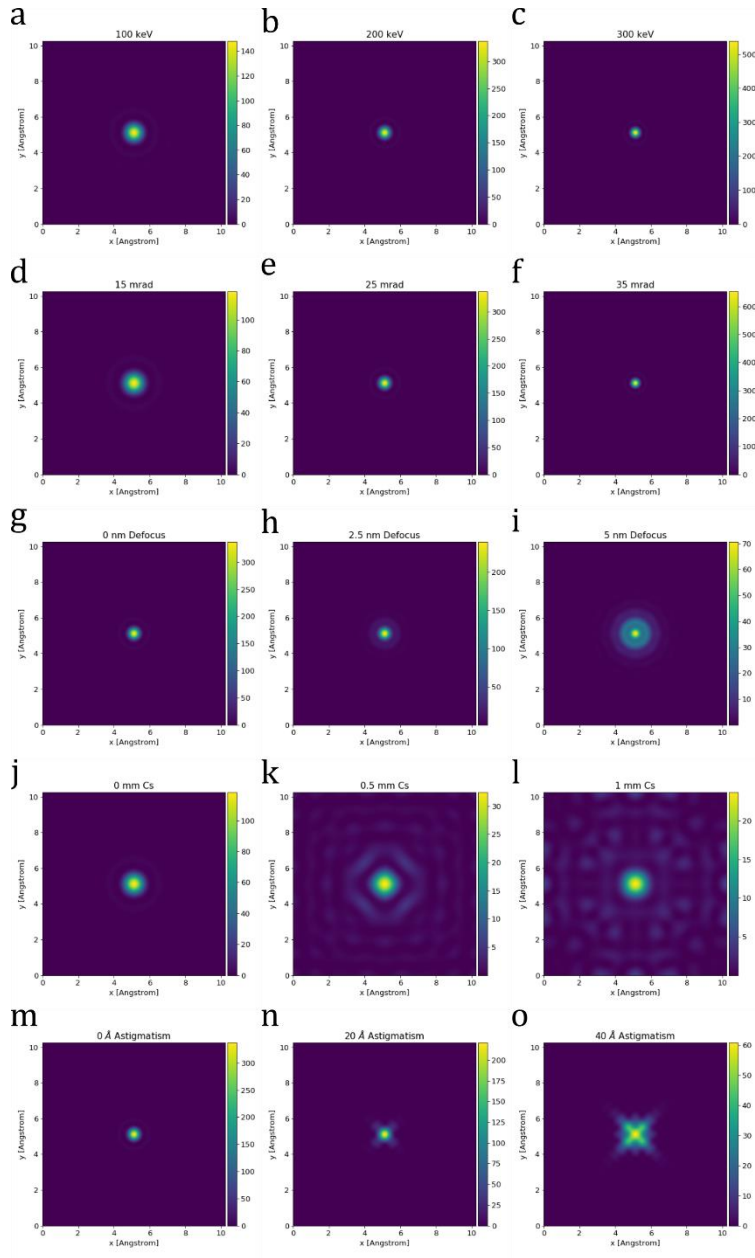


Figure 2-4 - Simulated electron probes under different conditions. It should be noticed that the size, shape and intensity of the probe all change. (a)-(c) effect of accelerating potential( $V_0$ ), 100, 200 and 300 kV,  $\alpha=25$  mrad, astigmatism= $0 \text{ \AA}$ ,  $C_s=0$  mm Scherzer defocus; (d)-(f) effect of convergence angle, 15, 25 and 35 mrad,  $V_0=200$  kV, astigmatism= $0 \text{ \AA}$ ,  $C_s=0$  mm, Scherzer defocus; (g)-(i) effect of defocus, 0, 2.5 and 5 nm,  $V_0=200$  kV,  $\alpha=25$  mrad, astigmatism= $0 \text{ \AA}$ ,  $C_s=0$  mm; (j)-(l) effect of  $C_s$ , 0, 0.5 and 1 mm,  $V_0=200$  kV,  $\alpha=15$  mrad, astigmatism= $0 \text{ \AA}$ , Scherzer defocus; (m)-(o) effect of astigmatism, 0, 20, 40  $\text{\AA}$ ,  $V_0=200$  kV,  $\alpha=25$  mrad,  $C_s=0$  mm, Scherzer defocus. Produced using PyQSTEM<sup>50</sup>

$$I_{coh}(r) = |\psi(r) \otimes P(r)|^2 \quad 2.9$$

A consequence of this convolution between the wave function and the probe function, is that the image contrast is sensitive to both the specimen and the condition of the

microscope. For a weak phase object, the contribution to the image from different spatial frequencies in the specimen is given by the phase contrast transfer function (PCTF). The PCTF is a sinusoidal oscillating function which is sensitive to the condition of the microscope including defocus. As a result, contrast reversal within an image depends both on spatial frequency and also the defocus of the electron probe.<sup>51</sup>

Scattering is considered incoherent when there is a loss of phase information.<sup>52</sup> This typically occurs when the electron scatters through a large angle after interacting with an atomic nucleus. Incoherent scattering can be approximated as a relativistic corrected Rutherford-like (equation 2.10). This describes the change in scattering cross section,  $\sigma$ , scattering into a solid angle,  $\Omega$ , where  $Z$  is atomic number and,  $a_0$  is the Bohr radius. The relativistic contraction,  $\gamma$ , is described in equation 2.11, the magnitude of the scattering vector is described in equation 2.12 and finally the magnitude of the wave vector is described in equation 2.6.<sup>53</sup>

$$\frac{d\sigma}{d\Omega} = \frac{4\gamma^2 Z^2}{a_0^2 q^4} \quad 2.10$$

$$\gamma = \left[ 1 - \frac{v^2}{c^2} \right]^{-\frac{1}{2}} \quad 2.11$$

$$q = |q| = 2K \sin\left(\frac{\theta}{2}\right) \quad 2.12$$

With the removal of the phase information, the intensity at the detector resulting from incoherent scattering is described in equation 2.13.<sup>52</sup> The intensity is equal to the product of the square of the probe function,  $P(r)$  (Equation 2.5) and the object function,  $O(r)$ . The object function is the square of the transmission function (equation 2.7), and describes the intensity of the electrons scattered by the atoms. The intensity of the signal generated can essentially be thought of the potential of the atoms blurred by the probe.<sup>35</sup>

$$I_{Incoh}(r) = |P(r)|^2 \otimes O(r) \quad 2.13$$

The difference derived for coherent and incoherent scattering (Equations 2.9 and 2.13) is subtle. However the manifestation in the contrast formation mechanism is significant.<sup>54</sup> Instead of a PCTF, as in the case of coherent scattering, incoherent scattering contrast is described by the optical transfer function (OTF). The OTF is a continuously positive monotonically decreasing function, which results in no phase reversal across the full range of spatial frequencies, extending out to twice the spatial frequency of the chosen aperture.<sup>54</sup> Consequently, incoherent scattering produces images which are directly interpretable, with resolutions comparable to coherent phase contrast images.

#### **2.1.2.1.1. Bright field (BF) STEM image contrast**

BF STEM imaging primarily utilises the coherently scattered electrons, which are scattered through small angles, and is achieved by placing a detector on the optic axis. As such, BF STEM and BF CTEM are mathematically equivalent due to reciprocity, which was demonstrated in 1970.<sup>55</sup> The detector only subtends a small scattering range, which is known as the collection angle  $\beta$  ( $< 40$  mrad, more typically  $\approx 15$  mrad).<sup>13</sup> The contrast generated within the image is produced by three contrast mechanisms; mass thickness, diffraction and phase contrast.

If we consider the electron probe passing through vacuum, the electrons pass without scattering. The entire probe intensity will be collected by the BF aperture/detector provided  $\beta \geq \alpha$ . If a specimen is placed in the beam path, some of the electrons will be scattered outside of the BF disc.<sup>56</sup> Thus the intensity of the beam is reduced compared with a beam travelling through vacuum. These scattering events will be more numerous and/or more probable for a thicker or denser material.<sup>56</sup> If the sample is inhomogeneous, the scattering events will vary as a function of probe position, generating contrast in the image collected. This is mass thickness contrast, and is generated regardless of the samples crystallinity. Mass thickness is the primary contrast mechanism in CTEM biological imaging.<sup>57</sup>

Diffraction and phase contrast are only present in crystalline samples and contribute the majority of contrast to the image for crystalline samples. When the electron beam interacts with a crystalline sample, the beam will be diffracted if it satisfies the Bragg

condition<sup>58</sup>. As a convergent beam is used, instead of the forming discrete spots, as in CTEM, discs will be formed in the back focal plane. If the separation between discs is larger than the BF detector, the intensity reaching the detector will be reduced; this is the basis of diffraction contrast.<sup>59</sup> As diffraction contrast is extremely sensitive to changes in lattice orientation, it is used extensively for the studying of defects in crystalline samples.<sup>58,59</sup>

If a sufficiently large objective aperture is used such that there is a triple overlap region (overlap between the direct beam and  $\pm$  scattered beams), then coherent interference can occur.<sup>36,60</sup> This condition is only achieved when a convergence semi angle is equal or larger than the scattering vector. The interference is very sensitive to the sample and is more information rich than mass thickness and diffraction contrast. It has been shown that phase contrast in BF STEM is equivalent to phase contrast in CTEM, as such the BF STEM is also determined by the PCTF.<sup>55</sup>

While BF imaging is perhaps the most information rich form of imaging, the sinusoidal nature of the PCTF is a severe limitation for ease of interpretation; as even small changes in defocus (or other microscope parameters) will change the PCTF and can result in contrast reversals.<sup>35</sup> Comparison with simulation is required with accurate modelling of both the specimen and the microscope conditions. While BF STEM images have been used in my work for qualitative analysis, the majority of imaging has been high angle annular dark field (HAADF) STEM.

#### **2.1.2.1.2. High angle annular dark field (HAADF) STEM image contrast**

Sampling incoherently scattered electrons through the use of a HAADF STEM detector has a number of advantages over BF STEM. Not only are the images directly interpretable (discussed below), but it allows for the simultaneous collection of the inelastically scattered electrons. The technique was first demonstrated in 1980 by Crewe.<sup>61</sup> The HAADF detector is an annular detector centred on the optic axis, with a large inner angle. The surface area allows for the collection of a substantial range of scattering angles, approximately 100 mrad.<sup>36</sup> Through reciprocity one can draw the comparison with TEM, where the sample is illuminated with an annular incoherent source.

The justification of HAADF STEM being incoherent is primarily based on two arguments, geometric and thermal diffuse scattering (TDS). The geometry of the HAADF detector allows for the collection of multiple diffracted beams, and consequently multiple interface regions. As a large number of these interfaces are summed together, the contribution of an individual overlap region is minor compared to the total detected signal, and the sensitivity to the phase is destroyed. To ensure the geometry imposes incoherent scattering, the inner angle of the HAADF detector must be sufficiently large. The inner angle is typically chosen to be at two or three times the convergence angle ( $\approx 20\text{-}35$  mrad), requiring inner angles greater than 50 mrad for modern corrected STEMs.<sup>35</sup>

Alternatively the incoherence of HAADF images may be explained by the scattering of the probe electrons with pre-existing phonons within the specimen. This scattering process is known as TDS, and is responsible for the majority of the signal in a HAADF image.<sup>62,63</sup> While strictly an inelastic process, the energy transfer is so small it is not readily measurable, and so may be treated as pseudo-elastic. If the lattice is assumed to behave as an Einstein Solid, in which the atoms vibrate independently, the scattering will be incoherent as there is no phase relation between movements of neighbouring atoms. More accurately, phonon vibrations impose correlation between neighbouring atom positions, as such the coherence cannot be completely destroyed.<sup>64</sup> However Muller et al. have shown that for HAADF images the specimens can be approximated as Einstein solids, rather than using a realistic phonon dispersion.<sup>65</sup>

If we assume a Rutherford scattering approximation then the HAADF intensity should be proportional to the square of atomic number (equation 2.14).<sup>66</sup>

$$I \propto \sigma_{MSD}^2 Z^2 \quad 2.14$$

Where,  $\sigma_{MSD}$ , is the mean square displacement and  $Z$  is atomic number. The contribution of mean square displacement gives increased contrast in low  $Z$ , highly mobile materials such as polymers.<sup>66</sup> For more accurate modelling it is necessary to consider relativistic shielding of atomic nuclei, such that the scattering intensity is proportional to  $Z^\zeta$ , where  $\zeta$  is typically 1.7 but is sample dependent.<sup>67,68</sup> This

proportionality is also affected by the scattering angles collected by the detector, and only valid if scattering is purely incoherent.<sup>69,70</sup>

HAADF image contrast is further complicated by channelling along atomic columns, which occurs when a specimen is orientated to a low zone axis.<sup>71,72</sup> When the probe is located over an atomic column, the probe electron will oscillate along the column due to the positive potential of the nuclei, effectively trapping the electron on the column. Channelling introduces coherence to the scattering and can alter the intensity of the signal as a function of thickness as the beam passes through the specimen.<sup>54</sup> Contrast arising from channelling cannot be easily interpreted as it has been shown to be dependant on the inner angle of the detector and specimen thickness.<sup>73</sup> However, channelling can be advantageous with regards to acquiring an atomic resolution image as it localises the beam within an atomic column, so at these positions HAADF images will show higher intensity than might otherwise be predicted.<sup>74</sup>

The exact quantitative nature of HAADF imaging is beyond the scope of this thesis, a full description can be found in Martinez et.al.<sup>75</sup>, Jones<sup>76</sup> and de Backer et.al.<sup>77</sup>. To a good approximation we can treat the HAADF contrast as purely incoherent scattering. This allows for the interpretation that bright regions correspond to atomic positions, with thicker regions or those composed of heavier atoms being proportionally brighter.

A weakness of HAADF STEM is that the proportion of electrons scattered to high angles is much lower than those weakly scattered and collected in BF STEM. As a consequence, the amount of electrons reaching the HAADF detector is typically lower than BF which can reduce the signal to noise ratio (SNR). This is particularly true at higher angles, so often lower inner angles may be used (medium angle ADF) in lieu of true HAADF conditions, which will introduce some phase information into the image but give an improved SNR.<sup>78</sup>

Within this body of work the HAADF STEM images were collected with a sufficiently large inner angle, such that images were assumed to be formed from incoherently scattered electrons. The images were then interpreted in a semi-quantitative manner, with  $I \propto Z^2$  relationship.



### 2.1.2.2. Inelastic Scattering

Inelastically scattered electrons are those where energy is transferred from the probe to specimen due to an interaction with the electron cloud of the specimen. This interaction is the basis for all the spectroscopic techniques used in TEM. The average distance an electron travels within the specimen before an inelastic scattering event is known as the inelastic mean free path (MFP),  $\lambda_{inel}$ , where  $N_v$  is the number of atoms per unit volume and  $\sigma_{inel}$  is the inelastic cross section for the materials (equation 2.15).<sup>35</sup>

$$\lambda_{inel} = \frac{1}{(N_v \sigma_{inel})} \quad 2.15$$

It should be noted that inelastic scattering events are necessarily incoherent.<sup>79</sup> There are a number of different spectroscopic signals available within the microscope, which include electron energy loss spectroscopy (EELS), energy dispersive X-ray (EDX) spectroscopy, cathodoluminescence and Auger electron spectroscopy.<sup>47</sup> A principal advantage of STEM is the ability to obtain a spectrum at each pixel position, providing chemical information at high spatial resolutions. The two most utilised spectroscopic STEM techniques are EELS and EDX, which collect complimentary information.

#### 2.1.2.2.1. Electron energy loss spectroscopy (EELS)

The transfer of energy from the probe to the specimen can manifest through a number of processes including the creation of: phonons, plasmons or ionisation events.<sup>47</sup> In a typical EELS spectra there are three primary features; the zero loss peak (ZLP), plasmon peak and 'core edges' (Figure 2-5).

The ZLP corresponds to the un-scattered and elastically scattered electrons. The ZLP full width half maximum (FWHM) is dictated by the energy dispersion of the probe and represents the best possible energy resolution of the EELS spectra. The actual resolution will depend on the number of channels in the spectrometer, the detector quantum efficiency, and the choice in energy dispersion per channel.<sup>80</sup> Due to limitations in electron sources, the ZLP FWHM ranges from 0.3 to 3 eV depending on electron source.<sup>81</sup> Monochromators are able to produce probes with ZLPs with a FWHM as low as 7 meV and with sufficiently low tail intensities that it is possible to examine phonon vibrations.<sup>82</sup> More commonly, the ZLP FWHM is closer to 1-2 eV, as

such we will consider all transfers below 1 eV as pseudo-elastic scattering and contained within the ZLP (including phonons responsible for TDS).

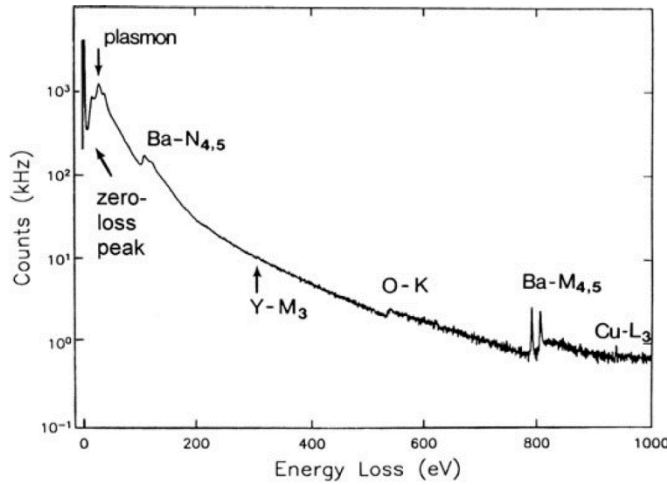


Figure 2-5 - Example EELS spectrum containing zero loss, plasmon and characteristic elemental edges, and showing the power-law background. The intensity of the zero loss peak, containing all electrons which have not inelastically scattered dwarfs the other components. Note the array of elemental edges shapes and intensities. (Reproduced with permission from<sup>47</sup> Copyright © 2011, Springer Science Business Media, LLC)

When the electron probe interacts with the specimen it may excite a collective oscillation of the electrons, a plasmon. While the plasmon peak may be studied, for example to measure optical properties<sup>83</sup>, bandgaps<sup>84</sup>, or the temperature of the sample<sup>85</sup>, it is more generally used to estimate sample thickness.<sup>86</sup> If the sample is thinner than the inelastic MFP, there will only be a single plasmon peak, with thicker samples containing multiple plasmon peaks. The multiple peaks indicate multiple inelastic scattering events for a probe electron passing through the specimen.<sup>47</sup> A precise method for measuring thickness of the sample is achieved by the log-ratio method (equation 2.16).<sup>86</sup> Where,  $t$  is sample thickness,  $\lambda_{inel}$  is the inelastic mean free path, and  $I_T$  and  $I_{ZLP}$  are the intensity of the plasmon and ZLP peak respectively.

$$t = \lambda_{inel} \ln \left( \frac{I_T}{I_{ZLP}} \right) \quad 2.16$$

Both the ZLP and plasmon peak reside in the 'low loss' region of the EELS spectra, which is the most intense region. Higher energy losses than approximately 100 eV are considered the high loss region, which is significantly less intense (one to two orders of magnitude). 'Core edges' present in the high loss region of the spectrum correspond to ionising events.<sup>47</sup> The shape and position of the edge provides details such as chemical

environment and oxidation state.<sup>87</sup> Much of the challenge associated with EELS comes from the post processing of the data, where specimen information must be deconvolved from the background.<sup>88</sup>

Commonly EELS data is acquired by placing an electromagnetic prism on the optic axis, and collecting the direct and weakly scattered electrons in lieu of a BF detector. HAADF or ADF detectors may still be used, allowing for the simultaneous collection of images and EELS spectrum images. While an invaluable technique in many regards, there are some associated weaknesses. The estimation of elemental concentrations is extremely sensitive to the post processing method used, although recent advances have allowed for a more quantitative analysis.<sup>88</sup> SNR is also a significant issue, due to the low number of inelastic scattering events; this is particularly true for low cross section materials i.e. those composed of high atomic number elements.<sup>47</sup> Additionally, due to a large difference in the intensity of the low and high loss regions of the spectra as well as limitations in spectrometers, the EELS experiment must be tailored to particular elements. Depending on elemental composition, multiple EELS spectra with different energy offsets may be required to measure all the elements with the sample. This may result in drift in the ZLP position, leading to inaccuracies in peak assignment. To compensate for the drift, dual EELS is performed, in which both low and high loss regions are collected simultaneously, allowing for the accurate alignment of the spectra post collection.<sup>89</sup> Generally EELS is particularly suited to the examining low Z elements, and so complements EDX spectroscopy.

#### **2.1.2.2.2. Energy dispersive X-ray (EDX) spectroscopy**

When an atom is ionised by the electron beam, a hole is created which is rapidly filled by an electron from a higher orbital, returning the atom to its ground state configuration. Electrons from different orbitals may be ejected by the ionisation technique, which in turn may be filled from a number of different orbitals, providing it satisfies the selection rules, leading to characteristic transitions for a single element. This requires an energy emission process, equal to the difference between the energy levels of the orbitals.<sup>15</sup> As such the emission spectra produced is unique to each element. The emission is achieved by two competing processes; X-ray emission and ejection of an Auger electron. The dominant process depends on atomic number, with Auger preferred in light elements and X-ray emission in heavy elements.<sup>90</sup>

The intensity of the X-rays emitted,  $I_A$ , for element  $A$  in a sample, can be described by equation 2.17.<sup>15</sup>

$$I_A = \left( \frac{C_A \omega_A \sigma_A a_A t}{A_A} \right) \varepsilon_A \quad 2.17$$

Where  $C_A$  is the weight fraction of  $A$ ,  $\omega_A$  is the fluorescence yield,  $a_A$  is the fraction of total intensity measured,  $\sigma_A$  is total ionisation cross section,  $t$  is sample thickness,  $A_A$  is atomic weight of element  $A$ , and  $\varepsilon_A$  is the efficiency of the detector. The photons produced by light elements are typically low in energy and are less efficiently detected.<sup>90,91</sup> The poor detection of light elements, and the increased probability of fluorescence for higher atomic weight elements, makes EDX better suited for the detection of heavier elements, complimentary to EELS.

EDX is generally a less efficient technique than EELS, due to the low probability of X-ray generation and small annular collection efficiency for the detectors.<sup>92</sup> However, there are a number of ways to maximise the signal, the most obvious of which is to collect the spectra for a longer period of time. This will improve the SNR, but its implementation is limited by a number of factors, including sample drift, contamination build up, and beam induced sample damage. Similarly a higher beam current may be used, so as to generate more signal, however this limits resolution and will exacerbate beam damage. Alternatively the detector may be optimised so as to maximise the detected signal. This may be achieved by increasing detector efficiency and/or increasing the detector size. Recent developments in the use of silicon drift detectors have increased detection efficiency, and increased the solid angle of the detectors.<sup>93</sup> Additionally, multiple detectors may be incorporated, increasing the total solid angle and capturing more of the emitted X-rays improving SNR. The super-X EDX system (as used in this work), has four detectors around the specimen to provide a larger collection solid angle of up to 0.9 sr.<sup>92,94</sup> A thicker specimen may also be used, which produces more X-rays for a given probe current and capture time. However, a larger interaction volume will reduce the spatial resolution of the X-ray signal, and limit the STEM imaging and EELS capabilities due to the increased scattering events.

Electron channelling may result in enhanced X-ray generation when the sample is orientated along a major zone axis.<sup>95,96</sup> This can complicate the quantitative analysis of the EDX spectra.<sup>97</sup> To maximise the quantitative accuracy of EDX spectra, the effect of

channelling should be minimised. This is achievable by tilting away from low zone axis and or by precessing the probe.<sup>97,98</sup>

In addition to the characteristic photons emitted by the sample, photons may be generated from a number of sources within the TEM column. The most abundant of which are continuous Bremsstrahlung X-rays, which form the background of the EDX spectra.<sup>15</sup> Bremsstrahlung radiation is a phenomena resulting from the deceleration of an electron, and forms a continuum as the electron may lose any amount of energy (up to the Duane-Hunt limit). The number of X-rays produced by this phenomena is calculated from Kramers' cross section.<sup>99</sup> This background must be removed in post processing, before quantitative analysis of the EDX spectra. Characteristic X-ray emission is isotropic, while the Bremsstrahlung is strongly forward scattered.<sup>100</sup> The SNR may therefore be maximised by placing the detector above the specimen.

A further concern is the generation of X-rays outside of the probe location, which may result in falsely attributing an element to the probe location. These X-rays may be generated by scattered electrons that may have interacted with a different region of the: specimen, specimen support, sample holder, or pole piece of the microscope. Copper (from the specimen support), iron (from the pole piece) and zirconium (from the EDX collimator), are common artefact peaks for my specimens. Secondary X-rays may also be produced by fluorescence from X-rays emitted with high energies, which are able to ionise other atoms. Minimisation of these X-rays can be achieved through experimental practice, such as minimising tilt of the holder, imaging away from grid bar and mounting specimens correctly. Low background EDX holders constructed with low atomic mass materials such as beryllium, and careful design can be used to reduce spurious X-rays from the holder.<sup>101</sup>

EDX spectrum images, HAADF and BF images (or EELS spectrum image in lieu of BF) may be collected simultaneously. The diverse collectable signals in the STEM, enabling the atomic structure and chemical identity to be assigned is an extraordinarily powerful for the study of nanomaterials.<sup>102-105</sup> This work primarily utilises HAADF STEM imaging and EDX spectrum imaging in the investigation of misfit layer chalcogenides (MLC).

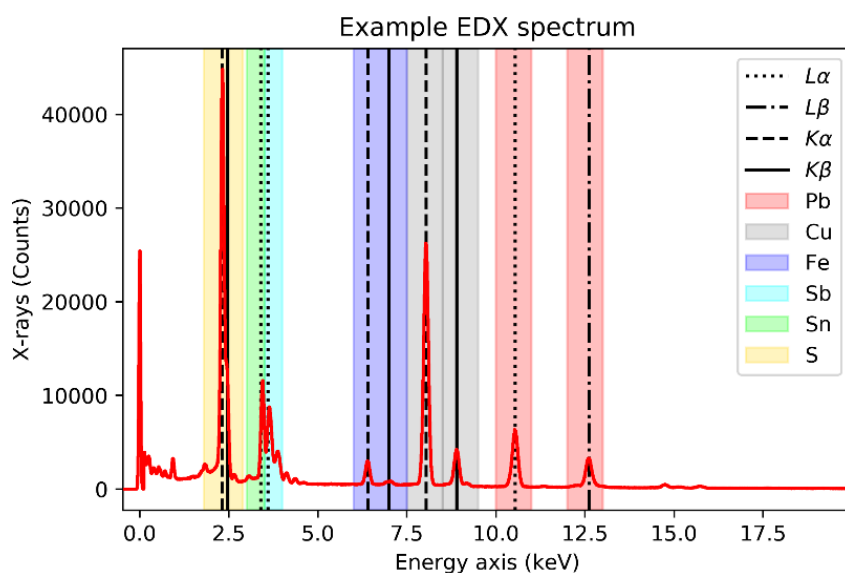


Figure 2-6- Example EDX spectrum of cylindrite sample, showing the characteristic elemental edges for Pb, Cu, Fe, Sb, Sn and S; and the Bremsstrahlung background. For clarity some peaks have not been labelled, including  $CK_{\alpha}$ ,  $OK_{\alpha}$ ,  $SbL_{\beta}$  and  $SnL_{\beta}$ .

### 2.1.2.3. Beam Damage

The quality of STEM data is often limited by specimen damage due to electron beam interaction.<sup>106</sup> The ultra-bright FEG electron sources with aberration correctors create very intense beams which exacerbate this damage. The damage propagates by two principal mechanisms, radiolysis and knock-on-damage.

Knock on damage is atomic displacement as a result of collisions between beam electrons with specimen nuclei.<sup>107</sup> Atomic displacement is the permanent relocation of an atom from its equilibrium position to an interstitial site, reducing the crystallinity of the sample.<sup>108</sup> Displacement of surface atoms can be removed to vacuum, resulting in electron induced sputtering of the sample. Atomic displacement occurs if the energy transfer is over a specimen dependant threshold energy.<sup>108</sup> Surface atoms are less strongly bonded than bulk atoms, and consequently will exhibit preferential sputtering.<sup>107</sup> Knock on damage may be alleviated by reducing beam energy, such that energy transfer is below the threshold energies. The sputtering rate may be reduced by adding a thin amorphous layer of high atomic mass material, on the exit surface.<sup>108</sup> It has also been shown that 2D materials encapsulated with graphene are more robust to knock on damage.<sup>109</sup>

Inelastic scattering events can induce radiolytic damage.<sup>108</sup> The transfer of energy to specimen nuclei may result in a single or grouped (plasmon) electronic transition. If while in an excited state the atom undergoes an atomic vibration, interatomic bonds may become broken, or may form a radical.<sup>110</sup> Consequently radiolysis may be reduced through the cooling of the sample, via the reduction in thermal phonons.<sup>110</sup> Radiolysis is more prevalent in insulators and semiconductors due to lower availability of free electrons compared to metals. The production of SEs in insulating and semiconducting samples can lead to additional ionisation events resulting in the cascade of radiolytic damage.<sup>110</sup> Further damage may be induced in insulating samples by electrostatic charging, which may result in sample damage by either ion migration or charge induced mechanical forces.<sup>110</sup> Radiolytic damage may be reduced by increasing beam energy, so as to increase the inelastic mean free path of the probe electrons.<sup>110</sup> However as discussed above, the higher incident beam energies will increase knock on damage. As such, beam energy should be selected to minimise the principal damage mechanism within the specimen; in conducting inorganic specimens this is knock on damage where insulating specimens are primarily limited by radiolytic damage.<sup>111</sup>

The most universal method to reduce beam damage is to reduce the specimen exposure to the electron probe. This has instigated the development of a number of “low dose” TEM techniques, including scanning solutions<sup>112,113</sup>, aloof beam techniques<sup>114</sup> and sparse sensing<sup>115,116</sup>. The charged nature of the electrons makes the applications of pulsed beams to mitigate beam damage challenging, as temporal confinement leads to spatial and energy spread of the probe due to coulomb repulsion.<sup>117,118</sup> Both total dose and dose rate are critical parameters for beam damage.<sup>108</sup> Jian and Spence demonstrated that specimen damage can be avoided, provided the dose rate is lower than the recovery rate of the specimen.<sup>119</sup> As such the effects of beam damage may be reduced through the use of sufficiently low beam currents. This damage recovery process has been studied in graphene, where sputtered holes were filled with semi-pristine graphene.<sup>120</sup> While beam damage is a hindrance for the characterisation of materials, it may be utilised to sculpt and manipulate materials at the nanoscale. This has been exploited in 2D materials in the formation of nanowires and nano-pores in graphene and TMDCs.<sup>121</sup>

The electron beam can also cause the build-up of mobile contamination, as it migrates to the charged region under the electron beam. Hydrocarbons are subsequently polymerised by the beam fixing the contaminants to the surface of the specimen.<sup>122,123</sup>

The build-up of contamination reduces the image resolution and contrast, and decreases EELS performance.<sup>124</sup> Contamination build up is worsened by the long acquisition times required for spectrum imaging. With the improvement in pump technology and use of liquid nitrogen cold traps, the majority of contamination comes from the sample itself rather than the microscope.<sup>125</sup> As such, effective sample preparation is crucial to ensure that contamination is minimised. Several techniques have been employed to reduce hydrocarbon contaminants, these include: plasma cleaning<sup>126</sup>, baking<sup>127</sup>, ultraviolet exposure<sup>128</sup>, washing in solvent<sup>127</sup>, cooling the specimen<sup>129</sup>, and “beam showering”<sup>108</sup>. “Beam showering” is the flooding of the surrounding regions, cracking the contaminants, reducing the build-up upon subsequent higher magnification scanning. These methods were reviewed by Mitchell<sup>124</sup>, who showed the preferred cleaning method is specimen dependant.

To minimise beam damage, I limited the exposure of the specimen to the beam and focused on a nearby area before moving to the region of interest. I took steps to mitigate the contamination by plasma cleaning the holder, and beam showering the sample when contamination was an issue.

#### **2.1.2.4. Specimen preparation**

There are a number of constraints on the samples which may be examined by TEM, in addition to those discussed in section 2.1.1. The lateral sample size is limited as the majority of TEM holders accept a 3mm disc specimen. As such the sample must be prepared in such a way that it may be securely loaded into the holder.

It is vital that the preparation step/s do not introduce artefacts. If artefacts are unavoidable it is vital they are minimised and are well characterised, so as to not lead to incorrect analysis of the data. To ensure faithful sample analysis and optimal imaging conditions, the crystallinity and structure of the sample must be retained, while the addition of amorphous layers should be minimised.

Crucially, the sample must also be sufficiently thin to allow for the electrons to transmit through the specimen. We have noted for optimal imaging and EELS



collection the electron may only undergo a single scattering event in the specimen. As the elastic scattering cross section is larger than the inelastic scattering cross section<sup>130</sup>, the elastic MFP,  $\lambda_{elas}$ , (equation 2.18, Where  $N_V$  is the number of atoms per unit volume and  $\sigma_{elas}$  is the elastic cross section)<sup>35</sup> can be used as a limit for specimen thickness.

$$\lambda_{elas} = \frac{1}{(N_V \sigma_{elas})} \quad 2.18$$

However, it is not always easy or even possible to prepare a sufficiently thin sample. A consequence of overly thick samples is a decrease in the obtainable resolution. This is, in part, due to a decrease in SNR and increase in apparent beam size. Equation 2.19 describes the minimum resolvable feature size,  $d_{feature}$ , which is a quadratic sum of the probe size due to the microscope  $d_{stem}$  (Equation 2.1), the size of the probe due to SNR,  $d_{SNR}$ , and  $d_{blur}$ , the size of the probe due to beam broadening.<sup>131</sup> For a feature to be visible and detectable, the SNR must be  $\geq 3$  and  $\geq 5$  respectively.<sup>132</sup> The minimum probe size due to SNR has been calculated by Schuh & de Jonge, and shown to be much larger than the probe in vacuum, in thick samples.<sup>133</sup> To maximise the SNR, contributions of noise signals should be minimised. Some common sources of background signal are the supportive substrates, embedding matrices and amorphous layers. Beam broadening is the increased diameter of the beam due to the elastic scattering as the electrons travel through the specimen. A thicker sample will have an increased number of scattering events, yielding an increased broadening effect.<sup>134</sup> The effect of beam broadening in thin films has been modelled in a number of different ways,<sup>135,136</sup> which were shown to be inaccurate when compared experimental data.<sup>131</sup> Gauvin & Rudinsky<sup>137</sup> successfully modelled beam broadening in a wide range of specimen thicknesses. The model produced predictions in good agreement with experimental data.<sup>131,134</sup> However, this model only applies to amorphous samples as it neglects the effects of electron channelling, which can reduce beam broadening within the specimen.<sup>134</sup> As such beam broadening may be minimised by using a thin sample and careful alignment of the specimen to a low zone axis.

$$d_{feature} = \sqrt{d_{STEM}^2 + d_{SNR}^2 + d_{blur}^2} \quad 2.19$$

There are numerous methods used to prepare samples suitable for TEM characterisation.<sup>138</sup> The best method is unique to each specimen and the desired viewing orientation (i.e. plan view or cross section). Within this work I prepared samples for cross section and plan view characterisation. The cross section samples were prepared using FIB. The dimensions of the materials investigated were typically between 100 – 500  $\mu\text{m}^2$  which required the site specific cross sectioning capabilities of FIB. The FIB is discussed in further detail in sections 2.1.4 and 3.5. Plan view samples were prepared by two methods, mechanical flake transfer of mechanically exfoliated flakes and drop casting liquid suspensions of crushed bulk material. The mechanical transfer allows for STEM characterisation of a specific flake of interest, which is well orientated to the [001] zone axis. However this method only allows for a small number of flakes to be examined. Drop casting allowed for a higher number of flakes to be deposited on a grid. Furthermore they are typically less aligned to the low order zone axis, which may improve elemental quantification by decreasing channelling.<sup>97</sup> These methods are described in further detail in sections 3.3 and 3.4 respectively.

### **2.1.3. The scanning electron microscope (SEM)**

The SEM was first developed in 1935 by Knoll<sup>139</sup>, and the first scanning electron instrument with sub-microscopic resolution was demonstrated in 1938 by von Ardenne<sup>140</sup>, utilising transmitted electrons. The creation of the modern SEM instrument is credited to Oatley's group, who extensively developed the SEM between 1950 and 1960.<sup>141</sup> The SEM forms a magnified image of a sample by scanning a focused electron probe (typically 1 – 30 keV) across a typically bulk sample. Comparisons may be drawn between STEM and SEM probe forming optics, and SEMs can be thought of as a low kV STEM. This comparison is validated further in the application of low kV STEM<sup>142</sup> and the inclusion of HAADF and BF electron detectors in some SEMS.<sup>143</sup> However, SEMs primarily image bulk specimens, through which electrons cannot transmit, and generate images by the collection of either BSEs or SEs. Modern SEMs are fitted with a range of electron detectors, with different geometries, producing images formed from different contrast mechanisms.<sup>144</sup> In addition to imaging, the crystallographic structure may be examined via electron backscattered diffraction (EBSD) detectors<sup>145</sup>, while local chemical information may be obtained through the inclusion of EDX or wavelength dispersive X-ray spectrometers.<sup>146</sup>

While the electron optics of SEMs are similar to STEMs, and often utilise FEGs as electron sources, the probe convergence semi-angle is substantially smaller than those used in STEM.<sup>147</sup> The smaller convergence semi-angle allows for a greater depth of focus, at the expense of a larger probe diameter. The SEM probe size is further increased compared to STEM, due to the lower beam energies and larger, typically uncorrected, aberrations. However the probe diameter is not as crucial in SEM as the resolution is dictated by the interaction volumes.

As discussed in previous sections (2.1.2), when the probe electron impinges with the specimen, the electron will undergo both elastic and inelastic scattering events. The loss of energy from the inelastic scattering events limits the distance an electron can travel through a specimen. As SEM is primarily used to analyse bulk samples, there are a sufficiently high number of inelastic events resulting in a sufficient energy loss that the electron may be absorbed by the sample.<sup>147</sup> Various methods have been used to estimate the distance an electron will travel in the specimen. A popular method was developed by Bethe in 1930<sup>100</sup>, in which the electron loses energy at a constant rate within the specimen. This method overestimates the penetration depth of the electrons, as it does not account for the change in path direction stemming from elastic collisions. The probabilistic nature of elastic scattering angles may be accounted for by describing an interaction volume, which provides a probability for an electron implanting in the specimen at a certain location. The interaction volume is sensitive to beam energy, specimen composition and tilt.<sup>148</sup> Kanaya and Okayama's method provides an estimation for a hemispherical interaction volume containing 95% of the electrons.<sup>149</sup> Accounting for the tortuous path of the electrons, induced by the elastic collisions, this radius is more accurate than the Bethe approximation. While useful to obtain an approximation for the interaction volume, accurate modelling may be achieved by Monte Carlo simulations.<sup>150</sup> These produce a random 3D trajectory for each electron within the specimen, for each of the thousands or millions of simulated electrons. The random trajectories provide a statistically accurate description of electron scattering within the specimen. In addition to producing electron trajectories, Monte Carlo simulations are able to estimate X-ray generation within the sample.<sup>151</sup>

The scattering angle of elastically scattered electrons ranges from a few degrees to 180 degrees (i.e. reflected). As such probe electrons entering the sample may be elastically

scattered through an angle greater than 90 degrees (by a single or multiple elastic scattering events) and exit the top surface. These electrons are referred to as BSE (Figure 2-7). The probability of elastic scattering is described by the elastic scattering cross section; the distance between scattering events is given by the elastic MFP (equation 2.18).<sup>35,147</sup> As elastic scattering preserves electron energy, BSE are highly energetic, keeping an appreciable amount of the original beam energy. However, as the electron will also undergo a random number of inelastic collisions within the specimen, the BSE will be emitted with a range of energies equal to or less than the original beam energy.<sup>148</sup> The distribution of BSE energies is dependent on both atomic number and beam energy. BSE emitted from heavier elements will retain a higher proportion of the original beam energy as the beam electrons undergo fewer inelastic scattering events before exiting the specimen.<sup>147</sup> The proportion of BSE emitted per incident beam electron is described by the BSE coefficient, which may not be greater than one. The BSE coefficient varies with the atomic number and crystal structure of the specimen, and as such SEM images produced from BSEs are sensitive to atomic composition.<sup>152</sup>

The transfer of energy from the beam electron to the specimen may also result in the emission of SEs. SEs are ejected outer shell electrons after the ionisation of an atom by the probe electron. These are arbitrarily defined as possessing less than 50 eV, although it is more common for SEs to have much lower energies.<sup>153</sup> After generation, SEs will undergo further energy loss events as they travel through the specimen further reducing their energy. Consequently the SEs may only travel a short distance before being absorbed, therefore only SE produced close to the surface will be emitted from the specimen.<sup>154</sup> An empirical model for the characteristic escape depth of SEs was described by Ono and Kanaya<sup>155</sup> (equation 2.20). Where  $d_{escape}$  is the characteristic depth (nm),  $A$  is the atomic weight,  $I$  is the first ionisation (eV) potential,  $\rho$  is the density and  $Z$  atomic number. The limited depth the electrons are able to emit from the sample make SEs extremely sensitive to local topography.

$$d_{escape} = \frac{0.267 A I}{(\rho Z^{0.66})} \quad 2.20$$

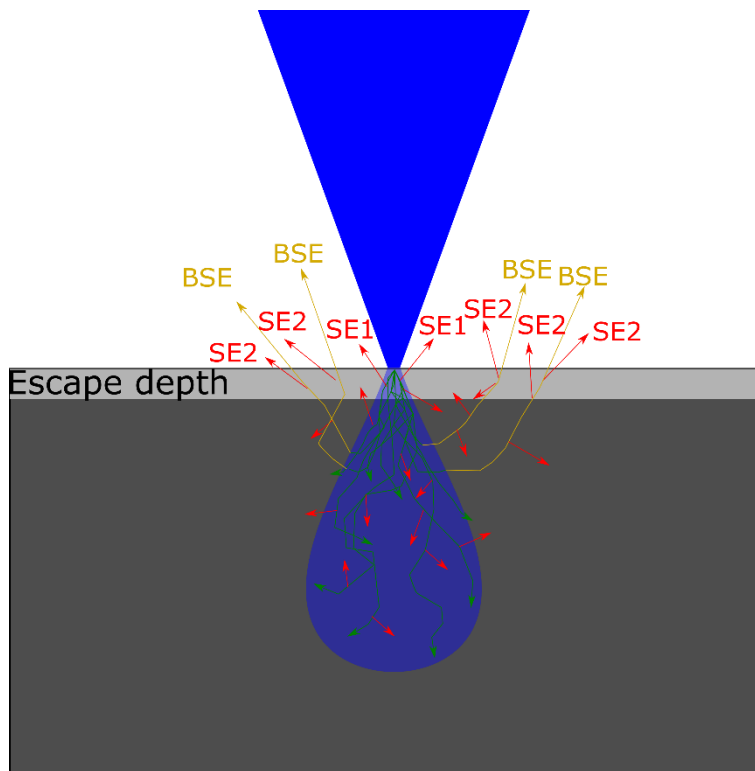


Figure 2-7 - Illustration of secondary electron (SE) generation in a bulk specimen. First generation SE (SE<sub>1</sub>) are generated as the probe electron enters the specimen and second generation SE (SE<sub>2</sub>) are generated as the back scattered electrons (BSE) exit the specimen. Note that only SE generated within the escape depth (light grey) successfully escape the specimen and are detectable. The light blue shaded region illustrates the interaction volume.

The SE coefficient, analogous to the BSE coefficient, describes the yield of detectable SEs per incident beam electron. The SE coefficient may be greater than one i.e. a single probe electron may produce more than one detectable SE. This is in part due to the possibility that the probe electron may undergo multiple inelastic scattering events within the escape depth of the specimen generating SE<sub>1</sub>. Detectable SEs are also produced by BSEs exiting the specimen undergoing inelastic collisions within the escape depth, these are assigned as SE<sub>2</sub>.<sup>156</sup> SEs may also be generated by interaction of BSE with internal surfaces of the SEM (e.g. chamber walls) or the probe impinging on misaligned apertures, denoted SE<sub>3</sub> and SE<sub>4</sub>.<sup>157</sup> The SE generation is summarised in Figure 2-7. SE<sub>1</sub> contain the most local information and therefore contribute the highest resolution information. SE<sub>2</sub>, generated from BSE, contain information corresponding to the BSE interaction volume, contributing lower resolution information. The number of SE<sub>2</sub> generated is greater than the number of SE<sub>1</sub>, with the ratio depending on both probe energy and specimen tilt.<sup>157</sup> For beam energies less than 5 keV, the SE<sub>2</sub>:SE<sub>1</sub> ratio

is approximately 4, and above 10 keV approximately 2. The  $SE_2:SE_1$  ratio decreases as the angle of the incidence of the probe electron increases.<sup>153</sup>

Within this work SEM SE imaging was performed, exploiting the sensitivity of SE to the sample topology.

#### **2.1.4. The focused ion beam (FIB)**

The FIB is similar to the SEM discussed in the previous section, except a focused probe of ions are used instead of electrons. The focused ion beam can be composed from metal ions (typically gallium)<sup>158</sup>, plasma<sup>159</sup> or helium ions<sup>160</sup>. The work presented here uses a gallium FIB. As such, discussion shall be limited to this type of instrument. When energetic ions impact on the specimen, as well as the generation of SEs as seen in the SEM, sample atoms may also be sputtered away from specimen, as charged or neutral species. The positively charged ions may be subsequently detected, offering a new imaging mode, although it is more typical to form an image by collecting ion generated SEs. However due to large chromatic aberrations and large source sizes, the imaging performance of ion beams is severely impaired. It is the ability to sputter material in a site specific manner, which is the primary function of the FIB and is a powerful technique for materials preparation and characterisation.

The key component to the FIB is the liquid metal source (LMS), which acts as the source of gallium ions. Within this, gallium wets a tungsten filament and ions are extracted by an electric field.<sup>161</sup> The ions are accelerated under a high potential (typically 1 – 30 kV) and formed into a focused beam by a series of apertures and electrostatic lenses. The LMS was originally developed for use in aerospace propulsion in the late 1950s, and successfully implemented in 1991.<sup>162</sup> Tangentially, the LMS was developed by the semiconductor industry and by the 1980s it was incorporated in to a single column instrument routinely used for device and lithography mask repair.<sup>163</sup>

The modern FIB instrument is a dual-beam system, in which ion and electron columns are combined into a single platform. Most instruments are fitted with additional features such as gas injection systems (GIS), micromanipulators, EDX and EBSD detectors. The GIS allows for the localised introduction of gasses to the specimen. These gasses allow for enhanced etch assisting<sup>164</sup> or local deposition of materials *in-situ*<sup>165</sup>. Etch assistant gasses (specimen specific) enhance etch rate by increasing the

volatility of the sputtered atoms reducing redeposition.<sup>166</sup> Alternatively, conducting or insulating layers may be deposited in a site specific manner. Precursor molecules are converted into deposited elemental material and volatile compounds, via ion or electron induced chemical reactions.<sup>165</sup> Deposited materials can be used to reduce charging, curtaining artefacts and ion beam damage which occurs during the milling process.<sup>167</sup> Micromanipulators allow for the precise handling of the specimen within the instrument. For TEM sample preparation, the manipulator allows for the *in-situ* transfer of the sample to the specialised TEM grid prior to thinning to electron transparency.<sup>167</sup> The combination of the two columns, GIS, micromanipulators, and various detectors, makes the modern dual beam FIB an extremely versatile instrument, which may be used in a range of applications such as: atom probe tip preparation<sup>168</sup>, failure analysis<sup>169</sup>, device modification<sup>170</sup>, chemical analysis<sup>171</sup>, biological applications<sup>172</sup> and TEM preparation.<sup>167</sup>

Energetic ions impacting on a sample will undergo a series of elastic and inelastic scattering events, before eventually implanting in the specimen; analogous to the fate of probe electrons in SEM. However as ions elastically scatter, the momentum transfer is sufficiently high as to sputter the material away, allowing for modification of the sample.<sup>173</sup> Furthermore each primary scattering event can go on to generate secondary collision events, a process known as a collision cascade.<sup>173</sup> The sputtering of material, is in competition with redeposition where the sputtered material deposits back on the specimen.<sup>174</sup> The effective milling rate is then given by the sputtering and redeposition rates. If the sputtering rate is equal to the redeposition rate, no milling will occur, but the sample will be damaged with a reduction in crystallinity.<sup>175</sup> The sputtering rate is affected by a number of specimen characteristics including surface binding energy, atomic number and density. There are a number of controllable parameters, the most important of which are the flux and energy of the ions which are controlled by ion beam current and acceleration potential respectively. The use of a higher current and accelerating potential will increase sputtering yield, but with less spatial resolution and increased beam damage.<sup>161</sup> The sputtering rate is also influenced by dwell time, crystal orientation and geometry of the milled region. Increased probe dwell times yield enhanced sputter rates, through the overlapping collision cascades.<sup>158,176</sup> If the sample is orientated to a low zone axis the ions will

experience channelling and travel further through the specimen. This was found to reduce both the milling and redeposition rate and produce a 'cleaner' mill, an effect more noticeable in copper than in silicon.<sup>177</sup> The geometry of the mill also dictates sputtering rate, with deep high aspect ratio mills particularly challenging to mill. This is due to the reduction in the ability of the sputtered atoms to escape, increasing the redeposition rate. For extremely deep trenches, an etchant gas may be used to increase the volatility of the sputtered atoms reducing the deposition.<sup>164</sup>

In addition to sputtering, as the cascade propagates through the sample, atoms will be displaced from their equilibrium positions resulting in highly defective/amorphous regions of the sample.<sup>175</sup> Relaxation to original crystal structure, is always accompanied by an amorphous region.<sup>178</sup> The relaxation process is sensitive to ion flux and energy, as it dictates the initial damage radius, and the ability of the specimen to recover crystallinity. The optimal ion beam energy and current is therefore a balance between minimising beam damage, and ensuring the sputtering rate is sufficiently high to be practically useful and limit amorphisation of the specimen. Furthermore recrystallisation is sensitive to temperature, unit cell, composition and material parameters.<sup>179</sup> Consequently beam conditions which may damage one material, will cause minimal damage to another, exemplified by induced amorphous regions in silicon while copper remains unchanged, under the same ion beam conditions.<sup>175</sup> The MLCs characterised in this work are complex materials and are composed of heavy elements (Pb, Sn, Sb, Fe, S) with a large unit cell and a complex phase relationship. As such it is expected that they will be less robust to beam induced amorphisation.

The FIB instrument is a powerful tool for TEM sample preparation as it is able to prepare samples in a site specific manner from different sample orientations. The preparation of TEM cross sections utilises all the features of a modern dual-beam system. The region of interest is identified using the SEM column, utilising its superior imaging capability while avoiding exposing the area to unnecessary ion beam exposure. Protective layers (I used Pt) are added *in-situ* by electron and ion beams induced deposition. The sample is milled free from the substrate and transferred to a specialised grid using a micro-manipulator *in-situ*. The sample is then subsequently thinned using lower beam energies and currents as the sample is progressively thinned



to electron transparency, in order to minimise damage. The procedure used within the work is described in section 3.5.

In addition to the ion beam induced damage discussed above, the accurate thickness determination of the lamellae in the FIB is challenging. Accurate thickness estimation is crucial for producing high quality TEM lamellae, as overly thick images will compromise imaging capabilities, while overly thin specimens will be exposed to the ion beam unnecessarily and may even be destroyed. Currently the assessment of lamellae thickness requires the experience of a skilled user, to qualitatively determine the thickness. Some quantitative methods have been developed<sup>180-183</sup> however they are currently insufficiently accurate or incompatible for use in TEM sample preparation. This topic is discussed extensively in section 6 where a novel approach for *in-situ* real time measurement of lamellae thickness is presented.

Cross sections prepared by FIB have been crucial in the characterisation of both 2D materials<sup>7,184-189</sup> and MLCs<sup>190-192</sup>. Within this work a dual beam FIB was used to prepare cross sections from MLCs exfoliated on Si/SiO<sub>2</sub> substrates for both STEM HAADF and STEM EDX characterisation.

## 2.1.5. References

- 1 Pennycook, S. J. The impact of STEM aberration correction on materials science. *Ultramicroscopy* **180**, 22-33 (2017).
- 2 Klar, T. A., Engel, E. & Hell, S. W. Breaking Abbe's diffraction resolution limit in fluorescence microscopy with stimulated emission depletion beams of various shapes. *Physical Review E* **64**, 066613 (2001).
- 3 Klar, T. A. & Hell, S. W. Subdiffraction resolution in far-field fluorescence microscopy. *Opt. Lett.* **24**, 954-956 (1999).
- 4 Williams, D. B. & Carter, C. B. in *Transmission Electron Microscopy: A Textbook for Materials Science* (eds David B. Williams & C. Barry Carter) 23-38 (Springer US, 2009).
- 5 Ruska, E. & Knoll, M. Die magnetische Sammelspule für schnelle Elektronenstrahlen. *The magnetic concentrating coil for fast electron beams.* *Z. techn. Physik* **12**, 389-400 (1931).
- 6 Knoll, M. & Ruska, E. Das Elektronenmikroskop. *Z. Physik* **78**, 318-339 (1932).
- 7 Withers, F., Del Pozo-Zamudio, O., Mishchenko, A., Rooney, A. P., Gholinia, A., Watanabe, K., Taniguchi, T., Haigh, S. J., Geim, A. K., Tartakovskii, A. I. & Novoselov, K. S. Light-emitting diodes by band-structure engineering in van der Waals heterostructures. *Nature materials* **14**, 301-306 (2015).
- 8 Li, C., Wu, Y., Poplawsky, J., Pennycook, T. J., Paudel, N., Yin, W., Haigh, S. J., Oxley, M. P., Lupini, A. R., Al-Jassim, M., Pennycook, S. J. & Yan, Y. Grain-Boundary-Enhanced Carrier Collection in CdTe Solar Cells. *Physical Review Letters* **112**, 156103 (2014).
- 9 Jasim, D. A., Murphy, S., Newman, L., Mironov, A., Prestat, E., McCaffrey, J., Ménard-Moyon, C., Rodrigues, A. F., Bianco, A., Haigh, S., Lennon, R. & Kostarelos, K. The Effects of Extensive Glomerular Filtration of Thin Graphene Oxide Sheets on Kidney Physiology. *ACS Nano* **10**, 10753-10767 (2016).
- 10 Radtke, G. & Botton, G. A. in *Scanning Transmission Electron Microscopy: Imaging and Analysis* (eds Stephen J. Pennycook & Peter D. Nellist) 207-245 (Springer New York, 2011).
- 11 Scherzer, O. Über einige Fehler von Elektronenlinsen. *Z. Physik* **101**, 593-603 (1936).
- 12 Scherzer, O. SPHARISCHE UND CHROMATISCHE KORREKTUR VON ELEKTRONEN-LINSEN. *Optik* **2**, 114-132 (1947).
- 13 Krivanek, O. L., Corbin, G. J., Dellby, N., Elston, B. F., Keyse, R. J., Murfitt, M. F., Own, C. S., Szilagy, Z. S. & Woodruff, J. W. An electron microscope for the aberration-corrected era. *Ultramicroscopy* **108**, 179-195 (2008).
- 14 Cowley, J. M. IMAGE CONTRAST IN A TRANSMISSION SCANNING ELECTRON MICROSCOPE. *Appl Phys Lett* **15**, 58-59 (1969).
- 15 Botton, G. in *Science of Microscopy* (eds Peter W. Hawkes & John C. H. Spence) 273-405 (Springer New York, 2007).
- 16 Slater, T. J. *Three Dimensional Chemical Analysis of Nanoparticles Using Energy Dispersive X-ray Spectroscopy* Doctor of Philosophy thesis, University of Manchester, (2015).
- 17 Crewe, A. V. Scanning transmission electron microscopy. *Journal of microscopy* **100**, 247-259 (1974).
- 18 Crewe, A. V., Wall, J. & Welter, L. M. A High-Resolution Scanning Transmission Electron Microscope. *Journal of Applied Physics* **39**, 5861-5868 (1968).

- 19 Treacy, M. M. J., Howie, A. & Wilson, C. J. Z contrast of platinum and palladium catalysts. *Philosophical Magazine A* **38**, 569-585 (1978).
- 20 Smith, D. J. The realization of atomic resolution with the electron microscope. *Reports on Progress in Physics* **60**, 1513 (1997).
- 21 Haider, M., Rose, H., Uhlemann, S., Schwan, E., Kabius, B. & Urban, K. A spherical-aberration-corrected 200kV transmission electron microscope. *Ultramicroscopy* **75**, 53-60 (1998).
- 22 Krivanek, O. L., Dellby, N. & Lupini, A. R. Towards sub-Å electron beams. *Ultramicroscopy* **78**, 1-11 (1999).
- 23 Zaluzec, N. J. The influence of Cs/Cc correction in analytical imaging and spectroscopy in scanning and transmission electron microscopy. *Ultramicroscopy* **151**, 240-249 (2015).
- 24 Hawkes, P. W. The correction of electron lens aberrations. *Ultramicroscopy* **156**, A1-A64 (2015).
- 25 Haigh, S. J. & Kirkland, A. I. in *Aberration-Corrected Analytical Transmission Electron Microscopy* (ed R. Brydson) (2011).
- 26 Williams, D. B. & Carter, C. B. *Transmission Electron Microscopy: A Textbook for Materials Science*. (Springer Science, 2009).
- 27 Buban, J. P., Ramasse, Q., Gipson, B., Browning, N. D. & Stahlberg, H. High-resolution low-dose scanning transmission electron microscopy. *Journal of Electron Microscopy* **59**, 103-112 (2010).
- 28 Hansen, P. L., Wagner, J. B., Helveg, S., Rostrup-Nielsen, J. R., Clausen, B. S. & Topsøe, H. Atom-Resolved Imaging of Dynamic Shape Changes in Supported Copper Nanocrystals. *Science* **295**, 2053-2055 (2002).
- 29 Yoshida, H., Kuwauchi, Y., Jinschek, J. R., Sun, K., Tanaka, S., Kohyama, M., Shimada, S., Haruta, M. & Takeda, S. Visualizing Gas Molecules Interacting with Supported Nanoparticulate Catalysts at Reaction Conditions. *Science* **335**, 317-319 (2012).
- 30 de Jonge, N. & Ross, F. M. Electron microscopy of specimens in liquid. *Nature nanotechnology* **6**, 695 (2011).
- 31 Jianbo, W., Hao, S., Wenlong, C., Xin, G., Peng, T., Chengyi, S., Wen, S. & Tao, D. In Situ Environmental TEM in Imaging Gas and Liquid Phase Chemical Reactions for Materials Research. *Advanced Materials* **28**, 9686-9712 (2016).
- 32 Parkinson, G. M. High resolution, in-situ controlled atmosphere transmission electron microscopy (CATEM) of heterogeneous catalysts. *Catalysis Letters* **2**, 303-307 (1989).
- 33 Chiu, C.-H., Huang, C.-W., Hsieh, Y.-H., Chen, J.-Y., Chang, C.-F., Chu, Y.-H. & Wu, W.-W. In-situ TEM observation of Multilevel Storage Behavior in low power FeRAM device. *Nano Energy* **34**, 103-110 (2017).
- 34 Pham, T., Gibb, A. L., Li, Z., Gilbert, S. M., Song, C., Louie, S. G. & Zettl, A. Formation and Dynamics of Electron-Irradiation-Induced Defects in Hexagonal Boron Nitride at Elevated Temperatures. *Nano letters* **16**, 7142-7147 (2016).
- 35 Nellist, P. D. in *Science of Microscopy* (eds Peter W. Hawkes & John C. H. Spence) 65-132 (Springer New York, 2007).
- 36 Nellist, P. D. in *Scanning Transmission Electron Microscopy: Imaging and Analysis* (eds Stephen J. Pennycook & Peter D. Nellist) 91-115 (Springer New York, 2011).

- 37 Dellby, N., Krivanek, L., Nellist, D., Batson, E. & Lupini, R. Progress in aberration-corrected scanning transmission electron microscopy. *Journal of Electron Microscopy* **50**, 177-185 (2001).
- 38 Zach, J. & Haider, M. Aberration correction in a low voltage SEM by a multipole corrector. *Nuclear Instruments and Methods in Physics Research Section A: Accelerators, Spectrometers, Detectors and Associated Equipment* **363**, 316-325 (1995).
- 39 Bleloch, A. & Ramasse, Q. in *Aberration-Corrected Analytical Transmission Electron Microscopy* (ed R. Brydson) (John Wiley & Sons, Ltd, 2011).
- 40 Terauchi, Tanaka, Tsuno & Ishida. Development of a high energy resolution electron energy-loss spectroscopy microscope. *Journal of microscopy* **194**, 203-209 (1999).
- 41 Mukai, M., Kim, J. S., Omoto, K., Sawada, H., Kimura, A., Ikeda, A., Zhou, J., Kaneyama, T., Young, N. P., Warner, J. H., Nellist, P. D. & Kirkland, A. I. The development of a 200kV monochromated field emission electron source. *Ultramicroscopy* **140**, 37-43 (2014).
- 42 Tiemeijer, P. C. Measurement of Coulomb interactions in an electron beam monochromator. *Ultramicroscopy* **78**, 53-62 (1999).
- 43 Essers, E., Benner, G., Mandler, T., Meyer, S., Mittmann, D., Schnell, M. & Höschen, R. Energy resolution of an Omega-type monochromator and imaging properties of the MANDOLINE filter. *Ultramicroscopy* **110**, 971-980 (2010).
- 44 Krivanek, O. L., Lovejoy, T. C., Dellby, N. & Carpenter, R. W. Monochromated STEM with a 30 meV-wide, atom-sized electron probe. *Microscopy* **62**, 3-21 (2013).
- 45 Haider, M., Müller, H., Uhlemann, S., Zach, J., Loebau, U. & Hoeschen, R. Prerequisites for a Cc/Cs-corrected ultrahigh-resolution TEM. *Ultramicroscopy* **108**, 167-178 (2008).
- 46 Kabius, B., Hartel, P., Haider, M., Müller, H., Uhlemann, S., Loebau, U., Zach, J. & Rose, H. First application of Cc-corrected imaging for high-resolution and energy-filtered TEM. *Journal of Electron Microscopy* **58**, 147-155 (2009).
- 47 Egerton, R. F. in *Electron Energy-Loss Spectroscopy in the Electron Microscope* 1-28 (Springer US, 2011).
- 48 Hetherington, C. Aberration correction for TEM. *Materials Today* **7**, 50-55 (2004).
- 49 Cowley, J. M. & Moodie, A. F. The scattering of electrons by atoms and crystals. I. A new theoretical approach. *Acta Crystallographica* **10**, 609-619 (1957).
- 50 Madsen, J., Liu, P., Wagner, J. B., Hansen, T. W. & Schiøtz, J. Accuracy of surface strain measurements from transmission electron microscopy images of nanoparticles. *Advanced Structural and Chemical Imaging* **3**, 14 (2017).
- 51 Kirkland, A. I., Chang, S. L.-Y. & Hutchison, J. L. in *Science of Microscopy* (eds Peter W. Hawkes & John C. H. Spence) 3-64 (Springer New York, 2007).
- 52 Nellist, P. D. & Pennycook, S. J. Incoherent imaging using dynamically scattered coherent electrons. *Ultramicroscopy* **78**, 111-124 (1999).
- 53 Goodhew, P. in *Aberration-Corrected Analytical Transmission Electron Microscopy* (ed R. Brydson) (John Wiley & Sons, Ltd, 2011).
- 54 Nellist, P. D. in *Aberration-Corrected Analytical Transmission Electron Microscopy* (ed R. Brydson) (John Wiley & Sons, Ltd, 2011).
- 55 Crewe, A. V. & Wall, J. A scanning microscope with 5 Å resolution. *Journal of Molecular Biology* **48**, 375-393 (1970).

- 56 Reimer, L. & Hagemann, P. Recording of mass thickness in scanning transmission electron microscopy. *Ultramicroscopy* **2**, 297-301 (1976).
- 57 Midgley, P. A. & Weyland, M. 3D electron microscopy in the physical sciences: the development of Z-contrast and EFTEM tomography. *Ultramicroscopy* **96**, 413-431 (2003).
- 58 Hirsch, P. B. & Whelan, M. J. A kinematical theory of diffraction contrast of electron transmission microscope images of dislocations and other defects. *Philosophical Transactions of the Royal Society of London. Series A, Mathematical and Physical Sciences* **252**, 499-529 (1960).
- 59 Phillips, P. J., Brandes, M. C., Mills, M. J. & De Graef, M. Diffraction contrast STEM of dislocations: Imaging and simulations. *Ultramicroscopy* **111**, 1483-1487 (2011).
- 60 Cowley, J. M. Coherent interference in convergent-beam electron diffraction and shadow imaging. *Ultramicroscopy* **4**, 435-449 (1979).
- 61 Crewe, A. V. The physics of the high-resolution scanning microscope. *Reports on Progress in Physics* **43**, 621 (1980).
- 62 Hall, C. R. & Hirsch, P. B. Effect of thermal diffuse scattering on propagation of high energy electrons through crystals. *Proceedings of the Royal Society of London. Series A. Mathematical and Physical Sciences* **286**, 158-177 (1965).
- 63 Amali, A. & Rez, P. Theory of Lattice Resolution in High-angle Annular Dark-field Images. *Microscopy and Microanalysis* **3**, 28-46 (1997).
- 64 Jesson, D. E. & Pennycook, S. J. Incoherent imaging of crystals using thermally scattered electrons. *Proceedings of the Royal Society of London. Series A: Mathematical and Physical Sciences* **449**, 273-293 (1995).
- 65 A. Muller, D., Edwards, B., J. Kirkland, E. & Silcox, J. Simulation of thermal diffuse scattering including a detailed phonon dispersion curve. *Ultramicroscopy* **86**, 371-380 (2001).
- 66 Van Dyck, D. Persistent misconceptions about incoherence in electron microscopy. *Ultramicroscopy* **111**, 894-900 (2011).
- 67 Hartel, P., Rose, H. & Dinges, C. Conditions and reasons for incoherent imaging in STEM. *Ultramicroscopy* **63**, 93-114 (1996).
- 68 Treacy, M. M. J. Z Dependence of Electron Scattering by Single Atoms into Annular Dark-Field Detectors. *Microscopy and Microanalysis* **17**, 847-858 (2011).
- 69 Ishikawa, R., Lugg, N. R., Inoue, K., Sawada, H., Taniguchi, T., Shibata, N. & Ikuhara, Y. Interfacial Atomic Structure of Twisted Few-Layer Graphene. *Scientific reports* **6**, 21273 (2016).
- 70 Shibata, N., Kohno, Y., Findlay, S. D., Sawada, H., Kondo, Y. & Ikuhara, Y. New area detector for atomic-resolution scanning transmission electron microscopy. *Journal of Electron Microscopy* **59**, 473-479 (2010).
- 71 Haruta, M., Komatsu, H., Kurata, H., Azuma, M., Shimakawa, Y. & Isoda, S. 117-118 (Springer Berlin Heidelberg).
- 72 Cowley, J. M. & Huang, Y. De-channelling contrast in annular dark-field STEM. *Ultramicroscopy* **40**, 171-180 (1992).
- 73 Yu, Z., Muller, D. A. & Silcox, J. Study of strain fields at a-Si/c-Si interface. *Journal of Applied Physics* **95**, 3362-3371 (2004).
- 74 Pennycook, S. J. & Jesson, D. E. High-resolution incoherent imaging of crystals. *Physical Review Letters* **64**, 938-941 (1990).

- 75 Martinez, G. T., Jones, L., De Backer, A., Béch , A., Verbeeck, J., Van Aert, S. & Nellist, P. D. Quantitative STEM normalisation: The importance of the electron flux. *Ultramicroscopy* **159**, 46-58 (2015).
- 76 Jones, L. Quantitative ADF STEM: acquisition, analysis and interpretation. *IOP Conference Series: Materials Science and Engineering* **109**, 012008 (2016).
- 77 De Backer, A., Jones, L., Lobato, I., Altantzis, T., Goris, B., Nellist, P. D., Bals, S. & Van Aert, S. Three-dimensional atomic models from a single projection using Z-contrast imaging: verification by electron tomography and opportunities. *Nanoscale* **9**, 8791-8798 (2017).
- 78 Krivanek, O. L., Chisholm, M. F., Dellby, N. & Murfitt, M. F. in *Scanning Transmission Electron Microscopy: Imaging and Analysis* (eds Stephen J. Pennycook & Peter D. Nellist) 615-658 (Springer New York, 2011).
- 79 Pennycook, S. J. in *Scanning Transmission Electron Microscopy: Imaging and Analysis* (eds Stephen J. Pennycook & Peter D. Nellist) 1-90 (Springer New York, 2011).
- 80 Brydson, R. in *Electron Energy Loss Spectroscopy* (ed P. Barlass) (Taylor & Francis, 2001).
- 81 Williams, D. B. & Carter, C. B. in *Transmission Electron Microscopy: A Textbook for Materials Science* 67-83 (Springer US, 1996).
- 82 Lovejoy, T. C., Bacon, N. J., Bleloch, A. L., Dellby, N., Hoffman, M. V. & Krivanek, O. L. Ultra-High Energy Resolution EELS. *Microscopy and Microanalysis* **23**, 1552-1553 (2017).
- 83 Brockt, G. & Lakner, H. Nanoscale EELS analysis of dielectric function and bandgap properties in GaN and related materials. *Micron* **31**, 435-440 (2000).
- 84 Park, J., Heo, S., Chung, J.-G., Kim, H., Lee, H., Kim, K. & Park, G.-S. Bandgap measurement of thin dielectric films using monochromated STEM-EELS. *Ultramicroscopy* **109**, 1183-1188 (2009).
- 85 Vendelbo, S. B., Kooyman, P. J., Creemer, J. F., Morana, B., Mele, L., Dona, P., Nelissen, B. J. & Helveg, S. Method for local temperature measurement in a nanoreactor for in situ high-resolution electron microscopy. *Ultramicroscopy* **133**, 72-79 (2013).
- 86 Egerton, R. F. in *Electron Energy-Loss Spectroscopy in the Electron Microscope* 293-397 (Springer US, 2011).
- 87 Schmid, H. K. & Mader, W. Oxidation states of Mn and Fe in various compound oxide systems. *Micron* **37**, 426-432 (2006).
- 88 Verbeeck, J. & Van Aert, S. Model based quantification of EELS spectra. *Ultramicroscopy* **101**, 207-224 (2004).
- 89 Scott, J., Thomas, P. J., MacKenzie, M., McFadzean, S., Wilbrink, J., Craven, A. J. & Nicholson, W. A. P. Near-simultaneous dual energy range EELS spectrum imaging. *Ultramicroscopy* **108**, 1586-1594 (2008).
- 90 Bambynek, W., Crasemann, B., Fink, R. W., Freund, H. U., Mark, H., Swift, C. D., Price, R. E. & Rao, P. V. X-Ray Fluorescence Yields, Auger, and Coster-Kronig Transition Probabilities. *Rev. Mod. Phys.* **44**, 716-813 (1972).
- 91 Krause, M. O. Atomic radiative and radiationless yields for K and L shells. *Journal of Physical and Chemical Reference Data* **8**, 307-327 (1979).
- 92 Von Harrach, H., Dona, P., Freitag, B., Soltau, H., Niculae, A. & Rohde, M. An integrated silicon drift detector system for FEI Schottky field emission transmission electron microscopes. *Microscopy and Microanalysis* **15**, 208 (2009).

- 93 Falke, M., Kroemer, R., Fissler, D. & Rohde, M. News on Silicon Drift Detectors for X-Ray Nanoanalysis in S/TEM. *Microscopy and Microanalysis* **16**, 2-3 (2010).
- 94 Slater, T. J. A., Camargo, P. H. C., Burke, M. G., Zaluzec, N. J. & Haigh, S. J. Understanding the limitations of the Super-X energy dispersive x-ray spectrometer as a function of specimen tilt angle for tomographic data acquisition in the S/TEM. *Journal of Physics: Conference Series* **522**, 012025 (2014).
- 95 Duncumb, P. Enhanced X-ray emission from extinction contours in a single-crystal gold film. *The Philosophical Magazine: A Journal of Theoretical Experimental and Applied Physics* **7**, 2101-2105 (1962).
- 96 Bramman, J. I. & Yates, G. Crystal orientation dependence of X-ray production in bulk specimens. *The Philosophical Magazine: A Journal of Theoretical Experimental and Applied Physics* **17**, 195-198 (1968).
- 97 Lugg, N. R., Kothleitner, G., Shibata, N. & Ikuhara, Y. On the quantitiveness of EDS STEM. *Ultramicroscopy* **151**, 150-159 (2015).
- 98 Liao, Y. & Marks, L. D. Reduction of electron channeling in EDS using precession. *Ultramicroscopy* **126**, 19-22 (2013).
- 99 Kramers, H. A. XCIII. On the theory of X-ray absorption and of the continuous X-ray spectrum. *The London, Edinburgh, and Dublin Philosophical Magazine and Journal of Science* **46**, 836-871 (1923).
- 100 Bethe, H. Zur Theorie des Durchgangs schneller Korpuskularstrahlen durch Materie. *Annalen der Physik* **397**, 325-400 (1930).
- 101 von Harrach, H. S., Freitag, B., Gerits, W. & Sandborg, A. Optimization of EDX performance in Tecnai TEMs. *Micron* **34**, 185-188 (2003).
- 102 Lewis, E. A., Haigh, S. J., Slater, T. J. A., He, Z., Kulzick, M. A., Burke, M. G. & Zaluzec, N. J. Real-time imaging and local elemental analysis of nanostructures in liquids. *Chemical communications* **50**, 10019-10022 (2014).
- 103 Senga, R. & Suenaga, K. Single-atom electron energy loss spectroscopy of light elements. *Nature communications* **6**, 7943 (2015).
- 104 Toth, P. S., Velický, M., Bissett, M. A., Slater, T. J. A., Savjani, N., Rabiou, A. K., Rakowski, A. M., Haigh, S. J., O'Brien, P. & Dryfe, R. A. W. *Construction of Asymmetric MoS<sub>2</sub>-Graphene Sandwiches: Preparation, Functionalization, Characterisation and Application* (Universtiy of Manchester, 2015).
- 105 Hu, S., Gopinadhan, K., Rakowski, A., Neek-Amal, M., Heine, T., Grigorieva, I. V., Haigh, S. J., Peeters, F. M., Geim, A. K. & Lozada-Hidalgo, M. Transport of hydrogen isotopes through interlayer spacing in van der Waals crystals. *Nature nanotechnology* **13**, 468-472 (2018).
- 106 Egerton, R. F., Wang, F. & Crozier, P. A. Beam-Induced Damage to Thin Specimens in an Intense Electron Probe. *Microscopy and Microanalysis* **12**, 65-71 (2006).
- 107 Egerton, R. F., McLeod, R., Wang, F. & Malac, M. Basic questions related to electron-induced sputtering in the TEM. *Ultramicroscopy* **110**, 991-997 (2010).
- 108 Egerton, R. F., Li, P. & Malac, M. Radiation damage in the TEM and SEM. *Micron* **35**, 399-409 (2004).
- 109 Zan, R., Ramasse, Q. M., Jalil, R., Georgiou, T., Bangert, U. & Novoselov, K. S. Control of Radiation Damage in MoS<sub>2</sub> by Graphene Encapsulation. *ACS Nano* **7**, 10167-10174 (2013).
- 110 Egerton, R. F. Control of radiation damage in the TEM. *Ultramicroscopy* **127**, 100-108 (2013).

- 111 Egerton, R. F. Mechanisms of radiation damage in beam-sensitive specimens, for TEM accelerating voltages between 10 and 300 kV. *Microscopy Research and Technique* **75**, 1550-1556 (2012).
- 112 Sang, X., Lupini, A. R., Unocic, R. R., Chi, M., Borisevich, A. Y., Kalinin, S. V., Endeve, E., Archibald, R. K. & Jesse, S. Dynamic scan control in STEM: spiral scans. *Advanced Structural and Chemical Imaging* **2**, 6 (2016).
- 113 Sader, K., Schaffer, B., Vaughan, G., Brydson, R., Brown, A. & Bleloch, A. Smart acquisition EELS. *Ultramicroscopy* **110**, 998-1003 (2010).
- 114 Egerton, R. F. Vibrational-loss EELS and the avoidance of radiation damage. *Ultramicroscopy* **159**, 95-100 (2015).
- 115 Binev, P., Dahmen, W., DeVore, R., Lamby, P., Savu, D. & Sharpley, R. in *Modeling Nanoscale Imaging in Electron Microscopy* (eds Thomas Vogt, Wolfgang Dahmen, & Peter Binev) 73-126 (Springer US, 2012).
- 116 Stevens, A., Yang, H., Carin, L., Arslan, I. & Browning, N. D. The potential for Bayesian compressive sensing to significantly reduce electron dose in high-resolution STEM images. *Microscopy* **63**, 41-51 (2014).
- 117 Armstrong, M. R., Boyden, K., Browning, N. D., Campbell, G. H., Colvin, J. D., DeHope, W. J., Frank, A. M., Gibson, D. J., Hartemann, F., Kim, J. S., King, W. E., LaGrange, T. B., Pyke, B. J., Reed, B. W., Shuttlesworth, R. M., Stuart, B. C. & Torralva, B. R. Practical considerations for high spatial and temporal resolution dynamic transmission electron microscopy. *Ultramicroscopy* **107**, 356-367 (2007).
- 118 Boersch, H. Experimentelle Bestimmung der Energieverteilung in thermisch ausgelösten Elektronenstrahlen. *Z. Physik* **139**, 115-146 (1954).
- 119 Jiang, N. & Spence, J. C. H. On the dose-rate threshold of beam damage in TEM. *Ultramicroscopy* **113**, 77-82 (2012).
- 120 Zan, R., Ramasse, Q. M., Bangert, U. & Novoselov, K. S. Graphene reknits its holes. *Nano letters* **12**, 3936-3940 (2012).
- 121 Susi, T., Meyer, J. C. & Kotakoski, J. Manipulating low-dimensional materials down to the level of single atoms with electron irradiation. *Ultramicroscopy* **180**, 163-172 (2017).
- 122 Stewart, R. L. Insulating Films Formed Under Electron and Ion Bombardment. *Physical Review* **45**, 488-490 (1934).
- 123 Ennos, A. E. The origin of specimen contamination in the electron microscope. *British Journal of Applied Physics* **4**, 101 (1953).
- 124 Mitchell, D. R. G. Contamination mitigation strategies for scanning transmission electron microscopy. *Micron* **73**, 36-46 (2015).
- 125 Soong, C., Hoyle, D., Malac, M. & Egerton, R. The sources of contamination of TEM samples and the means for its reduction. *Microscopy and Microanalysis* **18**, 1480-1481 (2012).
- 126 Griffiths, A. J. V. & Walther, T. Quantification of carbon contamination under electron beam irradiation in a scanning transmission electron microscope and its suppression by plasma cleaning. *Journal of Physics: Conference Series* **241**, 012017 (2010).
- 127 McGilvery, C. M., Goode, A. E., Shaffer, M. S. P. & McComb, D. W. Contamination of holey/lacey carbon films in STEM. *Micron* **43**, 450-455 (2012).
- 128 Hoyle, D., Malac, M., Trudeau, M. & Woo, P. UV Treatment of TEM/STEM Samples for Reduced Hydrocarbon Contamination. *Microscopy and Microanalysis* **17**, 1026-1027 (2011).



- 129 Egerton, R. F. & Rossouw, C. J. Direct measurement of contamination and etching rates in an electron beam. *Journal of Physics D: Applied Physics* **9**, 659 (1976).
- 130 Konstantin, I. & Kazutaka, M. Elastic scattering of 200 keV electrons in elemental solids: experimental observation of atomic-number-dependent oscillatory behavior. *Journal of Physics: Condensed Matter* **21**, 155402 (2009).
- 131 de Jonge, N., Verch, A. & Demers, H. The Influence of Beam Broadening on the Spatial Resolution of Annular Dark Field Scanning Transmission Electron Microscopy. *Microscopy and Microanalysis* **24**, 8-16 (2018).
- 132 Natusch, M. K. H., Humphreys, C. J., Menon, N. & Krivanek, O. L. Experimental and theoretical study of the detection limits in electron energy-loss spectroscopy. *Micron* **30**, 173-183 (1999).
- 133 Schuh, T. & de Jonge, N. Liquid scanning transmission electron microscopy: Nanoscale imaging in micrometers-thick liquids. *Comptes Rendus Physique* **15**, 214-223 (2014).
- 134 Drees, H., Müller, E., Dries, M. & Gerthsen, D. Electron-beam broadening in amorphous carbon films in low-energy scanning transmission electron microscopy. *Ultramicroscopy* **185**, 65-71 (2018).
- 135 Goldstein, J. I. in *Introduction to Analytical Electron Microscopy* (eds John J. Hren, Joseph I. Goldstein, & David C. Joy) 83-120 (Springer US, 1979).
- 136 Kohl, H. & Reimer, L. in *Transmission Electron Microscopy: Physics of Image Formation* 139-192 (Springer New York, 2008).
- 137 Gauvin, R. & Rudinsky, S. A universal equation for computing the beam broadening of incident electrons in thin films. *Ultramicroscopy* **167**, 21-30 (2016).
- 138 Williams, D. B. & Carter, C. B. in *Transmission Electron Microscopy: A Textbook for Materials Science* 173-193 (Springer US, 2009).
- 139 Knoll, M. Static potential and secondary emission of bodies under electron irradiation. *Z Tech Physik* **16**, 467 (1935).
- 140 von Ardenne, M. Das Elektronen-Rastermikroskop. *Z. Physik* **109**, 553-572 (1938).
- 141 Oatley, C. W. The early history of the scanning electron microscope. *Journal of Applied Physics* **53**, R1-R13 (1982).
- 142 Sasaki, T., Sawada, H., Hosokawa, F., Sato, Y. & Suenaga, K. Aberration-corrected STEM/TEM imaging at 15kV. *Ultramicroscopy* **145**, 50-55 (2014).
- 143 Beyer, Y., Beanland, R. & Midgley, P. A. Low voltage STEM imaging of multi-walled carbon nanotubes. *Micron* **43**, 428-434 (2012).
- 144 Goldstein, J. I., Newbury, D. E., Michael, J. R., Ritchie, N. W. M., Scott, J. H. J. & Joy, D. C. in *Scanning Electron Microscopy and X-Ray Microanalysis* (eds Joseph I. Goldstein et al.) 65-91 (Springer New York, 2018).
- 145 Wilkinson, A. J. & Britton, T. B. Strains, planes, and EBSD in materials science. *Materials Today* **15**, 366-376 (2012).
- 146 Porat, R., Porst, A., Lohse, J., Matke, G. & Rebien, M. in *2010 IEEE/SEMI Advanced Semiconductor Manufacturing Conference (ASMC)*. 123-128.
- 147 Goldstein, J. I., Newbury, D. E., Michael, J. R., Ritchie, N. W. M., Scott, J. H. J. & Joy, D. C. in *Scanning Electron Microscopy and X-Ray Microanalysis* (eds Joseph I. Goldstein et al.) 1-14 (Springer New York, 2018).
- 148 Joy, D. C. Beam interactions, contrast and resolution in the SEM. *Journal of microscopy* **136**, 241-258 (1984).

- 149 Kanaya, K. & Okayama, S. Penetration and energy-loss theory of electrons in solid targets. *Journal of Physics D: Applied Physics* **5**, 43 (1972).
- 150 Shimizu, R. & Ding, Z.-J. Monte Carlo modelling of electron-solid interactions. *Reports on Progress in Physics* **55**, 487 (1992).
- 151 Drouin, D., Couture, A. R., Joly, D., Tastet, X., Aimez, V. & Gauvin, R. CASINO V2.42—A Fast and Easy-to-use Modeling Tool for Scanning Electron Microscopy and Microanalysis Users. *Scanning* **29**, 92-101 (2007).
- 152 Skedros, J. G., Bloebaum, R. D., Bachus, K. N., Boyce, T. M. & Constantz, B. Influence of mineral content and composition on graylevels in backscattered electron images of bone. *Journal of Biomedical Materials Research* **27**, 57-64 (1993).
- 153 Reichelt, R. in *Science of Microscopy* (eds Peter W. Hawkes & John C. H. Spence) 133-272 (Springer New York, 2007).
- 154 Seiler, H. Secondary electron emission in the scanning electron microscope. *Journal of Applied Physics* **54**, R1-R18 (1983).
- 155 Ono, S. & Kanaya, K. The energy dependence of secondary emission based on the range-energy retardation power formula. *Journal of Physics D: Applied Physics* **12**, 619 (1979).
- 156 Joy, D. C. A model for calculating secondary and backscattered electron yields. *Journal of microscopy* **147**, 51-64 (1987).
- 157 Goldstein, J. I., Newbury, D. E., Michael, J. R., Ritchie, N. W. M., Scott, J. H. J. & Joy, D. C. in *Scanning Electron Microscopy and X-Ray Microanalysis* (eds Joseph I. Goldstein *et al.*) 29-37 (Springer New York, 2018).
- 158 Yamaguchi, H., Shimase, A., Haraichi, S. & Miyauchi, T. Characteristics of silicon removal by fine focused gallium ion beam. *Journal of Vacuum Science & Technology B: Microelectronics Processing and Phenomena* **3**, 71-74 (1985).
- 159 Garnier, A., Filoni, G., Hrnčíř, T. & Hladík, L. Plasma FIB: Enlarge your field of view and your field of applications. *Microelectronics Reliability* **55**, 2135-2141 (2015).
- 160 Maas, D. J. & van Gastel, R. in *Surface Science Techniques* (eds Gianangelo Bracco & Bodil Holst) 461-497 (Springer Berlin Heidelberg, 2013).
- 161 Giannuzzi, L. A. & Stevie, F. A. A review of focused ion beam milling techniques for TEM specimen preparation. *Micron* **30**, 197-204 (1999).
- 162 Mitterauer, J. Micropropulsion for small spacecraft: a new challenge for field effect electric propulsion and microstructured liquid metal ion sources. *Surface and Interface Analysis* **36**, 380-386 (2004).
- 163 Melngailis, J. Focused ion beam technology and applications. *Journal of Vacuum Science & Technology B: Microelectronics Processing and Phenomena* **5**, 469-495 (1987).
- 164 Young, R. J., Cleaver, J. R. A. & Ahmed, H. Gas-assisted focused ion beam etching for microfabrication and inspection. *Microelectronic Engineering* **11**, 409-412 (1990).
- 165 Langfischer, H., Basnar, B., Hutter, H. & Bertagnolli, E. Evolution of tungsten film deposition induced by focused ion beam. *Journal of Vacuum Science & Technology A* **20**, 1408-1415 (2002).
- 166 Casey, J. D., Doyle, A. F., Lee, R. G., Stewart, D. K. & Zimmermann, H. Gas-assisted etching with focused ion beam technology. *Microelectronic Engineering* **24**, 43-50 (1994).

- 167 Schaffer, M., Schaffer, B. & Ramasse, Q. Sample preparation for atomic-resolution STEM at low voltages by FIB. *Ultramicroscopy* **114**, 62-71 (2012).
- 168 Choi, P.-P., Al-Kassab, T. a., Kwon, Y.-S., Kim, J.-S. & Kirchheim, R. Application of Focused Ion Beam to Atom Probe Tomography Specimen Preparation from Mechanically Alloyed Powders. *Microscopy and Microanalysis* **13**, 347-353 (2007).
- 169 Shaver, D. C. & Ward, B. W. Integrated circuit diagnosis using focused ion beams. *Journal of Vacuum Science & Technology B: Microelectronics Processing and Phenomena* **4**, 185-188 (1986).
- 170 Melngailis, J., Musil, C. R., Stevens, E. H., Utlaut, M., Kellogg, E. M., Post, R. T., Geis, M. W. & Mountain, R. W. The focused ion beam as an integrated circuit restructuring tool. *Journal of Vacuum Science & Technology B: Microelectronics Processing and Phenomena* **4**, 176-180 (1986).
- 171 Hoener, C. F., Shaver, B. & Nguyen, T. T. Auger analysis of etch residues in submicrometer via holes using focused ion beam sample preparation. *Surface and Interface Analysis* **23**, 83-88 (1995).
- 172 Nalla, R. K., Porter, A. E., Daraio, C., Minor, A. M., Radmilovic, V., Stach, E. A., Tomsia, A. P. & Ritchie, R. O. Ultrastructural examination of dentin using focused ion-beam cross-sectioning and transmission electron microscopy. *Micron* **36**, 672-680 (2005).
- 173 Giannuzzi, L. A., Prenitzer, B. I. & Kempshall, B. W. in *Introduction to Focused Ion Beams: Instrumentation, Theory, Techniques and Practice* (eds Lucille A. Giannuzzi & Fred A. Stevie) 13-52 (Springer US, 2005).
- 174 Winter, D. A. M. d., Mulders, J. J. L. & E., P. Redeposition characteristics of focused ion beam milling for nanofabrication. *Journal of Vacuum Science & Technology B: Microelectronics and Nanometer Structures Processing, Measurement, and Phenomena* **25**, 2215-2218 (2007).
- 175 Rubanov, S. & Munroe, P. R. FIB-induced damage in silicon. *Journal of microscopy* **214**, 213-221 (2004).
- 176 Santamore, D., Edinger, K., Orloff, J., Melngailis, J., X., X., D., D. R. A., J., S. & J., M. Focused ion beam sputter yield change as a function of scan speed. *Journal of Vacuum Science & Technology B: Microelectronics and Nanometer Structures Processing, Measurement, and Phenomena* **15**, 2346-2349 (1997).
- 177 Kempshall, B. W., Schwarz, S. M., Prenitzer, B. I., Giannuzzi, L. A., Irwin, R. B., Stevie, F. A., E., F. R., G., K. E. C., A., C. J. R. & H., A. Ion channeling effects on the focused ion beam milling of Cu. *Journal of Vacuum Science & Technology B: Microelectronics and Nanometer Structures Processing, Measurement, and Phenomena* **19**, 749-754 (2001).
- 178 Morehead, F. F. & Crowder, B. L. A model for the formation of amorphous Si by ion bombardment. *Radiation Effects* **6**, 27-32 (1970).
- 179 Hooghan, K. B. N. in *Introduction to Focused Ion Beams: Instrumentation, Theory, Techniques and Practice* (eds Lucille A. Giannuzzi & Fred A. Stevie) 87-106 (Springer US, 2005).
- 180 van Mierlo, W., Geiger, D., Robins, A., Stumpf, M., Ray, M. L., Fischione, P. & Kaiser, U. Practical aspects of the use of the X<sup>2</sup> holder for HRTEM-quality TEM sample preparation by FIB. *Ultramicroscopy* **147**, 149-155 (2014).
- 181 Salzer, R., Graff, A., Simon, M. & Altmann, F. Standard Free Thickness Determination of Thin TEM Samples via Backscatter Electron Image Correlation. *Microscopy and Microanalysis* **15**, 340-341 (2009).

- 182 Golla-Schindler, U. in *EMC 2008 14th European Microscopy Congress 1–5 September 2008, Aachen, Germany: Volume 1: Instrumentation and Methods* (eds Martina Luysberg, Karsten Tillmann, & Thomas Weirich) 667-668 (Springer Berlin Heidelberg, 2008).
- 183 Hiscock, M., Dawson, M., Lang, C., Hartfield, C. & Statham, P. In-Situ Quantification of TEM Lamella Thickness and Ga Implantation in the FIB. *Microscopy and Microanalysis* **20**, 342-343 (2014).
- 184 Georgiou, T., Jalil, R., Belle, B. D., Britnell, L., Gorbachev, R. V., Morozov, S. V., Kim, Y. J., Gholinia, A., Haigh, S. J., Makarovskiy, O., Eaves, L., Ponomarenko, L. A., Geim, A. K., Novoselov, K. S. & Mishchenko, A. Vertical field-effect transistor based on graphene-WS<sub>2</sub> heterostructures for flexible and transparent electronics. *Nature nanotechnology* **8**, 100-103 (2013).
- 185 Haigh, S. J., Gholinia, A., Jalil, R., Romani, S., Britnell, L., Elias, D. C., Novoselov, K. S., Ponomarenko, L. A., Geim, A. K. & Gorbachev, R. Cross-sectional imaging of individual layers and buried interfaces of graphene-based heterostructures and superlattices. *Nature materials* **11**, 764-767 (2012).
- 186 Rooney, A. P., Kozikov, A., Rudenko, A. N., Prestat, E., Hamer, M. J., Withers, F., Cao, Y., Novoselov, K. S., Katsnelson, M. I., Gorbachev, R. & Haigh, S. J. Observing Imperfection in Atomic Interfaces for van der Waals Heterostructures. *Nano letters* **17**, 5222-5228 (2017).
- 187 Cao, Y., Mishchenko, A., Yu, G. L., Khestanova, E., Rooney, A. P., Prestat, E., Kretinin, A. V., Blake, P., Shalom, M. B., Woods, C., Chapman, J., Balakrishnan, G., Grigorieva, I. V., Novoselov, K. S., Piot, B. A., Potemski, M., Watanabe, K., Taniguchi, T., Haigh, S. J., Geim, A. K. & Gorbachev, R. V. Quality Heterostructures from Two-Dimensional Crystals Unstable in Air by Their Assembly in Inert Atmosphere. *Nano letters* **15**, 4914-4921 (2015).
- 188 Wang, L., Meric, I., Huang, P. Y., Gao, Q., Gao, Y., Tran, H., Taniguchi, T., Watanabe, K., Campos, L. M., Muller, D. A., Guo, J., Kim, P., Hone, J., Shepard, K. L. & Dean, C. R. One-dimensional electrical contact to a two-dimensional material. *Science* **342**, 614-617 (2013).
- 189 Cui, X., Lee, G.-H., Kim, Y. D., Arefe, G., Huang, P. Y., Lee, C.-H., Chenet, D. A., Zhang, X., Wang, L., Ye, F., Pizzocchero, F., Jessen, B. S., Watanabe, K., Taniguchi, T., Muller, D. A., Low, T., Kim, P. & Hone, J. Multi-terminal transport measurements of MoS<sub>2</sub> using a van der Waals heterostructure device platform. *Nature nanotechnology* **10**, 534 (2015).
- 190 Velický, M., Toth, P. S., Rakowski, A. M., Rooney, A. P., Kozikov, A., Woods, C. R., Mishchenko, A., Fumagalli, L., Yin, J., Zólyomi, V., Georgiou, T., Haigh, S. J., Novoselov, K. S. & Dryfe, R. A. W. Exfoliation of natural van der Waals heterostructures to a single unit cell thickness. *Nature communications* **8**, 14410 (2017).
- 191 Lin, Q., Smeller, M., Heideman, C. L., Zschack, P., Koyano, M., Anderson, M. D., Kykyneshi, R., Keszler, D. A., Anderson, I. M. & Johnson, D. C. Rational Synthesis and Characterization of a New Family of Low Thermal Conductivity Misfit Layer Compounds [(PbSe)<sub>0.99</sub>]<sub>m</sub>(WSe<sub>2</sub>)<sub>n</sub>. *Chemistry of Materials* **22**, 1002-1009 (2010).
- 192 Merrill, D. R., Moore, D. B., Ditto, J., Sutherland, D. R., Falmbigl, M., Winkler, M., Pernau, H.-F. & Johnson, D. C. The Synthesis, Structure, and Electrical Characterization of (SnSe)<sub>1.2</sub>TiSe<sub>2</sub>. *European Journal of Inorganic Chemistry* **2015**, 83-91 (2014).

## 2.2. 2D and van der Waals (vdW) materials

Van der Waals (vdW) materials are those which are composed of strongly covalent planes held together by weak van der Waals interactions. The weak interlayer bonding allows for the facile cleavage of the planes from the bulk. Cleavage vdW materials have been exploited in a variety of applications including pencils, dry lubricants<sup>1</sup> and for calibration of scanning tunnelling electron microscopes<sup>2</sup>. This cleavage was also exploited in the isolation of the first free standing atomic thin material graphene, which was cleaved from graphite.<sup>3</sup> It was long thought that 2D materials were unstable with respect to formation of other low dimensional allotropes, however graphene (and other 2D crystals) have been shown to be stable in a range of environments.<sup>4</sup> The stability of graphene (and other 2D crystals) is thought to be due to in part to creases introducing a 3D component to the structure.<sup>5</sup>

The isolation and characterisation of graphene was first achieved using micromechanical exfoliation of highly orientated pyrolytic graphene, colloquially known as the “scotch tape” method.<sup>3</sup> Utilising thin film interference, graphene was exfoliated onto a Si/SiO<sub>2</sub> substrate, so as to be visible in optical microscopes.<sup>4</sup> While seemingly trivial, the ability to view under standard optical microscopes has allowed for the great strides in graphene and 2D materials device fabrication.<sup>4</sup> Since the discovery of graphene more than a decade ago, the field of 2D materials has been heavily researched, spanning a broad range of subject areas.<sup>6</sup> A consequence of this broad interest in 2D materials, is the varied usage of the term ‘2D’. Here we shall define a 2D material as a one which exhibits a large aspect ratio between the lateral and thickness dimensions.

The properties of these 2D crystals often demonstrate a thickness dependence. This is perhaps most apparent in graphene’s band structure, transitioning from a linear dispersion in monolayer with massless Dirac fermions as charge carriers, to a non-linear dispersion with massive Dirac fermion charge carries in bilayer. The band structure of bulk graphite is recovered quickly with additional graphene layers.<sup>7</sup>

Concerted research effort has led to the isolation of a large number of new 2D materials, yielding an extensive library of materials with unique electrical, mechanical, chemical properties.<sup>8</sup> Two of the most important are insulating hexagonal boron

nitride (h-BN)<sup>9</sup> and transition metal dichalcogenides (TMDCs)<sup>10</sup>. TMDCs are of particular relevance as the misfit layer chalcogenides (MLCs) investigated in this work typically contain TMDC like layers. As such these TMDC materials are discussed in some depth. TMDCs are a group of compounds with a general formula of  $TX_2$ , where T is a transition metal (Ti, Zr, Hf, V, Nb, Ta, Mo, W, Tc, Re, Pd and Pt) and X is a chalcogen (S, Se or Te). They consist of a three atom thick covalently bonded monolayers, in which the metal is sandwiched by chalcogen atoms.<sup>11</sup> The planes are held together by weak out-of-plane vdW interactions between chalcogen atoms, allowing for facile cleavage. The metals are arranged in a hexagonal lattice, and coordinated to six chalcogen atoms. The coordination environment varies between octahedral or trigonal prismatic. Multilayer TMDCs may also exist in different stacking sequences (polytypes), with the most common being tetragonal with a octahedral metal coordination(1T), hexagonal with trigonal metal coordination(2H), and rhombohedral with trigonal metal coordination (3R) (Figure 2-8).<sup>11</sup> The preferred coordination environment and polytype depends on both the metal and chalcogen.<sup>12</sup> Most TMDCs are produced synthetically by chemical vapour transport methods<sup>13</sup>, with  $MoS_2$ <sup>14</sup>, and  $WS_2$ <sup>15</sup> also formed as natural minerals. It has been shown that synthesis conditions affect the coordination, stacking and properties.<sup>16</sup>

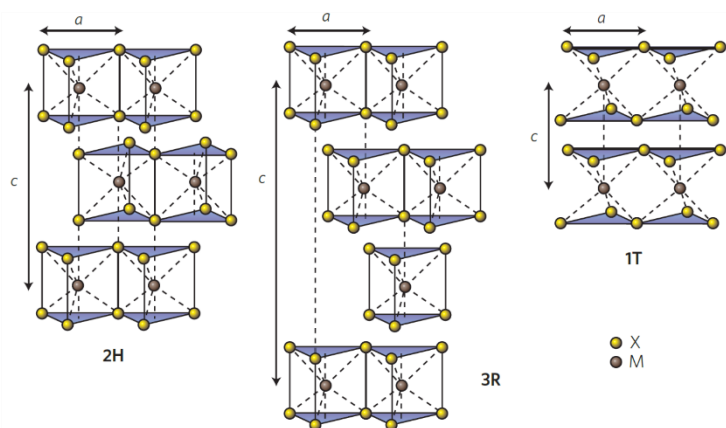


Figure 2-8 Illustrations of the typical stacking types in TMDCs, 2H with AbA BcB stacking; 3R AbA BcB CaC stacking; and 1T AbC stacking. Where the uppercase and lower case letters denote chalcogen and metal positions respectively.(Altered with permission from Copyright © 2012, Springer Nature<sup>10</sup>)

TMDCs have a diverse range of electronic properties, including semi-conducting, semi-metallic, metallic and super conducting.<sup>8,10</sup> Currently the most widely researched TMDCs are  $MoS_2$ ,  $MoSe_2$ ,  $WS_2$  and  $WSe_2$ . All of these exhibit a transition from indirect

to direct gap semiconductors, and a change in band gap as the thickness is reduced to monolayer. Monolayer materials possess direct band gaps with a technologically useful band gaps range, 1.5 – 2.1 eV, and unique band structure making them well suited to range of applications.<sup>10</sup> Interestingly TMDCs may be arguably be the first class of materials to be successfully characterised as a 2D material, when Frindt exfoliated MoS<sub>2</sub> using “...stripping technique using adhesive tape.” in 1966.<sup>17</sup> Despite this the exploration of TMDCs as isolated 2D materials only occurred after the isolation of graphene in 2004.

In addition to graphene, h-BN and TMDCs, the 2D materials library includes poor metal monochalcogenides<sup>18,19</sup>, ‘xene’ crystals, silicene<sup>20</sup>, germanene<sup>21</sup>, stanene<sup>22</sup> and phosphorene<sup>23</sup>; micas and high temperature superconductors<sup>24</sup>. Detailed discussion of the properties of these crystals is beyond the scope of this thesis, but it is important to note that the properties are diverse and highly complementary with: insulating, semi-conducting, metallic, topological insulating and superconducting 2D crystals available.<sup>8</sup> As such, by selectively layering individual 2D crystals on top of each other it is possible to create increasingly more complex structures with tailored properties. These layers are held together by vdW interactions and are known as vdW heterostructures.<sup>8,24</sup> One of the simplest vdW heterostructures, graphene encapsulated in h-BN, has been vital in realising graphene’s full potential. It was understood very quickly that inherent defects, inhomogeneity in the silicon dioxide substrate, in addition to trapped contamination, impacted the electrical properties of graphene. It was shown that using h-BN as an atomically flat, chemically inert substrate allowed the theoretical limits of graphene’s properties to be realised.<sup>25</sup> Boron nitride substrates have subsequently been shown to be vitally useful for contacting 2D crystals<sup>9</sup>, researching fundamental electrical properties of graphene<sup>26</sup> and use as a tunnel barrier<sup>27</sup>. More complex vdW heterostructure devices have been demonstrated for use as light emitting diodes<sup>28</sup>, transistors<sup>29</sup>, optoelectronics<sup>10</sup>, and molecular sensors<sup>30,31</sup>.

Bespoke 3D structures are typically formed by mechanical stacking of individual 2D layers, building the heterostructure a single layer at a time.<sup>32</sup> This enables the precise placement and alignment of flakes, and allows for any arbitrary layering order. Furthermore, the interfaces are often atomically sharp, and are not limited by lattice mismatch of the layers, which plagues traditional techniques such as molecular beam

epitaxy (MBE).<sup>32</sup> This micromechanical exfoliation and stacking may also be applied to atmospherically sensitive crystals, such as black phosphorus or NbSe<sub>2</sub>, through the use of an inert atmosphere glovebox.<sup>33</sup> However, this mechanical exfoliation and stacking technique is a slow process and incompatible with industrial scale production. Alternative production methods include inkjet printed heterostructures from liquid exfoliated 2D crystals<sup>34,35</sup>, chemical vapour deposition (CVD) and molecular epitaxy methods<sup>8</sup>.

Inkjet printing has been demonstrated to be useful in certain applications, including identity tags<sup>34</sup>, flexible electronics<sup>35</sup>, hydrogen evolution<sup>36</sup> and photovoltaics<sup>37</sup>. However, the number of 2D crystals available by liquid exfoliation is substantially reduced, and typically yield low concentrations of monolayer flakes.<sup>38</sup> Furthermore, the inability to produce atomically defined interfaces, and issues with inhomogeneous flake sizes and solvent affects, limit the application of these printed heterostructures.<sup>34</sup> Bottom up synthetic method CVD has been shown to be a promising technique, via successful demonstrations of h-BN encapsulated monolayer graphene<sup>39</sup>, with various combinations of TMDCs/graphene/h-BN vdW heterostructures formed<sup>8,40</sup> and in-plane heterostructures.<sup>41</sup> However, again CVD is currently restricted in the number of accessible crystals, primarily limited to TMDCs MoS<sub>2</sub>/MoSe<sub>2</sub>/WS<sub>2</sub>/WSe<sub>2</sub>, graphene and h-BN. There are also difficulties in control of the number of layers, and ability to form repeated layering<sup>42</sup> Further limitations include small domain sizes<sup>43,44</sup>, defects, doping and contamination<sup>42</sup>. As such CVD, while promising, is currently unable to fabricate high quality large area devices for a wide range of 2D crystals.



### 2.2.1. References

- 1 Domínguez-Meister, S., Rojas, T. C., Brizuela, M. & Sánchez-López, J. C. Solid lubricant behavior of MoS<sub>2</sub> and WSe<sub>2</sub>-based nanocomposite coatings. *Science and Technology of Advanced Materials* **18**, 122-133 (2017).
- 2 Chang, H. & Bard, A. J. Observation and characterization by scanning tunneling microscopy of structures generated by cleaving highly oriented pyrolytic graphite. *Langmuir : the ACS journal of surfaces and colloids* **7**, 1143-1153 (1991).
- 3 Novoselov, K. S., Geim, A. K., Morozov, S. V., Jiang, D., Zhang, Y., Dubonos, S. V., Grigorieva, I. V. & Firsov, A. A. Electric Field Effect in Atomically Thin Carbon Films. *Science* **306**, 666-669 (2004).
- 4 Geim, A. K. & Novoselov, K. S. The rise of graphene. *Nature materials* **6**, 183-191 (2007).
- 5 Meyer, J. C., Geim, A. K., Katsnelson, M. I., Novoselov, K. S., Booth, T. J. & Roth, S. The structure of suspended graphene sheets. *Nature* **446**, 60 (2007).
- 6 Novoselov, K. S., Falko, V. I., Colombo, L., Gellert, P. R., Schwab, M. G. & Kim, K. A roadmap for graphene. *Nature* **490**, 192-200 (2012).
- 7 Neto, A. C., Guinea, F., Peres, N., Novoselov, K. S. & Geim, A. K. The electronic properties of graphene. *Rev. Mod. Phys.* **81**, 109 (2009).
- 8 Novoselov, K. S., Mishchenko, A., Carvalho, A. & Castro Neto, A. H. 2D materials and van der Waals heterostructures. *Science* **353** (2016).
- 9 Wang, L., Meric, I., Huang, P. Y., Gao, Q., Gao, Y., Tran, H., Taniguchi, T., Watanabe, K., Campos, L. M., Muller, D. A., Guo, J., Kim, P., Hone, J., Shepard, K. L. & Dean, C. R. One-dimensional electrical contact to a two-dimensional material. *Science* **342**, 614-617 (2013).
- 10 Wang, Q. H., Kalantar-Zadeh, K., Kis, A., Coleman, J. N. & Strano, M. S. Electronics and optoelectronics of two-dimensional transition metal dichalcogenides. *Nature nanotechnology* **7**, 699 (2012).
- 11 Chhowalla, M., Shin, H. S., Eda, G., Li, L.-J., Loh, K. P. & Zhang, H. The chemistry of two-dimensional layered transition metal dichalcogenide nanosheets. *Nature chemistry* **5**, 263 (2013).
- 12 Wilson, J. A. & Yoffe, A. D. The transition metal dichalcogenides discussion and interpretation of the observed optical, electrical and structural properties. *Advances in Physics* **18**, 193-335 (1969).
- 13 Schutte, W. J., De Boer, J. L. & Jellinek, F. Crystal structures of tungsten disulfide and diselenide. *Journal of Solid State Chemistry* **70**, 207-209 (1987).
- 14 Stotu, U. & Marntall, T. Molybdenite polytypes in theory and occurrence. II. Some naturally-occurring polytypes of molybdenite. *The American Mineralogist* **55** (1970).
- 15 Gait, R. & Mandarino, J. Polytypes of tungstenite. *The Canadian Mineralogist* **10**, 729-731 (1970).
- 16 Lee, J.-U., Kim, K., Han, S., Ryu, G. H., Lee, Z. & Cheong, H. Raman Signatures of Polytypism in Molybdenum Disulfide. *ACS Nano* **10**, 1948-1953 (2016).
- 17 Frindt, R. F. Single Crystals of MoS<sub>2</sub> Several Molecular Layers Thick. *Journal of Applied Physics* **37**, 1928-1929 (1966).
- 18 Bandurin, D. A., Tyurnina, A. V., Yu, G. L., Mishchenko, A., Zólyomi, V., Morozov, S. V., Kumar, R. K., Gorbachev, R. V., Kudrynskyi, Z. R., Pezzini, S., Kovalyuk, Z. D., Zeitler, U., Novoselov, K. S., Patanè, A., Eaves, L., Grigorieva, I. V., Fal'ko, V.

- I., Geim, A. K. & Cao, Y. High electron mobility, quantum Hall effect and anomalous optical response in atomically thin InSe. *Nature nanotechnology* **12**, 223 (2016).
- 19 Hu, P., Wen, Z., Wang, L., Tan, P. & Xiao, K. Synthesis of Few-Layer GaSe Nanosheets for High Performance Photodetectors. *ACS Nano* **6**, 5988-5994 (2012).
- 20 Zhao, J., Liu, H., Yu, Z., Quhe, R., Zhou, S., Wang, Y., Liu, C. C., Zhong, H., Han, N., Lu, J., Yao, Y. & Wu, K. Rise of silicene: A competitive 2D material. *Progress in Materials Science* **83**, 24-151 (2016).
- 21 Dávila, M. E., Xian, L., Cahangirov, S., Rubio, A. & Lay, G. L. Germanene: a novel two-dimensional germanium allotrope akin to graphene and silicene. *New Journal of Physics* **16**, 095002 (2014).
- 22 Zhu, F.-f., Chen, W.-j., Xu, Y., Gao, C.-l., Guan, D.-d., Liu, C.-h., Qian, D., Zhang, S.-C. & Jia, J.-f. Epitaxial growth of two-dimensional stanene. *Nature materials* **14**, 1020-1025 (2015).
- 23 Liu, H., Neal, A. T., Zhu, Z., Luo, Z., Xu, X., Tománek, D. & Ye, P. D. Phosphorene: An Unexplored 2D Semiconductor with a High Hole Mobility. *ACS Nano* **8**, 4033-4041 (2014).
- 24 Geim, A. K. & Grigorieva, I. V. Van der Waals heterostructures. *Nature* **499**, 419-425 (2013).
- 25 Dean, C. R., Young, A. F., Meric, I., Lee, C., Wang, L., Sorgenfrei, S., Watanabe, K., Taniguchi, T., Kim, P., Shepard, K. L. & Hone, J. Boron nitride substrates for high-quality graphene electronics. *Nature nanotechnology* **5**, 722 (2010).
- 26 Krishna Kumar, R., Bandurin, D. A., Pellegrino, F. M. D., Cao, Y., Principi, A., Guo, H., Auton, G. H., Ben Shalom, M., Ponomarenko, L. A., Falkovich, G., Watanabe, K., Taniguchi, T., Grigorieva, I. V., Levitov, L. S., Polini, M. & Geim, A. K. Superballistic flow of viscous electron fluid through graphene constrictions. *Nature Physics* **13**, 1182 (2017).
- 27 Lee, G.-H., Yu, Y.-J., Lee, C., Dean, C., Shepard, K. L., Kim, P. & Hone, J. Electron tunneling through atomically flat and ultrathin hexagonal boron nitride. *Appl Phys Lett* **99**, 243114 (2011).
- 28 Withers, F., Del Pozo-Zamudio, O., Mishchenko, A., Rooney, A. P., Gholinia, A., Watanabe, K., Taniguchi, T., Haigh, S. J., Geim, A. K., Tartakovskii, A. I. & Novoselov, K. S. Light-emitting diodes by band-structure engineering in van der Waals heterostructures. *Nature materials* **14**, 301-306 (2015).
- 29 Britnell, L., Gorbachev, R. V., Jalil, R., Belle, B. D., Schedin, F., Mishchenko, A., Georgiou, T., Katsnelson, M. I., Eaves, L., Morozov, S. V., Peres, N. M., Leist, J., Geim, A. K., Novoselov, K. S. & Ponomarenko, L. A. Field-effect tunneling transistor based on vertical graphene heterostructures. *Science* **335**, 947-950 (2012).
- 30 Li, H., Yin, Z., He, Q., Li, H., Huang, X., Lu, G., Fam, D. W. H., Tok, A. I. Y., Zhang, Q. & Zhang, H. Fabrication of Single- and Multilayer MoS<sub>2</sub> Film-Based Field-Effect Transistors for Sensing NO at Room Temperature. *Small* **8**, 63-67 (2011).
- 31 Schedin, F., Geim, A. K., Morozov, S. V., Hill, E. W., Blake, P., Katsnelson, M. I. & Novoselov, K. S. Detection of individual gas molecules adsorbed on graphene. *Nature materials* **6**, 652 (2007).
- 32 Frisenda, R., Navarro-Moratalla, E., Gant, P., Pérez De Lara, D., Jarillo-Herrero, P., Gorbachev, R. V. & Castellanos-Gomez, A. Recent progress in the assembly

- of nanodevices and van der Waals heterostructures by deterministic placement of 2D materials. *Chemical Society reviews* **47**, 53-68 (2018).
- 33 Cao, Y., Mishchenko, A., Yu, G. L., Khestanova, E., Rooney, A. P., Prestat, E., Kretinin, A. V., Blake, P., Shalom, M. B., Woods, C., Chapman, J., Balakrishnan, G., Grigorieva, I. V., Novoselov, K. S., Piot, B. A., Potemski, M., Watanabe, K., Taniguchi, T., Haigh, S. J., Geim, A. K. & Gorbachev, R. V. Quality Heterostructures from Two-Dimensional Crystals Unstable in Air by Their Assembly in Inert Atmosphere. *Nano letters* **15**, 4914-4921 (2015).
  - 34 McManus, D., Vranic, S., Withers, F., Sanchez-Romaguera, V., Macucci, M., Yang, H., Sorrentino, R., Parvez, K., Son, S.-K., Iannaccone, G., Kostarelos, K., Fiori, G. & Casiraghi, C. Water-based and biocompatible 2D crystal inks for all-inkjet-printed heterostructures. *Nature nanotechnology* **12**, 343 (2017).
  - 35 Withers, F., Yang, H., Britnell, L., Rooney, A. P., Lewis, E., Felten, A., Woods, C. R., Sanchez Romaguera, V., Georgiou, T., Eckmann, A., Kim, Y. J., Yeates, S. G., Haigh, S. J., Geim, A. K., Novoselov, K. S. & Casiraghi, C. Heterostructures produced from nanosheet-based inks. *Nano letters* **14**, 3987-3992 (2014).
  - 36 Yang, J., Voiry, D., Ahn, S. J., Kang, D., Kim, A. Y., Chhowalla, M. & Shin, H. S. Two-Dimensional Hybrid Nanosheets of Tungsten Disulfide and Reduced Graphene Oxide as Catalysts for Enhanced Hydrogen Evolution. *Angewandte Chemie* **125**, 13996-13999 (2013).
  - 37 Finn, D. J., Lotya, M., Cunningham, G., Smith, R. J., McCloskey, D., Donegan, J. F. & Coleman, J. N. Inkjet deposition of liquid-exfoliated graphene and MoS<sub>2</sub> nanosheets for printed device applications. *Journal of Materials Chemistry C* **2**, 925-932 (2014).
  - 38 Coleman, J. N., Lotya, M., O'Neill, A., Bergin, S. D., King, P. J., Khan, U., Young, K., Gaucher, A., De, S., Smith, R. J., Shvets, I. V., Arora, S. K., Stanton, G., Kim, H.-Y., Lee, K., Kim, G. T., Duesberg, G. S., Hallam, T., Boland, J. J., Wang, J. J., Donegan, J. F., Grunlan, J. C., Moriarty, G., Shmeliov, A., Nicholls, R. J., Perkins, J. M., Grieveson, E. M., Theuvsen, K., McComb, D. W., Nellist, P. D. & Nicolosi, V. Two-Dimensional Nanosheets Produced by Liquid Exfoliation of Layered Materials. *Science* **331**, 568 (2011).
  - 39 Wu, Q., Jang, S. K., Park, S., Jung, S. J., Suh, H., Lee, Y. H., Lee, S. & Song, Y. J. In situ synthesis of a large area boron nitride/graphene monolayer/boron nitride film by chemical vapor deposition. *Nanoscale* **7**, 7574-7579 (2015).
  - 40 Lin, Y.-C., Ghosh, R. K., Addou, R., Lu, N., Eichfeld, S. M., Zhu, H., Li, M.-Y., Peng, X., Kim, M. J., Li, L.-J., Wallace, R. M., Datta, S. & Robinson, J. A. Atomically thin resonant tunnel diodes built from synthetic van der Waals heterostructures. *Nature communications* **6**, 7311 (2015).
  - 41 Levendorf, M. P., Kim, C.-J., Brown, L., Huang, P. Y., Havener, R. W., Muller, D. A. & Park, J. Graphene and boron nitride lateral heterostructures for atomically thin circuitry. *Nature* **488**, 627-632 (2012).
  - 42 Cai, Z., Liu, B., Zou, X. & Cheng, H.-M. Chemical Vapor Deposition Growth and Applications of Two-Dimensional Materials and Their Heterostructures. *Chemical Reviews* **118**, 6091-6133 (2018).
  - 43 Tang, S., Ding, G., Xie, X., Chen, J., Wang, C., Ding, X., Huang, F., Lu, W. & Jiang, M. Nucleation and growth of single crystal graphene on hexagonal boron nitride. *Carbon* **50**, 329-331 (2012).
  - 44 Wang, L., Wu, B., Chen, J., Liu, H., Hu, P. & Liu, Y. Monolayer Hexagonal Boron Nitride Films with Large Domain Size and Clean Interface for Enhancing the

Mobility of Graphene-Based Field-Effect Transistors. *Advanced Materials* **26**, 1559-1564 (2013).

## 2.3. Misfit layer chalcogenides (MLCs)

### 2.3.1. Introduction

Misfit layer compounds belong to the collection of compounds known as incommensurate composite crystals and are formed from two alternating independent lattices. Misfit layer compounds may be categorised into two groups, oxides or chalcogenides. The work presented here exclusively concerns MLCs, and as such the discussion is limited to these compounds. For details on the structure and applications of oxygen containing misfit layer compounds the reader is directed to the following references.<sup>1-9</sup>

MLCs take the general form of  $[(MX)_n]_{1+x}[(TX_2)_m]$ , where M= Pb, Sb, Sn, Bi or a rare earth metal, T= Sn, Fe, Ti, V, Cr, Nb, or Ta and X is a chalcogen S, Se or Te.<sup>10,11</sup> They are composed of distorted pseudo tetragonal (T) PbS like and pseudo hexagonal (H) TMDC like layers (Figure 2-9a, b). The term misfit refers to a difference in the unit cells sizes of the two subsystems, resulting in an incommensurate relationship along at least one of the in-plane axes. The mismatch in unit cells is largest along the [100] direction, and the irrational relationship is approximated by the parameter,  $x$ , ranging from 0.08 to 0.28, which describes the adjustment in stoichiometry required to account for the mismatch.<sup>12</sup> The misfit in unit cells is sufficiently small along the [010] that through contraction and expansion, the unit cells can become commensurate (Figure 2-9c).<sup>13</sup> These T and H layers stack sequentially in the [001] direction and the number of each type of layer in the complete unit cell is indicated by parameters,  $n$  and  $m$ , referring to the number of T and H layers respectively (Figure 2-9d-f). The interactions between the layers are complex and involve additional interactions to the simple vdWs bonding seen in TMDCs, which partly accounts of the high stability of the MLC crystals. Charge transfer<sup>12,14</sup>, substitutions<sup>15,16</sup> and covalent interactions<sup>17-19</sup> all play a role and these interactions are discussed in further detail in section 2.3.3

It should be noted that the choice of unit cell crystallographic directions differs in various publications. Within this thesis the principal incommensurate direction is referred to as [100] or **a**, the semi-commensurate direction as [010] or **b** and the stacking direction as [001] or **c**, and will adapt all literature references to be consistent with this nomenclature.

### 2.3.2. Structure

The TX<sub>2</sub> layers in MLCs are equivalent to TMDC layers as discussed earlier, and consist of a three atom thick sandwich structure with a distorted pseudo hexagonal lattice containing primarily tetravalent cations and divalent anions, as in TMDCs. The H (TX<sub>2</sub>) layers can adopt the 1T or 2H coordination, with the SnS<sub>2</sub> layers investigated here adopting an octahedral structure.<sup>20</sup> As in TMDCs, the intralayer bonding is strong and of a covalent nature, while the interlayer bonding consists of weak vdW interactions. In MLCs the space between the layers known as the vdW gap, is intercalated by MX layers. The MX layer forms a distorted rock salt structure such that the metals are on the outside with sulphur buckled inwards (Figure 2-10a)<sup>21</sup> These T (MX) layers are composed of divalent (Pb and Sn) or trivalent (Sb, Bi rare earth) cations. MLCs are then constructed by alternate stacking of these T and H layers. The regular ordering in which the T and H layers are repeated along [001] is given by n and m (Figure 2-9). It has been shown that it is possible to synthesise compounds containing 1.5 T layers, i.e. 3 atom thick layers<sup>22-25</sup>. This flexibility of stacking allows for the creation of a large homologous series of compounds by simply changing n and/or m.<sup>26</sup> It is also possible to create systems with more than two subsystems.<sup>27</sup>

While MLCs form a single thermodynamic compound, the T and H layers have independent lattice parameters. A result of the incommensurate relationship between the T and H unit cells sizes is a loss of translational symmetry for the crystal. Translational symmetry underpins modern crystallography and is seen as a requirement for long range order in a crystal.<sup>28</sup> As such, attempts to rationalise MLCs using traditional 3D crystallography techniques proved unsuccessful.<sup>29</sup> Instead, a new framework is required to explain the crystallography of these structures. The superspace method was introduced by de Wolff<sup>30,31</sup>, Janner and Janssen<sup>32,33</sup> and introduces extra dimensions which allow for the description of incommensurate crystals. Here we will restrict our discussion to MLCs, but the same super space approach may also be used in characterising incommensurately modulated compounds and quasi crystals.<sup>28</sup> Super space has 3 + d dimensions, where d is the number of incommensurate axis. For most MLCs, d may take the value of 1 or 2, more usually 1.<sup>34</sup> We will discuss the super space indexing of a MLC with an incommensurate relationship along the **a** axis as this is the form of the crystals studied in this thesis.

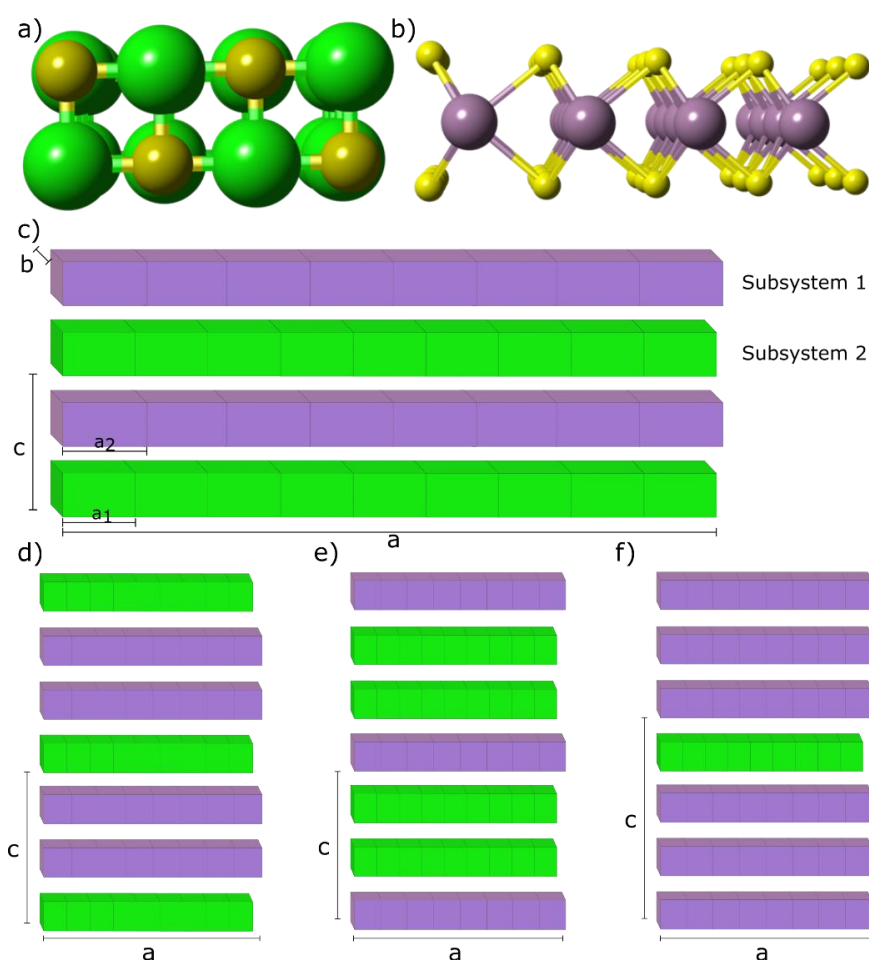


Figure 2-9 – Illustration of layer types and stacking sequences in MLCs. Atomic models for (a) two atom thick rock salt layer (T layer like) and (b) transition metal dichalcogenide (MoS<sub>2</sub>) monolayer (H layer like), (c)-(f) illustrative example of misfit layer compounds and the planar composite structure. Showing the irrational relationship along the  $a$  axis, where  $a_1 \neq a_2$ , where stacking sequences are (c)  $n, m = 1$ , (d)  $n=1, m=2$ , (e)  $n=2, m=1$  and (f)  $n=1, m=3$

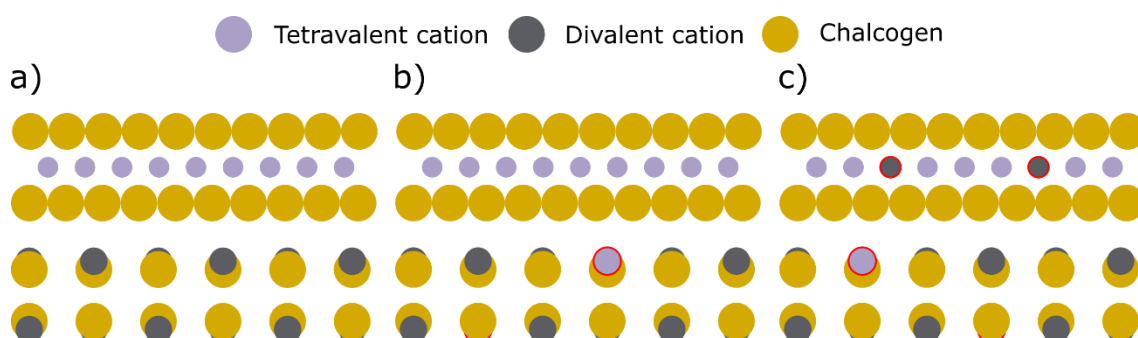


Figure 2-10 – Illustrative model of misfit layer chalcogen T and H layers. (a) Pristine structure with no substitution, note the buckled rock salt MX layer in which the chalcogen are distorted inwards while the metals are distorted outwards. (b) Stoichiometric substitution of cations from TX<sub>2</sub> layer into MX layer, (c) cross stoichiometric substitution of cations from TX<sub>2</sub> and MX layers into MX and TX<sub>2</sub> layers respectively. Red border indicates a substituted atom.

First we assign the H and T layers, as subsystem 1 and 2 respectively. We may then define the reciprocal lattices of each subsystem, as equation 2.21 where  $\nu$  denotes the subsystem.

$$\Lambda^* = \{a_{\nu 1}^*, a_{\nu 2}^*, a_{\nu 3}^*\} \quad 2.21$$

For commensurate crystals where  $a_{11}^* = a_{21}^*$ ,  $a_{12}^* = a_{22}^*$  and  $a_{13}^* = a_{23}^*$ , any Bragg reflection may be described by the three indices h,k,l. However in MLCs  $a_{11}^* \neq a_{21}^*$  and  $a_{11}^*:a_{21}^*$  yields an irrational number. To successfully index a Bragg reflection requires the addition of another dimension such that the reciprocal lattice may be described as  $a_1^* = a_{11}^*$ ,  $a_2^* = a_{12}^* = a_{22}^*$ ,  $a_3^* = a_{13}^* = a_{23}^*$  and  $a_4^* = a_{21}^*$ . Bragg diffraction spots are subsequently characterised by four indices h,k,l,m. This misfit is reflected in the 1+x description of the crystal. If the MLC is incommensurate along a single axis, the degree of misfit is calculated as  $1+x = 2a(TX_2)/a(MX)$ .<sup>12</sup> An alternative approach has more recently been proposed without the requirement for additional dimensions as in the super space approach<sup>35</sup>.

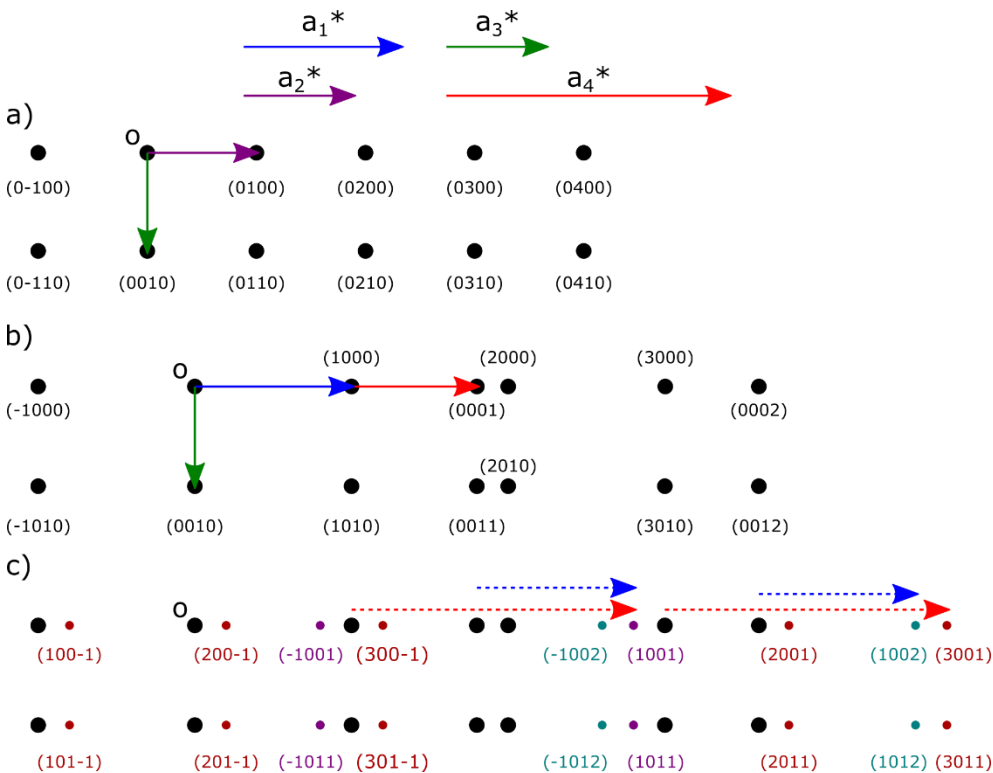


Figure 2-11 –Reciprocal lattice of orthorhombic MLC with a modulation along the a axis. (a) Projected along the incommensurate axes, showing common reciprocal planes. (b) Projected along common axis [0k00], with the main peaks corresponding to (h0l0) and (00lm) reflections peaks. (c) Projected along common axis [0k00] showing main and first order satellite peaks. Adapted from<sup>34</sup>



### 2.3.3. Interlayer interactions

In order to consider MLCs as a route to new 2D heterostructures it is important to consider the potential to exfoliate these systems into few layer sheets. In the case of materials such as graphite the intralayer interactions are strong covalent bonds and the interlayer interactions are purely vdW, allowing for the facile cleavage along this gap. In the case of MLCs the heterogeneous interface between the two incommensurate crystals gives rise to a range of interlayer interactions. While vdW forces are undoubtedly present, these do not entirely account for the stability of the MLCs. There are three other proposed interactions which account for the stability of these compounds, intrinsic charge transfer<sup>12,14</sup>, substitution induced charge transfer<sup>15,16</sup> and covalent interactions<sup>17-19</sup>.

MLCs may be considered intercalated TMDCs, with the MX layer behaving as an infinite 2D intercalant. This analysis is justified by the potential for electron donation from the MX layer to the TX<sub>2</sub> layer. While this is certainly the case where M is a trivalent cation, there is discussion over the magnitude of the charge transfer and the contribution to the stability of the crystals for divalent cations.<sup>36</sup> The evidence for charge transfer is best exemplified in the formation of a CrS<sub>2</sub> as the H layer in [(LaS)][(CrS<sub>2</sub>)].<sup>12,14-16</sup> Cr<sup>4+</sup> is not stable in the presence of sulphur, due poor mixing of the d band in Cr with the sp band of the sulphur.<sup>12</sup> However it is possible to form CrS<sub>2</sub> when it is intercalated with a metal, allowing for the 3+ oxidation state of the Cr. CrS<sub>2</sub> has been successfully formed when intercalated with sodium<sup>37,38</sup>, silver and copper<sup>39</sup> with the intercalant residing in the vdW gap between the CrS<sub>2</sub> layers, analogous to the MX layer in MLCs. The ability to form CrS<sub>2</sub> slabs is indirect evidence for the charge transfer, with magnetic studies showing chromium in the 3+ oxidation state providing direct evidence.<sup>40-42</sup> This formal reduction is a result of the charge transfer from the MX layer to the TX<sub>2</sub> layer. A range of MLC with lanthanide containing T layers and CrS<sub>2</sub> H layers have been synthesised<sup>42,43</sup>, however there have been no reported examples of CrS<sub>2</sub> formation with a divalent cation (e.g. Pb, Sn) T layer. This suggests that the charge transfer is significantly reduced between the layers. This reduction in charge transfer is further exemplified by the inability to intercalate [(SmS)][(NbS<sub>2</sub>)], while [(PbS)][(NbS<sub>2</sub>)] intercalates readily.<sup>44</sup> While it is generally accepted that the charge transfer is reduced for divalent ions, there is significant dispute as to the degree to which it is reduced and

its effect on the stability of the MLCs. Ettema and Haas suggested that there is no significant charge transfer from MX layers containing Pb, Sn or even Bi.<sup>17</sup> Bi is a surprising example as it is also found to be in the trivalent state; the additional electron density was attributed to Bi-Bi and Bi-Se bonds. It should also be noted that in the preparation of these samples for X-ray photoemission spectroscopy (XPS) analysis, the samples were 'freshened' by mechanical exfoliation.<sup>17</sup>

However, there is evidence in the case of [(PbS)]<sub>1.18</sub>[(TiS<sub>2</sub>)] that there is charge transfer which adds to charge stability.<sup>14</sup> Angle-resolved photoelectron spectroscopy (ARPES) showed the filling of the TiS<sub>2</sub> conduction band which was attributed to charge transfer from the PbS layer. This charge transfer in divalent cation MX layers was also supported by theoretical and XPS studies of the charge from the T to H layer in [(SnS)]<sub>1.17</sub>[NbS<sub>2</sub>]<sup>18,45</sup>, with a transfer of 0.4 e<sup>-</sup> into the 4dz<sup>2</sup> orbital of the NbS<sub>2</sub> from the SnS layer.<sup>18</sup> An additional consideration in understanding the interlayer interactions in MLCs is the stacking ordering of the layers, given by n and m. It has been shown that the charge transfer between the T to H layer is affected by the number of T layers, with more T layers (i.e. n > 1) resulting in a higher charge transfer to the H layer.<sup>46</sup> Interestingly, computational calculations of [(SnS)][(SnS<sub>2</sub>)] predict a charge transfer from the SnS<sub>2</sub> layer to SnS<sup>47</sup>, and a similar transfer is predicted in [(PbS)][(SnS<sub>2</sub>)] with a transfer from SnS<sub>2</sub> to PbS<sup>48</sup>. Both of these transfers are non-intuitive as it suggests the donation from the highly oxidised system to the more reduced system. In both systems, the level of transfer was low, approximately 0.1 e<sup>-</sup> per SnS<sub>2</sub> unit. The justification for this was that as SnS<sub>2</sub> is not a transition metal, the electron transfer does not occur from Sn<sup>4+</sup> but instead the S in SnS<sub>2</sub> donates electron density to the Sn<sup>2+</sup>.<sup>49</sup> This 'reversed' charge transfer is not common and has not been shown in literature where the H layer contains a transition metal.

In a model proposed by Moël et al., it was suggested that T cations may substitute into the MX layer which allows for the change in the charge balance, and subsequent charge transfer (Figure 2-10b). This deviation was reflected in a change in the T/M cation ratio for a range of MLCs, as analysed by electron microprobe.<sup>16</sup> This substitution of the divalent M cation for a tetravalent T cation in the MX layer requires deviation from ideal stoichiometry. Building on this work, it was proposed that in addition to this T cation substitution in to the MX layer, there is also M cation substitution into TX<sub>2</sub> layer (Figure

2-10c).<sup>36</sup> Using XPS to measure  $[(\text{PbS})]_{1.13}[(\text{TaS}_2)]$ , it was found that Ta was substituted into the MX layer as expected, but Pb was found in the TX<sub>2</sub> layer. As such, the same charge imbalance between the layers responsible for stabilising charge transfer can be achieved without the requirement for the deviation in stoichiometry. A substitution of 5-20% was found to induce a charge transfer of  $\sim 0.1 e^-$  per TaS<sub>2</sub> from the MX to TX<sub>2</sub> layer. This charge transfer of  $\sim 0.1 e^-$  per unit is comparable to the charge transfer reported in many of the other divalent systems mentioned above. As such it is possible that this is the mechanism responsible for the charge transfers in all divalent cation systems.

The final explanation for the stability between the layers in MLCs has been ascribed to a covalent interaction between the layers. In an XPS and computational study by Fang<sup>18</sup> it was shown that in  $[(\text{SnS})]_{1.20}[(\text{NbS}_2)]$  covalent bonding had a significant contribution to interlayer stability. This was shown by a mixing between the Sn 5s and S 3p of the NbS<sub>2</sub> layer, estimating an interlayer binding energy of 0.84 eV, per Sn. Further studies have shown similar covalent interactions between layers in  $[(\text{SnS})]_{1.2}[(\text{TiS}_2)]$ .<sup>19</sup> However this finding conflicts with other computational studies in which  $[(\text{LaS})(\text{SrS})_{0.2}][(\text{CrS}_2)]$ <sup>12</sup> and  $[(\text{La}_{1-x}\text{S})]_{1.20}[(\text{CrS}_2)]$ <sup>50</sup> were shown to have a purely ionic interaction between the layers. This was attributed to the orbitals of the lone pair on S in the CrS<sub>2</sub> layer pointing away from the La atoms.<sup>12</sup> This ionic interaction was also confirmed experimentally by XPS in the rare earth  $[(\text{LaS})]_{1.14}[(\text{NbS}_2)]$  MLC.<sup>51</sup>

In summary, the interlayer bonding in the MLCs is more complex than in TMDCs. In the case of rare earth containing compounds the interactions are largely electrostatic, brought about by charge transfer from the MX layer to the TX<sub>2</sub>. In the case of divalent (and Bi<sup>3+</sup>) it is unclear what the ultimate stabilising force is. The charge transfer of MX layers containing divalent cations can be affected by either stoichiometric or non-stoichiometric substitutions of M and T cations. Additionally, in the case of divalent cations, the nature and degree of covalency in this charge transfer is not widely understood and possibly varies depending on the subsystems, and stacking sequence, of the T and H layers.

#### 2.3.4. Properties

There are a vast range of possible MLCs that could be synthesised. Analogous to TMDCs, MLCs can exhibit a wide range of electronic properties. MLCs have been shown to be

Mott-Insulators<sup>43</sup>, semiconductors, metals<sup>52</sup>, and superconductors<sup>53,54</sup>. This is analogous to TMDCs, which is intuitive as it has been shown that the conduction takes place in the TMDC like H layers. It been shown in  $[(\text{LaSe})][(\text{NbS}_2)]$  that conduction takes place in the  $\text{NbS}_2$  layer, with the  $\text{LaSe}$  layer acting as an insulator.<sup>43,55,56</sup> This has also been shown in a variety of other crystals, in which the conduction occurs exclusively in the  $\text{TX}_2$  layer.<sup>12,18,19,51</sup>

The electronic effect of the MX layer is often to dope the  $\text{TX}_2$  layer, which manifests in several ways. Firstly, through different choices of MX it is possible to affect the critical temperature,  $T_c$ , in superconducting  $\text{TaS}_2$ ,  $\text{NbS}_2$  and  $\text{NbSe}_2$  layers.<sup>57</sup> This is also shown by the effects of substitutions and the role of vacancies on the electrical properties.<sup>12,43,58</sup> Alternatively, the electrical properties may be tuned by choosing different chalcogenides in the  $\text{TX}_2$  layers.<sup>57,59,60</sup> The ability to combine insulating MX layers with superconducting  $\text{TX}_2$  layers allows for the creation of intrinsic Josephson junctions.<sup>61</sup> These compounds have been used to explore the Josephson phenomena and also as a method to study more complex anisotropic superconductors, such as high  $T_c$  types. The effects of stacking order,  $n$  and  $m$ , have also been shown to influence the electronic properties of MLC.<sup>62</sup> Finally, the ability to access other TMDCs that are unstable when isolated to single unit cell thicknesses (e.g.  $\text{CrS}_2$ ), offers a route to explore new materials with a wide range of proposed uses, such as photovoltaic applications and photocatalysts.<sup>63,64</sup>

The unique crystallography of MLCs also has consequences for their physical properties. An example of this is the effect on the stoichiometry of the crystals, in the  $1+x$  factor. If we take the example of  $\text{Ln}^{3+}$  cation occupying the MX layer, if there was no mismatch, each  $\text{Ln}$  cation would reduce a single cation in the T layer, via the charge transfer discussed above. In this scenario electroneutrality would be met. However, due to the incommensurate relationship, the  $1+x$  factor dictates that there is excess charge, equal to  $x$ , in the T layer. As such this would violate electroneutrality and the crystal cannot exist. Consequently, MLC containing  $\text{Ln}^{3+}$  cations must contain vacancies in the T layer equal to the excess amount  $x$ , i.e.  $[(\text{Ln}[\ ]_x\text{S})]_{1+x}[(\text{TX}_2)]$  where  $[\ ]$  represents a vacancy. This substitution has been examined closely in a number of systems, notably in the well-studied  $[(\text{LnS})][(\text{CrS}_2)]$  MLCs<sup>12,43,58</sup> which were shown to be semiconductors in part due to these vacancies. Alternatively, it is possible to meet electroneutrality requirements

via substitution to avoid the necessity for these vacancies i.e.  $2 \text{Ln}^{3+} + [] \rightarrow 3 \text{M}^{2+}$ , whilst maintaining charge neutrality. The MLC  $[(\text{La}_{1.17-x}\text{Sr}_x\text{S})]_{1.17}[(\text{VS}_2)]$  in which  $\text{La}^{3+}$  is substituted for  $\text{Sr}^{2+}$  has been demonstrated to behave as a Mott-insulator, with insulating behaviour at  $x=0.17$  and metallic  $x>0.3$ .<sup>58</sup> The layered structure results in a large anisotropy between the in-plane and out-of-plane conductivities<sup>21,57</sup>, while the incommensurate structure has been demonstrated to induce a small in-plane anisotropy.<sup>65,66</sup>

In addition to their electronic properties, the ability to include magnetic elements into the MLCs allows for interesting magnetic properties to be explored. 2D magnetism can be designed by having a single layer of magnetic elements surrounded by non-magnetic elements to confine the magnetism to a 2D plane.<sup>22-25,67</sup> Furthermore the flexibility in stacking sequences in MLCs allows for excellent control in the spacing between these 2D magnetic layers. Additionally, by changing the levels of magnetic dopants it is possible to change from paramagnetic to ferromagnetic behaviour.<sup>66,68,69</sup> Magnetic studies examining  $[(\text{LaS})][(\text{CrS}_2)]$  have shown a lack of long range magnetic order along the **a** direction, which was attributed to the incommensurate structure.<sup>40,42</sup> It was also shown that the contribution of the LaS layer to the magnetic structure of the compound was negligible, yielding 2D magnetic  $\text{CrS}_2$  layers. These 2D magnetic layers behave as a spin glass due to topological frustrations and the incommensurate structure.<sup>40</sup> 2D magnetism was also observed in the T layer for  $[(\text{CeS})][(\text{TS}_2)_m]$  where  $T=\text{Ta}, \text{V}, \text{Nb}$  and  $m=1,2$ .<sup>70,71</sup> Interestingly, the conduction was still shown to be exclusively along the H layer. Ferromagnetic ordering was present within the CeS layers, and the interaction between the layers was dependant on the stacking sequence, with antiferromagnetic ordering for  $m=1$  and ferromagnetic for  $m=2$ . As a simple binary compound, CeS exhibits anti-ferromagnetic ordering<sup>72</sup>; as such it seems for the MLC where  $m=2$ , the CeS layers are sufficiently decoupled so as to act as individual layers. It was theorised that the placement of superconducting layers on magnetic insulating layers will result in the formation of a superconductor-topological insulator interface, where Majorana fermions may form.<sup>73</sup> As such the MLC  $[(\text{CeS})][(\text{NbS}_2)]$  described above would seem to demonstrate potential for formation of these states.  $\text{Bi}_2\text{Te}_3/\text{NbSe}_2$  heterostructures have already been used for the investigation of Majorana fermions formation.<sup>74</sup> These heterostructures were grown by MBE, and while a lattice mismatch is noted, it is not

investigated.<sup>75</sup> Both  $\text{Bi}_2\text{Te}_3$  T layers<sup>76</sup>, and  $\text{NbSe}_2$  H layers<sup>57</sup>, have been prepared in MLCs, consequently it is likely these  $\text{Bi}_2\text{Te}_3/\text{NbSe}_2$  heterostructures are MLCs. As such the incommensurate relationship, and its effects on Majorana fermion formation require further investigation. Additionally a MLC with layers composed of electrically conducting H layers and magnetic T layers may offer promise for memory storage solutions.<sup>77,78</sup>

Thermoelectric materials in which heat is converted into electricity are useful for a number of green technologies.<sup>79</sup> The performance of a thermoelectric material is given by the unitless figure of merit,  $ZT$ , with a higher value corresponding to increased performance.<sup>79</sup>  $ZT$  may be increased by improving the electrical performance (power factor) or by decreasing the thermal conductivity.<sup>80</sup> An ideal material therefore is one in which electrons traverse the specimen easily, and phonons are strongly scattered. This was termed a phonon-glass electron-crystal<sup>80</sup>, and it was proposed that MLCs could match this description. MLCs may be prepared with disordered layering resulting in low thermal conductivities.<sup>26</sup> Both n-type  $[(\text{LaS})]_{1.2}[(\text{CrS}_2)]$  and p-type  $[(\text{LaS})]_{1.14}[(\text{NbS}_2)]$  thermoelectric materials have been produced, with  $ZT$  of  $\sim 0.15$  at 950K.<sup>81</sup> However this value is substantially lower than oxides such as  $\text{Na}_x\text{CoO}_2$  ( $ZT \sim 1.2$ )<sup>9</sup> and the commercial target of  $ZT = 2$ .<sup>79</sup>

### **2.3.5. Formation**

MLCs can be sourced as minerals or formed synthetically. The minerals discussed in this thesis are all naturally occurring minerals, from the cylindrite-franckeite series of sulfosalts.<sup>82</sup> However the majority of MLCs discussed in literature are synthetic, produced by chemical vapour transport<sup>66</sup> (CVT) or molecular beam epitaxy<sup>83,84</sup> (MBE). In the section below we will briefly explore the cylindrite-franckeite series and discuss the methodologies, capabilities and limitations for synthetic MLCs.

#### **2.3.5.1. Naturally occurring misfit layer chalcogenides – The cylindrite – franckeite series**

The cylindrite – franckeite mineralogical family consists of four minerals belonging to the 3.1.4 Dana group<sup>82</sup>: cylindrite<sup>85</sup>, franckeite<sup>86</sup>, potosiite<sup>87</sup> and incaite<sup>88</sup>. The series is described as regularly alternating layered structures with two incommensurable sheets, one a pseudo tetragonal and the other a pseudo hexagonal (see section 2.3.2).<sup>89</sup> As such the series can be thought of as naturally occurring MLCs. The four minerals are

composed of T layers containing primarily  $\text{Pb}_{1-x}\text{Sb}_x\text{S}$ , and H layers composed of  $\text{Sn}_{1-x}\text{Fe}_x\text{S}_2$ . Cylindrite differs from franckeite, potosiite and incaite, by the stacking order; for cylindrite  $n,m=1$  while for franckeite, potosiite and incaite  $n=2$ ,  $m=1$ . The latter 'franckeite-type' minerals then differ from each in their elemental ratios, incaite being Pb poor, and potosiite Pb rich compared to franckeite. A striking difference between franckeite and cylindrite is the macroscopic forms the minerals take with cylindrite forming tightly scrolled cylinders, from which it takes its name, and the franckeite-type forming tabular (flat) crystals. These distinct formations appear to be a result of the slight difference in elemental compositions and the change in stacking ordering.

Using Strunz<sup>89</sup> mineralogical classification method the family can be expanded further to include both lévyclaudite<sup>90</sup> and lengenbachite<sup>91</sup>, where lévyclaudite belongs to a cylindrite-like group and lengenbachite to the franckeite-type. However, both have different elemental compositions; lévyclaudite incorporates Bi in to the T layers and Cu in the H layers, whereas lengenbachite integrates Ag and Cu dopants and a five atom thick  $\text{As}_2\text{S}_3$  H layer. There are also a number of similar minerals which could likely be part of these groups, but have not yet been included in the latest classifications. For example, merelaniite<sup>92</sup>, a cylindrite-like mineral with a  $\text{MoS}_2$  H layer and V substituted for Fe, and coiraite<sup>93</sup>, a franckeite like mineral containing As and no Sb. As these are naturally occurring minerals dopant atoms may be substituted in, depending on the elements available in the surrounding environment and resulting in slightly different minerals to the ideal mineral phases described above. There have also been successful synthetic analogues created for some of these naturally occurring MLCs.<sup>90,94</sup>

### 2.3.5.2. Synthetic

The synthesis of most MLCs is achieved by CVT, in which elements or simple sulphur binary analogues are added in stoichiometric quantities to an evacuated quartz tube, with a transport agent such as  $\text{I}_2$ .<sup>14,66,90,94-96</sup> The reaction vessel is then heated to temperatures typically ranging from 500-1000°C, for a period of time of the order of weeks to months. The synthesis protocol varies between MLCs, but it has been shown to be crucial to include an annealing step which homogenises the crystal.<sup>44</sup> This is typically a heating stage, followed by the grinding of the resulting product, concluding with subsequent heating stages. This technique allows for the formation of a

tremendous number of different MLCs. Additionally it is possible to precisely control the dopants and alter the properties of the MLC in a facile synthesis methodology.<sup>58</sup> It has also been shown that the crystals can be formed on different substrates, including NaCl, CaF<sub>2</sub> and SiO<sub>2</sub> glass,<sup>66</sup> achievable using a close space variation of CVT. The choice of substrate was shown to impact the orientation of the MLC and even allow for the upright growth of synthetic cylindrite cylinders.<sup>66</sup> The formation of these cylindrical structures had previously not been reported for growth on substrates.<sup>97-99</sup>

MBE has been pioneered as an alternative method for the synthesis of MLCs by Johnson et al.<sup>83,84</sup> By depositing alternating amorphous thin films in stoichiometric ratios corresponding to MX and TX<sub>2</sub> layers, the MLC structure is built up layer by layer on a silicon (100) substrate. After the depositions are finished the sample is subsequently annealed, yielding the desired MLC, which highlights the thermodynamic stability of these compounds.<sup>100</sup> It should be noted that multiple minima may exist in the formation of these structures, which can lead to faults in the layering sequence. Furthermore the energy landscape may be more complicated in MLCs where the M or T elements can exist in either MX or TX<sub>2</sub> layers i.e. SnSe and SnSe<sub>2</sub>. For example in [(SnSe)][(VSe<sub>2</sub>)], layers of SnSe<sub>2</sub> were found to form if annealing temperature was not sufficiently high.<sup>101</sup> MBE has shown to be particularly capable of creating MLCs incorporating selenium and tellurium as the chalcogenide,<sup>10,83</sup> although it should be noted that compounds containing Se can also be formed by CVT.<sup>102</sup> MBE has also shown appreciable flexibility in the elements incorporated into the structure, with the potential for sequential deposition of different layers e.g. [(SnSe)][(MoSe<sub>2</sub>)][(SnSe)][(NbSe<sub>2</sub>)].<sup>27</sup> Additional flexibility arises from the generic crystal structures of MLCs such that layers other than the pseudo hexagonal TX<sub>2</sub> layers can be included. This is exemplified in the synthesis of [(LaSe)]<sub>1.17</sub>[(V<sub>n(1+y)+1</sub>Se<sub>2n+2</sub>)], where n and y vary such that the traditionally TX<sub>2</sub> type H layer varies between VSe<sub>2</sub> and VSe, including V<sub>3</sub>Se<sub>4</sub>.<sup>103</sup> Alternatives to the normal TMDC like three atom thick H layers have also been successfully synthesised, with the inclusion of a five atom thick Bi<sub>2</sub>Se<sub>3</sub> layer<sup>80,104</sup>, similar to the As<sub>2</sub>S<sub>3</sub> layers found in lengenbachite. More complex structural features have been reported for BiSe T layers, where anti-phase boundaries form, altering the structure from the simple distorted rock salt structure, which directly affects the properties of the MLC.<sup>105</sup> The approach to creating MLCs by MBE offers improved flexibility for incorporating different elements and crystal



structures. However it is less suitable for mass production and is a more labour intensive process than production by CVT.

### 2.3.6. Intercalation

As mentioned in section 2.3.3, there has been interest in intercalating MLCs to induce and study physical phenomena such as doping, charge density waves (CDWs), superconductivity<sup>106</sup> and interlayer interactions<sup>44</sup>, as well as inherent interest into the intercalation process.<sup>102</sup> The process by which intercalation was attempted varied from simple immersion in metal containing solutions<sup>102</sup> to electrochemical intercalation<sup>44</sup>. A summary of some of the more interesting results is presented below.

Whether the intercalation is successful or not, it can allow for the estimation of the charge transfer between layers.<sup>44</sup> This is particularly useful as one can compare the MLC with intercalation of the parent TMDC.<sup>106</sup> In addition, one can estimate the structure of the T and H layers through the degree of intercalation.<sup>102</sup> It has been shown that  $[(\text{PbS})][(\text{NbS}_2)]$  ( $n, m = 1$ ) was difficult to intercalate with  $\text{Na}^+$  whereas  $[(\text{PbS})][(\text{NbS}_2)_2]$  ( $n=1, m=2$ ), was readily intercalated.<sup>107</sup> It was suggested that this is due to the protrusion of the M cation ions from the T layer into the T-H interface, making it energetically unfavourable for  $\text{Na}^+$  ions to intercalate, while  $m=2$  readily intercalates, which suggests that it is the vdW gap that is intercalated (as in bulk  $\text{NbS}_2$ ). The MLC was less able to be intercalated than the bulk TMDC, which is likely due to charge transfer from the T layer. The difference in intercalations and stacking sequence was observed with  $\text{Li}^+$ ; again  $m=2$ , which intercalated more than  $m=1$ .<sup>108</sup> It was also found that the structural stability of the compounds was reduced upon intercalation, eventually decomposing after a few hours of lithiation<sup>109</sup> or sodium intercalation<sup>107</sup>. This may be a result of total filling of the octahedral sites and the subsequent filling of the smaller tetrahedral sites, which may destabilise the structure.

Copper intercalated  $\text{TiSe}_2$  is known to be a superconductor, and there is interest in elucidating the dimensionality dependence of its superconductivity.<sup>110</sup> MLCs offer the potential for studying this layer dependence through the creation of a homologue series. It has previously been demonstrated that  $[(\text{BiSe})]_{1.15}[(\text{TiSe}_2)]$  does not exhibit superconducting behaviour. The next homologue,  $[(\text{BiSe})]_{1.15}[(\text{TiSe}_2)_2]$  was prepared, and it was shown to readily intercalate with Cu without disrupting the crystal

structure.<sup>106</sup> A similar expansion in the *c* axis is observed in both  $\text{TiSe}_2$  and  $[(\text{BiSe})]_{1.15}[(\text{TiSe}_2)_2]$  upon intercalation. While the intercalation was successful, transport measurements showed no superconducting behaviour. It was noted that the CDW present in bulk Cu intercalated  $\text{TiSe}_2$  was not present in either  $[(\text{BiSe})]_{1.15}[(\text{TiSe}_2)]$  or Cu intercalated  $[(\text{BiSe})]_{1.15}[(\text{TiSe}_2)_2]$ . It is possible that the anti-phase boundaries previously observed in BiSe T layers may disrupt the formation of the CDW.<sup>105</sup> The similar MLC  $[(\text{PbSe})][(\text{TiSe}_2)_2]$  has demonstrated superconducting behaviour without the requirement of intercalation.<sup>111</sup> Furthermore, the authors attribute the superconducting behaviour to CDW suppression due to charge transfer from the T layer. It is currently unclear what is the exact relationship between the CDW and superconductivity<sup>110</sup>, and as such further studies are required. No homologue beyond  $m=2$  has been successfully prepared for the BiSe MLC. However there is an expectation that at some value of *m*, both CDW formation and superconducting behaviour would be realised, allowing for the study of the transition between these two states. Further effects of dimensionality will be discussed in section 2.3.7.

### 2.3.7. Allotropes and cleavage

The MLC compounds discussed so far have been 3D bulk crystals, but as with many other systems, MLCs are capable of alternative allotropic forms, spanning all dimensions, analogous to carbon, i.e. 3D bulk materials, 2D MLC sheets<sup>44</sup>, 1D MLC nanotubes<sup>112-118</sup> and 0D ML fullerenes<sup>48,119</sup>. This is perhaps not surprising given the similarities to other vdW materials discussed. The main focus of this work is the potential for producing 2D forms of MLCs. We consider 2D materials to consist of a single unit cell thickness material (monolayer) or few unit cells thick material (multilayers), such that the in-plane crystal dimensions are orders of magnitude larger than the out-of-plane dimensions, analogous to the treatment of other 2D materials. It has been shown that the MLCs can be exfoliated to single unit cell thickness, by liquid and chemical exfoliation and reach this 2D limit.<sup>44</sup> This is possible due to the large anisotropy between the interlayer and intralayer bond strengths, which allows for cleavage between the layers (perpendicular to the [001] direction), similar to exfoliation in traditional vdW materials.

However, the exfoliation of MLCs is more complicated than that of TMDCs due to the different types of layers. If we consider a MLC with 2 subsystems, there are four stacking scenarios (ignoring the vacuum interfaces):  $n$  and  $m = 1$ ;  $n = 1$   $m > 1$ ;  $n > 1$   $m = 1$ ; and  $n$  and

$m > 1$ . In the first instance, any cleavage must occur at the interface between the two different crystals. For the  $n = 1, m > 1$  crystals, there is the additional possibility of cleavage along the H-H interface. For  $n > 1, m = 1$  compounds, cleavage could occur between the T-H or T-T interfaces. Finally, for  $n$  and  $m > 1$  compounds, there is potential to cleave between all 3 interface types. For MLCs with more than 2 subsystems additional interfaces will be created such as T-T', T'-H, H'-T etc. Prior to 2017, only  $n=1, m=2$  systems have been cleaved to the 2D limit, which was shown in  $[(MS)][(NbS_2)_2]$  where  $M = Pb$  or  $Sm$ .<sup>44</sup> The exfoliation was deduced to cleave along the H-H interface. Considering that  $NbS_2$  has been shown to readily cleave to monolayers by liquid and chemical exfoliation<sup>120,121</sup>, and that T-H layers have been found to have additional interlayer interactions supports this conclusion.<sup>44</sup> Hence we can consider the exfoliation of this compound as a further example of cleavage of vdW materials; a decade before graphene was reported by cleaving graphite.<sup>122</sup> However, it remained unclear whether MLCs which do not contain a pure vdW gap, i.e.  $m=1$ , can be cleaved to single layer thickness, and if so which is the preferred interface to cleave.

A range of bulk MLCs with various elemental substituents and  $n, m$  stacking orders have been cleaved in preparation for surface sensitive analytical techniques XPS and ARPES.<sup>14,17,18,36,45,123</sup> However it is unknown if this is cleavage along a fault in the crystal or true cleavage along the interfaces, and the exfoliated material was never examined. In the synthetic MLC  $[(LaSe)][(NbS_2)]$  scanning tunnelling microscope (STM)<sup>124</sup> images have suggested both cubic and hexagonal features on the cleaved surfaces, although the evidence for the cubic surface is tentative with the cubic features in the Fourier transform of the image poorly visible. Similar STM studies of the MLCs  $[(Pb_{1-x}Sb_xS)_n]_{1+x}[(TS_2)]$ , where  $T=Ti$  and  $Nb$  and  $n = 1$  or  $2$ , found that no T layer was present on the surface of the sample for the case of  $n=1$  but was observed for  $n=2$ .<sup>46</sup> Subsequent work using STM and atomic force microscopy (AFM) have replicated these findings, for  $[(Pb, Sb)S_2]_{1.14}[(NbS_2)]$ , showing both T and H layer motifs.<sup>125</sup> Wang and Kuo cleaved cylindrite ( $n, m=1$ ) and franckeite ( $n=2, m=1$ ) samples by mechanical exfoliation, and examined specimens by CTEM, which demonstrated the presence of the expected hexagonal and cubic diffraction patterns for cylindrite samples.<sup>29</sup> The question remains as to whether this dependence on  $n$  and T layer visibility is an artefact of the

STM measurements; perhaps single T layers are not stable and degrade or cleavage occurs due to a layering error and adjacent H layers are cleaved.

### 2.3.8. Characterisation

Structural characterisation of MLCs has been achieved primarily using X-ray diffraction (XRD) of bulk crystals.<sup>22,23,62,83,84,102</sup> Primarily XRD allows accurate structural refinement<sup>22</sup>, but it is also used to assess the quality and stacking sequence of layering<sup>10,62,83</sup>. Cylindrite and franckeite have both been extensively characterised by XRD, producing refined structures for the incommensurate modulations.<sup>29,126</sup> However, there are discrepancies in the described modulations, and structure of these compounds<sup>29,126</sup> which may stem from variations present in the natural minerals. However it should be noted that due to the poor quality of the crystals, X-ray structure determination is difficult. Furthermore as a bulk technique, XRD is limited in its ability to characterise nanostructure and stacking faults in MLCs.

As such TEM, has been widely used for the examination of these compounds, both in plan view<sup>21</sup> and cross section<sup>26,85</sup>. Plan view CTEM studies of cylindrite and franckeite examined the structural properties of the crystals using imaging and selected area electron diffraction.<sup>29,129</sup> Furthermore in both cylindrite and franckeite specimens, a Moiré pattern is clearly visible, due to the incommensurate crystallography.<sup>29,85</sup> While plan view characterisation has been useful, the most important features are the layers, stacking sequences and the interfaces between the layers. Consequently the vast majority of TEM characterisation is along either the [100] or [010] directions. HAADF STEM imaging in particular is well suited to the examination of these structures, which due to their large and complex unit cells, are difficult to simulate. Cross sectional STEM images have been used to demonstrate stacking sequence faults<sup>127</sup>, disorder between the layers<sup>128</sup> and faults within the individual layers such as anti-phase boundaries.<sup>105</sup> Furthermore HAADF STEM images have been crucial in confirming stacking sequences and correlating to XRD data.<sup>26,123</sup> However, despite the extensive use of cross sectional STEM, there is limited spatially resolved spectroscopic data for MLCs.<sup>48,129,130</sup>

Lajaunie et.al. utilised spatially resolved STEM-EELS for the examination of mixed chalcogen MLC nanotubes [(LnX)][(TaS/Se<sub>2</sub>)] where Ln = La, Ce, Nd, and Ho, and X = S

and Se.<sup>129</sup> For [(LaS/Se)][(TaSe<sub>2</sub>)] nanotubes, the EELS spectrum image line profile successfully demonstrated the segregation of the La and Ta, however the La signal is overestimated. The authors conclude that the MLC nanotube [(HoS/Se)][(TaS/Se<sub>2</sub>)] exhibits preferential occupation of S on Ho sites and Se on Ta sites. This interpretation is questionable, as the sulphur SNR is very low and not easily resolved. Additionally the stoichiometry of HoSe and TaSe<sub>2</sub> would lead to an increased Se signal in the Ta layers. STEM EDX was utilised for the analysis of MLC composed from three different layers, [(PbSe)<sub>n</sub>][(TiSe<sub>2</sub>)<sub>m</sub>][(SnSe<sub>2</sub>)<sub>n</sub>][(TiSe<sub>2</sub>)<sub>m</sub>].<sup>130</sup> The EDX analysis shows the clear elemental segregation of the Pb, Ti and Sn metals, and that a small amount of intermixing is present in the Pb and Sn layers. However Merrill et.al. failed to investigate the sulphur signal, presumably due to the insensitivity of EDX to low atomic weight elements.

### 2.3.9. References:

- 1 Leligny, H., Grebille, D., Pérez, O., Masset, A.-C., Herveieu, M., Michel, C. & Raveau, B. A bismuth cobaltite with an intrinsically modulated misfit layer structure:  $\text{Bi}_{0.87}\text{SrO}_{22}\text{CoO}_{21.8}$ . *Comptes Rendus de l'Académie des Sciences - Series IIC - Chemistry* **2**, 409-414 (1999).
- 2 Lambert, S., Leligny, H. & Grebille, D. Three Forms of the Misfit Layered Cobaltite  $[\text{Ca}_2\text{CoO}_3][\text{CoO}_2]_{1.62}$ : A 4D Structural Investigation. *Journal of Solid State Chemistry* **160**, 322-331 (2001).
- 3 Boullay, P., Domengès, B., Hervieu, M., Groult, D. & Raveau, B. Evidence for the First Misfit Layer Oxide  $\text{Tl}_{0.41}(\text{Sr}_{0.9}\text{O})_{1.12}\text{CoO}_2$ . *Chemistry of Materials* **8**, 1482-1489 (1996).
- 4 Boullay, P., Seshadri, R., Studer, F., Hervieu, M., Groult, D. & Raveau, B. Chemical and Physical Aspects of the Misfit Layer Oxides  $\text{Tl}_x[(\text{Sr}_{1-y}\text{Ca}_y)\text{O}]_{1+x}(\text{CoO}_2)$ . *Chemistry of Materials* **10**, 92-102 (1998).
- 5 Hervieu, M., Boullay, P., Michel, C., Maignan, A. & Raveau, B. A New Family of Misfit Layered Oxides with Double Rock Salt Layers  $\text{Bi}_x(\text{A}_{0.75\pm x}\text{Bi}_{0.25\pm x}\text{O})_{(3+3x)/2}\text{MO}_2$  ( $\text{A}=\text{Ca, Sr}$  and  $\text{M}=\text{Co, Cr}$ ). *Journal of Solid State Chemistry* **142**, 305-318 (1999).
- 6 Masset, A. C., Michel, C., Maignan, A., Hervieu, M., Toulemonde, O., Studer, F., Raveau, B. & Hejtmanek, J. Misfit-layered cobaltite with an anisotropic giant magnetoresistance:  $\text{Ca}_3\text{Co}_4\text{O}_9$ . *Physical Review B* **62**, 166-175 (2000).
- 7 Grebille, D., Lambert, S., Bouree, F. & Petricek, V. Contribution of powder diffraction for structure refinements of aperiodic misfit cobalt oxides. *Journal of Applied Crystallography* **37**, 823-831 (2004).
- 8 Baran, J. D., Molinari, M., Kulwongwit, N., Azough, F., Freer, R., Kepaptsoglou, D., Ramasse, Q. M. & Parker, S. C. Tuning Thermoelectric Properties of Misfit Layered Cobaltites by Chemically Induced Strain. *The Journal of Physical Chemistry C* **119**, 21818-21827 (2015).
- 9 Baran, J. D., Kepaptsoglou, D., Molinari, M., Kulwongwit, N., Azough, F., Freer, R., Ramasse, Q. M. & Parker, S. C. Role of Structure and Defect Chemistry in High-Performance Thermoelectric Bismuth Strontium Cobalt Oxides. *Chemistry of Materials* **28**, 7470-7478 (2016).
- 10 Moore, D. B., Beekman, M., Disch, S. & Johnson, D. C. Telluride Misfit Layer Compounds:  $[(\text{PbTe})_{1.17}]_m(\text{TiTe}_2)_n$ . *Angewandte Chemie International Edition* **53**, 5672-5675 (2014).
- 11 Rouxel, J., Meerschaut, A. & Wiegers, G. A. Chalcogenide misfit layer compounds. *Journal of Alloys and Compounds* **229**, 144-157 (1995).
- 12 Cario, L., Johrendt, D., Lafond, A., Felser, C., Meerschaut, A. & Rouxel, J. Stability and charge transfer in the misfit compound  $(\text{LaS})(\text{SrS})_{0.2}\text{CrS}_2$ : Ab initio band-structure calculations. *Physical Review B* **55**, 9409-9414 (1997).
- 13 Garbrecht, M., Spiecker, E., Tillmann, K. & Jäger, W. Quantitative atom column position analysis at the incommensurate interfaces of a  $(\text{PbS})_{1.14}\text{NbS}_2$  misfit layered compound with aberration-corrected HRTEM. *Ultramicroscopy* **111**, 245-250 (2011).
- 14 Brandt, J., Kipp, L., Skibowski, M., Krasovskii, E. E., Schattke, W., Spiecker, E., Dieker, C. & Jäger, W. Charge transfer in misfit layered compounds. *Surface Science* **532-535**, 705-710 (2003).

- 15 Kallane, M., Rossnagel, K., Marczyński-Buhlow, M., Kipp, L., Starnberg, H. I. & Stoltz, S. E. Stabilization of the misfit layer compound  $(\text{PbS})_{1.13}\text{TaS}_2$  by metal cross substitution. *Phys Rev Lett* **100**, 065502 (2008).
- 16 Moelo, Y., Meerschaut, A., Rouxel, J. & Auriel, C. Precise Analytical Characterization of Incommensurate Sandwiched Layered Compounds  $[(\text{Pb},\text{Sn})\text{S}]_{1+x}[(\text{Nb},\text{Ti})\text{S}_2]_m$  ( $0.08 \leq x \leq 0.28$ ,  $m = 1-3$ ). Role of Cationic Coupling on the Properties and the Structural Modulation. *Chemistry of Materials* **7**, 1759-1771 (1995).
- 17 Ettema, A. R. H. F. & Haas, C. An X-ray photoemission spectroscopy study of interlayer charge transfer in some misfit layer compounds. *Journal of Physics: Condensed Matter* **5**, 3817 (1993).
- 18 Fang, C. M., Ettema, A. R. H. F., Haas, C., Wiegers, G. A., van Leuken, H. & de Groot, R. A. Electronic structure of the misfit-layer compound  $(\text{SnS})_{1.17}\text{NbS}_2$  deduced from band-structure calculations and photoelectron spectra. *Physical Review B* **52**, 2336-2347 (1995).
- 19 Fang, C. M., Groot, R. A. d., Wiegers, G. A. & Haas, C. Electronic structure of the misfit layer compound  $(\text{SnS})_{1.2}\text{TiS}_2$ : band structure calculations and photoelectron spectra. *Journal of Physics: Condensed Matter* **8**, 1663 (1996).
- 20 Greenaway, D. L. & Nitsche, R. Preparation and optical properties of group IV–VI<sub>2</sub> chalcogenides having the  $\text{CdI}_2$  structure. *Journal of Physics and Chemistry of Solids* **26**, 1445-1458 (1965).
- 21 Wiegers, G. A., Meetsma, A., van Smaalen, S., Haange, R. J., Wulff, J., Zeinstra, T., de Boer, J. L., Kuypers, S., Van Tendeloo, G., Van Landuyt, J., Amelinckx, S., Meerschaut, A., Rabu, P. & Rouxel, J. Misfit layer compounds  $(\text{MS})_n\text{TS}_2$  ( $\text{M} = \text{Sn}$ ,  $\text{Pb}$ ,  $\text{Bi}$ , rare earth elements;  $\text{T} = \text{Nb}$ ,  $\text{Ta}$ ;  $n = 1.08 - 1.19$ ), a new class of layer compounds. *Solid State Communications* **70**, 409-413 (1989).
- 22 Cario, L., Meerschaut, A., Deudon, C. & Rouxel, J. Synthesis and crystal structure determination of a new misfit compound:  $[(\text{EuS})_{1.5}]_{1.15}\text{NbS}_2$ . *Comptes Rendus de l'Académie des Sciences - Series IIC - Chemistry* **1**, 269-276 (1998).
- 23 Lafond, A., Deudon, C., Meerschaut, A., Palvadeau, P., Moëlo, Y. & Briggs, A. Structure Determination and Physical Properties of the Misfit Layered Compound  $(\text{Pb}_2\text{FeS}_3)_{0.58}\text{NbS}_2$ . *Journal of Solid State Chemistry* **142**, 461-469 (1999).
- 24 Deudon, C., Lafond, A., Leynaud, O., Moëlo, Y. & Meerschaut, A. Quantification of the Interlayer Charge Transfer, via Bond Valence Calculation, in 2D Misfit Compounds: The Case of  $(\text{Pb}(\text{Mn}, \text{Nb})_{0.5}\text{S}_{1.5})_{1.15}\text{NbS}_2$ . *Journal of Solid State Chemistry* **155**, 1-8 (2000).
- 25 Cario, L., Lafond, A., Palvadeau, P., Deudon, C. & Meerschaut, A. Evidence of a Mixed-Valence State for Europium in the Misfit Layer Compound  $[(\text{EuS})_{1.5}]_{1.15}\text{NbS}_2$  by Means of a Superspace Structural Determination, Mössbauer Spectroscopy, and Magnetic Measurements. *Journal of Solid State Chemistry* **147**, 58-67 (1999).
- 26 Lin, Q., Smeller, M., Heideman, C. L., Zschack, P., Koyano, M., Anderson, M. D., Kykyneshi, R., Keszler, D. A., Anderson, I. M. & Johnson, D. C. Rational Synthesis and Characterization of a New Family of Low Thermal Conductivity Misfit Layer Compounds  $[(\text{PbSe})_{0.99}]_m(\text{WSe}_2)_n$ . *Chemistry of Materials* **22**, 1002-1009 (2010).

- 27 Westover, R. D., Ditto, J., Falmbigl, M., Hay, Z. L. & Johnson, D. C. Synthesis and Characterization of Quaternary Monolayer Thick MoSe<sub>2</sub>/SnSe/NbSe<sub>2</sub>/SnSe Heterojunction Superlattices. *Chemistry of Materials* **27**, 6411-6417 (2015).
- 28 Van Smaalen, S. Incommensurate crystal structures. *Crystallography Reviews* **4**, 79-202 (1995).
- 29 Wang, S. & Kuo, K. H. Crystal lattices and crystal chemistry of cylindrite and franckeite. *Acta Crystallographica Section A* **47**, 381-392 (1991).
- 30 De Wolff, P. M. The Pseudo-Symmetry of Modulated Crystal Structures. *Acta Crystallographica Section A* **30**, 777-785 (1974).
- 31 de, P. Symmetry operations for displacively modulated structures. *Acta Crystallographica Section A* **33**, 493-497 (1977).
- 32 Janner, A. & Janssen, T. Symmetry of periodically distorted crystals. *Physical Review B* **15**, 643-658 (1977).
- 33 Janner, A. & Janssen, T. Symmetry of incommensurate crystal phases. II. Incommensurate basic structure. *Acta Crystallographica Section A* **36**, 408-415 (1980).
- 34 Smaalen, S. v. *Incommensurate crystallography*. (Oxford University Press, 2007).
- 35 Kocian, P. Incommensurate crystallography without additional dimensions. *Acta Crystallographica Section A* **69**, 374-387 (2013).
- 36 Kalläne, M., Rosnagel, K., Marczyński-Bühlow, M., Kipp, L., Starnberg, H. I. & Stoltz, S. E. Stabilization Of The Misfit Layer Compound (PbS)<sub>1.13</sub>TaS<sub>2</sub> By Metal Cross Substitution. *Physical Review Letters* **100**, 065502 (2008).
- 37 Rüdorff, W. & Stegemann, K. Kristallstruktur und magnetisches Verhalten der Alkalithiochromite. *Zeitschrift für anorganische und allgemeine Chemie* **251**, 376-395 (1943).
- 38 Boon, J. W. & Mac Gillavry, C. H. The crystal structure of potassium thioferrite KFeS<sub>2</sub> and sodium thiochromite NaCrS<sub>2</sub>. *Recueil des Travaux Chimiques des Pays-Bas* **61**, 910-920 (1942).
- 39 Hahn, H. & Lorent, C. D. Untersuchungen über ternäre Chalkogenide. XII. Über ternäre Chalkogenide des Chroms mit einwertigem Kupfer und Silber. *Zeitschrift für anorganische und allgemeine Chemie* **290**, 68-81 (1957).
- 40 Lafond, A., Meerschaut, A., Rouxel, J., Tholence, J. L. & Sulpice, A. Spin-glass-like behavior of the incommensurate composite phase LaCrS<sub>3</sub>. *Physical Review B* **52**, 1112-1119 (1995).
- 41 Kazuya, S., Tetsuo, K., Makoto, I. & Toshiaki, E. Variety of Magnetism in Incommensurate Misfit Layer Compounds (RE)<sub>x</sub>TS<sub>2</sub> (RE = Rare Earths, T = Ta, V, Ti, Cr). *Japanese Journal of Applied Physics* **32**, 341 (1993).
- 42 Lafond, A., Molinie, P., Sulpice, A., Tholence, J. L., Meerschaut, A. & Monceau, P. Magnetic-Susceptibility Study On (LaS)<sub>1.19</sub>CrS<sub>2</sub> and (NdS)<sub>1.23</sub>CrS<sub>2</sub> Compounds. *Comptes Rendus De L Academie Des Sciences Serie II* **315**, 1667-1673 (1992).
- 43 Meerschaut, A., Moëlo, Y., Cario, L., Lafond, A. & Deudon, C. Charge Transfer in Misfit Layer Chalcogenides, [(MX)<sub>n</sub>]<sub>1+x</sub>(TX<sub>2</sub>)<sub>m</sub>: a Key for Understanding their Stability and Properties. *Molecular Crystals and Liquid Crystals Science and Technology. Section A. Molecular Crystals and Liquid Crystals* **341**, 1-8 (2000).
- 44 Bonneau, P., Mansot, J. L. & Rouxel, J. Intercalation and exfoliation of misfit-layer compounds [MNb<sub>2</sub>S<sub>5</sub> (M = Pb, Sm)]. *Materials Research Bulletin* **28**, 757-766 (1993).



- 45 Ohno, Y. Optical properties and the optical joint density of states of the misfit-layer compounds  $(\text{MS})_{1+x}\text{TS}_2$ . *Journal of Physics: Condensed Matter* **6**, 8655 (1994).
- 46 Ohno, Y. & Wada, T. Scanning Tunneling Microscopy, X-Ray Photoelectron Spectroscopy and Electron Energy-Loss Spectroscopy Studies of the Misfit Layer Compounds  $\{(\text{Pb}_{1-x}\text{Sb}_x\text{S})_{1+y}\}_m\text{TS}_2$  ( $\text{T}=\text{Ti}$  and  $\text{Nb}$ ;  $m=1$  and  $2$ ). *Journal of the Physical Society of Japan* **70**, 2082-2091 (2001).
- 47 Lorenz, T., Joswig, J.-O. & Seifert, G. Combined  $\text{SnS}@\text{SnS}_2$  double layers: charge transfer and electronic structure. *Semiconductor Science and Technology* **29**, 064006 (2014).
- 48 Brontvein, O., Albu-Yaron, A., Levy, M., Feuerman, D., Popovitz-Biro, R., Tenne, R., Enyashin, A. & Gordon, J. M. Solar Synthesis of  $\text{PbS}-\text{SnS}_2$  Superstructure Nanoparticles. *ACS Nano* **9**, 7831-7839 (2015).
- 49 Lorenz, T., Joswig, J.-O. & Seifert, G. Two-dimensional and tubular structures of misfit compounds: Structural and electronic properties. *Beilstein Journal of Nanotechnology* **5**, 2171-2178 (2014).
- 50 Fang, C. M., De Groot, R. A., Wiegers, G. A. & Haas, C. Electronic structure and evidence for La vacancies in the misfit layer compound  $(\text{La}_{1-x}\text{S})_{1.20}\text{CrS}_2$ . *Journal of Physics and Chemistry of Solids* **58**, 1103-1109 (1997).
- 51 Fang, C. M., Smaalen, S. v., Wiegers, G. A., Haas, C. & Groot, R. A. d. Electronic structure of the misfit layer compound  $(\text{LaS})_{1.14}\text{NbS}_2$ : band-structure calculations and photoelectron spectra. *Journal of Physics: Condensed Matter* **8**, 5367 (1996).
- 52 Meerschaut, A. Misfit layer compounds. *Current Opinion in Solid State and Materials Science* **1**, 250-259 (1996).
- 53 Song, Y. J., Kim, M. J., Jung, W. G., Kim, B.-J. & Rhyee, J.-S. Superconducting properties of the misfit-layer compound  $(\text{SnSe})_{1.18}(\text{TiSe}_2)_2$ . *physica status solidi (b)* **253**, 1517-1522 (2016).
- 54 Lafond, A., Nader, A., Moëlo, Y., Meerschaut, A., Briggs, A., Perrin, S., Monceau, P. & Rouxel, J. X-Ray structure determination and superconductivity of a new layered misfit compound with a franckeite-like stacking,  $[(\text{Pb,Sb})\text{S}]_{2.28}\text{NbS}_2$ . *Journal of Alloys and Compounds* **261**, 114-122 (1997).
- 55 Szabo, P., Samuely, P., Kacmarcik, J., Jansen, A. G., Briggs, A., Lafond, A. & Meerschaut, A. Interlayer transport in the highly anisotropic misfit-layer superconductor  $[(\text{LaSe})_{(1.14)}](\text{NbSe}_2)$ . *Phys Rev Lett* **86**, 5990-5993 (2001).
- 56 Berner, D., Leihenseder, H., Widder, K., Geserich, H. P., Burlakov, V. M., Mavrin, B. N., Denisov, V. N., Roesky, R., Gressier, P. & Meerschaut, A.  $(\text{LaSe})_{1.14}(\text{NbSe}_2)_2$  - a metal - insulator quantum well crystal? *Journal of Physics: Condensed Matter* **9**, 10545 (1997).
- 57 Wiegers, G. A. Misfit layer compounds: Structures and physical properties. *Progress in Solid State Chemistry* **24**, 1-139 (1996).
- 58 Nishikawa, T., Yasui, Y. & Sato, M. Transport Anomalies of Misfit-Layer Compounds  $\text{La}_{1.17-x}\text{Sr}_x\text{VS}_{3.17}$  with Mott Metal-Insulator Transition. *Journal of the Physical Society of Japan* **63**, 3218-3221 (1994).
- 59 Duan, X., Wang, C., Fan, Z., Hao, G., Kou, L., Halim, U., Li, H., Wu, X., Wang, Y., Jiang, J., Pan, A., Huang, Y., Yu, R. & Duan, X. Synthesis of  $\text{WS}_{2x}\text{Se}_{2-2x}$  Alloy Nanosheets with Composition-Tunable Electronic Properties. *Nano letters* **16**, 264-269 (2016).

- 60 Fong, C. Y. & Cohen, M. L. Electronic Energy-Band Structure of SnS<sub>2</sub> and SnSe<sub>2</sub>. *Physical Review B* **5**, 3095-3101 (1972).
- 61 Kačmarčík, J., Szabó, P., Samuely, P., Rodrigo, J. G., Suderow, H., Vieira, S., Lafond, A. & Meerschaut, A. Intrinsic Josephson junction behaviour of the low T<sub>c</sub> superconductor (LaSe)<sub>1.14</sub>(NbSe<sub>2</sub>). *Physica C: Superconductivity and its Applications* **468**, 543-546 (2008).
- 62 Heideman, C. L. & Johnson, D. C. Structural influence on transport properties in [(PbSe)<sub>1.00</sub>]<sub>m</sub>(MoSe<sub>2</sub>)<sub>n</sub> misfit layered compounds. *Semiconductor Science and Technology* **29**, 064007 (2014).
- 63 Zhuang, H. L., Johannes, M. D., Blonsky, M. N. & Hennig, R. G. Computational prediction and characterization of single-layer CrS<sub>2</sub>. *Appl Phys Lett* **104**, 022116 (2014).
- 64 Bongers, P. F., Van Bruggen, C. F., Koopstra, J., Omloo, W. P. F. A. M., Wiegers, G. A. & Jellinek, F. Structures and magnetic properties of some metal (I) chromium (III) sulfides and selenides. *Journal of Physics and Chemistry of Solids* **29**, 977-984 (1968).
- 65 Ruscher, C. H., Haas, C., Smaalen, S. v. & Wiegers, G. A. Investigation of the optical reflectivity of misfit layer compounds: (MS)<sub>n</sub>TS<sub>2</sub> (T=Ta, Nb; M=Sn, Pb, Sm, Tb, La; 1.08<n<1.23). *Journal of Physics: Condensed Matter* **6**, 2117 (1994).
- 66 Kaden, R., Wagner, G., Sturm, C., Schmidt-Grund, R., von Wenckstern, H., Prager, A., Bente, K. & Grundmann, M. Synthesis and physical properties of cylindrite micro tubes and lamellae. *physica status solidi (b)* **247**, 1335-1350 (2010).
- 67 Leynaud, O., Lafond, A., Moëlo, Y., Palvadeau, P. & Meerschaut, A. Crystal Structures and Magnetic Properties of the Two Misfit Layer Compounds: [SrGd<sub>0.5</sub>S<sub>1.5</sub>]<sub>1.16</sub>NbS<sub>2</sub> and [Sr(Fe,Nb)<sub>0.5</sub>S<sub>1.5</sub>]<sub>1.13</sub>NbS<sub>2</sub>. *Journal of Solid State Chemistry* **168**, 41-51 (2002).
- 68 Salyer, P. A. & Haar, L. W. t. Magnetic properties of the mineral, cylindrite (FePb<sub>3</sub>Sn<sub>4</sub>Sb<sub>2</sub>S<sub>14</sub>). *Journal of Applied Physics* **81**, 5163-5165 (1997).
- 69 Salyer, P. A. & Haar, L. W. t. Single-crystal magnetic studies of cylindrite (FePb<sub>3</sub>Sn<sub>4</sub>Sb<sub>2</sub>S<sub>14</sub>). *Journal of Applied Physics* **87**, 6025-6027 (2000).
- 70 Suzuki, K., Kondo, T., Enoki, T. & Bandow, S. Conduction mechanism and two-dimensional magnetism in incommensurate layered compounds (RE)<sub>x</sub>MS<sub>2</sub> (RE=rare earth metal, M=Ta,V). *Synthetic Metals* **56**, 1741-1746 (1993).
- 71 Terashima, T. & Kojima, N. Magnetic Properties of Incommensurate Layer Compounds, (CeS)<sub>1.2</sub>NbS<sub>2</sub> and (CeS)<sub>0.6</sub>NbS<sub>2</sub>. *Journal of the Physical Society of Japan* **61**, 3303-3312 (1992).
- 72 Hulliger, F., Natterer, B. & Ott, H. R. Magnetic properties of the cerium monochalcogenides. *Journal of Magnetism and Magnetic Materials* **8**, 87-98 (1978).
- 73 Fu, L. & Kane, C. L. Superconducting Proximity Effect and Majorana Fermions at the Surface of a Topological Insulator. *Physical Review Letters* **100**, 096407 (2008).
- 74 Xu, J.-P., Wang, M.-X., Liu, Z. L., Ge, J.-F., Yang, X., Liu, C., Xu, Z. A., Guan, D., Gao, C. L., Qian, D., Liu, Y., Wang, Q.-H., Zhang, F.-C., Xue, Q.-K. & Jia, J.-F. Experimental Detection of a Majorana Mode in the core of a Magnetic Vortex inside a Topological Insulator-Superconductor Bi<sub>2</sub>Te<sub>3</sub>/NbSe<sub>2</sub> Heterostructure. *Physical Review Letters* **114**, 017001 (2015).

- 75 Wang, M.-X., Liu, C., Xu, J.-P., Yang, F., Miao, L., Yao, M.-Y., Gao, C. L., Shen, C., Ma, X., Chen, X., Xu, Z.-A., Liu, Y., Zhang, S.-C., Qian, D., Jia, J.-F. & Xue, Q.-K. The Coexistence of Superconductivity and Topological Order in the Bi<sub>2</sub>Se<sub>3</sub> Thin Films. *Science* **336**, 52 (2012).
- 76 Harris, F. R., Standridge, S. & Johnson, D. C. The Synthesis of [(Bi<sub>2</sub>Te<sub>3</sub>)<sub>x</sub>{(TiTe<sub>2</sub>)<sub>y</sub>}<sub>1.36</sub>] Superlattices from Modulated Elemental Reactants. *Journal of the American Chemical Society* **127**, 7843-7848 (2005).
- 77 Grünberg, P. Layered magnetic structures in research and application. *Acta Materialia* **48**, 239-251 (2000).
- 78 Mitchell, K. & Ibers, J. A. Rare-Earth Transition-Metal Chalcogenides. *Chemical Reviews* **102**, 1929-1952 (2002).
- 79 Zheng, X. F., Liu, C. X., Yan, Y. Y. & Wang, Q. A review of thermoelectrics research – Recent developments and potentials for sustainable and renewable energy applications. *Renewable and Sustainable Energy Reviews* **32**, 486-503 (2014).
- 80 Jood, P. & Ohta, M. Hierarchical Architecturing for Layered Thermoelectric Sulfides and Chalcogenides. *Materials* **8** (2015).
- 81 Jood, P., Ohta, M., Nishiate, H., Yamamoto, A., Lebedev, O. I., Berthebaud, D., Suekuni, K. & Kunii, M. Microstructural Control and Thermoelectric Properties of Misfit Layered Sulfides (LaS)<sub>1+m</sub>TS<sub>2</sub> (T = Cr, Nb): The Natural Superlattice Systems. *Chemistry of Materials* **26**, 2684-2692 (2014).
- 82 Gaines, R. V., Skinner, H. C. W., Foord, E. E., Mason, B. & Rosenzweig, A. *Dana's new mineralogy : the system of mineralogy of James Dwight Dana and Edward Salisbury Dana*. 8th ed. / entirely rewritten and greatly enl. by Richard V. Gaines .. [et al.] / and with illustrations by Eric Dowty. edn, (John Wiley & Sons, inc., 1997).
- 83 Lin, Q., Heideman, C. L., Nguyen, N., Zschack, P., Chiritescu, C., Cahill, D. G. & Johnson, D. C. Designed Synthesis of Families of Misfit-Layered Compounds. *European Journal of Inorganic Chemistry* **2008**, 2382-2385 (2008).
- 84 Heideman, C., Nyugen, N., Hanni, J., Lin, Q., Duncombe, S., Johnson, D. C. & Zschack, P. The synthesis and characterization of new [(BiSe)<sub>1.10</sub>]<sub>m</sub>[NbSe<sub>2</sub>]<sub>n</sub>, [(PbSe)<sub>1.10</sub>]<sub>m</sub>[NbSe<sub>2</sub>]<sub>n</sub>, [(CeSe)<sub>1.14</sub>]<sub>m</sub>[NbSe<sub>2</sub>]<sub>n</sub> and [(PbSe)<sub>1.12</sub>]<sub>m</sub>[TaSe<sub>2</sub>]<sub>n</sub> misfit layered compounds. *Journal of Solid State Chemistry* **181**, 1701-1706 (2008).
- 85 Williams, T. B. & Hyde, B. G. Electron microscopy of cylindrite and franckeite. *Physics and Chemistry of Minerals* **15**, 521-544 (1988).
- 86 Stelzner, A. Über Franckeit, ein neues Erz aus Bolivia. *Neues Jahrbuch für Mineralogie* **2**, 114-124 (1893).
- 87 Kissin, S. A. & Owens, D. The properties and modulated structure of potosiite from the Cassiar District, British Columbia. *Canadian Mineralogist* **24**, 45-50 (1986).
- 88 Makovicky, E. Mineralogical data on cylindrite and incaite. *Neues Jahrbuch für Mineralogie, Monatshefte* **1974**, 235-256 (1974).
- 89 Strunz, H. *Strunz mineralogical tables : chemical-structural mineral classification system*. 9th ed. / by Hugo Strunz and Ernest H. Nickel. edn, (Stuttgart : Schweizerbart, 2001).
- 90 Evain, M., Petricek, V., Moelo, Y. & Maurel, C. First (3+2)-dimensional superspace approach to the structure of levyclaudite-(Sb), a member of the cylindrite-type minerals. *Acta Crystallogr. Sect. B-Struct. Sci.* **62**, 775-789 (2006).

- 91 Williams, T. B. & Pring, A. Structure of lengenbachite: A high-resolution transmission electron microscope study. *American Mineralogist* **73**, 1426-1433 (1988).
- 92 Jaszczak, J., Rumsey, M., Bindi, L., Hackney, S., Wise, M., Stanley, C. & Spratt, J. Merelaniite,  $\text{Mo}_4\text{Pb}_4\text{VSbS}_{15}$ , a New Molybdenum-Essential Member of the Cylindrite Group, from the Merelani Tanzanite Deposit, Lelatema Mountains, Manyara Region, Tanzania. *Minerals* **6**, 115 (2016).
- 93 Paar, W., Moëlo, Y., Mozgova, N., Organova, N., Stanley, C., Roberts, A., Culetto, F., Effenberger, H., Topa, D. & Putz, H. Coiraite,  $(\text{Pb}, \text{Sn}^{2+})_{12.5}\text{As}_3\text{Fe}^{2+}\text{Sn}^{4+5}\text{S}_{28}$ : a franckeite-type new mineral species from Jujuy Province, NW Argentina. *Mineralogical Magazine* **72**, 1083-1101 (2008).
- 94 Sachdev, S. C. & Chang, L. L. Y. Phase relations in the system tin-antimony-lead sulfides and the synthesis of cylindrite and franckeite. *Economic Geology* **70**, 1111-1122 (1975).
- 95 Wieggers, G. A., Meetsma, A., Haange, R. J. & de Boer, J. L. Crystal growth, structure and some properties of  $\text{PbNbS}_3$ ,  $\text{SnNbS}_3$ ,  $\text{LaNbS}_3$  and related misfit layer compounds. *Solid State Ionics* **32-33**, 183-191 (1989).
- 96 Lourdes, H., Julián, M., Jayasree, P. & L., T. J. Preparation and Characterization of New Misfit Layer Selenides  $\text{SnVSe}_3$  and  $\text{SnNb}_2\text{Se}_5$ . *Chemistry Letters* **20**, 1981-1984 (1991).
- 97 Landa-Cánovas, A. R., Gómez-Herrero, A. & Carlos Otero-Díaz, L. Electron microscopy study of incommensurate modulated structures in misfit ternary chalcogenides. *Micron* **32**, 481-495 (2001).
- 98 Bernaerts, D., Amelinckx, S., Van Tendeloo, G. & Van Landuyt, J. Microstructure and formation mechanism of cylindrical and conical scrolls of the misfit layer compounds  $\text{PbNb}_n\text{S}_{2n+1}$ . *Journal of Crystal Growth* **172**, 433-439 (1997).
- 99 Gómez-Herrero, A., Landa-Cánovas, A. R., Hansen, S. & Otero-Díaz, L. C. Electron microscopy study of tubular crystals  $(\text{BiS})_{1+\delta}(\text{NbS}_2)_n$ . *Micron* **31**, 587-595 (2000).
- 100 Merrill, D., Moore, D., Bauers, S., Falmbigl, M. & Johnson, D. Misfit Layer Compounds and Ferecrystals: Model Systems for Thermoelectric Nanocomposites. *Materials* **8**, 2000-2029 (2015).
- 101 Falmbigl, M., Esters, M. & Johnson, D. C. Formation of a Selenide-Based Heterostructure From a Designed Precursor†. *Crystal Research and Technology* **52**, 1700067-n/a (2017).
- 102 Lourdes, H., Julián, M., Jayasree, P. & L., T. J. Preparation and Characterization of New Misfit Layer Selenides  $\text{SnVSe}_3$  and  $\text{SnNb}_2\text{Se}_5$ . *Chemistry Letters* **20**, 1981-1984 (1991).
- 103 Gunning, N. S., Dankwort, T., Falmbigl, M., Ross, U., Mitchson, G., Hamann, D. M., Lotnyk, A., Kienle, L. & Johnson, D. C. Expanding the Concept of van der Waals Heterostructures to Interwoven 3D Structures. *Chemistry of Materials* **29**, 8292-8298 (2017).
- 104 Shelimova, L. E., Karpinskii, O. G. & Zemskov, V. S. X-ray diffraction study of ternary layered compounds in the  $\text{PbSe-Bi}_2\text{Se}_3$  system. *Inorganic Materials* **44**, 927 (2008).
- 105 Hite, O. K., Nellist, M., Ditto, J., Falmbigl, M. & Johnson, D. C. Transport properties of  $\text{VSe}_2$  monolayers separated by bilayers of  $\text{BiSe}$ . *Journal of Materials Research* **31**, 886-892 (2015).

- 106 Trump, B. A., Livi, K. J. T. & McQueen, T. M. The new misfit compound  $(\text{BiSe})_{1.15}(\text{TiSe}_2)_2$  and the role of dimensionality in the  $\text{Cu}_x(\text{BiSe})_{1+\delta}(\text{TiSe}_2)_n$  series. *Journal of Solid State Chemistry* **209**, 6-12 (2014).
- 107 Hernán, L., Morales, J., Sánchez, L. & Tirado, J. L. Electrochemical intercalation of sodium into  $\text{PbNbS}_3$  and  $\text{PbNb}_2\text{S}_5$  misfit layer compounds. *Solid State Ionics* **58**, 179-184 (1992).
- 108 Hernán, L., Lavela, P., Morales, J., Pattanayak, J. & Tirado, J. L. Structural aspects of lithium intercalated  $\text{PbVS}_3$ ,  $\text{PbTiS}_3$ ,  $\text{PbTi}_2\text{S}_5$  and  $\text{SnNbS}_3$  misfit layer compounds. *Materials Research Bulletin* **26**, 1211-1218 (1991).
- 109 Hernán, L., Morales, J., Pattanayak, J. & Tirado, J. L. Lithium intercalation into  $\text{PbNb}_2\text{S}_5$ ,  $\text{PbNbS}_3$ ,  $\text{SnNb}_2\text{Se}_5$ ,  $\text{BiVS}_3$ ,  $\text{SnVSe}_3$ , and  $\text{PbNb}_2\text{Se}_5$  misfit layer chalcogenides. *Journal of Solid State Chemistry* **100**, 262-271 (1992).
- 110 Morosan, E., Zandbergen, H. W., Dennis, B. S., Bos, J. W. G., Onose, Y., Klimczuk, T., Ramirez, A. P., Ong, N. P. & Cava, R. J. Superconductivity in  $\text{Cu}_x\text{TiSe}_2$ . *Nature Physics* **2**, 544 (2006).
- 111 Giang, N., Xu, Q., Hor, Y. S., Williams, A. J., Dutton, S. E., Zandbergen, H. W. & Cava, R. J. Superconductivity at 2.3 K in the misfit compound  $(\text{PbSe})_{1.16}(\text{TiSe}_2)_2$ . *Physical Review B* **82**, 024503 (2010).
- 112 Panchakarla, L. S., Popovitz-Biro, R., Houben, L., Dunin-Borkowski, R. E. & Tenne, R. Lanthanide-based functional misfit-layered nanotubes. *Angewandte Chemie* **53**, 6920-6924 (2014).
- 113 Panchakarla, L. S., Radovsky, G., Houben, L., Popovitz-Biro, R., Dunin-Borkowski, R. E. & Tenne, R. Nanotubes from Misfit Layered Compounds: A New Family of Materials with Low Dimensionality. *J Phys Chem Lett* **5**, 3724-3736 (2014).
- 114 Radovsky, G., Popovitz-Biro, R. & Tenne, R. Nanotubes from the Misfit Layered Compounds  $\text{MS-TaS}_2$ , Where M = Pb, Sn, Sb, or Bi: Synthesis and Study of Their Structure. *Chemistry of Materials* **26**, 3757-3770 (2014).
- 115 Radovsky, G., Popovitz-Biro, R., Staiger, M., Gartsman, K., Thomsen, C., Lorenz, T., Seifert, G. & Tenne, R. Synthesis of copious amounts of  $\text{SnS}_2$  and  $\text{SnS}_2/\text{SnS}$  nanotubes with ordered superstructures. *Angewandte Chemie* **50**, 12316-12320 (2011).
- 116 Panchakarla, L. S., Lajaunie, L., Tenne, R. & Arenal, R. Atomic Structural Studies on Thin Single-Crystalline Misfit-Layered Nanotubes of  $\text{TbS-CrS}_2$ . *The Journal of Physical Chemistry C* **120**, 15600-15607 (2016).
- 117 Tenne, R. Fullerene-like structures and nanotubes from inorganic compounds. *Endeavour* **20**, 97-104 (1996).
- 118 Radovsky, G., Popovitz-Biro, R., Lorenz, T., Joswig, J.-O., Seifert, G., Houben, L., Dunin-Borkowski, R. E. & Tenne, R. Tubular structures from the  $\text{LnS-TaS}_2$  (Ln = La, Ce, Nd, Ho, Er) and  $\text{LaSe-TaSe}_2$  misfit layered compounds. *Journal of Materials Chemistry C* **4**, 89-98 (2016).
- 119 Hong, S. Y., Popovitz-Biro, R., Prior, Y. & Tenne, R. Synthesis of  $\text{SnS}_2/\text{SnS}$  Fullerene-like Nanoparticles: A Superlattice with Polyhedral Shape. *Journal of the American Chemical Society* **125**, 10470-10474 (2003).
- 120 Murphy, D. W. & Jr., G. W. H. Monodispersed tantalum disulfide and adsorption complexes with cations. *The Journal of Chemical Physics* **62**, 973-978 (1975).
- 121 Liu, C., Singh, O., Joensen, P., Curzon, A. E. & Frindt, R. F. X-ray and electron microscopy studies of single-layer  $\text{TaS}_2$  and  $\text{NbS}_2$ . *Thin Solid Films* **113**, 165-172 (1984).

- 122 Novoselov, K. S., Geim, A. K., Morozov, S. V., Jiang, D., Zhang, Y., Dubonos, S. V., Grigorieva, I. V. & Firsov, A. A. Electric Field Effect in Atomically Thin Carbon Films. *Science* **306**, 666-669 (2004).
- 123 Mitchson, G., Hadland, E., Göhler, F., Wanke, M., Esters, M., Ditto, J., Bigwood, E., Ta, K., Hennig, R. G., Seyller, T. & Johnson, D. C. Structural Changes in 2D BiSe Bilayers as n Increases in  $(\text{BiSe})_{1+\delta}(\text{NbSe}_2)_n$  ( $n = 1-4$ ) Heterostructures. *ACS Nano* **10**, 9489-9499 (2016).
- 124 Kačmarčík, J., Szabó, P., Samuely, P., Rodrigo, J. G., Suderow, H., Vieira, S., Lafond, A. & Meerschaut, A. Intrinsic Josephson junction behaviour of the low  $T_c$  superconductor  $(\text{LaSe})_{1.14}(\text{NbSe}_2)$ . *Physica C: Superconductivity and its Applications* **468**, 543-546 (2008).
- 125 Bengel, H., Jobic, S., Moëlo, Y., Lafond, A., Rouxel, J., Seo, D. K. & Whangbo, M. H. Distribution of the Pb and Sb Atoms in the (Pb, Sb)S Layers of the Franckeite-Type Misfit Compound  $[(\text{Pb}, \text{Sb})\text{S}]_{2.28}\text{NbS}_2$  Examined by Scanning Tunneling and Atomic Force Microscopy. *Journal of Solid State Chemistry* **149**, 370-377 (2000).
- 126 Makovicky, E., Petricek, V., Dusek, M. & Topa, D. The crystal structure of franckeite,  $\text{Pb}_{21.7}\text{Sn}_{9.3}\text{Fe}_{4.0}\text{Sb}_{8.1}\text{S}_{56.9}$ . *American Mineralogist* **96**, 1686-1702 (2011).
- 127 Smeller, M. M., Heideman, C. L., Lin, Q., Beekman, M., Anderson, M. D., Zschack, P., Anderson, I. M. & Johnson, D. C. Structure of Turbostratically Disordered Misfit Layer Compounds  $[(\text{PbSe})_{0.99}]_1[\text{WSe}_2]_1$ ,  $[(\text{PbSe})_{1.00}]_1[\text{MoSe}_2]_1$ , and  $[(\text{SnSe})_{1.03}]_1[\text{MoSe}_2]_1$ . *Zeitschrift für anorganische und allgemeine Chemie* **638**, 2632-2639 (2012).
- 128 Heideman, C. L., Rostek, R., Anderson, M. D., Herzing, A. A., Anderson, I. M. & Johnson, D. C. Synthesis and Electronic Properties of the Misfit Layer Compound  $[(\text{PbSe})_{1.00}]_1[\text{MoSe}_2]_1$ . *Journal of Electronic Materials* **39**, 1476-1481 (2010).
- 129 Lajaunie, L., Radovsky, G., Tenne, R. & Arenal, R. Quaternary Chalcogenide-Based Misfit Nanotubes  $\text{LnS}(\text{Se})\text{-TaS}(\text{Se})_2$  ( $\text{Ln} = \text{La}, \text{Ce}, \text{Nd}, \text{and Ho}$ ): Synthesis and Atomic Structural Studies. *Inorganic Chemistry* **57**, 747-753 (2018).
- 130 Merrill, D. R., Sutherland, D. R., Ditto, J. J., Moore, D. B., Falmbigl, M., Medlin, D. L. & Johnson, D. C. The synthesis of  $[(\text{PbSe})_{1+\delta}]_m(\text{TiSe}_2)_n[(\text{SnSe}_2)_{1+\gamma}]_m(\text{TiSe}_2)_n$  heterostructures with designed nanoarchitectures by self assembly of amorphous precursors. *Nanoscale* **8**, 13646-13651 (2016).

### 3. Experimental Methods

#### 3.1. Chemicals

CHEMICAL	PURITY	SUPPLIER
<b>POLYDIMETHYLGLUTARIMIDE (PMGI)</b>	SF6 – Proprietary	Microchem
<b>POLYMETHYLMETHACRYLATE (PMMA)</b>	3 % (950k mol w.t.)	Microchem
<b>PROPAN-2-OL (IPA)</b>	≥99.9%	Sigma Aldrich
<b>HEXANE</b>	≥99.9%	Sigma Aldrich
<b>ACETONE</b>	≥99.9%	Sigma Aldrich
<b>METHANOL</b>	≥99.9%	Sigma Aldrich
<b>ETHANOL</b>	≥99.9%	Sigma Aldrich
<b>DEIONISED WATER (DI WATER)</b>	18.2 MΩcm	Mili-Q (Millipore Corp.)
<b>NITROGEN GAS</b>	≥99.998%	BOC

Table 3-1 - Chemicals list, purity and supplier

#### 3.2. Minerals

The cylindrite and franckeite samples are naturally occurring minerals mined from Poopo, Bolivia.

#### 3.3. Plan view sample preparation by dry stamp transfer

Samples were prepared in a class 100 clean room (National Graphene Institute, University of Manchester, UK). The mineral (Poopo, Bolivia) was mechanically exfoliated using the scotch tape method<sup>1</sup> onto a PMGI/PMMA bilayer on a silicon wafer. The membrane surrounding the region of interest was scratched, floated off the silicon wafer and transferred to a silicon/silicon nitride TEM grid (fabricated in house) by mechanical transfer<sup>2</sup>. The silicon/silicon nitride TEM grid was plasma cleaned (low power O<sub>2</sub>/Ar) prior to transfer. After transfer, the PMMA was removed by submersion in acetone, IPA, DI water and hexane baths.

#### 3.4. Plan view TEM sample preparation by drop casting

The mineral (Poopo, Bolivia) was mechanically ground in an agate pestle and mortar in minimal liquid nitrogen and subsequently diluted in ethanol or methanol. After which a

drop containing approximately 2 mg of material was deposited on to a Quantifoil grid (R1.2/1.3 200 copper mesh). The grid was dried under a gentle nitrogen flow until the solvent had fully evaporated. This process was repeated five times.

### **3.5. Cross section STEM lamellae preparation by focused ion beam**

The samples were prepared on either a FEI Novalab 600i or FEI Helios 660 (School of Materials, University of Manchester, UK). Both instruments are dual-beam systems, fitted with micro-manipulators and gas injection systems (GISs). Samples were prepared by exfoliating mineral (Poopo, Bolivia) onto a silicon/silicon oxide (290 nm) using the scotch tape method<sup>1</sup>, in a class 100 cleanroom (National graphene institute, University of Manchester, UK.). The samples were sputter coated *ex-situ* with 10 nm of amorphous carbon, and 3 nm of gold/palladium (60:40) using a Q150T coater (Quorum Technologies). The specimens were prepared using a modified version of the *in-situ* method, described by Schafer et.al.<sup>3</sup>. The region of interest was identified and aligned to a crystallographic edge, using the SEM column. The sample is aligned to the coincidence point of the ion and electron columns. A protective platinum strap (height: 500 nm, width: 2  $\mu$ m, length: 5 – 15  $\mu$ m) was added by electron induced deposition (5 kV, 1.6 nA). A further 2  $\mu$ m of platinum (height: 2  $\mu$ m, width: 2  $\mu$ m, length: 5 – 15  $\mu$ m) was deposited by ion beam induced deposition (30 kV, 400 pA). Corse trenches (depth: 2.5 – 6  $\mu$ m, length: 8  $\mu$ m, width: 5 – 15  $\mu$ m) were milled (30 kV 2.5 nA) around the region of interest. The trenches were further milled (30 kV, 700 pA) with an over tilt of  $\pm 2^\circ$ , until the Pt strap is approximately 1.5  $\mu$ m thick. The lamellae was partially cut free using a “J-cut”. The micro-manipulator was lowered until it contacted the sample, and welded by platinum deposition. The lamella was milled free and lifted from the sample and mounted on to a copper Omniprobe half grid. The lamella was welded to the gird by further platinum deposition, and freed from the micro-manipulator. The lamella was subsequently thinned until electron transparent, using decreasing ion beam energies and currents to minimise specimen damage. The typical parameters used are presented in Table 3-2.



<i>Beam Energy (kV)</i>	<i>Beam Current</i>	<i>Stage Tilt (°)</i>	<i>Depth (μm)</i>	<i>To lamella thickness (nm)</i>
30	0.23 nA	4	2	~1000
16	0.22 nA	2.5	2-5	~700
5	68 pA	1.5	2	~100
2	9 pA	0.5	1	~20 - 80

Table 3-2 typical focused ion beam milling parameters

### 3.6. STEM imaging

HAADF STEM images were collected using a probe side aberration corrected FEI G2 80-200 kV super-twin Titan (School of Materials, University of Manchester, UK). The STEM was equipped with an X-FEG electron source, Super-X EDXS system (0.7 srad collection angle) and a Gatan Imaging Filter (GIF) Quantum ER system. The microscope was operated with a 200 kV acceleration voltage, convergence angle of 21 mrad, and a HAADF inner angle of 54-64 mrad. The probe current was 90 pA for high resolution imaging and 180 pA for collection of EDX spectra. Cross section samples were orientated using the silicon substrate Kikuchi bands. Images were processed using Gatan Digital Microscope, and EDX data was processed using Bruker Esprit software, and the open source python library Hyperspy<sup>4</sup>.

### 3.7. Raman spectroscopy

Raman spectra were collected using a Horiba XploRA PLUS (School of Physics, University of Manchester, UK) with a 532 nm excitation wavelength, operated with a powers ranging from 125 μW – 2.15 mW, with a 100x objective lens. The spectra were aligned to the 519 cm<sup>-1</sup> Si peak. Data was analysed using Horiba's LabSpec 6, Origin, and open source Python packages.

### 3.8. AFM

AFM maps were collected using either a Bruker Dimeson Icon or a Bruker FastScan instrument (School of Physics, University of Manchester, UK), operating in PeakForce tapping mode with a frequency of 2 kHz. With a Scan Asyst-fluid plus tip, force constant 0.7 Nm<sup>-1</sup>. The images were processed using NanoScope 1.9, WSxM<sup>5</sup> and Gwydeion. The 'Flatten plus'<sup>6</sup> algorithm was used to flatten the substrates, and

background noise was removed with the application of median filtering and polynomial subtraction.

### 3.9. References

- 1 Novoselov, K. S., Geim, A. K., Morozov, S. V., Jiang, D., Zhang, Y., Dubonos, S. V., Grigorieva, I. V. & Firsov, A. A. Electric Field Effect in Atomically Thin Carbon Films. *Science* **306**, 666-669 (2004).
- 2 Dean, C. R., Young, A. F., Meric, I., Lee, C., Wang, L., Sorgenfrei, S., Watanabe, K., Taniguchi, T., Kim, P., Shepard, K. L. & Hone, J. Boron nitride substrates for high-quality graphene electronics. *Nature nanotechnology* **5**, 722 (2010).
- 3 Schaffer, M., Schaffer, B. & Ramasse, Q. Sample preparation for atomic-resolution STEM at low voltages by FIB. *Ultramicroscopy* **114**, 62-71 (2012).
- 4 de la Pena, F., Ostasevicius, T., Tonaas Fauske, V., Burdet, P., Jokubauskas, P., Nord, M., Sarahan, M., Prestat, E., Johnstone, D. N., Taillon, J., Jan Caron, u., Furnival, T., MacArthur, K. E., Eljarrat, A., Mazzucco, S., Migunov, V., Aarholt, T., Walls, M., Winkler, F., Donval, G., Martineau, B., Garmannslund, A., Zagonel, L.-F. & Iyengar, I. Electron Microscopy (Big and Small) Data Analysis With the Open Source Software Package HyperSpy. *Microscopy and Microanalysis* **23**, 214-215 (2017).
- 5 Horcas, I., Fernández, R., Gómez-Rodríguez, J. M., Colchero, J., Gómez-Herrero, J. & Baro, A. M. WSXM: A software for scanning probe microscopy and a tool for nanotechnology. *Review of Scientific Instruments* **78**, 013705 (2007).
- 6 Gimeno, A., Ares, P., Horcas, I., Gil, A., Gómez-Rodríguez, J. M., Colchero, J. & Gómez-Herrero, J. 'Flatten plus': a recent implementation in WSxM for biological research. *Bioinformatics* **31**, 2918-2920 (2015).

## 4. Paper 1 – Exfoliation of natural van der Waals heterostructures to a single unit cell thickness

This chapter demonstrates the exfoliation of franckeite ( $n=2$ ,  $m=1$ ) to single unit cell thickness. This is the first reported exfoliation of a MLC that does not contain a traditional vdW gap. Bulk and exfoliated specimens were characterised using HAADF STEM and EDX spectroscopy, and the layer interface was examined using cross sectional analytical STEM. A range of other techniques, including AFM and Raman spectroscopy, were used to characterise the exfoliated flakes. Furthermore, the specimens' electrochemical properties were extensively investigated, and found to be excellent. This manuscript is presented as published, it is important to note that the in-plane axes are reversed compared with the rest of the manuscript. i.e. the incommensurate relationship is along the **b** axis ([010]) and the semi-commensurate axis is along the **a** axis ([100]).

The franckeite crystal was initially purchased as ' $\text{Pb}_{1-x}\text{Sn}_x\text{S}$ ', and the sample was provided to the author by Dr. Matěj Velický for elemental analysis to estimate the Pb:Sn ratio. However upon preliminary CTEM characterisation, striations were present in BF CTEM images and the diffraction pattern showed satellite spots. Subsequent plan view STEM EDX spectra showed the presence of antimony and iron signals, in addition to the expected lead, tin and sulphur. Furthermore, high resolution HAADF STEM images also showed the presence of striations. The crystal was subsequently demonstrated to exfoliate, after which cross section samples were prepared by FIB, and analysed using analytical STEM. From this analysis the ' $\text{Pb}_{1-x}\text{Sn}_x\text{S}$ ' specimen was determined to be the naturally occurring MLC franckeite. This paper demonstrates two important themes of this thesis, firstly that the exfoliation of MLCs which do not contain a vdW gap (i.e.  $m=1$ ) may be exfoliated, and secondly that analytical STEM, particularly when specimens are viewed parallel to the basal planes, is an invaluable tool for the analysis of MLCs.

**Contributions to work:**

Dr. Matěj Velický designed and directed the work, characterised the specimens using optical microscopy, Raman spectroscopy and electrochemical measurements, and analysed the XPS data; Prof. Sarah Haigh assisted with the collection of STEM data; Dr. Aidan Rooney assisted with the preparation of cross section samples by FIB and produced the atomic model; Dr. Peter Toth collected the SEM images and assisted with the collection of Raman data; Dr. Alexy Kozikov fabricated the devices, and characterised the samples with optical imaging and AFM; Dr. Collin Woods assisted with the collection of AFM data; Dr. Artem Mishchenko and Dr. Jun Yin collected and analysed the electrical transport data; Dr. Laura Fumagalli collected EFM data; Dr. Thanasis Georgiou performed liquid exfoliation studies; Dr. Viktor Zólyomi performed the DFT calculations. Dr. Matěj Velický drafted the final manuscript, Prof. Sarah Haigh and I analysed TEM data and co-wrote the section related to TEM characterisation. All authors contributed to the discussions.

# Exfoliation of natural van der Waals heterostructures to a single unit cell thickness

Matěj Velický,<sup>\*1</sup> Peter S. Toth,<sup>1</sup> Alexander M. Rakowski,<sup>2</sup> Aidan P. Rooney,<sup>2</sup> Aleksey Kozikov,<sup>3</sup> Colin R. Woods,<sup>3</sup> Artem Mishchenko,<sup>3</sup> Laura Fumagalli,<sup>3</sup> Jun Yin,<sup>3</sup> Viktor Zólyomi,<sup>3</sup> Thanasis Georgiou,<sup>4</sup> Sarah J. Haigh,<sup>2</sup> Kostya S. Novoselov,<sup>3</sup> and Robert A.W. Dryfe<sup>\*1</sup>

<sup>1</sup> School of Chemistry, University of Manchester, Oxford Rd, Manchester, M13 9PL, UK

<sup>2</sup> School of Materials, University of Manchester, Oxford Rd, Manchester, M13 9PL, UK

<sup>3</sup> School of Physics and Astronomy, University of Manchester, Oxford Rd, Manchester, M13 9PL, UK.

<sup>4</sup> Manchester Nanomaterials Ltd, 83 Ducie Street, Manchester, M1 2JQ, UK\*

To whom correspondence should be addressed. Tel: +44 (0)161-306-4522; Fax: +44 (0)161-275-4598, e-mail: matej.velicky@manchester.ac.uk or robert.dryfe@manchester.ac.uk.

## Abstract

Weak interlayer interactions in van der Waals crystals facilitate their mechanical exfoliation to monolayer and few-layer two-dimensional materials, which often exhibit striking physical phenomena absent in their bulk form. Here we utilise mechanical exfoliation to produce a two-dimensional form of a mineral franckeite and show that the phase segregation of chemical species into discrete layers at the sub-nanometre scale facilitates franckeite's layered structure and basal cleavage down to a single unit cell thickness. This behaviour is likely to be common in a wider family of complex minerals and could be exploited for a single-step synthesis of van der Waals heterostructures, as an alternative to artificial stacking of individual two-dimensional crystals. We demonstrate p-type electrical conductivity and remarkable electrochemical properties of the exfoliated crystals, showing promise for a range of applications, and use the density functional theory calculations of franckeite's electronic band structure to rationalise the experimental results.

## Introduction

The research on two-dimensional (2D) materials has so far been mainly focused on unary and binary crystals such as graphene and  $\text{MoS}_2$ <sup>1</sup> and little attention has been paid to more complex layered materials.<sup>2</sup> However, preferential phase segregation strongly dependent on chemical composition, which is a phenomenon that has previously been observed in ternary sulphides such as  $\text{PbSnS}_2$ ,<sup>3</sup> could lead to formation of layered structures and van der Waals heterostructures. Franckeite is a natural, thermodynamically stable, mixed-metal sulphide mineral, composed of lead, tin, antimony, iron, and sulphur, first discovered in 1893.<sup>4</sup> It exhibits a distinctly layered structure, which is related to its complex chemical composition. Band gap of the individual metal sulphides, which combine to constitute franckeite, ranges from 0.37 eV in PbS (galenite) to 2.1 eV in  $\text{SnS}_2$  (berndtite),<sup>5</sup> with the band gap of franckeite itself being previously determined by diffusive reflectance spectroscopy as 0.65 eV.<sup>6</sup> Many other complex sulphides exist, with the band structure depending on their exact chemical composition and structure.<sup>6</sup> This offers great opportunities in band gap engineering,<sup>7</sup> phase engineering,<sup>8</sup> thermoelectric materials,<sup>3</sup> and solar control coatings,<sup>9</sup> which could all be realised through synthesis of complex metal-sulphides with on-demand properties.

Here, we show that franckeite is a natural heterostructure exhibiting phase segregation into discrete layers held together by van der Waals forces, which facilitates its basal cleavage. We use scanning electron microscopy (SEM), transmission electron microscopy (TEM), energy-dispersive X-ray spectroscopy (EDXS), and X-ray photoelectron spectroscopy (XPS) to determine franckeite structure and chemical composition. Importantly, we show that franckeite can be exfoliated to a single unit cell thickness (1.85 nm), resulting in a high ratio between the lateral size and thickness of the exfoliated crystals, as confirmed using optical microscopy, atomic force microscopy (AFM), and Raman spectroscopy. The electronic transport measurements reveal that franckeite is a p-doped degenerate semiconductor and the electrochemical measurements show that it has a high intrinsic electric double-layer capacitance showing promise in energy storage applications. The density functional theory (DFT) calculations of franckeite's electronic band structure indicate only weak interactions between the individual van der Waals layers, also confirmed by the independence of

franckeite's Raman spectrum of the number of layers and the incommensurate lattice matching observed by the high-angle annular dark-field (HAADF) scanning transmission electron microscopy (STEM).

## Results

### Morphology and chemical composition of bulk franckeite

The SEM images in Figure 4-1a–c reveal franckeite's layered nature, which facilitates its facile mechanical exfoliation. In the highest magnification image (Figure 4-1), terraces of micro-/nano-scopic width are clearly visible. The TEM-EDXS elemental maps in Figure 4-1d–h show that the main elements, lead, tin, antimony, iron, and sulphur, are homogeneously distributed when viewed perpendicular to the layers (along the [001] direction). The averaged EDXS spectrum in Figure 4-1i and quantification in Table 4-1 were the basis for the composition stoichiometry analysis, resulting in an approximate chemical formula of  $\text{Pb}_{6.0}\text{Sn}_{3.1}\text{Sb}_{2.5}\text{Fe}_{1.1}\text{S}_{12.0}\text{O}_{1.1}$ . This indeed best matches franckeite, a member of a complex group of metal sulphide minerals also including cylindrite, potosiite, and incaite, which are found in the southwest of Bolivia, and have a generic chemical formula  $\left(\text{Pb, Sn}\right)_{6+x}^{2+} \text{Sb}_2^{3+} \text{Fe}^{2+} \text{Sn}_2^{4+} \text{S}_{14+x}$ , where  $-1 \leq x \leq 0.25$ .<sup>10</sup> The approximate chemical formula determined from the EDXS is not completely charge-balanced (with ca. 5 – 10 % excess positive charge, depending on the exact oxidation states of the metals) and it also does not fully fit the generic chemical formula of franckeite. This is mainly caused by the low sensitivity of the EDXS, overlap between S  $K\alpha$  and Pb  $M\alpha$  peaks, and the presence of O, C, and Ag impurities. Further SEM characterisation and full TEM-EDXS quantification are found in Supplementary Note 1, SI Figure 4-8, and SI Table 4-3.

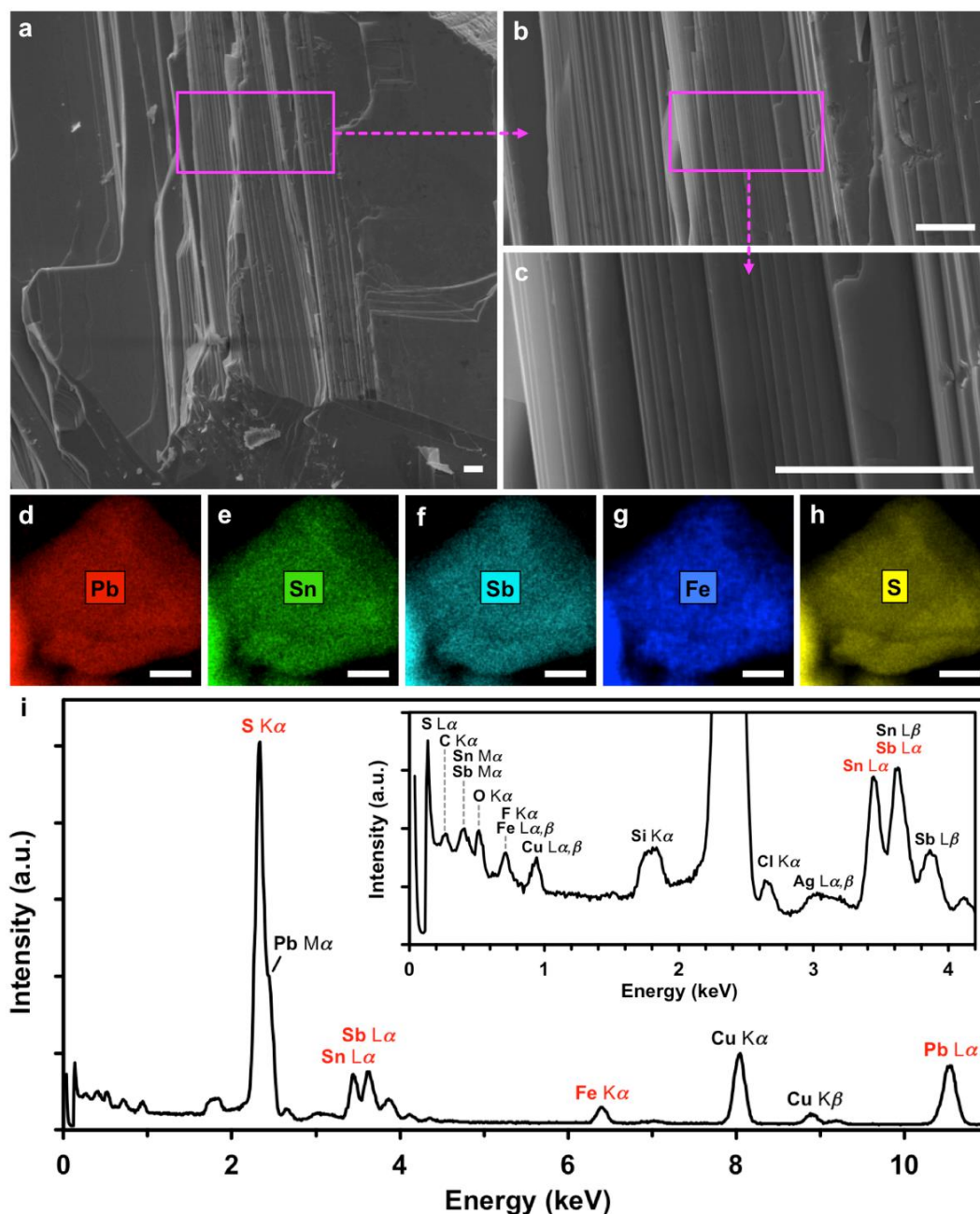


Figure 4-1 - **SEM and TEM-EDXS characterisation of franckeite.** a–c, SEM images of franckeite immobilised on a conductive carbon support. Zoom areas are highlighted by the magenta rectangles. The scale bars denote 5  $\mu\text{m}$ . d–h, TEM-EDXS maps of a franckeite crystal showing lead, tin, antimony, iron, and sulphur, respectively. The scale bars denote 30 nm. i, Averaged EDXS spectra with the inset showing the low-intensity peaks at low energies. The peaks of the five major elements used for the quantification shown in Table 1 are marked in red. The secondary peaks and the peaks originating from the substrate and impurities, which were de-convoluted and excluded from the quantification, are marked in black.



element	concentration (at%)
Pb	24.1 ± 4.9
Sn	12.5 ± 2.5
Sb	10.2 ± 2.1
Fe	4.6 ± 0.4
S	48.6 ± 3.1

Table 4-1 - EDXS quantification of bulk franckeite

### Crystal structure and phase segregation of franckeite

Figure 4-2 summarises the high-angle annular dark-field (HAADF) scanning transmission electron microscopy (STEM) characterisation of franckeite. The structure of this complex layered misfit compound mineral has troubled mineralogists, crystallographers, and electron microscopists for several decades,<sup>11-13</sup> until significant advances in understanding of its exact structure have eventually been achieved.<sup>14-16</sup> Our results confirm phase segregation into discrete Sn-rich, pseudo-hexagonal (H) and Pb-rich, pseudo-tetragonal (T) layers with a van der Waals gap between them. A cross-section through a thin exfoliated franckeite crystal was extracted to reveal a unit cell height of ~1.85 nm (Figure 4-2b and e). The two layers, H and T, are incommensurate with differing lattice dimensions in the [010] direction, which results in a mismatch periodicity of ~4.3 nm visible as moiré fringes when viewed along the [001] direction in the TEM. This is also confirmed by the relative atomic displacements of the two layers in the cross-section (see Supplementary Note 2, SI Figure 4-9 and SI Figure 4-10). Atomic-resolution HAADF-STEM (Figure 4-2e) and STEM-EDXS elemental analyses of this structure (Figure 4-2c and f) reveal significant compositional segregation at the atomic scale. Specifically, Pb in the inner two atomic planes of T layers is partially replaced by Sb, resulting in an alternating Pb–Sb–Pb arrangement (see the structure model in Figure 4-2d). Small amount of Sn in the T layer (~8 – 10 at%) could indicate a partial replacement of Pb and/or Sb atoms by Sn. The average composition for the two layers individually is determined as Pb<sub>6.3</sub>Sb<sub>2</sub>S<sub>9</sub> (T) and Sn<sub>2.3</sub>FeS<sub>5.6</sub> (H), resulting in an overall average chemical formula of Pb<sub>6.3</sub>Sn<sub>2.3</sub>Sb<sub>2.0</sub>FeS<sub>14.6</sub>.

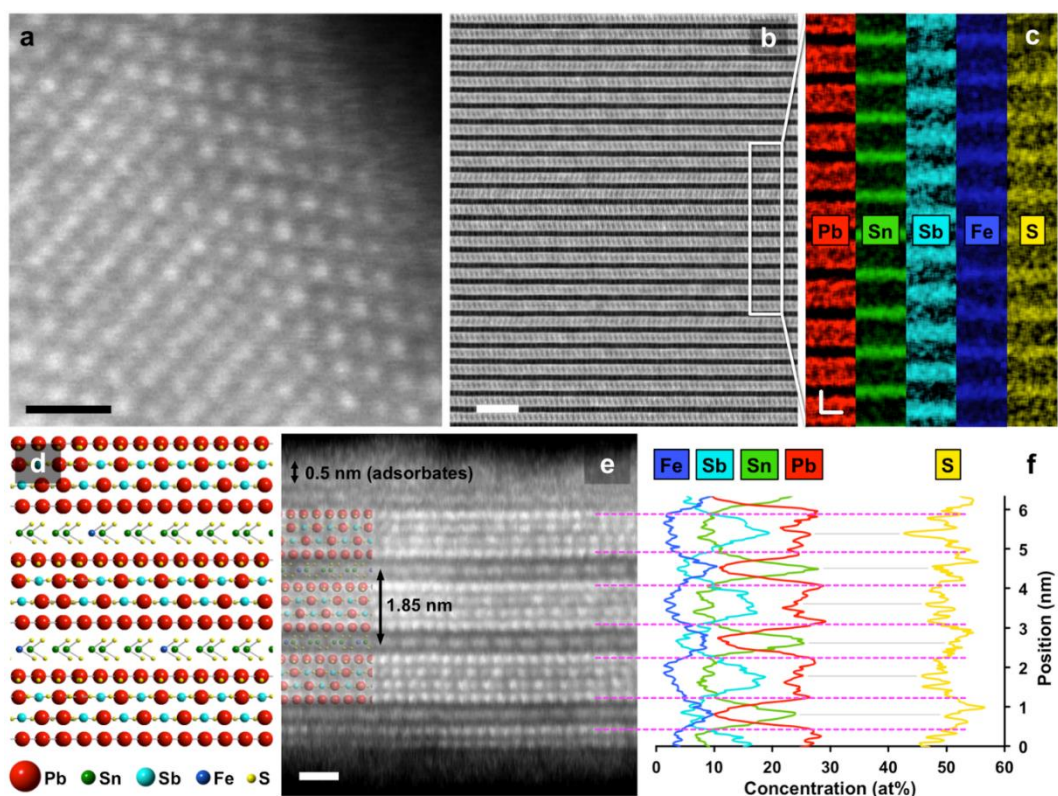


Figure 4-2 - **HAADF-STEM imaging of franckeite.** **a**, High-resolution image of the crystal lattice viewed along the [001] direction (plan view of the basal plane). The scale bar corresponds to 1 nm. **b**, Cross-sectional image of the layering viewed along the [100] direction. The scale bars corresponds to 5 nm. **c**, Corresponding EDXS elemental intensity maps with the two-axis scale bar corresponding to 1 nm. **d**, Proposed structure model of franckeite, with the relative size of atoms corresponding to their brightness in HAADF. **e**, Atomic-resolution image of the cross-section for a few-layer crystal. The inset shows overlaid franckeite structure, the scale bar corresponds to 1 nm. **f**, Corresponding EDXS concentration profiles showing compositional variation both between and within the individual layers. In contrast, no compositional variations are detected for the crystal viewed along the [001] direction. The pink dashed lines are a guide for the eye correlating the EDXS profile with the cross-sectional HAADF. The grey solid lines are a guide for the eye correlating the concentration peaks (Pb and Sn) and troughs (S).

Interestingly, the cross-sectional STEM images also show stacking faults, consisting of irregular lateral displacements of the  $\text{SnS}_2$  layers along the [010] direction, which is likely to cause the forbidden lattice spots appearing in the electron diffraction data (see Supplementary Note 2, SI Figure 4-9 and SI Figure 4-10). The thinnest region cross-sectioned for STEM analysis was  $\sim 6$  nm (or  $\sim 3$  unit cells) thick with the upper (freshly cleaved) surface terminating at the H layer and being covered with  $\sim 0.5$  nm thick layer of carbonaceous adsorbates (Figure 4-2e–f). Surprisingly, the lower, substrate-bound surface terminates part way through the Pb-rich layer. It is likely that such imperfect cleavage may be associated with a stacking fault, which locally weakens the structure.

Such anomalies have also been confirmed by the observation of terraces with a sub-monolayer height. The structural analysis above suggests that the incommensurate stacking of the individual H and T layers (and therefore weak interaction between them) leads to a predominantly uniaxial basal cleavage of franckeite and a weak or no dependence of the electronic and structural properties of franckeite on the number of layers (see below).

Other related minerals such as SnS and SnS<sub>2</sub> have been recently shown to be readily exfoliated<sup>17,18</sup> and preferential elemental segregation to a single Pb-rich atomic plane within a PbSnS<sub>2</sub> lattice was also previously observed.<sup>3</sup> The phase segregation observed here, which gives rise to a van der Waals gap between the H and T layers, proves the concept of a naturally occurring heterostructure material, a phenomenon, which is likely to be common among many complex minerals. This could be exploited simultaneously with the emerging advances in synthesis of metal chalcogenides and tailoring of their properties,<sup>19</sup> in order to create man-made van der Waals heterostructures with properties tailored to specific applications.

### **Surface chemical composition of franckeite**

The surface sensitivity and a few-nanometre penetration depth of the XPS technique were utilised to determine the surface chemical composition of franckeite including the atomic oxidation states and the extent of surface impurities. Figure 4-3a shows an XPS spectrum of franckeite used for the quantification of the major elements shown in Table 4-2. The high-resolution spectra of Pb 4*f*, Sn 3*d*, Sb 3*d*, and S 2*p* binding energy regions are shown in Figure 4-3b–e. Compositional stoichiometry analysis yields a surface composition chemical formula of Pb<sub>6.0</sub>Sn<sub>2.0</sub>Sb<sub>2.4</sub>S<sub>13.8</sub>O<sub>1.0</sub>. Peak fitting was used to determine the oxidation states of individual elements. Lead and tin (Figure 4-3b and c, respectively) are present as Pb<sup>2+</sup> and Sn<sup>2+</sup> (both ~80%), and Pb<sup>4+</sup> and Sn<sup>4+</sup> (both ~20 %). Antimony (Figure 4-3d) is present as Sb<sup>3+</sup> (~60 %) and Sb<sup>5+</sup> (~40 %). Sulphur (e) is present exclusively as S<sup>2-</sup> and oxygen is bound both in metal oxides (O<sup>2-</sup>) and carbonaceous adsorbates. In comparison to the bulk-sensitive EDXS, only a negligible amount of Fe (<0.5 at%) and relatively lower concentration of Sn are detected from the surface-sensitive XPS. This suggests that the Sn- and Fe-rich H layers (Figure 4-2c and f) are underrepresented on the surface of franckeite, possibly due to the surface being unstable upon exfoliation and degrading in air. Stoichiometric analysis, full

quantification, and comparison of the freshly cleaved and air-aged crystals can be found in Supplementary Note 3, SI Figure 4-10, SI Figure 4-11, SI Table 4-4 and SI Table 4-5.

element	concentration range (at%)	average concentration (at%)
Pb	23.5 – 26.8	$24.7 \pm 0.3$
Sn	7.1 – 9.0	$8.1 \pm 0.2$
Sb	9.0 – 13.1	$10.1 \pm 0.2$
S	51.7 – 60.1	$57.0 \pm 0.5$

Table 4-2 - XPS quantification of franckeite surface

### Preparation and characterisation of thin franckeite

Importantly, we succeeded in isolating monolayer (single unit cell thick) franckeite crystals. Thin franckeite layers were mechanically exfoliated onto an SiO<sub>2</sub> substrate and characterised using optical microscopy, AFM, and Raman spectroscopy. Bright-field and dark-field optical images of a monolayer franckeite crystal with adjacent few-layer and bulk crystals are shown in Figure 4-4a and b. Corresponding AFM image and the height profile of the monolayer region are shown in Figs. 4c and 4d. The monolayers have typical thicknesses of 2.4 – 3.5 nm, which is in good agreement with the single unit cell repeat period determined from cross-sectional TEM (~1.85 nm), considering the additional increase in height originating from the AFM instrumental offset, layer of carbonaceous adsorbates, and impurities or moisture trapped between the crystal and substrate, which are known to beset characterisation of 2D materials.<sup>2,20,21</sup>

Furthermore, small terraces with less than a monolayer thickness were occasionally observed (SI Figure 4-13). Through mechanical exfoliation of a large number of crystals, we have discovered that length of the few-layer crystals is typically tens of  $\mu\text{m}$ , but their width rarely exceeds 0.5 – 1  $\mu\text{m}$ , resulting in characteristic, needle-like, thin crystals with a large length-to-width aspect ratio (SI Figure 4-14). This preferential uniaxial basal cleavage is supported by the commensurate and incommensurate lattice stacking in the [100] and [010] directions, respectively, observed in the TEM/STEM.

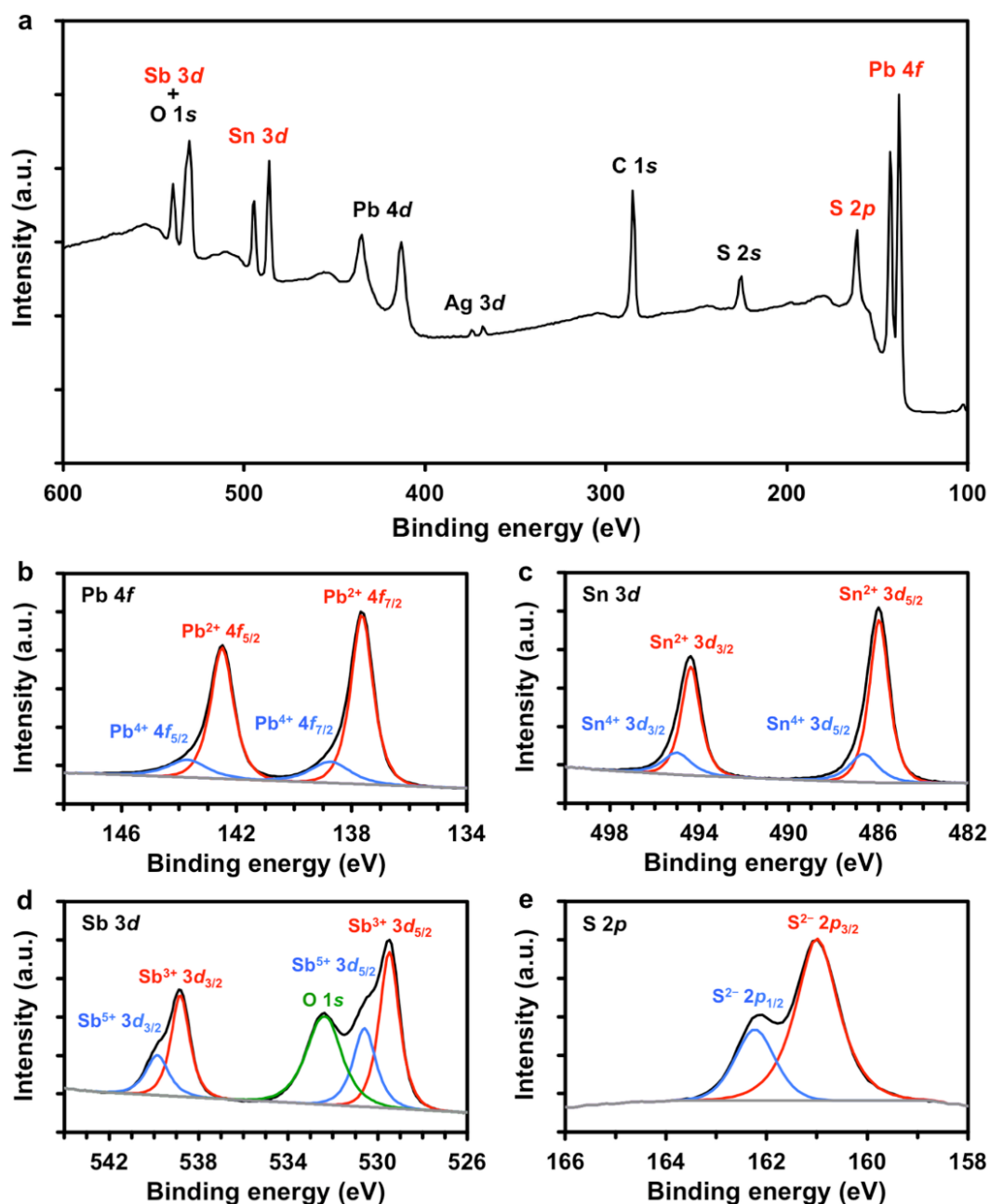


Figure 4-3 - XPS characterisation of franckeite surface. **a**, Average XPS spectrum of franckeite obtained from multiple individual measurements, referenced to the adventitious carbon C 1s peak at 284.7 eV.<sup>22</sup> The peaks labelled in red were used for the quantification shown in Table 2. Other significant peaks, which were not used in quantification, are labelled in black. **b–e**, High-resolution spectra of Pb 4f, Sn 3d, Sb 3d (+ O 1s), and S 2p binding energy regions. The intensities are normalised to the most intense peak within the respective spectral region.

Raman spectra of monolayer, few-layer and bulk franckeite obtained using a 532 nm laser excitation wavelength are shown in Figure 4-4e (AFM was used to determine the thickness of individual franckeite flakes). Due to the small lateral size of thin franckeite crystals, only well isolated flakes were used for Raman spectroscopy measurements to avoid signal overlap with any adjacent thicker regions. Low laser power density was used to avoid franckeite degradation and a large number of individual measurements

(14 – 28) at different locations on each flake were accumulated to build up each spectrum (substrate-uncorrected spectra are shown in SI Figure 4-15).

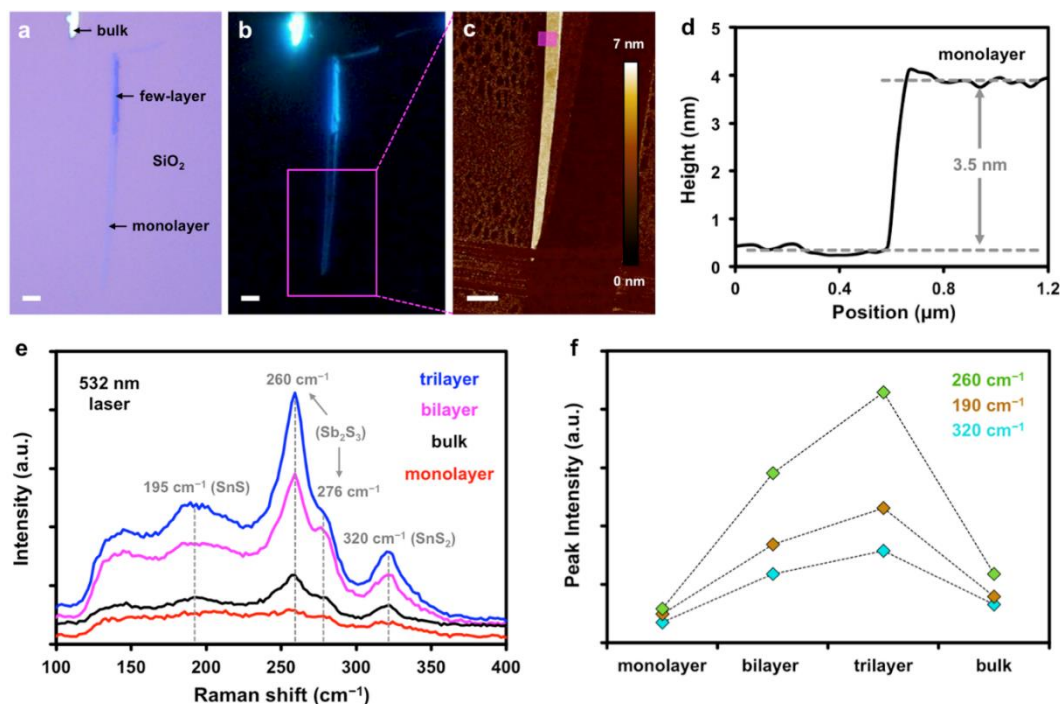


Figure 4-4 - **Optical microscopy, AFM, and Raman spectroscopy identification of thin franckeite.** **a,b**, Bright-field and dark-field optical images of a franckeite crystal exfoliated on an SiO<sub>2</sub>/Si substrate. **c**, AFM image of a selected monolayer area indicated by the magenta rectangle in **(b)**. All scale bars denote 2  $\mu$ m. **d**, Step-height profile of monolayer franckeite flakes taken from an area indicated by the transparent magenta rectangle in **(c)**. **e**, Raman spectra of monolayer, bilayer, trilayer, and bulk franckeite using a 532 nm laser excitation wavelength at 19 kW cm<sup>-2</sup> power density. Spectrum of the underlying Si substrate is subtracted from the thin layer spectra ( $\leq 3$ ). **f**, Intensity of the three major peaks as a function of thickness.

Despite the lack of Raman literature on franckeite, we make a tentative assignment of the main franckeite peaks based on the available Raman data for the individual metal sulphides. We infer that the Raman spectrum of franckeite is dominated by Sb<sub>2</sub>S<sub>3</sub> (stibnite) vibrations with a corresponding peak at 260 cm<sup>-1</sup> and a shoulder at 276 cm<sup>-1</sup>.<sup>23</sup> SnS<sub>2</sub> (berndtite) vibrations are most likely to produce the peak at 320 cm<sup>-1</sup>.<sup>24</sup> Both Sb<sub>2</sub>S<sub>3</sub> and SnS<sub>2</sub> have large optical band gaps of 1.72 and 2.10 eV,<sup>5</sup> respectively, and therefore exhibit comparatively weaker light absorption and hence stronger Raman scattering than PbS (0.37 eV),<sup>5</sup> which is a relatively weak Raman scatterer and does not contribute to the signal significantly.<sup>25</sup> A weak broad band, centred around 195 cm<sup>-1</sup> in bulk franckeite, which is hardly observable in monolayer could originate from SnS (1.01 eV) vibrations.<sup>5,26</sup> No significant changes in the frequency of these Raman modes are observed for different franckeite thicknesses, which is to be

expected due to the incommensurate stacking of the T and H layers. There is, however, a noticeable increase in the Raman intensity for bilayer and trilayer in contrast to monolayer and bulk (Figure 4-4d). Such enhancement has previously been observed for other 2D materials including graphene,<sup>27</sup> MoS<sub>2</sub>,<sup>28</sup> and MoSe<sub>2</sub>,<sup>29</sup> and it can be explained by an optical interference in the 2D crystal/SiO<sub>2</sub>/Si system and corresponding optical field enhancement for certain 2D crystal thicknesses.<sup>30</sup> Furthermore, no photoluminescence was detected within a 532 – 900 nm range for monolayer or bulk (SI Figure 4-16), which agrees with the indirect mid-/far-infrared band gap of franckeite determined by the transport measurements and predicted by the DFT.

Raman spectroscopy data suggest that the electronic and structural properties of franckeite do not depend on the number of layers, which is to be expected given the incommensurate stacking and hence weak interaction between the T and H layers. Importantly, the phase segregation into discrete van der Waals layers, which is likely to be a common denominator for a wider family of naturally occurring complex minerals, could be utilised for preparation of man-made van der Waals heterostructures as a formidable alternative to their painstaking construction by stacking of the individual 2D materials on top of each other.<sup>31</sup> Furthermore, thin franckeite shows remarkable thermodynamic stability upon exfoliation in air up to more than 6 months, as confirmed by optical microscopy, AFM, Raman spectroscopy. Transport and electrostatic force microscopy (EFM) measurements, which are more sensitive to crystal degradation, show that all but monolayer franckeite flakes are conductive. Such stability is exceptional in comparison to some other novel 2D materials, such as phosphorene or NbSe<sub>2</sub>, which often degrade in air when isolated in their mono- or few-layer form.<sup>32</sup> Further characterisation using optical microscopy, AFM, and Raman spectroscopy, including laser-induced degradation and surface ablation is detailed in Supplementary Note 4, SI Figure 4-17 and SI Figure 4-18.

### **Electrochemistry and liquid-phase exfoliation of franckeite**

In order to explore the potential use of franckeite in energy storage and conversion applications, we have determined its electrochemical properties using a micro-droplet cell measurement, representative results of which are summarised in Figure 4-5. This

approach was previously applied to topography-dependent electrochemical measurements on graphene and MoS<sub>2</sub>.<sup>20,33,34</sup> Since the cleavage of franckeite is mostly limited to a single plane, we use the term ‘basal’ here to describe its low-defect (001) surface, and term ‘edge’ to describe other surfaces with an increased density of edges, terraces, and defects. We have found that the average electric double-layer capacitance measured by cyclic voltammetry on the basal surface is  $27.4 \pm 2.2 \mu\text{F cm}^{-2}$  and further increases to  $153 \pm 62.8 \mu\text{F cm}^{-2}$  on the edge surface (Figure 4-5a). In comparison, typical capacitance values measured using the same method are ca. 15 – 30  $\mu\text{F cm}^{-2}$  for unpolished platinum, 2 – 4  $\mu\text{F cm}^{-2}$  for the basal plane of MoS<sub>2</sub>, and 1 – 2  $\mu\text{F cm}^{-2}$  for the basal plane of graphene. It is important to note here that the basal plane surface of mechanically exfoliated 2D materials is very flat, unlike the disordered and porous surface of multi-flake materials, typically prepared by liquid-phase exfoliation. The real surface area of liquid-phase exfoliated 2D materials is often orders of magnitude larger than the apparent surface area, resulting in artificially inflated capacitance values.<sup>35-37</sup> The high capacitance in our case therefore indicates a degenerate semiconducting nature of franckeite, also confirmed by independence of the voltammetric response of illumination intensity, and an additional contribution from a redox activity, which can be observed when the potential window is extended (see Supplementary Note 5, SI Figure 4-19 and SI Figure 4-20). We argue that this is directly related to franckeite’s electronic structure as it has been previously proposed for MoS<sub>2</sub> that steric accessibility of metallic orbitals at the crystal edges increases its electrochemical performance.<sup>38</sup> We cannot completely rule out that edges/defects on the surface, or even solution-induced delamination of the crystals, may contribute to the capacitance increase. However, this would in fact aid franckeite liquid-phase exfoliation and ion intercalation.

To demonstrate the feasibility of this approach, we perform ultrasonication-assisted liquid-phase exfoliation of franckeite in five different solvents, results of which are summarised in Figure 4-5d–f. Similarly to other 2D materials, N-methyl-2-pyrrolidone (NMP) offers the highest concentration of the exfoliated material,<sup>39,40</sup> followed by N,N-dimethylformamide (DMF), and acetone (Figure 4-5d). No visible material remains in suspension after exfoliation in isopropyl alcohol (IPA) or water. A representative AFM image in Figure 4-5e shows that the exfoliated flakes tend to re-stack into large



agglomerates, although thin individual crystals with thickness less than 5 layers are still found (Figure 4-5f). These results demonstrate that liquid-phase exfoliation could be used as an alternative, scalable method of thin franckeite production.

Heterogeneous electron transfer rate measurement using two common redox mediators,  $\text{Ru}[(\text{NH}_3)_6]^{3+/2+}$  and  $[\text{Fe}(\text{CN})_6]^{3-/4-}$ , is shown in Figure 4-5b, yielding average values of the standard rate constant of  $(0.62 \pm 0.34) \times 10^{-3} \text{ cm s}^{-1}$  for  $\text{Ru}[(\text{NH}_3)_6]^{3+/2+}$  and  $(0.90 \pm 0.17) \times 10^{-3} \text{ cm s}^{-1}$  for  $[\text{Fe}(\text{CN})_6]^{3-/4-}$ . These values exceed those determined on graphite and  $\text{MoS}_2$  using the same experimental method.<sup>20</sup> Hydrogen evolution, an important technological reaction, was difficult to quantify in a diffusion-limited regime within the micro-droplet electrochemical cell. Nevertheless, some hydrogen evolution activity is observed on basal surface in 1 M HCl solution as compared to the blank electrolyte solution (Figure 4-5c).

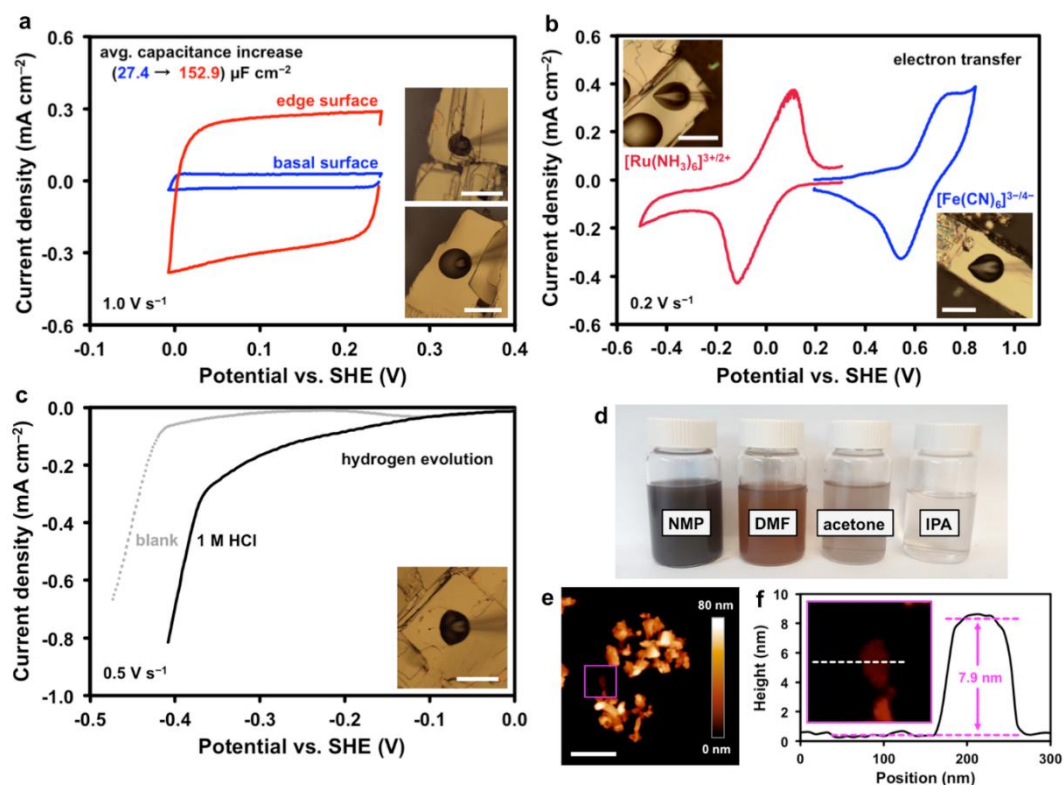


**Figure 4-5 - Electrochemical characterisation and liquid-phase exfoliation of franckeite.** **a**, Capacitance measurement on the basal and edge surface using a 6 M LiCl aqueous supporting electrolyte. **b**, Electron transfer measurement on basal surface using  $\text{Ru}[(\text{NH}_3)_6]^{3+/2+}$  and  $[\text{Fe}(\text{CN})_6]^{3-/4-}$  redox mediators in 6 M LiCl. **c**, Hydrogen evolution measurement using 1 M HCl in 6 M LiCl. The optical images in the inset show the micro-droplet electrochemical cells utilised for the measurement, scale bars are 50 μm. **d**, Photograph of franckeite suspensions in NMP, DMP, acetone, and IPA, after an ultrasonication-assisted liquid-phase exfoliation of 5 mg ml<sup>-1</sup> franckeite solution and subsequent centrifugation. **e**, AFM image of an agglomerate of thin franckeite flakes following a drop-cast transfer of the NMP suspension onto an SiO<sub>2</sub>/Si substrate and subsequent solvent evaporation. The scale bar corresponds to 500 nm. **f**, Height profile of a 4-layer franckeite flake corresponding to the white dashed line in the inset AFM image.

### Transport measurement of thin franckeite

We also measured the electronic transport properties of devices with various franckeite thicknesses (selected device images are shown in SI Figure 4-21). Despite numerous attempts, we failed to observe conductivity in monolayer devices (6 in total), most likely due to franckeite degradation caused by the loss of certain atomic species or surface oxidation as suggested by the XPS results. Bilayer devices, on the other hand, do repeatedly conduct. Figure 4-6 demonstrates the typical transport characteristics of bilayer and 5-layer franckeite. Devices of both thicknesses display electric field-effect behaviour (Figure 4-6a and b), with the bilayer device (Figure 4-6c) showing stronger conductance modulation than the 5-layer device (Figure 4-6d). From the gate voltage dependence, we conclude that the material is a p-doped semiconductor. Current-bias voltage characteristics are non-linear, suggesting the formation of a Schottky barrier at the interface between the metal and franckeite, also supported by the strong temperature dependence of current-voltage characteristics (Figure 4-6e). Additional data for a device of 4-layer thickness are presented in Supplementary Note 6 and SI Figure 4-22. The Arrhenius plots of the zero-bias conductance dependence on temperature (Figure 4-6e) allowed us to extract the activation energies of 220 meV for bilayer, 170 meV for 4-layer, and 80 meV for 5-layer devices. Such activation energies are comparable with the size of the band gap predicted by our DFT calculations (0.25 – 0.35 eV) but it is lower than the band gap determined previously by the diffuse reflectance spectroscopy (0.65 eV).<sup>6</sup> We also verified the transport measurements results by performing electrostatic force microscopy (EFM) measurements on thin franckeite, and confirmed, that while the bilayer and thicker franckeite layers are conductive, the monolayers are insulating (see Supplementary Note 6 and SI Figure 4-23).

### Electronic band structure calculations

In order to understand the transport, electrochemistry, and Raman spectroscopy results, we performed DFT calculations of the electronic band structure of franckeite. First, we calculated the electronic structure of T and H layers using a simplified stoichiometry:  $\text{Pb}_3\text{SbS}_4$  for the T layer and  $\text{SnS}_2$  for the H layer. The resulting band structures in Figure 4-7a(T layer) and Figure 4-7 b(H layer) reveal a very large difference in the work functions for the two layers (3.76 eV). Furthermore, the T layer

exhibits a small direct band gap of 0.36 eV at the C point, whereas the H layer has a large indirect band gap of 1.48 eV, with the conduction band minimum at the C point and the valence band maximum half way between the Y and  $\Gamma$  points. The T–H heterostructure (frankeite monolayer) is modelled in a commensurate approximation, for which the band structure displays a prominent energy gap just below the Fermi level (Figure 4-7c). This gap is indirect with the conduction band minimum at the  $\Gamma$  point and the valence band maximum at the C point, and its magnitude is 0.35 eV, which is almost identical with that of the T layer (0.36 eV). The separation between the mean planes of the T and H layers was found to be 0.9054 nm, which compares reasonably well with the value obtained experimentally from the HAADF-STEM (0.925 nm, Figure 4-2). In practice, we expect that the crystal reconstruction and the moiré pattern formation should occur locally to accommodate a local van der Waals interaction, which is indeed observed in the TEM (SI Figure 4-9). An important consequence of the strongly incommensurate lattice parameters of the T and H layers is that the interaction between the layers should be weak and that the physical properties of frankeite should not depend strongly on the number of layers, which is indeed observed by the Raman spectroscopy.

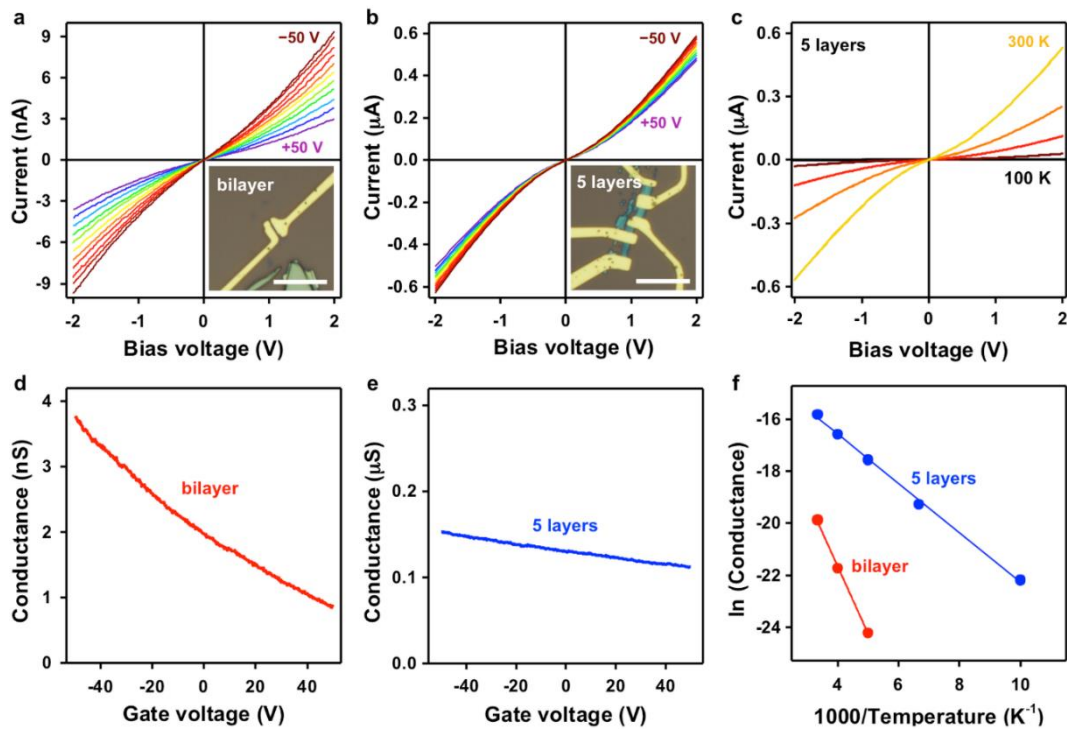


Figure 4-6 - **Transport characterisation of frankeite.** **a**, Gate voltage dependence of the current-voltage for bilayer frankeite device between  $-50$  and  $50$  V (brown to violet), in  $10$  V increments at  $300$  K. Bottom-right inset: an optical image of the device, the scale bar

corresponds to 10  $\mu\text{m}$ . **b**, Same as (**a**) for a 5-layer franckeite. **c**, Current-voltage curves for the 5-layer device between 300 and 100 K (yellow to black), in 50 K increments. **d**, Conductance dependence on gate voltage (300 K) for the bilayer device. **e**, Same as (**d**) for the 5-layer device. **f**, Temperature dependence of the zero-bias conductance for the bilayer (red) and 5-layer (blue) device, solid lines are Arrhenius fits.

The density of states (DOS) for the monolayer (T–H), one and a half monolayer (T–H–T), bilayer (T–H–T–H), and bulk franckeite, are presented in Figure 4-7d. The band gap is predicted to be around 250 – 350 meV and it decreases with increasing number of layers, which corresponds reasonably well with the observed gaps in our transport experiments, and also with the absence of photoluminescence in the visible spectrum. At the same time, our calculations predict the system to be n-doped, which is caused by the use of simplified stoichiometry. In reality, the presence of a small amount of Sn in the T layer and Fe in the H layer would have to be taken into account. These atoms will create donor and acceptor states in T and H layers of franckeite, respectively, strongly reducing the expected charge transfer between the layers once they are brought together. This drives the system towards a gapped semiconductor state due to the acceptor states countering the rise of the Fermi level in the H layer and the donor states countering the fall of the Fermi level in the T layer, which is energetically favourable. Further discussion of this complex behaviour is detailed in Supplementary Note 7.

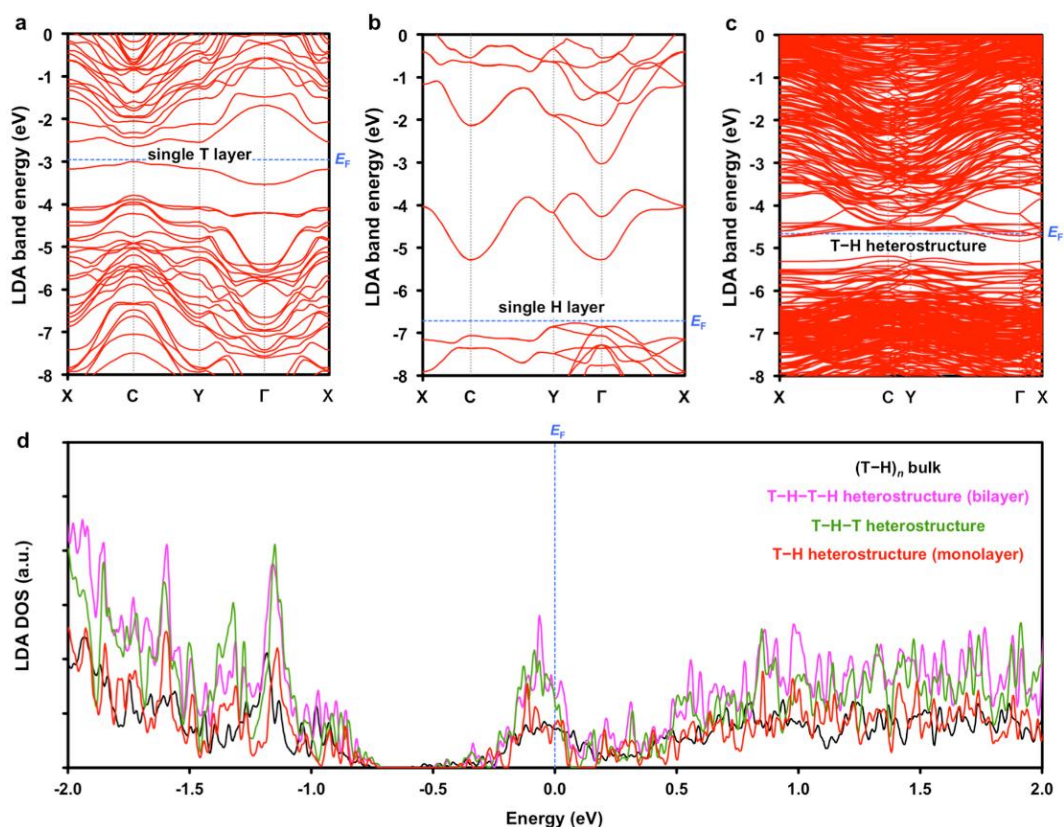


Figure 4-7 - **DFT calculations of franckeite's electronic band structure.** **a-c**, Electronic band structure of the T layer, H layer, and T-H heterostructure (franckeite monolayer), respectively, determined using the local density approximation (LDA) of DFT. The vertical grey dotted lines follow the high symmetry points in the Brillouin zone. **d**, LDA DOS for the T-H heterostructure (monolayer), T-H-T heterostructure, T-H-T-H heterostructure (bilayer), and bulk franckeite. The blue dashed lines in all panels correspond to the Fermi level.

## Discussion

In summary, we have succeeded in mechanical exfoliation of a mineral franckeite to a single unit cell thickness, which is facilitated through phase segregation into discrete layers at the nanometre scale. We show that this material exfoliates to thin, needle-like monolayer and few-layer crystals and we also demonstrate feasibility of its liquid-phase exfoliation in several solvents as a scalable production alternative. The key electrochemical properties of franckeite, capacitance and electron transfer rate, are considerably higher than those of more common 2D materials. In particular, the capacitance of franckeite exceeds that of graphene and MoS<sub>2</sub> by one order of magnitude, which is promising for emerging energy storage technologies based on supercapacitors. The electronic transport measurements show that franckeite is a p-doped semiconductor with a mid-/far-infrared band gap, and the EFM measurements confirm that crystals of all thicknesses, except for the monolayer, are conductive. Based on the Raman spectroscopy, electron microscopy, and DFT results we suggest

that the electronic and structural properties of franckeite do not depend on the number of layers. The important findings of the current work are the role of the polar nature of the double-layer structure, charge transfer between the individual layers, and role of the impurities, which balance the large charge transfer. Even though it is yet unclear whether this particular material will be used in applications, these findings are an important milestone in studying the principles of formation and stability of a new class of complex van der Waals crystals, which can be utilised for preparation of man-made heterostructures.

## Methods

### Sample preparation

Samples were prepared by the ‘scotch-tape’ mechanical exfoliation of natural franckeite crystals originating from Poopo, Oruro Department, Bolivia (Manchester Nanomaterials Ltd, UK) onto three different types of substrate: carbon adhesive discs for the SEM and XPS analyses, lacey carbon-coated copper grids for the STEM, TEM and EDXS analyses (both Agar Scientific, UK), and oxidised silicon wafers (IDB Technologies, UK) for the electrochemical measurements, Raman spectroscopy, transport measurements, EFM, and focused ion beam (FIB) milling. Exfoliated crystals were stable in air for at least 6 months, based on no observable changes in optical microscopy, Raman spectroscopy, and AFM, except for monolayer franckeite, which was not conductive in the transport measurements and EFM, indicating possible degradation. Two-terminal devices for the transport measurements were prepared using electron-beam lithography followed by evaporation of Cr/Au (4/50 nm) contacts (insets of Figure 4-6a–b). Some of the devices were encapsulated in thin layers of hexagonal boron nitride (hBN) to protect franckeite from oxidation and contamination (SI Figure 4-13 and SI Figure 4-21). To achieve this, hBN was mechanically exfoliated onto an Si-supported polymethylglutarimide (PMGI)/poly(methyl methacrylate) (PMMA) substrate and then transferred on top of the selected franckeite flakes. The PMGI/PMMA stack was later dissolved using acetone. 1D contacts to the hBN-encapsulated franckeite flake were made following previously described procedure,<sup>41</sup> in which the first electron-beam lithography was used to define a mask on top of the

hBN/franckeite heterostructure. The regions inside the mask were etched using an O<sub>2</sub>/Ar plasma and the franckeite flake was connected using Cr/Au contact evaporation.

### **SEM and XPS characterisation**

SEM images were collected using Philips XL30 ESEM-FEG scanning electron microscope (FEI Company, USA) operating at 15 kV accelerating voltage. XPS spectra were obtained using a K-Alpha monochromated XPS spectrometer (Thermo Fisher Scientific Inc) and analysed using CasaXPS software v.2.3 (Casa Software Ltd).

### **TEM/STEM/EDXS characterisation**

Electron diffraction patterns were collected using a Philips CM20 TEM operated at 200 kV accelerating voltage. STEM images and EDXS elemental maps were obtained using a Titan G2 STEM (FEI Company, USA) operated at 200 kV, equipped with a Super-X EDX detector and GIF quantum energy filter. HAADF-STEM images were acquired with a convergence angle of 21 mrad, an inner angle of 54 mrad and a probe current of ~75 pA, EDXS data was quantified using Esprit software version 1.9 (Bruker, USA). The crystals were aligned using Kikuchi bands in the SiO<sub>2</sub>/Si substrate. Cross-sectional sample preparation was performed using a dual FIB Nova NanoLab instrument (FEI Company, USA) fitted with an Omniprobe™ nano-manipulator (Oxford Instruments, UK). More details of the milling procedures can be found in Supplementary Note 2.

### **Optical microscopy and Raman spectroscopy**

A Nikon Eclipse LV100ND optical microscope and a DS-Fi2 U3 CCD camera (Nikon Metrology, UK Ltd.) were used to image franckeite flakes in both bright-field and dark-field illumination modes. Raman spectroscopy was measured with an inVia spectrometer, using either 532 or 633 nm laser excitation wavelength, and a 100× objective (Renishaw plc, UK), resulting in a laser spot size of ca. 0.8 μm<sup>2</sup>.

### **AFM and EFM measurements**

AFM measurements were performed with a Bruker Dimension 3100V instrument in a tapping mode with a tip resonance frequency of ~350 kHz. EFM measurements were carried out using a direct current (DC) bias voltage applied between doped silicon tip (Nanosensors PPP-FMR, 0.5 – 9.5 N/m) and the underlying doped silicon substrate.

### **Electrochemical measurements**

Franckeite crystals were electrically contacted to a copper wire using a silver conductive paint (RS Components Ltd, UK). Aqueous micro-droplets of either pure 6 M LiCl electrolyte, 3 mM redox mediator ( $\text{Ru}(\text{NH}_3)_6\text{Cl}_3$  or  $\text{K}_3\text{Fe}(\text{CN})_6$ ) in 6 M LiCl, or 1 M hydrochloric acid in 6 M LiCl, deposited onto the flake surface using a pressure-controlled glass micropipette, were used as microscopic electrochemical cells. Ultra-pure deionised water (18.2 M $\Omega$  cm, Milli-Q Direct 8, Merck Millipore, USA) was used for preparation of these solutions. Electrochemical measurements were controlled by a PGSTAT302N potentiostat (Metrohm Autolab B.V., The Netherlands) and were carried out in a three-electrode configuration, employing the crystal surface as a working electrode, and platinum wire and silver chloride wire as a counter and a reference electrode, respectively. All measurements were performed at room temperature (25 – 28°C) and the potential is referenced to the standard hydrogen electrode (SHE). All chemicals were of 98 % or higher purity and were purchased from Sigma-Aldrich, UK. Copper, silver and platinum wires (>99.9 %) were purchased from Advent Research Materials, UK. Further details can be found in Supplementary Note 5, and in our previous publications.<sup>20,33,34</sup>

### Electrochemical analysis

The heterogeneous electron transfer rate constant,  $k^0$ , of the redox mediator oxidation/reduction was calculated from the following equation.<sup>42</sup>

$$k^0 = 2.18 \left( \frac{\alpha n F D \nu}{RT} \right)^{0.5} e^{-\frac{\alpha^2 n F}{RT} \Delta E_p} \quad (1)$$

where  $\alpha$  (assumed to equal 0.5 due to the reaction symmetry) is the transfer coefficient,  $n$  is the number of electrons exchanged in the reaction ( $n = 1$  for both redox mediators),  $F$  is the Faraday constant,  $D$  is the diffusion coefficient of the redox mediator,  $\nu$  is the scan rate,  $R$  is the universal gas constant,  $T$  is the thermodynamic temperature, and  $\Delta E_p$  (larger than 220 mV) is the peak-to-peak separation of a redox mediator reduction/oxidation reaction. The Nicholson method, based on the following equation, was used for  $\Delta E_p$  smaller than 220 mV.<sup>43,44</sup>

$$Y = \frac{(-0.629 + 0.002 n \Delta E_p)}{(1 - 0.017 n \Delta E_p)} = k^0 \sqrt{\frac{RT}{\nu n F D}} n^{-0.5} \quad (2)$$



$\Delta E_p$  was measured for each micro-droplet for a range of scan rates (0.1 – 1.0 V s<sup>-1</sup>) and the mean  $k^0$  value determined using the equations (1) and (2).

The electric double-layer capacitance,  $C_{EDL}$ , in a 6 M LiCl aqueous supporting electrolyte was determined from cyclic voltammetry using the following equation.<sup>33,45</sup>

$$C_{EDL} = \frac{1}{2\nu(E_{max} - E_{min})} \oint_E I(E) dE \quad (3)$$

where  $E$  is the applied potential and  $E_{max}(E_{min})$  are the maximum(minimum) potentials, which limit the voltammetric scan. The mean  $C_{EDL}$  was determined from several measurements at different scan rates between 0.3 – 3.0 V s<sup>-1</sup>.

### Liquid-phase exfoliation

Millimetre-size, bulk crystals of franckeite were ground in a mortar and pestle. The resulting fine powder was loaded in 20 ml of NMP, DMF, acetone, IPA, and water, respectively, at a fixed concentration of 5 mg ml<sup>-1</sup>. The powder-solvent mixtures were sonicated in a PC620R-1 Branson ultrasonic bath for 1 hr at constant temperature (15 °C). The resulting suspensions were then centrifuged twice at 3000 rpm for 20 min using a Corning LSE Compact centrifuge in order to remove thicker non-exfoliated material. The recovered supernatant was then transferred on an SiO<sub>2</sub>/Si substrate by drop-casting and subsequent evaporation of the solvent for characterisation by AFM.

### Transport measurements

Standard two-terminal DC transport measurements were performed in a helium atmosphere using a variable temperature insert fitted into a He-4 cryostat. Sample temperature was controlled using an ITC503S temperature controller (Oxford Instruments). Current-bias voltage characteristics were measured at different gate voltages using a 2614b Keithley dual-channel source meter.

### Density functional theory calculations

The optimal crystal structures of T and H layers have been calculated within the LDA of DFT using the VASP code.<sup>46</sup> The structure was approximated so that no Sn and Fe atoms were assumed to be present in the T and H layer, respectively. In order to calculate the electronic band structure of the T–H heterostructure (franckeite

monolayer), a super-cell containing 128 atoms with a tolerance set to 0.05 nm was constructed. More details on the DFT calculations are found in Supplementary Note 7.

**Data availability** The data that support the findings of this study are available from the corresponding authors upon request.

### **Acknowledgments**

This work was supported by the EPSRC (grants EP/I005145/1, EP/K016954/1, EP/K016946/1, EP/M010619/1, EP/L01548X/1, EP/G03737X/1, EP/K000225/1, and EP/N007131/1), ERC, Graphene Flagship (contract No. NECTICT-604391), Royal Society, Defense Threat Reduction Agency (grant HDTRA1-12-1-0013), N8 HPC facilities, CSF cluster at the University of Manchester, US Army Research Office, US Navy Research Office, and US Airforce Research Office. The Titan was funded by H.M government UK. Authors also thank NEXUS at nanoLAB (Newcastle University) for the XPS measurement.

### **Author contributions**

M.V. conceived and designed the project, prepared and characterised the samples using the optical microscopy, Raman spectroscopy and electrochemistry, analysed the XPS data and wrote the manuscript, P.S.T. carried out the SEM and contributed to the Raman spectroscopy, S.J.H, A.P.R, and A.M.R carried out the FIB, TEM, STEM and EDXS measurements and analysis, A.K carried out the device fabrication and characterisation using optical microscopy and AFM, C.R.W contributed to the AFM measurements, A.M. and J.Y performed and analysed the transport measurements, L.F performed the EFM measurements, T.G carried out the liquid-phase exfoliation, and VZ performed the DFT calculations. S.J.H., K.S.N., R.A.W.D. and all other authors contributed to the discussion and interpretation of the results.

### **Additional Information**

Supplementary information is available in the online version of the paper. Reprints and permissions information is available online at [www.nature.com/reprints](http://www.nature.com/reprints).

Correspondence and requests for materials should be addressed to M.V or R.A.W.D.

### **Competing financial interests**

The authors declare no competing financial interests.

## References

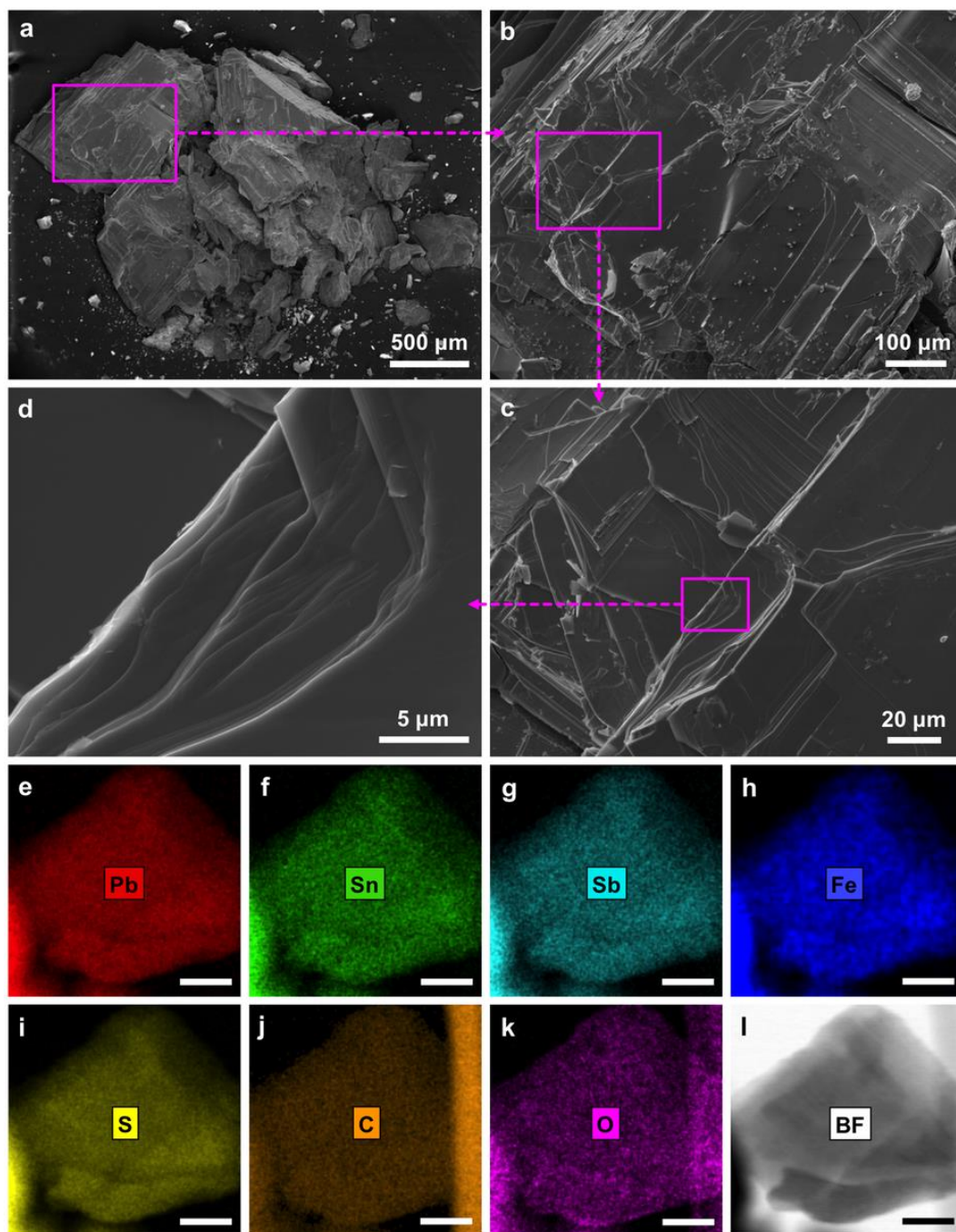
- 1 Novoselov, K. S., Jiang, D., Schedin, F., Booth, T. J., Khotkevich, V. V., Morozov, S. V. & Geim, A. K. Two-dimensional atomic crystals. *Proc. Natl. Acad. Sci. U. S. A.* **102**, 10451-10453 (2005).
- 2 Butler, S. Z., Hollen, S. M., Cao, L., Cui, Y., Gupta, J. A., Gutiérrez, H. R., Heinz, T. F., Hong, S. S., Huang, J., Ismach, A. F., Johnston-Halperin, E., Kuno, M., Plashnitsa, V. V., Robinson, R. D., Ruoff, R. S., Salahuddin, S., Shan, J., Shi, L., Spencer, M. G., Terrones, M., Windl, W. & Goldberger, J. E. Progress, Challenges, and Opportunities in Two-Dimensional Materials Beyond Graphene. *ACS Nano* **7**, 2898-2926 (2013).
- 3 He, J., Girard, S. N., Zheng, J. C., Zhao, L., Kanatzidis, M. G. & Dravid, V. P. Strong phonon scattering by layer structured PbSnS<sub>2</sub> in PbTe based thermoelectric materials. *Advanced Materials* **24**, 4440-4444 (2012).
- 4 Stelzner, A. W. Über Franckeit, ein neues Erz aus Bolivia. *Neues Jahrbuch für Mineralogie* **2**, 114-124 (1893).
- 5 Xu, Y. & Schoonen, M. A. A. The absolute energy positions of conduction and valence bands of selected semiconducting minerals. *American Mineralogist* **85**, 543-556 (2000).
- 6 Boldish, S. I. & White, W. B. Optical band gaps of selected ternary sulfide minerals. *American Mineralogist* **83**, 865-871 (1998).
- 7 Unuchak, D. M., Bente, K., Kloess, G., Schmitz, W., Gremenok, V. F., Ivanov, V. A. & Ukhov, V. Structure and optical properties of PbS-SnS mixed crystal thin films. *Physica Status Solidi C: Current Topics in Solid State Physics* **6**, 1191-1194 (2009).
- 8 Soriano, R. B., Malliakas, C. D., Wu, J. & Kanatzidis, M. G. Cubic Form of Pb<sub>2-x</sub>Sn<sub>x</sub>S<sub>2</sub> Stabilized through Size Reduction to the Nanoscale. *Journal of the American Chemical Society* **134**, 3228-3233 (2012).
- 9 Nair, P. K., Nair, M. T. S., Fernandez, A. & Ocampo, M. Prospects of chemically deposited metal chalcogenide thin films for solar control applications. *Journal of Physics D: Applied Physics* **22**, 829-836 (1989).
- 10 Moh, G. H. Mutual Pb<sup>2+</sup>/Sn<sup>2+</sup> substitution in sulfosalts. *Mineralogy and Petrology* **36**, 191-204 (1987).
- 11 Coulon, M., Heitz, F. & Le Bihan, M. T. Contribution à l'étude structurale d'un sulfure de plomb, d'antimoine et d'étain: la franckéite. *Bulletin de la Société française de Minéralogie et Cristallographie* **84**, 350-353 (1961).
- 12 Williams, T. B. & Hyde, B. G. Electron microscopy of cylindrite and franckeite. *Physics and Chemistry of Minerals* **15**, 521-544 (1988).
- 13 Wang, S. & Kuo, K. H. Crystal lattices and crystal chemistry of cylindrite and franckeite. *Acta Crystallogr., Sect. A: Found. Crystallogr.* **47**, 381-392 (1991).
- 14 Wang, S. & Buseck, P. R. High-angle annular dark-field microscopy of franckeite. *American Mineralogist* **80**, 1174-1178 (1995).
- 15 Henriksen, R. B., Makovicky, E., Stipp, S. L. S., Nissen, C. & Eggleston, C. M. Atomic-scale observations of franckeite surface morphology. *American Mineralogist* **87**, 1273-1278 (2002).
- 16 Makovicky, E., Petricek, V., Dusek, M. & Topa, D. The crystal structure of franckeite, Pb<sub>21.7</sub>Sn<sub>9.3</sub>Fe<sub>4.0</sub>Sb<sub>8.1</sub>S<sub>56.9</sub>. *American Mineralogist* **96**, 1686-1702 (2011).

- 17 Brent, J. R., Lewis, D. J., Lorenz, T., Lewis, E. A., Savjani, N., Haigh, S. J., Seifert, G., Derby, B. & O'Brien, P. Tin(II) Sulfide (SnS) Nanosheets by Liquid-Phase Exfoliation of Herzenbergite: IV–VI Main Group Two-Dimensional Atomic Crystals. *Journal of the American Chemical Society* **137**, 12689-12696 (2015).
- 18 Burton, L. A., Whittles, T. J., Hesp, D., Linhart, W. M., Skelton, J. M., Hou, B., Webster, R. F., O'Dowd, G., Reece, C., Cherns, D., Fermin, D. J., Veal, T. D., Dhanak, V. R. & Walsh, A. Electronic and optical properties of single crystal SnS<sub>2</sub>: an earth-abundant disulfide photocatalyst. *Journal of Materials Chemistry A* **4**, 1312-1318 (2016).
- 19 Feng, W., Zhenxing, W., Qisheng, W., Fengmei, W., Lei, Y., Kai, X., Yun, H. & Jun, H. Synthesis, properties and applications of 2D non-graphene materials. *Nanotechnology* **26**, 292001 (2015).
- 20 Velický, M., Bissett, M. A., Toth, P. S., Patten, H. V., Worrall, S. D., Rodgers, A. N. J., Hill, E. W., Kinloch, I. A., Novoselov, K. S., Georgiou, T., Britnell, L. & Dryfe, R. A. W. Electron transfer kinetics on natural crystals of MoS<sub>2</sub> and graphite. *Physical Chemistry Chemical Physics* **17**, 17844-17853 (2015).
- 21 Li, Z., Kozbial, A., Nioradze, N., Parobek, D., Shenoy, G. J., Salim, M., Amemiya, S., Li, L. & Liu, H. Water Protects Graphitic Surface from Airborne Hydrocarbon Contamination. *ACS Nano* **10**, 349-359 (2016).
- 22 Barr, T. L. & Seal, S. Nature of the use of adventitious carbon as a binding energy standard. *Journal of Vacuum Science & Technology, A: Vacuum, Surfaces, and Films* **13**, 1239-1246 (1995).
- 23 Makreski, P., Petruševski, G., Ugarković, S. & Jovanovski, G. Laser-induced transformation of stibnite (Sb<sub>2</sub>S<sub>3</sub>) and other structurally related salts. *Vibrational Spectroscopy* **68**, 177-182 (2013).
- 24 Mead, D. G. & Irwin, J. C. Raman spectra of SnS<sub>2</sub> and SnSe<sub>2</sub>. *Solid State Communications* **20**, 885-887 (1976).
- 25 Smith, G. D., Firth, S., Clark, R. J. H. & Cardona, M. First- and second-order Raman spectra of galena (PbS). *Journal of Applied Physics* **92**, 4375-4380 (2002).
- 26 Chandrasekhar, H. R., Humphreys, R. G., Zwick, U. & Cardona, M. Infrared and Raman spectra of the IV-VI compounds SnS and SnSe. *Physical Review B* **15**, 2177-2183 (1977).
- 27 Wang, Y. Y., Ni, Z. H., Shen, Z. X., Wang, H. M. & Wu, Y. H. Interference enhancement of Raman signal of graphene. *Appl Phys Lett* **92**, 043121 (2008).
- 28 Li, H., Zhang, Q., Yap, C. C. R., Tay, B. K., Edwin, T. H. T., Olivier, A. & Baillargeat, D. From bulk to monolayer MoS<sub>2</sub>: Evolution of Raman scattering. *Advanced Functional Materials* **22**, 1385-1390 (2012).
- 29 Tonndorf, P., Schmidt, R., Böttger, P., Zhang, X., Börner, J., Liebig, A., Albrecht, M., Kloc, C., Gordan, O., Zahn, D. R. T., De Vasconcellos, S. M. & Bratschitsch, R. Photoluminescence emission and Raman response of monolayer MoS<sub>2</sub>, MoSe<sub>2</sub>, and WSe<sub>2</sub>. *Optics Express* **21**, 4908-4916 (2013).
- 30 Lee, C., Yan, H., Brus, L. E., Heinz, T. F., Hone, J. & Ryu, S. Anomalous lattice vibrations of single- and few-layer MoS<sub>2</sub>. *ACS Nano* **4**, 2695-2700 (2010).
- 31 Withers, F., Del Pozo-Zamudio, O., Mishchenko, A., Rooney, A. P., Gholinia, A., Watanabe, K., Taniguchi, T., Haigh, S. J., Geim, A. K., Tartakovskii, A. I. & Novoselov, K. S. Light-emitting diodes by band-structure engineering in van der Waals heterostructures. *Nat. Mater.* **14**, 301-306 (2015).
- 32 Cao, Y., Mishchenko, A., Yu, G. L., Khestanova, E., Rooney, A. P., Prestat, E., Kretinin, A. V., Blake, P., Shalom, M. B., Woods, C., Chapman, J., Balakrishnan,

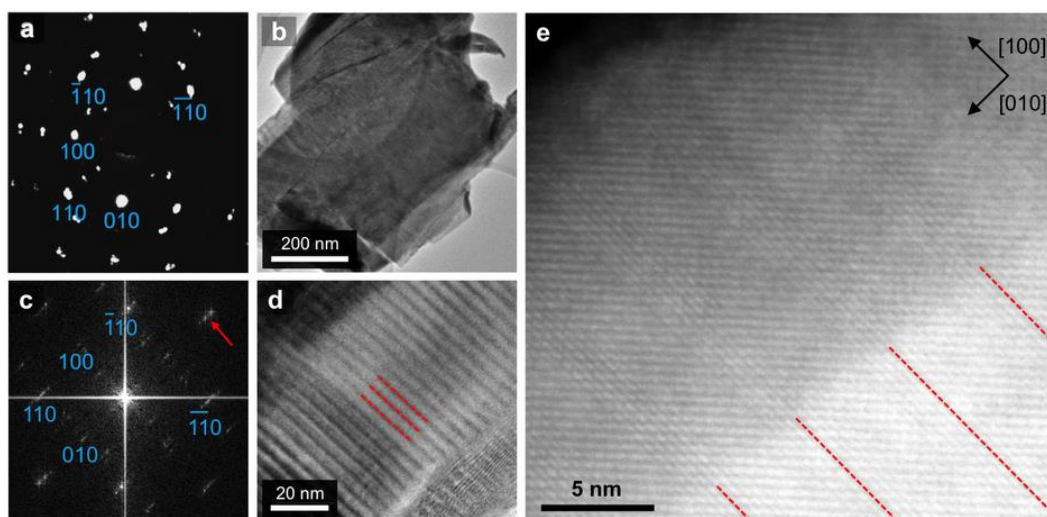
- G., Grigorieva, I. V., Novoselov, K. S., Piot, B. A., Potemski, M., Watanabe, K., Taniguchi, T., Haigh, S. J., Geim, A. K. & Gorbachev, R. V. Quality Heterostructures from Two-Dimensional Crystals Unstable in Air by Their Assembly in Inert Atmosphere. *Nano letters* **15**, 4914-4921 (2015).
- 33 Velický, M., Bradley, D. F., Cooper, A. J., Hill, E. W., Kinloch, I. A., Mishchenko, A., Novoselov, K. S., Patten, H. V., Toth, P. S., Valota, A. T., Worrall, S. D. & Dryfe, R. A. W. Electron Transfer Kinetics on Mono- and Multilayer Graphene. *ACS Nano* **8**, 10089-10100 (2014).
- 34 Velický, M., Bissett, M. A., Woods, C. R., Toth, P. S., Georgiou, T., Kinloch, I. A., Novoselov, K. S. & Dryfe, R. A. W. Photoelectrochemistry of Pristine Mono- and Few-Layer MoS<sub>2</sub>. *Nano letters* **16**, 2023-2032 (2016).
- 35 Winchester, A., Ghosh, S., Feng, S., Elias, A. L., Mallouk, T., Terrones, M. & Talapatra, S. Electrochemical characterization of liquid phase exfoliated two-dimensional layers of molybdenum disulfide. *ACS Applied Materials and Interfaces* **6**, 2125-2130 (2014).
- 36 Acerce, M., Voiry, D. & Chhowalla, M. Metallic 1T phase MoS<sub>2</sub> nanosheets as supercapacitor electrode materials. *Nature nanotechnology* **10**, 313-318 (2015).
- 37 Bissett, M. A., Worrall, S. D., Kinloch, I. A. & Dryfe, R. A. W. Comparison of Two-Dimensional Transition Metal Dichalcogenides for Electrochemical Supercapacitors. *Electrochimica Acta* **201**, 30-37 (2016).
- 38 Ahmed, S. M. & Gerischer, H. Influence of crystal surface orientation on redox reactions at semiconducting MoS<sub>2</sub>. *Electrochimica Acta* **24**, 705-711 (1979).
- 39 Coleman, J. N., Lotya, M., O'Neill, A., Bergin, S. D., King, P. J., Khan, U., Young, K., Gaucher, A., De, S., Smith, R. J., Shvets, I. V., Arora, S. K., Stanton, G., Kim, H. Y., Lee, K., Kim, G. T., Duesberg, G. S., Hallam, T., Boland, J. J., Wang, J. J., Donegan, J. F., Grunlan, J. C., Moriarty, G., Shmeliov, A., Nicholls, R. J., Perkins, J. M., Grievson, E. M., Theuwissen, K., McComb, D. W., Nellist, P. D. & Nicolosi, V. Two-dimensional nanosheets produced by liquid exfoliation of layered materials. *Science* **331**, 568-571 (2011).
- 40 Hernandez, Y., Nicolosi, V., Lotya, M., Blighe, F. M., Sun, Z., De, S., McGovern, I. T., Holland, B., Byrne, M., Gun'ko, Y. K., Boland, J. J., Niraj, P., Duesberg, G., Krishnamurthy, S., Goodhue, R., Hutchison, J., Scardaci, V., Ferrari, A. C. & Coleman, J. N. High-yield production of graphene by liquid-phase exfoliation of graphite. *Nat. Nanotechnol.* **3**, 563-568 (2008).
- 41 Wang, L., Meric, I., Huang, P. Y., Gao, Q., Gao, Y., Tran, H., Taniguchi, T., Watanabe, K., Campos, L. M., Muller, D. A., Guo, J., Kim, P., Hone, J., Shepard, K. L. & Dean, C. R. One-dimensional electrical contact to a two-dimensional material. *Science* **342**, 614-617 (2013).
- 42 Klingler, R. J. & Kochi, J. K. Electron-transfer kinetics from cyclic voltammetry. Quantitative description of electrochemical reversibility. *Journal of Physical Chemistry* **85**, 1731-1741 (1981).
- 43 Nicholson, R. S. Theory and application of cyclic voltammetry for measurement of electrode reaction kinetics. *Analytical Chemistry* **37**, 1351-1355 (1965).
- 44 Lavagnini, I., Antiochia, R. & Magno, F. An extended method for the practical evaluation of the standard rate constant from cyclic voltammetric data. *Electroanalysis* **16**, 505-506 (2004).
- 45 Xiong, G., Meng, C., Reifengerger, R. G., Irazoqui, P. P. & Fisher, T. S. A review of graphene-based electrochemical microsupercapacitors. *Electroanalysis* **26**, 30-51 (2014).

- 46 Kresse, G. & Furthmüller, J. Efficient iterative schemes for *ab initio* total-energy calculations using a plane-wave basis set. *Physical Review B: Condensed Matter and Materials Physics* **54**, 11169-11186 (1996).

#### 4.1. Supplementary information

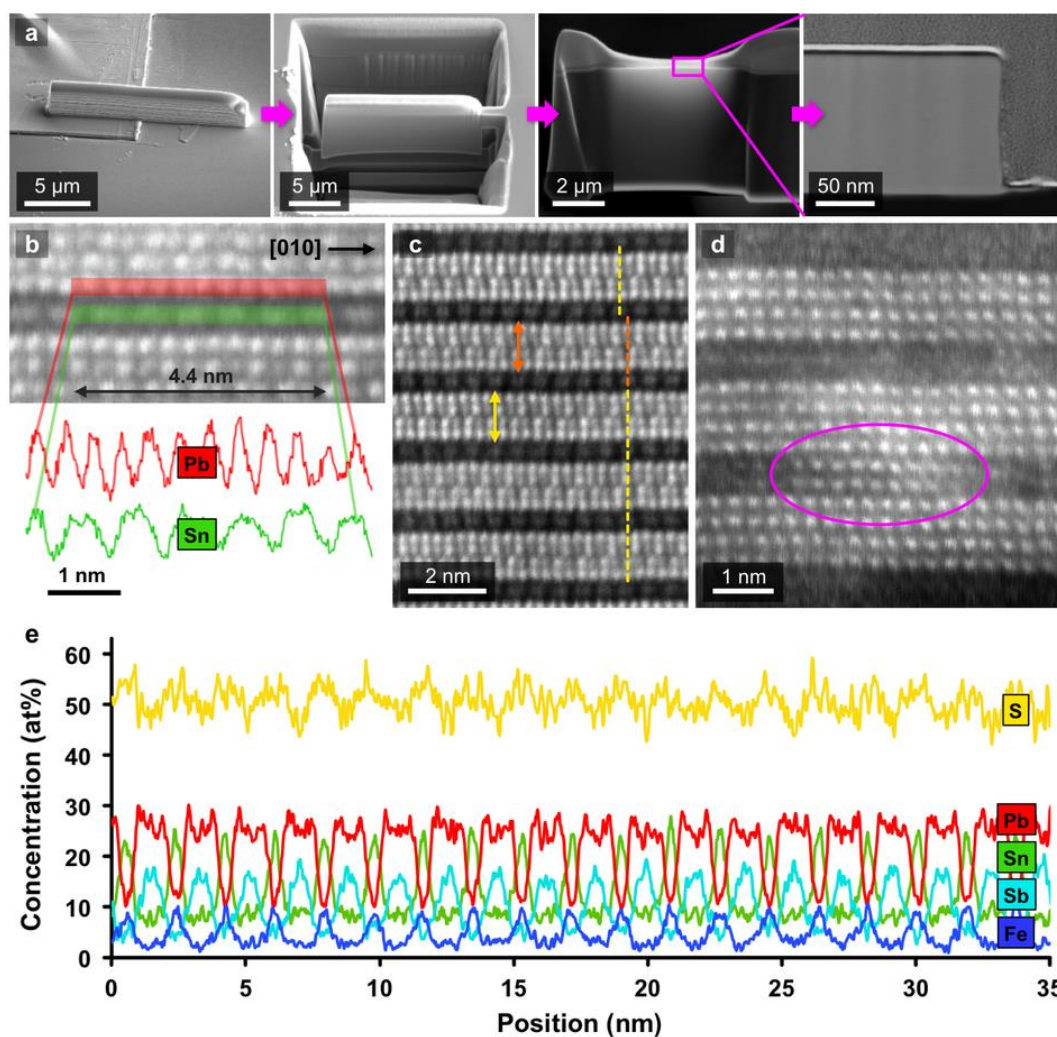


SI Figure 4-8 - SEM images and TEM-EDXS mapping of franckeite. **a–d**, SEM images of a franckeite crystal immobilised on a conductive carbon support. Zoom areas are highlighted in (**a–c**) by the magenta rectangles. **e–k**, EDXS maps of lead, tin, antimony, iron, sulphur, carbon, and oxygen, respectively, within another crystal. **l**, BF-TEM image of the same crystal. The scale bars in (**e–l**) denote 30 nm. Electron beam accelerating voltages of 15 kV and 200 kV were used for the SEM and TEM-EDXS, respectively.

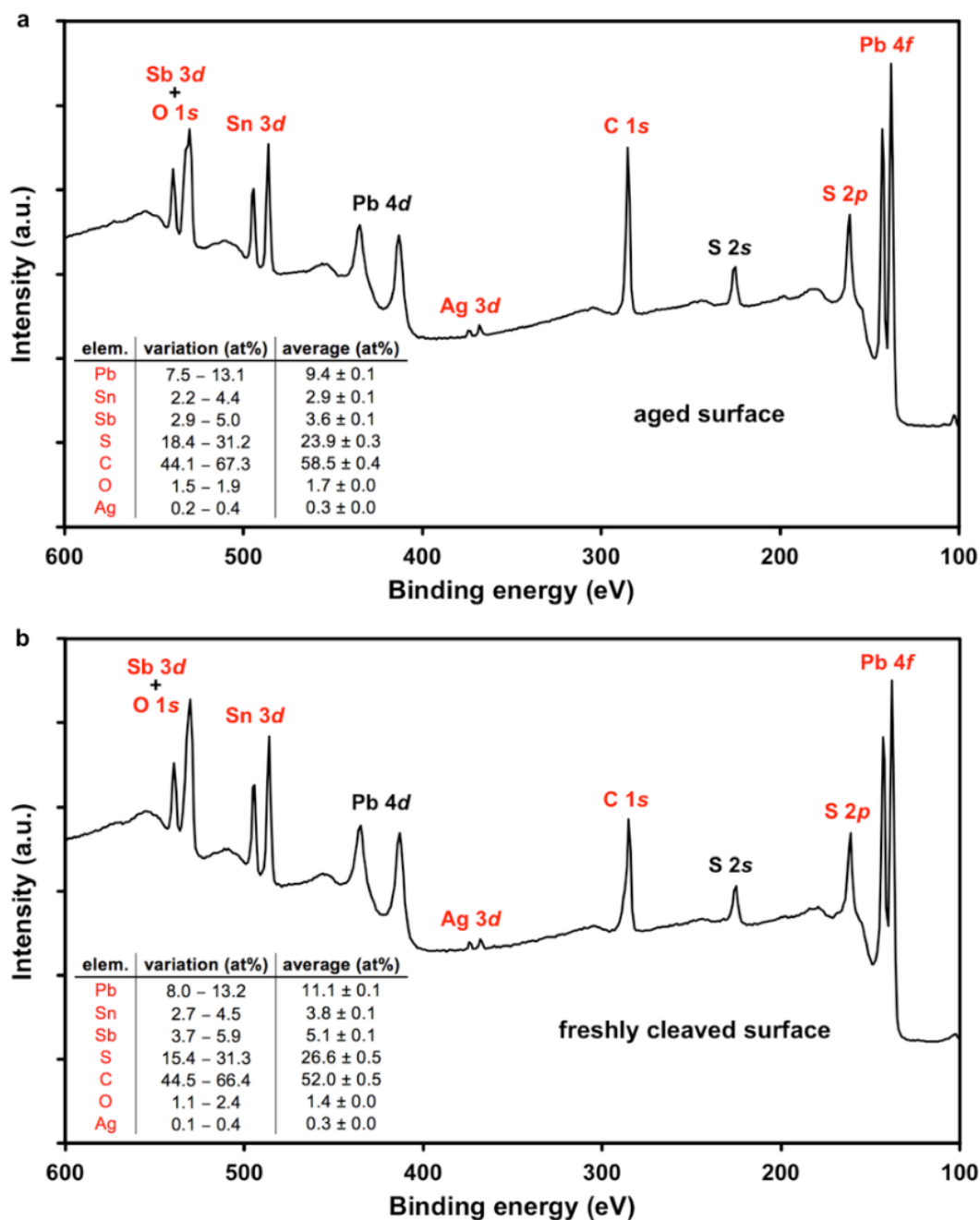


SI Figure 4-9 - TEM imaging of franckeite viewed along the  $[001]$  direction (perpendicular to the basal plane). **a**, Indexed electron diffraction pattern. **b,d,e**, TEM images of franckeite viewed along the  $[001]$  direction. **c**, corresponding Fourier transform of the high resolution image in **(e)**. These TEM images clearly show the  $\sim 4.4$  nm moiré fringes, highlighted by the red dashed lines in **(d)** and **(e)**. These fringes are also present in the Fourier transform image **(c)**, causing additional spots indicated by the red arrow to appear.

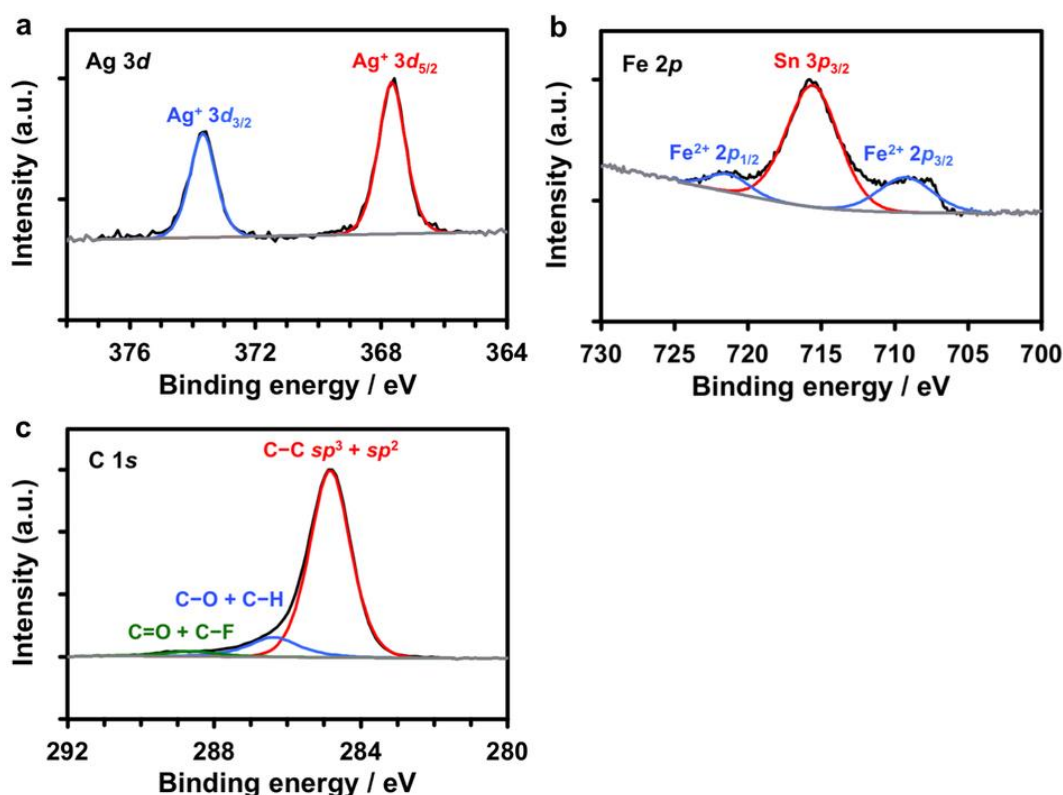




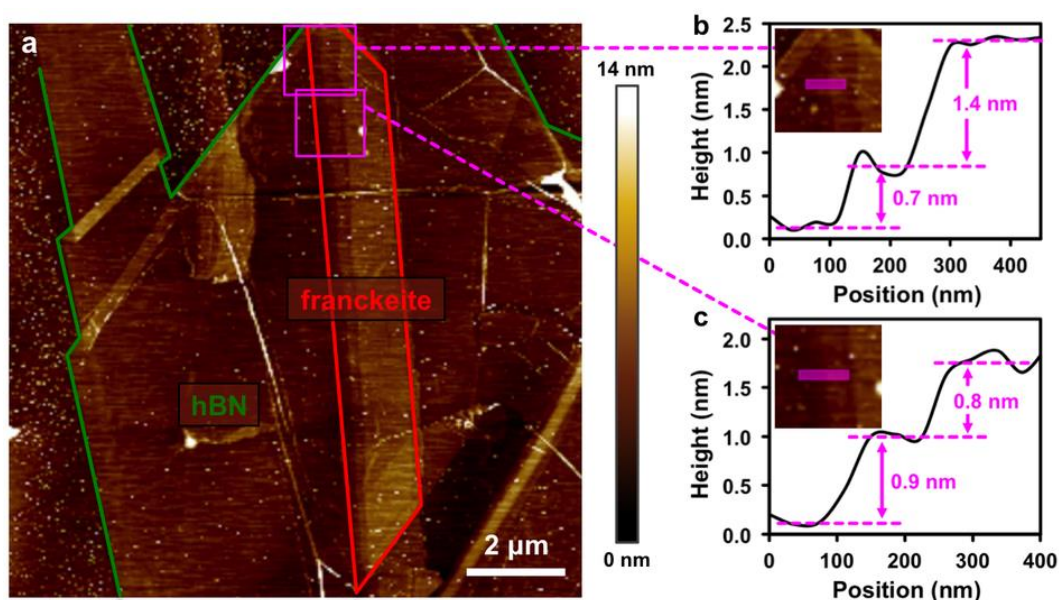
SI Figure 4-10 - Cross-sectional HAADF-STEM imaging of franckeite along the  $[100]$  direction (parallel to the basal plane). **a**, SEM and STEM images illustrating the process of FIB cross-sectional sample preparation from a crystal mechanically exfoliated on an  $\text{SiO}_2/\text{Si}$  substrate. **b**, Intensity line profiles reveal the incommensurate stacking between the H layer (green) and the adjacent T layer (red). **c**, Variations in stacking between the consecutive H layers. The yellow arrow separates the H layers in which the Sn atoms are positioned on top of one another, whereas the orange arrow indicates the H layers that have a relative displacement along the  $[010]$  direction. **d**, Electron beam induced restructuring of the H layer, where a continuous PbS link between Pb-rich layers is formed. **e**, EDXS concentration profiles of a large portion of the cross-section.



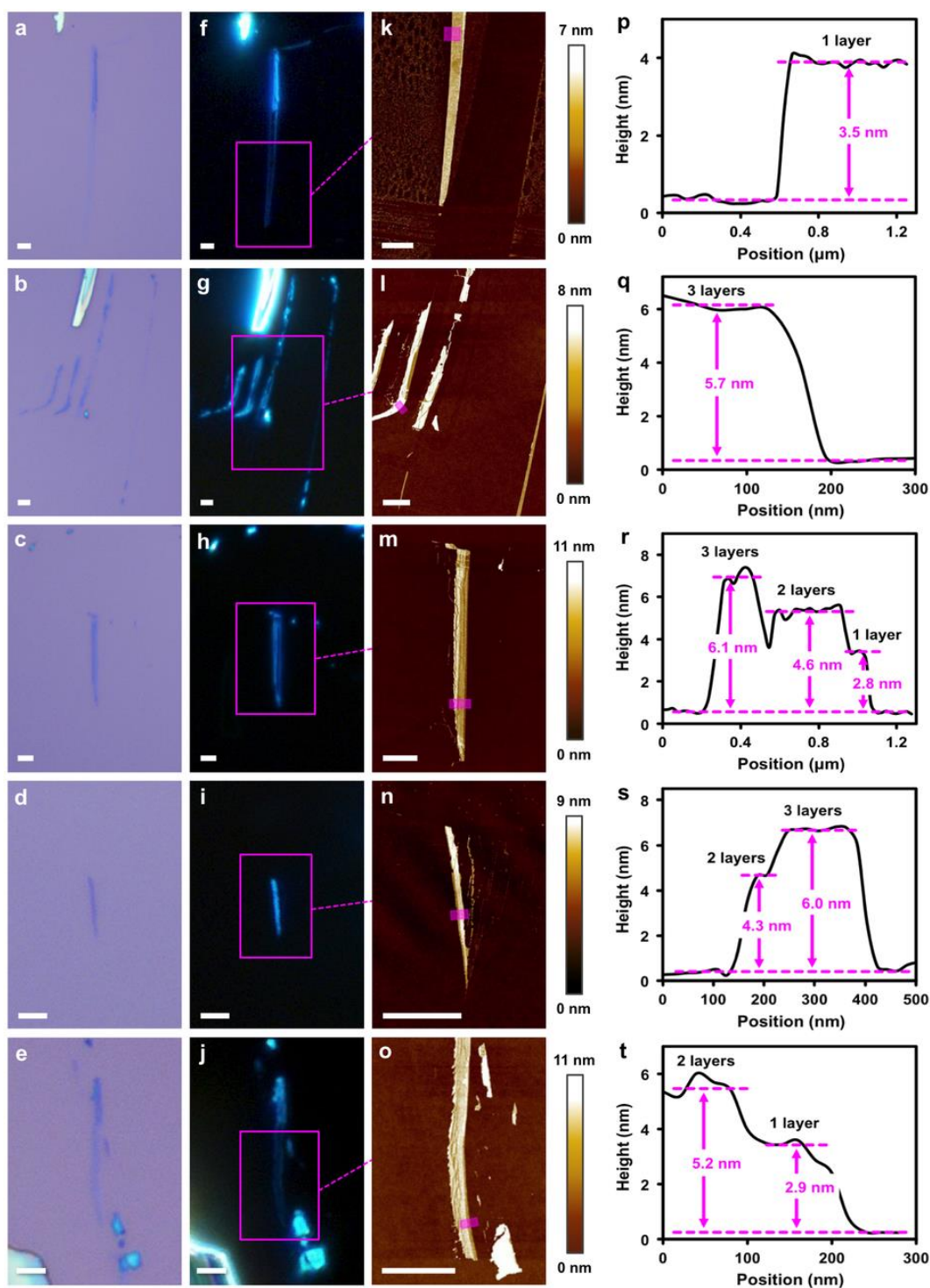
SI Figure 4-11 - XPS of the aged and freshly cleaved franckeite surface. **a**, XPS spectrum of the aged franckeite surface. **b**, XPS spectrum of the freshly cleaved franckeite surface. Each spectrum is an average of 5 individual measurements from different parts of the crystal. The peaks used for the quantification in the inset tables are labelled in red, other major peaks are labelled in black. The spectra are normalised to the intensity of the Pb 4f<sub>7/2</sub> peak (137.6 eV) with the adventitious carbon C 1s peak positioned at 284.7 eV.<sup>1</sup>



SI Figure 4-12 - High-resolution XPS spectra of the impurity elements. **a-c**, High-resolution XPS of the Ag 3d, Fe 2p, and C 1s spectral regions, respectively. The measured spectra are shown in black, deconvoluted components in colour, and background in grey. The intensities are normalised to the most intense peak within the respective spectral region.

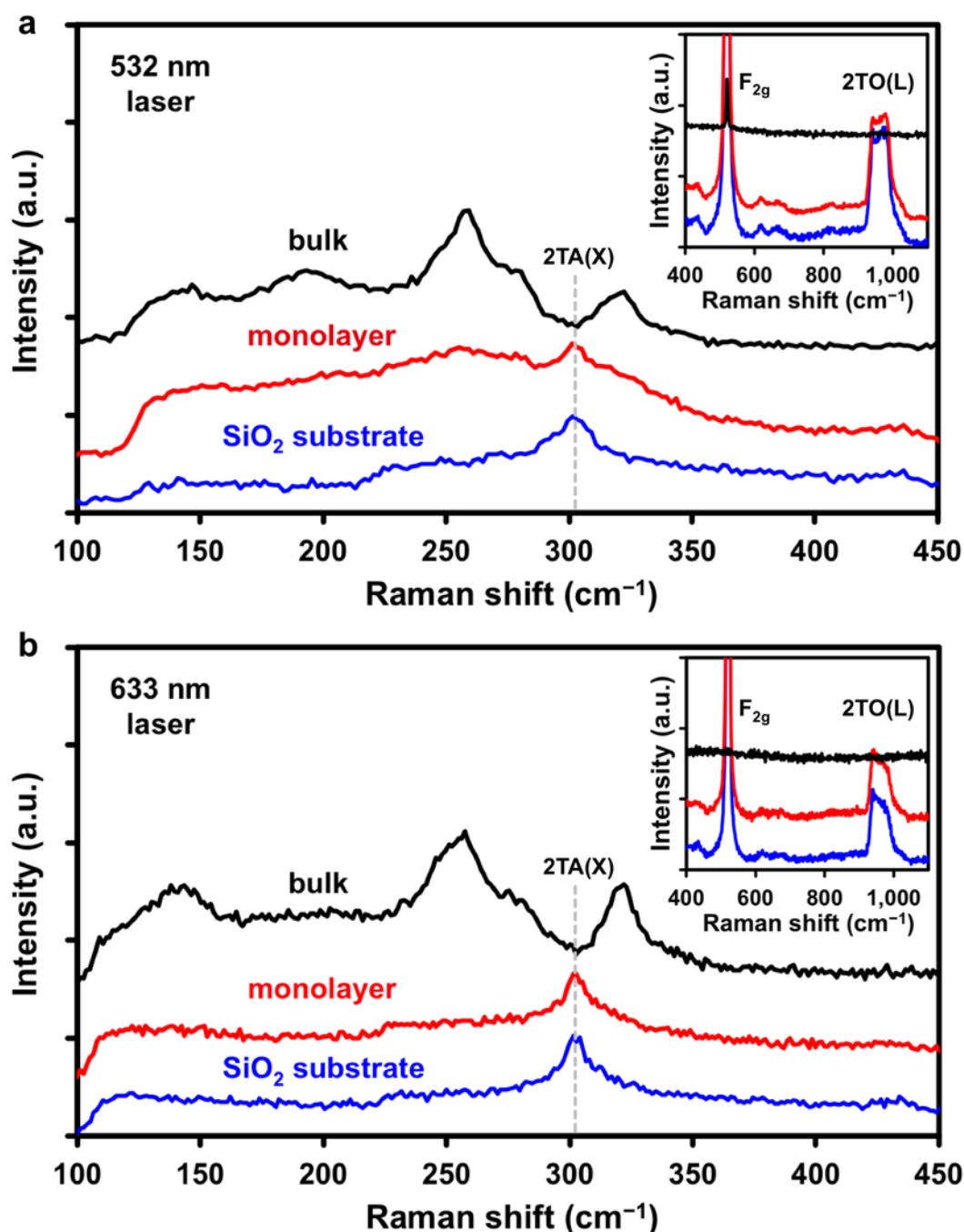


SI Figure 4-13 - AFM characterisation of franckeite with a sub-monolayer thickness. **a**, AFM image of a franckeite crystal (red) encapsulated in hBN crystal (green). **b-c**, Height profiles of the sub-monolayer terraces taken from areas indicated by the magenta rectangles.

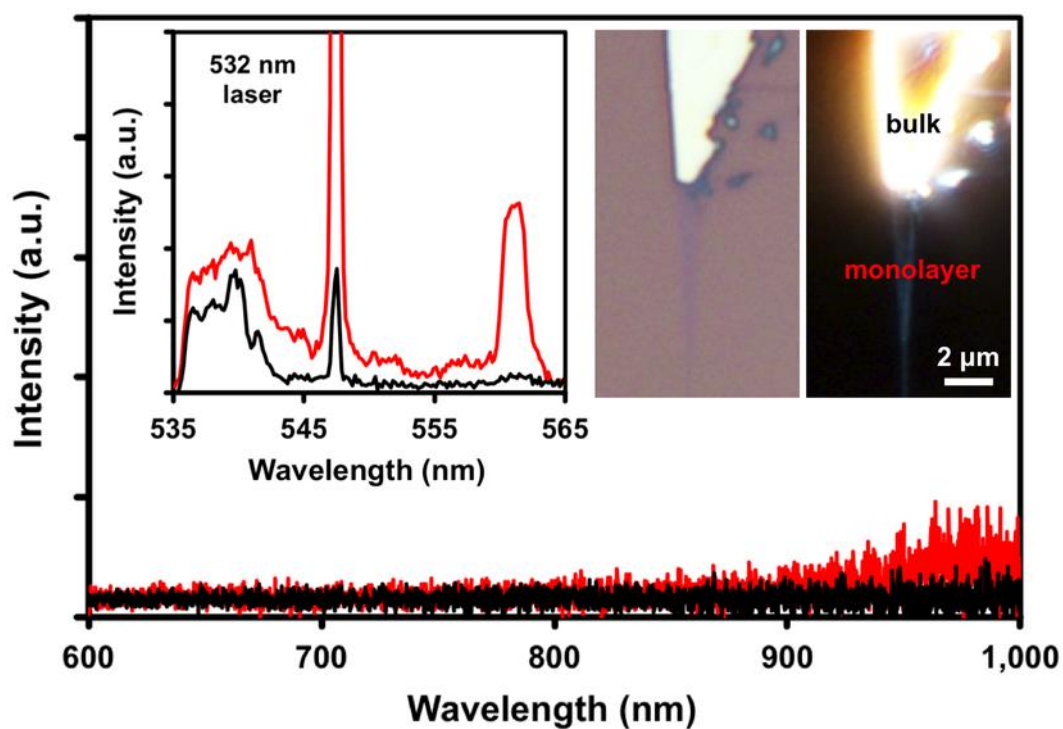


SI Figure 4-14 - Optical and AFM characterisation of thin franckeite crystals. **a–e**, BF optical images of thin franckeite crystals exfoliated onto an  $\text{SiO}_2/\text{Si}$  substrate. **f–j**, corresponding dark-field (DF) optical images. **k–o**, AFM images of a selected area indicated by magenta rectangles in (**f–j**). **p–t**, Step-height profiles taken from areas indicated by the transparent magenta rectangles in the (**k–o**). All scale bars corresponds to 2  $\mu\text{m}$ .

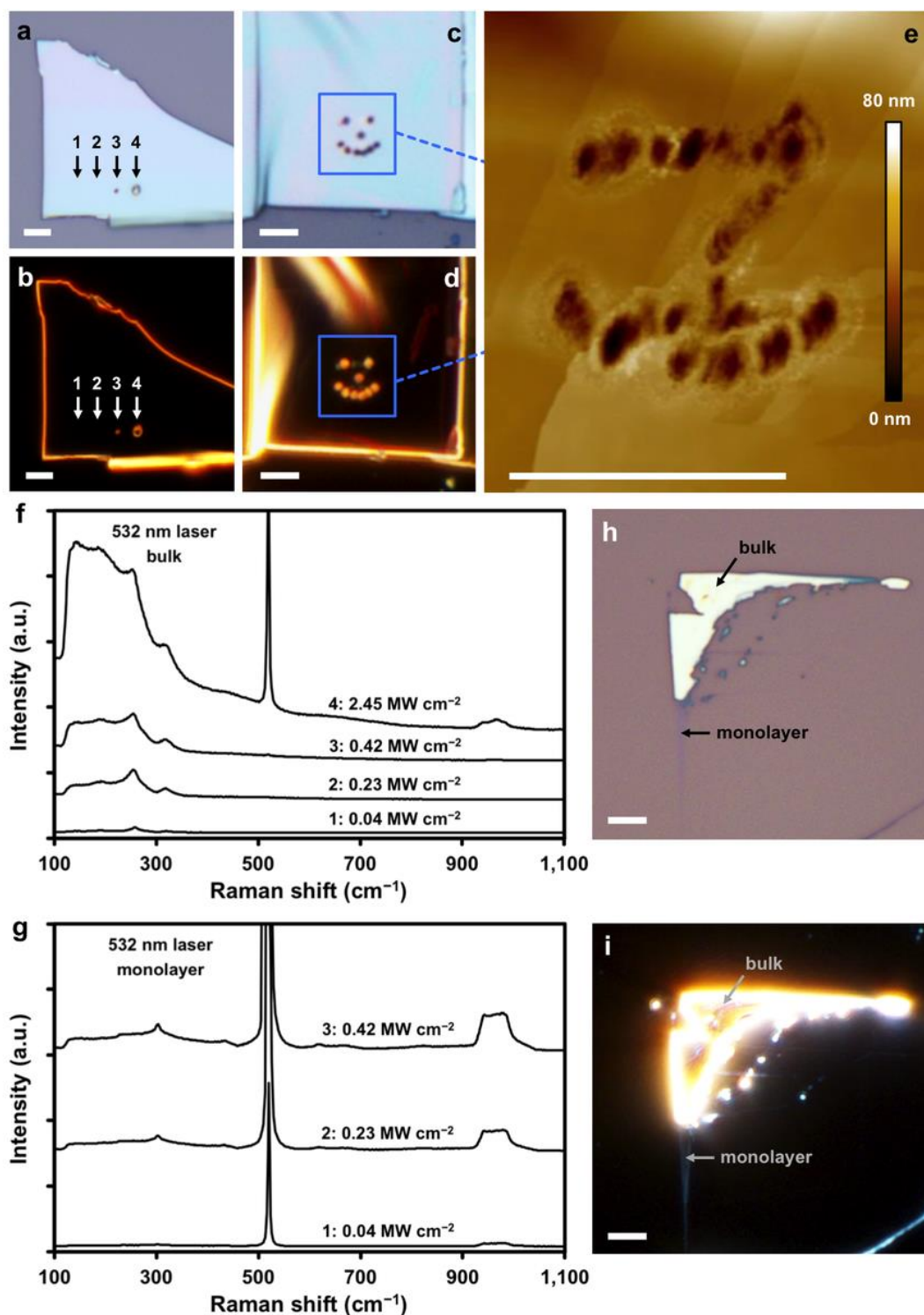




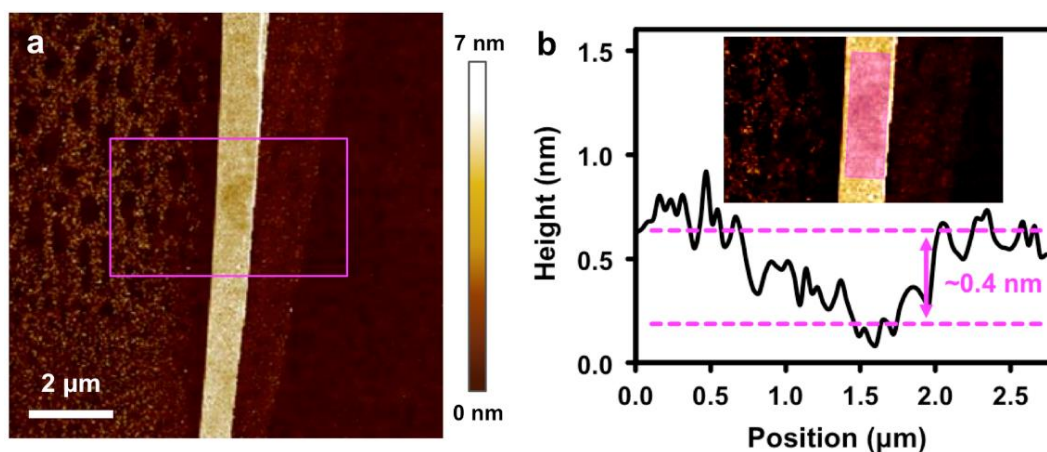
SI Figure 4-15 -Raman spectra of monolayer franckeite, bulk franckeite, and SiO<sub>2</sub>/Si substrate. a–b, Raman spectra of monolayer franckeite, bulk franckeite, and the SiO<sub>2</sub>/Si substrate, using a 532 nm laser at 19 kW cm<sup>-2</sup> power density (a) and 633 nm laser at 14 kW cm<sup>-2</sup> power density (b). The insets show the spectral region encompassing the first- and second-order Raman Si bands. The spectra are vertically offset for clarity. More than 130 individual measurements were collected at different locations to accumulate these spectra.



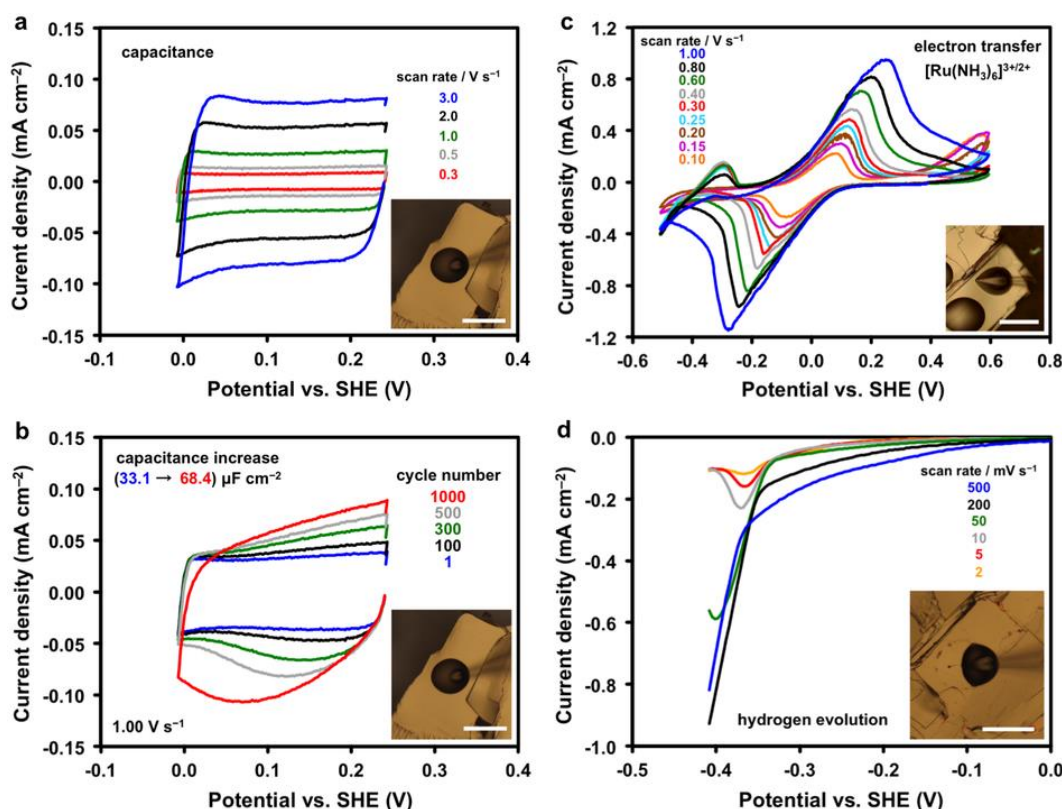
SI Figure 4-16 - PL measurement of monolayer and bulk frankeite. Representative PL spectra of a monolayer (red) and bulk (black) frankeite crystal using 532 nm laser excitation wavelength. No PL was observed within the range of 532 – 900 nm. The inset on the left shows the Raman spectra on the same intensity scale. The insets on the right are BF and DF optical images of the measured crystals. The spectra were recorded at 35 kW cm<sup>-2</sup> laser power density for 30 s.



SI Figure 4-17 - Laser-induced degradation of franckeite. **a–b**, BF and DF optical images of bulk franckeite subjected to increasingly higher laser irradiance for 30 s (1, 2, 3, and 4 correspond to 0.04, 0.23, 0.42, and 2.45 MW cm<sup>-2</sup>, respectively). **c–d**, BF and DF optical images of a laser-induced pattern using 0.42 MW cm<sup>-2</sup> for 30 s per laser spot. **e**, AFM image of the same pattern. **f–g**, Raman spectra of bulk and monolayer at varied laser power density. **h–i**, BF and DF optical images of the corresponding bulk and monolayer crystals. 532 nm laser excitation wavelength was used throughout. All scale bars denote 3 μm.

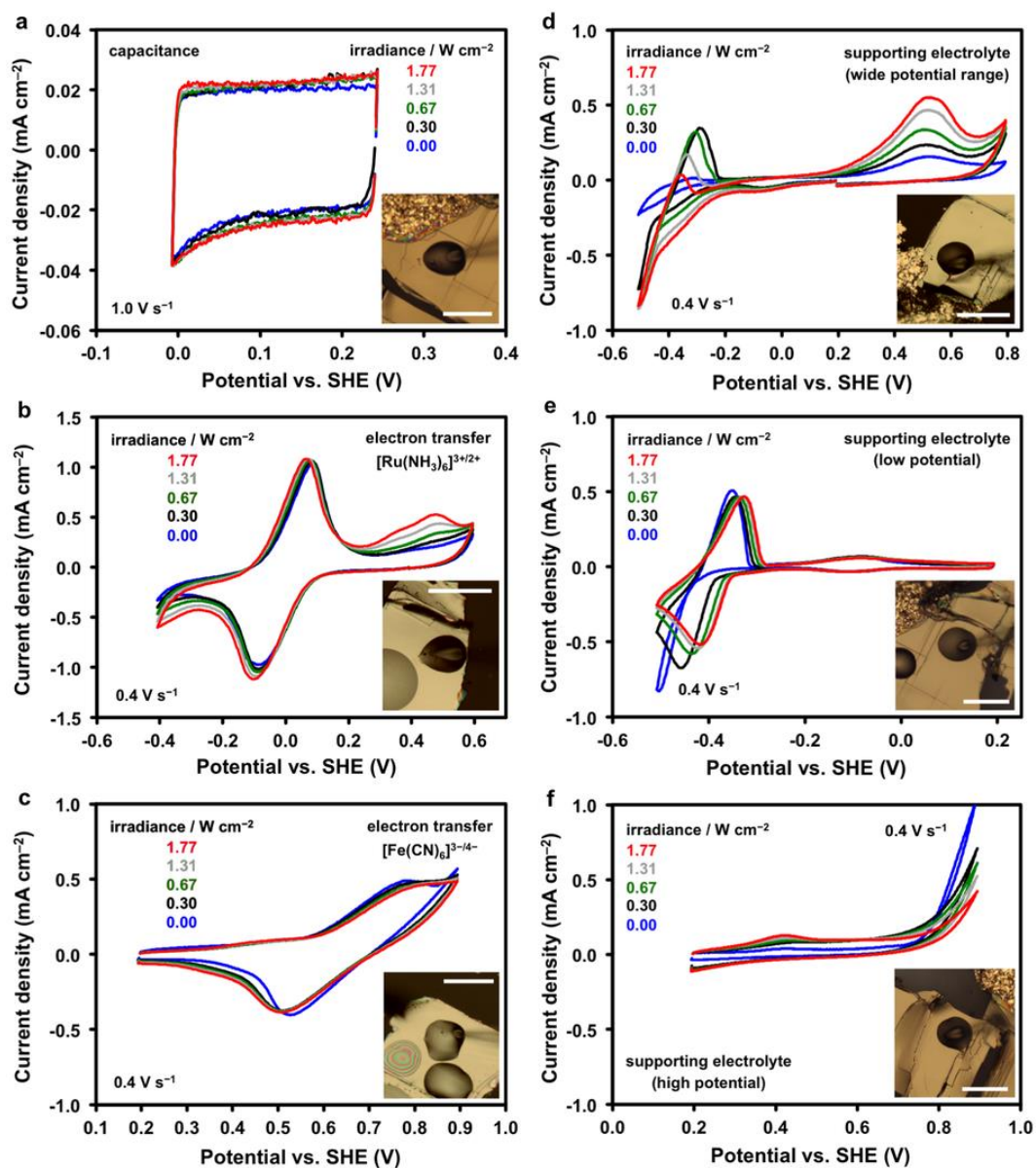


SI Figure 4-18 - Laser ablation of franckeite surface. **a**, AFM image of a monolayer franckeite flake showing a laser-induced ablation spot after 60 s exposure to 532 nm laser at  $22 \text{ kW cm}^{-2}$  power density. **b**, Step-height profile of ablation spot taken from the area indicated by a transparent magenta rectangles in the inset AFM image.

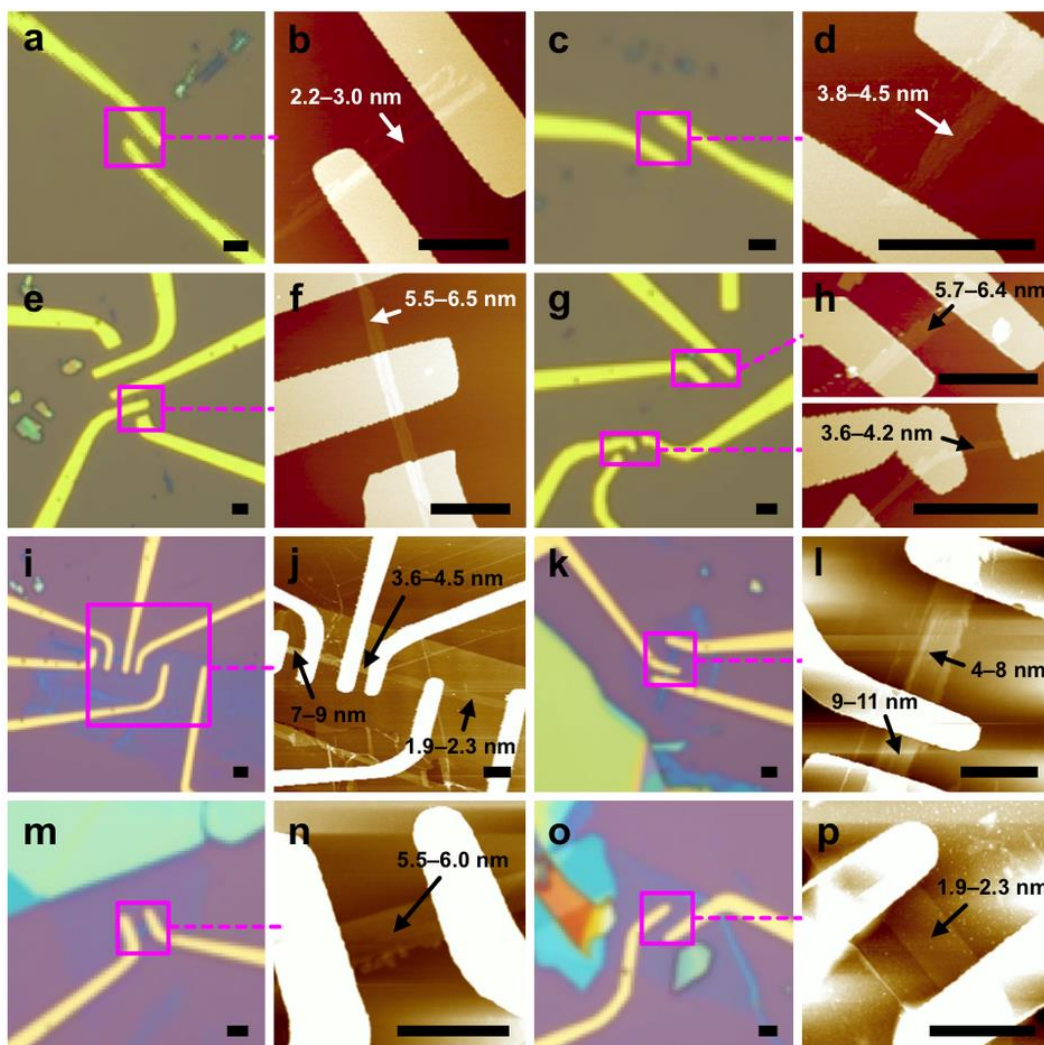


SI Figure 4-19 - Capacitance, electron transfer, and hydrogen evolution measurements. **a**, Capacitance measurement using cyclic voltammetry at varied scan rates (6 M LiCl). **b**, Capacitance dependence on consecutive voltammetric cycling. **c**, Electron transfer measurement using cyclic voltammetry at varied scan rate (with a  $[\text{Ru}(\text{NH}_3)_6]^{3+/2+}$  redox mediator in 6 M LiCl). **d**, Hydrogen evolution measured using linear sweep voltammetry at varied scan rates (1 M HCl in 6 M LiCl). Optical images of the micro-droplet cells used for the measurement are shown in the insets. All scale bars denote  $50 \mu\text{m}$ .

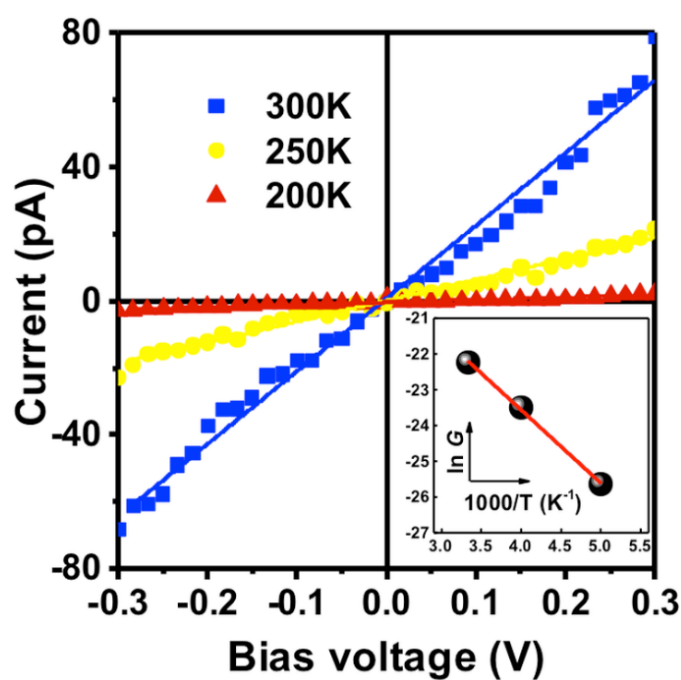




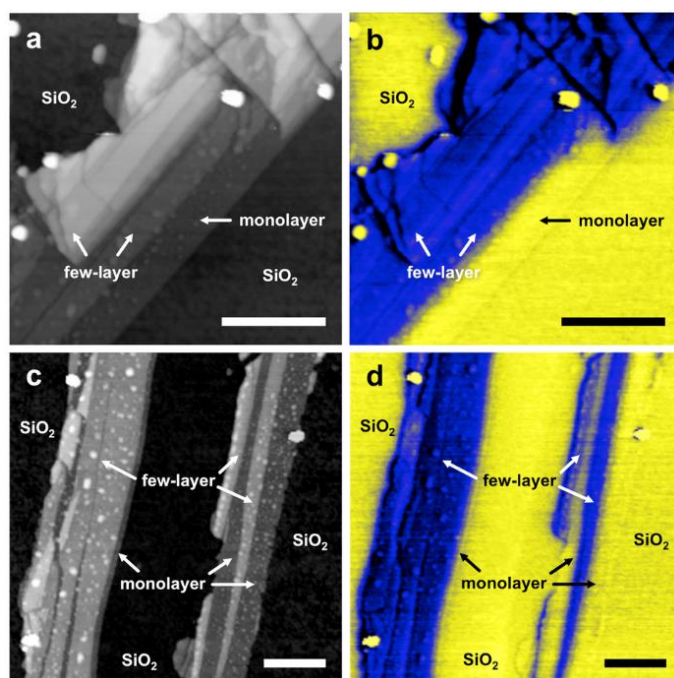
SI Figure 4-20 - Voltammetry under varied illumination intensity. **a–c**, Measurements of capacitance in 6 M LiCl, electron transfer using [Ru(NH<sub>3</sub>)<sub>6</sub>]<sup>3+/2+</sup>, and electron transfer [Fe(CN)<sub>6</sub>]<sup>3-/4-</sup> at varied irradiance (illumination intensity). **d–f**, Wide range, low, and high potential voltammograms in 6 M LiCl supporting electrolyte at varied irradiance. Optical images of the liquid micro-droplets on franckeite surface, which were used for the measurement, are shown in the insets. All scale bars denote 50 μm.



SI Figure 4-21 -Device fabrication and characterisation. **a,c,e,g,i,k,m,o**, BF optical images of frankeite devices fabricated for transport and EFM measurements. **b,d,f,h,j,l,n,p**, Corresponding AFM images taken from areas indicated by the magenta rectangles showing the average flake thickness for individual channels. Devices in **a–h** have been prepared by direct exfoliation of frankeite onto an  $\text{SiO}_2/\text{Si}$  substrate, devices in **i–p** have additionally been encapsulated in a protective layer of hBN. All scale bars corresponds to 2  $\mu\text{m}$ .



SI Figure 4-22 - Transport characterisation of a 4-layer franckeite crystal. Current-bias voltage measurement as a function of temperature for a 4-layer franckeite device. Inset shows the dependence of the zero-bias conductance ( $G$ ) on temperature, the solid red line is the Arrhenius fit.



SI Figure 4-23 - Electrostatic force microscopy measurements. **a,c**, Topography (first-pass) images of franckeite monolayer and few-layer regions. **b,d**, Corresponding EFM-phase (second-pass) images with +3 V DC voltage applied to the tip. The conducting and insulating regions are imaged in blue and yellow hues, respectively. All scale bars correspond to 500 nm.

SI Table 4-3 - EDXS quantification of bulk franckeite including impurities.

element	quantity / at%
Pb	$21.1 \pm 4.2$
Sn	$10.9 \pm 2.2$
Sb	$8.9 \pm 1.8$
Fe	$4.0 \pm 0.3$
S	$42.5 \pm 2.7$
O*	$3.7 \pm 0.5$
C*	$7.7 \pm 0.9$
Ag*	$1.1 \pm 0.3$

\*surface contamination and bulk impurities

SI Table 4-4 - Composition stoichiometry parameters determined from XPS.

species	$x_i$	$f_j$	$z_j$
Pb <sup>2+</sup>	0.238	0.815	2
Pb <sup>4+</sup>		0.185	4
Sn <sup>2+</sup>	0.078	0.785	2
Sn <sup>4+</sup>		0.215	4
Sb <sup>3+</sup>	0.097	0.637	3
Sb <sup>5+</sup>		0.363	5
O <sup>2-</sup>	0.038	0.243*	-2
O <sub>(carb.)</sub>		0.757	N/A
S <sup>2-</sup>	0.549	1.000	-2

\*oxide fraction determined from the charge neutrality condition, Supplementary Equation (3)

SI Table 4-5- Elemental stoichiometric coefficients

element	$\nu_i$	$4.2 \times \nu_i$	$25.2 \times \nu_i$
Pb	0.24	1.00	6.00
Sn	0.08	0.33	1.97
Sb	0.10	0.41	2.44
O	0.04	0.16	0.96
S	0.55	2.31	13.83

### Supplementary Note 1

#### Scanning/transmission electron microscopy and energy-dispersive X-ray spectroscopy.

Additional scanning electron microscopy (SEM) images of franckeite crystals at four different magnifications are shown in SI Figure 4-81a–d. Low-magnification image (SI Figure 4-8a) shows the ‘crumbly’ character of these crystals at the millimetre scale. High-magnification images (SI Figure 4-8–d) reveal a layered nature of franckeite at the micrometre scale, which facilitates mechanical exfoliation to thin, needle-like crystals, thus yielding a large surface area material, suitable for applications in energy storage, conversion, and catalysis. Transmission electron microscope (TEM) energy-dispersive X-ray spectroscopy (EDXS) mapping of the elemental distribution within a franckeite crystal is shown in SI Figure 4-8e–l. The EDXS maps reveal that Pb, Sn, Sb, Fe, and S (SI Figure 4-8e–i), all display homogeneous spatial distribution, and closely follow the topography of the crystal observed in the bright-field (BF)-TEM image (SI Figure 4-8l). This implies that all the metals and sulphur are evenly distributed throughout the material. On the other hand, this distribution-topography correlation is completely absent for carbon (SI Figure 4-8j), which suggests that it is purely a surface contaminant. Oxygen shows somewhat weak distribution-topography correlation (SI Figure 4-8k), which suggests that it is bound both in metal oxides and in surface carbonaceous contamination. This is also evidenced by the X-ray photoelectron spectroscopy (XPS) results – see Supplementary Note 3.

SI Table 4-3 shows the average elemental composition determined from the EDXS spectrum of the entire crystal in SI Figure 4-8e–l, including the main impurity elements

(C, O, and Ag). Carbon concentration (~8 at%) is much lower than that determined from the XPS (~50 at%, Supplementary Figure 4), confirming that carbon is present purely as a surface contaminant. On the other hand, the relative silver concentration is similar for both techniques, suggesting that it is a bulk contaminant. As mentioned in the main text, the EDXS quantification is approximate, as is the chemical formula derived from it. The accuracy of quantification in EDXS is generally known to be no better than ~5 at% due to adsorption and geometric considerations, especially in the absence of reference standards.<sup>2</sup> Quantification is also notoriously challenging for the low atomic number elements due to the effects of absorption in the sample and in the detector, so we would expect the sulphur concentration to be underestimated and its quantification errors to be largest. This is likely to be the cause for the reduction of the S content in the EDXS quantification in comparison to the expected stoichiometry for the crystal. The quantification is further complicated by the presence of impurities mentioned above (O, C, and Ag). These elements combined make up around 13 at% of the mineral (SI Table 4-3) and they have not been taken into account in determining the literature formula of franckeite.<sup>3</sup>

## Supplementary Note 2

**Transmission/scanning transmission electron microscopy.** SI Figure 4-9 shows the indexed electron diffraction pattern and the high-resolution TEM/scanning electron microscopy (STEM) images along the [001] direction, which reveal distinct moiré fringes originating from the H (Sn-rich) and T (Pb-rich) layer lattice mismatch, discussed in the main text. We also note that it was challenging to isolate a suitable franckeite single crystal for electron diffraction,<sup>4</sup> and the pattern in SI Figure 4-9a contains contributions from more than one crystal.

The sample for cross-sectional characterisation was prepared using focused ion beam (FIB) milling as shown schematically in SI Figure 4-10a. An *ex-situ* sputter coating of a 7 nm thick amorphous carbon film was followed by deposition of a 2 nm thick Au-Pd film (Q150T, Quorum Technologies Ltd, Lewes, UK). A dual-beam FIB (Nova NanoLab, FEI) with FEG-SEM and gallium FIB columns were then used for a cross-section preparation with an *in-situ* lift out approach. The region of interest was identified using SEM and a Pt protective strip (500 nm high) was formed using electron beam-induced deposition

of trimethyl (methylcyclopentadienyl) platinum(IV), followed by a FIB Pt deposition (1.5 µm high). Trenches were milled (30 kV, 10 – 1 nA) until the lamella thickness was 1 – 1.5 µm. Then, an *in-situ* lift out was performed using a micromanipulator (Omniprobe™), attached to the protective Pt layer of the cross-section, with further Pt deposition. The lamella was then transferred to a three-post FIB grid and thinned (30 kV at 0.5 – 0.1 nA, 5 kV at 50 pA and finally 2 kV at 90 pA) until electron transparent (20 – 50 nm in thickness).<sup>5</sup> The moiré pattern observed along the [001] direction (SI Figure 4-9d and 2e) is rationalised by the high-angle annular dark-field (HAADF)-STEM imaging in SI Figure 4-10b, which reveals incommensurate stacking of the H (Sn-rich) and T (Pb-rich) layers in respect to one another. The crystal unit cells of these two layers along the [010] direction have different dimensions and only come into phase every ~4.4 nm (giving rise to the moiré fringes shown in SI Figure 4-9d and e). SI Figure 4-10c shows the relative displacement of the H layers and SI Figure 4-10d shows substitution of the H layers with a continuous PbS layer under the electron beam. Supplementary Figure 3e shows the EDXS concentration profile for a 35 nm thick cross-section. Note that while the periodicity in concentration is very obvious for the four metallic elements, it is not so for sulphur, due to its low atomic number and hence lower EDXS sensitivity.

### Supplementary Note 3

**X-ray photoelectron spectroscopy.** The compositional stoichiometry of franckeite surface based on the XPS measurements was determined using Supplementary Equations (1–4). This analysis is based on the balance between the atomic fractions and oxidation states of lead, tin, antimony, sulphur, and oxygen. Supplementary Equation (1) expresses the material balance for different elements on franckeite surface.

$$\sum_i x_i = 1 \quad (1)$$

$x_i$  is the atomic fraction of an element  $i$  (e.g. Pb or Sn) determined from XPS quantification. Supplementary Equation (2) expresses the material balance for different species of the same element.

$$\sum_j f_j = 1 \quad (2)$$

$f_j$  is the fraction of a species  $j$  (e.g.  $\text{Pb}^{2+}$  or  $\text{Pb}^{4+}$ ) determined from the high-resolution XPS spectra. Supplementary Equation (3) expresses the charge neutrality condition for the chemical formula.

$$\sum_i \sum_j x_i f_j z_j = 0 \quad (3)$$

$z_j$  is the charge number of a species  $j$  (e.g.  $z_j = -2$  for  $j = \text{S}^{2-}$ ). The atomic fractions, species fractions, and charge numbers are listed in SI Table 4-4. The stoichiometric coefficient  $v_i$  of an element  $i$  in the surface chemical formula is determined from Supplementary Equation (4).

$$v_i = \frac{x_i}{\sum_i x_i} = x_i \quad (4)$$

The normalised stoichiometric coefficients of the elements are listed in SI Table 4-5.

The chemical formula was therefore determined as  $\text{Pb}_{6.0}\text{Sn}_{2.0}\text{Sb}_{2.4}\text{S}_{13.8}\text{O}_{1.0}$ .

The charge neutrality condition, Supplementary Equation (3), has been found to be fully satisfied assuming only ~24 % of the oxygen is bound in metal oxides. From this follows that the remaining ~76 % of oxygen is bound as surface carbonaceous adsorbates, which is also indirectly evidenced by shape of the O 1s peak at 532.3 eV (Figure 4-3d). A large width of this peak suggests that it is, in fact, made up of several oxygen-bound species with differing binding energies (metal-oxides: ~529 – 531 eV, organic oxygen: ~531 – 533 eV).<sup>6</sup>

Considering previous reports of oxidation and carbonaceous contamination of other layered materials,<sup>7-10</sup> it is useful to compare the surface composition of crystals that have been exposed to air for more than 24 h (aged surface) with those exposed immediately prior to the transfer to the XPS vacuum chamber (freshly cleaved surface). The XPS spectra obtained on aged and freshly cleaved franckeite surface are shown in SI Figure 4-11a and b, respectively. Quantification tables embedded in SI Figure 4-11a and b suggest that the variations in element quantities are similar for both aged and freshly cleaved surfaces. There is a small increase in the average amount of surface carbon (by 13%) and oxygen (by 20%). Overall, it can be concluded that the differences between the aged and freshly cleaved surface are small and one would have to significantly decrease the time between the cleaving and XPS measurement in order to observe more pronounced changes. Adventitious carbon and trace elements (Ag, Fe, Cl, and F, all below 1 at%), which were observed intermittently, were not included in this analysis. It is reasonable to assume that the amounts of positively and negatively



charged species of these elements will more or less balance out, thus contributing a near-zero net charge to the chemical formula, having little impact on the stoichiometric analysis described above. The differences between the EDXS and XPS quantification, in particular the relative concentrations of Sn and Fe, which are related to the difference between bulk and surface of franckeite crystals, are discussed in the main text.

SI Figure 4-12 displays a high-resolution XPS spectra of the minority metallic elements, silver and iron, and the adventitious surface carbon. SI Figure 4-12a shows the Ag 3*d* doublet peak. Deconvolution of the Fe 2*p* doublet peak, superimposed on the Sn 3*p*<sub>3/2</sub> peak, is shown in SI Figure 4-12b. Note that silver, as well as iron, are common contaminants in galenite (PbS) and are therefore likely to follow more complex galenite-derived minerals, such as franckeite.<sup>3,11</sup> The C 1*s* peak and its deconvolution to three components are shown in SI Figure 4-12c. Due to the large variation in the reported values of organic carbon binding energies and for the sake of simplicity, we have grouped the carbon-bound species into three categories, based on their approximate binding energy.<sup>6</sup> These are: 1) carbon-carbon *sp*<sup>2</sup> and *sp*<sup>3</sup> bonds (red), 2) carbon-hydrogen and carbon-oxygen (single) bonds (blue), and 3) carbon-oxygen (double) and carbon-halogen bonds (green).

#### Supplementary Note 4

**Optical microscopy, Raman spectroscopy, and atomic force microscopy.** Occasionally, terraces of franckeite with sub-monolayer thickness (< 1.85 nm) were observed. SI Figure 4-13 shows atomic force microscopy (AFM) characterisation of such case, for a thin franckeite flake encapsulated in a hexagonal boron nitride (hBN) crystal. Thickness of the sub-monolayer terraces, which are not visible under an optical microscope, varies between 0.7 – 1.5 nm (height profiles are shown in SI Figure 4-13b and c). This could either be a result of local faults in the crystal structure and/or an indirect evidence that the exfoliation of franckeite can also occur at other than the van der Waals planes, e.g. half way through the T layer. This scenario is also supported by the TEM results (SI Figure 4-10d and Figure 4-2e). As mentioned in the main text, the length of the exfoliated few-layer crystals was typically on the order of tens of μm, but their width rarely exceeded 0.5 – 1 μm, resulting in characteristic needle-like crystals with a high length-to-width aspect ratio. We have exfoliated a large number of thin

frankeite crystals and concluded that this is a universal behaviour of frankeite, irrespective of the mechanical exfoliation conditions. SI Figure 4-14 shows optical and AFM characterisation of several such crystals, which were used for the Raman spectroscopy measurements.

SI Figure 4-15 shows the raw Raman spectra of monolayer and bulk frankeite (not corrected for the Si/SiO<sub>2</sub> substrate background) as well as the reference spectra of the underlying SiO<sub>2</sub>/Si substrate for 532 nm (SI Figure 4-15a) and 633 nm (SI Figure 4-15b) laser excitation wavelengths. The 532 nm laser was used in most of our measurements due to the stronger Raman signal. SI Figure 4-15 shows that the decrease in the flake thickness is accompanied by an appearance of a minor Si peak, 2TA(X) peak at 302 cm<sup>-1</sup>, and two major Si peaks, F<sub>2g</sub> at 520 cm<sup>-1</sup> and 2TO(L) at 970 cm<sup>-1</sup>, in the monolayer Raman spectra.<sup>12</sup> The intensities of these peaks, originating from the underlying Si, are greatly reduced in thick bulk crystals (> 100 nm thickness). There is currently no reliable Raman literature on frankeite and available databases only provide spectra recorded at high laser power densities,<sup>13</sup> which damage metal chalcogenides minerals. We have also attempted to measured photoluminescence (PL) spectra of frankeite. No appreciable PL was detected within the 532 – 900 nm wavelength range from bulk or monolayer frankeite (SI Figure 4-16), which is to be expected given the small infrared band gap determined from the transport measurements (80 – 220 meV, attributed to Schottky barrier) and predicted from theory (~350 meV). Raman spectra on the same intensity scale collected during the PL acquisition and the optical images of the measured bulk and monolayer crystals are shown in the inset of the figure. All the Raman spectra shown so far (both here and in the main article) were recorded at low laser power density, namely  $\leq 35 \text{ kW cm}^{-2}$  for the green laser and  $\leq 73 \text{ kW cm}^{-2}$  for the red laser, and for short exposure time, typically 20 – 30 s. Frankeite crystals were also subjected to increasingly higher laser power densities of 0.04 MW cm<sup>-2</sup>, 0.23 MW cm<sup>-2</sup>, 0.42 MW cm<sup>-2</sup>, and 2.45 MW cm<sup>-2</sup>, as shown by the BF and DF optical images in Supplementary Figures 10a–b. Laser-induced degradation of the crystals is visible for the high laser power densities ( $\geq 0.42 \text{ MW cm}^{-2}$ ). Supplementary Figures 10c and 10d show BF and DF optical images of a laser-irradiation pattern obtained at 0.42 MW cm<sup>-2</sup>. An AFM image of this pattern in SI Figure 4-17e reveals radial damage, matching the dimensions of the spherical laser spot size ( $\sim 0.8 \mu\text{m}^2$ ). Comparison between the laser-induced degradation of bulk and monolayer crystals was also

examined. Raman spectrum of bulk crystal changes the shape at high laser power densities and is followed by an appearance of the underlying Si Raman peaks at  $520\text{ cm}^{-1}$  and  $970\text{ cm}^{-1}$  (Supplementary Figure 10f). Raman spectrum of the monolayer crystal shows almost complete disappearance of franckeite signal at high laser power density and an increase in the intensity of the minor Si peak at  $302\text{ cm}^{-1}$  (SI Figure 4-17g). The BF and DF optical images of bulk and monolayer crystals, which were used to obtain these Raman spectra are shown in SI Figure 4-17h and i.

Prolonged exposure ( $>60\text{ s}$ ) of monolayer franckeite to laser irradiation at low power density ( $22\text{ kW cm}^{-2}$ ) has revealed signs of shallow ablation of the surface. A circular depression is observed where the laser was focused on the surface (SI Figure 4-18a). The AFM profile of the depression reveals reduction of the flake thickness by about  $0.4\text{ nm}$  (SI Figure 4-18b). There are two likely explanations for this observation. First, the terminating layer of franckeite could be undergoing heat-induced removal from the surface. The shallow nature of the ablation suggests that this would be the thin H layer rather than the four-atom thick T layer. Second, the laser irradiation could be removing the ubiquitous carbonaceous adsorbates from franckeite surface. In order to prevent even a partial degradation of franckeite, we used significantly shorter exposure time ( $20\text{ s}$ ) for the collection of the Raman spectra in the main text.

### Supplementary Note 5

**Electrochemical measurements.** Cyclic voltammograms in a pure electrolyte (for the capacitance measurement) obtained at varied scan rates and their dependence on consecutive cycling at a constant scan rate are shown in SI Figure 4-19a and b, respectively. Cyclic voltammograms with a redox mediator (for the electron transfer measurement) at varied scan rates are shown in SI Figure 4-19c. Cyclic voltammograms in hydrochloric acid (for the hydrogen evolution measurement) are shown in SI Figure 4-19d. The basal surface of franckeite is very flat (root mean squared roughness,  $R_q$ , was typically  $0.5 - 1.0\text{ nm}$ ) and therefore the geometric/active surface area effects are negligible. On the other hand, the uncertainty in the geometric vs. active surface area on edge/defective surfaces means that their electrochemical performance is more difficult to quantify.

The capacitance and electron transfer measurements were also examined at varied white light illumination intensity (irradiance), results of which are shown in SI Figure

4-20. Illumination of the crystals was realised using a 20× optical microscope objective and the irradiance was calibrated using the 843-R power meter (Newport Spectra-Physics Ltd, UK). SI Figure 4-20a, b, and c show the cyclic voltammograms in a pure 6 M LiCl electrolyte, in an electrolyte with a  $[\text{Ru}(\text{NH}_3)_6]^{3+/2+}$  redox mediator, and in an electrolyte with a  $[\text{Fe}(\text{CN})_6]^{3-/4-}$  redox mediator, respectively, obtained at constant scan rate and varied irradiance. Only small changes are observed with varying irradiance and they are likely to be irradiation-induced thermal effects. This agrees with our transport measurements of franckeite's narrow infrared band gap (0.1 – 0.2 eV). The capacitance calculated from equation (3) slightly increases (by ~15 %) for the maximum irradiance in comparison to the zero-irradiance. The peak-to-peak separation of the  $[\text{Ru}(\text{NH}_3)_6]^{3+/2+}$  reduction/oxidation decreases by 8 mV for the maximum irradiance, indicating a slightly faster electron transfer (by ~14 %) in comparison to the zero-irradiance. Dependence of the  $[\text{Fe}(\text{CN})_6]^{3-/4-}$  reduction/oxidation peak-to-peak separation on irradiance is complex, initially increasing and then decreasing slightly at high irradiance. It is possible that the  $[\text{Fe}(\text{CN})_6]^{3-/4-}$  mediator adsorbs at the surface and obscures the measurement, as observed previously on graphite.<sup>7</sup> In a word, small changes in the capacitance and electron transfer rate indicate franckeite is a degenerate, narrow band gap semiconductor.

The voltammetric background in pure supporting electrolyte over a large potential range was also examined at varied irradiance. Series of cyclic voltammograms in SI Figure 4-20d show a redox activity in a wide potential region, which significantly increases with increasing irradiance. In order to deconvolute the contribution of the low and high potentials to the overall activity, separate voltammograms of the low and high potential regions were recorded (SI Figure 4-20e and 13f). Analysis of the voltammograms indicates that the broad oxidative peak, centred around +0.5 V is associated with the reductive current at low potentials (below -0.35 V). Performing voltammetry in the low potential region (SI Figure 4-20e) reveals a well-defined redox process, which becomes near-reversible at highest irradiance. When voltammetry is performed within the high potential region (SI Figure 4-20f) the peak at +0.5 V disappears and the potential window is extended to ca. +0.8 V. This redox activity most likely contributes to the increased inherent capacitance within the narrow potential window (0 – 0.25 V vs. SHE) and therefore results in a pseudo-capacitive behaviour.

The redox activity undoubtedly originates from transitions between different oxidation states of the metals, although the exact peak assignment is difficult due to uncertainties in metal sulphides' standard redox potentials.<sup>14</sup>

### Supplementary Note 6

**Transport and electrostatic force microscopy measurements.** A large number of devices have been fabricated for the transport and electrostatic force microscopy (EFM) characterisation. SI Figure 4-21 shows a selection of thin franckeite flakes ranging from monolayer (~2 – 3 nm) to 5 layers (~10 nm), electrically connected using a deposition of Cr/Au contacts. The devices shown in SI Figure 4-21 a–h have been prepared by direct exfoliation of franckeite onto an SiO<sub>2</sub>/Si substrate, while the devices in SI Figure 4-21i–p have additionally been encapsulated in a thin layer of hBN in order to protect franckeite crystals from oxidation and contamination.

SI Figure 4-22 shows additional transport measurement results for a 4-layer thick franckeite crystal. The current-bias voltage curves were measured at three different temperatures, and from the zero-bias conductance on temperature in the inset, the Arrhenius fit was plotted and activation energy of 170 meV extracted.

EFM phase measurements in a double-pass mode were carried out to investigate the conductivity of thin franckeite flakes. In the first-pass, topography of the layers was imaged in a non-contact AFM mode. In the second-pass taken along the same scan line, the tip was lifted to 30 nm height from the surface while mechanically oscillating on resonance (out-of-feedback) and a direct current (DC) bias voltage was applied between the doped silicon tip (Nanosensors PPP-FMR, 0.5 – 9.5 N/m) and the underlying doped silicon substrate. The second-pass phase images directly map the conductivity of the sample by probing the second derivative of the tip-substrate capacitance,  $d^2C/dz^2$ , showing negative contrast (larger capacitance) for conductive nanostructures over an insulating substrate and no or positive contrast (smaller capacitance) for insulating nanostructures as previously described.<sup>15,16</sup> SI Figure 4-23 shows the AFM topography images and the corresponding EFM phase images recorded using a +3V DC bias voltage. Blue hues in SI Figure 4-23 b and d indicate conductive material and correspond to bilayer and thicker franckeite. On the other hand, yellow

hues indicate insulating material and correspond to the SiO<sub>2</sub> substrate and monolayer franckeite.

### Supplementary Note 7

**Density functional theory calculations of the electronic band structure.** The optimal crystal structure of T and H layers have been calculated within the local density approximation (LDA) of density functional theory using the VASP code.<sup>17</sup> A plane-wave cut-off of 400 eV and a 12 × 12 **k**-point grid was used in the calculations. The structure was approximated so that no Sn and Fe atoms were assumed to be present in the T and H layer, respectively. This corresponds to approximating the T layer with Pb<sub>3</sub>SbS<sub>4</sub> stoichiometry and the H layer with SnS<sub>2</sub> stoichiometry, based on the EDXS concentration profiles. The lattice parameters of the T layer are  $a = 5.735$  Å and  $b = 5.730$  Å, and the lattice parameters of the H layer are  $a = 3.616$  Å and  $b = 6.264$  Å. These compare well with the previously reported experimental values obtained for bulk franckeite,<sup>18</sup> which found  $a = 5.805(8)$  Å and  $b = 5.856(16)$  Å for the T layer, and  $a = 3.665(8)$  Å and  $b = 6.2575(16)$  Å for the H layer.

The LDA was utilized to calculate the band structure of the T and H layers and the T–H heterostructure, i.e. franckeite monolayer (Figure 4-7). The results show that the T layer exhibits a small direct band gap of 0.36 eV at the C point, while the H layer has a large indirect band gap of 1.48 eV, with the conduction band minimum at the C point and the valence band maximum half way between the Y and  $\Gamma$  points. A scissor correction of these band gaps can be performed by calculating the density of states (DOS) using the HSE06 hybrid density functional, which yields corrected band gaps of 0.79 eV and 2.46 eV for the T and H layers, respectively.

Experiments indicate that the in-plane lattice vectors of the T and H layers are aligned in bulk franckeite, hence it is in principle possible to construct a super-cell geometry out of the T and H layers to study the T–H heterostructure (franckeite monolayer). The mismatch between the lattice parameters requires a relatively large super-cell, and even then, each lattice must undergo some stretching or compression. A compromise can be achieved by setting a tolerance of 0.5 Å as the mismatch between the lattice parameters of the stretched layer super-cells and their non-stretched counterparts; in this case it is sufficient to use a single unit cell along the **b** lattice vector, while along

the **a** vector 5 cells of the T layer unit cell and 8 cells of the H layer unit cell must be taken. The resulting T–H heterostructure contains 128 atoms with  $a = 28.8 \text{ \AA}$  and  $b = 5.996 \text{ \AA}$ . The distance between the mean planes of the T and H layer was optimized and found to be  $9.054 \text{ \AA}$ . Note that this is slightly larger than the separation in bulk franckeite, for which the optimal distance was found to be  $8.894 \text{ \AA}$ . Note also, that in the bulk calculation the approximation was made so that the **c** vector is perpendicular to the plane stretched by the **a** and **b** vectors. T–H heterostructure (monolayer) band structure displays a prominent energy gap just below the Fermi level. This gap is indirect with the conduction band minimum at the  $\Gamma$  point and the valence band maximum at the C point, and its magnitude is  $0.35 \text{ eV}$ , which is almost identical with that of the T layer ( $0.36 \text{ eV}$ ). The finding that the T–H heterostructure is metallic is a consequence of the alignment of the bands in the T and H layers seen in Figure 4-7. The T layer dopes the H layer with electrons due to the relative position of the Fermi levels, hence the T–H heterostructure is a type III broken-gap semiconductor interface. The number of electrons transferred corresponds to one electron per  $\text{Pb}_3\text{SbS}_4$  unit of the T layer. The appearance of an energy gap below the Fermi level is in agreement with this finding as well.

The DOS obtained for this super-cell T–H heterostructure (monolayer) predicts that it is metallic (Figure 4-7d). A similar finding can be seen for the T–H–T heterostructure (one and a half monolayer), the T–H–T–H heterostructure (bilayer), and bulk franckeite. It is worth noting that most of the major DOS features in these heterostructures are the same, except for the size of the energy gap below the Fermi level, which decreases with increasing number of layers.

The situation is expected to be quite different if the non-zero concentration of Sn in the T layer and Fe in the H layer were to be taken into account. The XPS spectra indicate that franckeite contains both  $2+$  and  $4+$  valence states of Sn. Assuming  $\text{Sn}^{4+}$  cations are present in the H layer, their substitution by  $\text{Fe}^{2+}$  cations will introduce acceptor states within the H layer. Similarly, substitution of  $\text{Sb}^{3+}$  cations within the T layer by  $\text{Sn}^{4+}$  cations will create donor states within the T layer, as will substitution of  $\text{Pb}^{2+}$  cations by  $\text{Sb}^{3+}$  cations, which is an important substitution to consider given the approximation made in the modelling of the T layer. As an example, let us consider a slightly exaggerated T layer composed of only  $\text{Pb}^{2+}$ ,  $\text{Sb}^{3+}$ , and  $\text{S}^{2-}$  ions, in a stoichiometry of  $\text{Pb}_6\text{Sb}_2\text{S}_8$ . Substitution of a half of the  $\text{Sb}^{3+}$  cations with  $\text{Sn}^{4+}$  cations

and of one in every six  $\text{Pb}^{2+}$  ions with  $\text{Sb}^{3+}$  cations corresponds to turning  $\text{Pb}_6\text{Sb}_2\text{S}_8$  into  $\text{Pb}_5\text{Sb}_2\text{SnS}_8$ , gaining two extra electrons from these substitutions. From the DOS, the number of electrons removed from the T layer in the T–H heterostructure is one electron per  $\text{Pb}_3\text{SbS}_4$ , which is an equivalent of two electrons per  $\text{Pb}_6\text{Sb}_2\text{S}_8$  unit. The above substitution counteracts the removal of electrons and promotes the formation of a gapped system. It is therefore expected that the substitutions, which were neglected in the DFT calculations, will create donor states in the T layer and acceptor states in the H layer. This will drive the system towards a gapped semiconductor state due to the acceptor states countering the rise of the Fermi level in the H layer and the donor states countering the fall of the Fermi level in the T layer, which is energetically favourable. An important implication of this finding is that the T layer with the substitutions included contains free charge carriers in the conduction band, while the H layer contains charge carriers (holes) in the valence band. This therefore predicts that successful isolation of either T or H layer of franckeite would yield a 2D doped semiconductor.



## Supplementary References

- 1 Barr, T. L. & Seal, S. Nature of the use of adventitious carbon as a binding energy standard. *Journal of Vacuum Science & Technology, A: Vacuum, Surfaces, and Films* **13**, 1239-1246 (1995).
- 2 Williams, D. B. & Carter, C. B. *Transmission Electron Microscopy: A Textbook for Materials Science*. (Springer Science, 2009).
- 3 Moh, G. H. Mutual  $\text{Pb}^{2+}/\text{Sn}^{2+}$  substitution in sulfosalts. *Mineralogy and Petrology* **36**, 191-204 (1987).
- 4 Wang, S. & Kuo, K. H. Crystal lattices and crystal chemistry of cylindrite and franckeite. *Acta Crystallogr., Sect. A: Found. Crystallogr.* **47**, 381-392 (1991).
- 5 Schaffer, M., Schaffer, B. & Ramasse, Q. Sample preparation for atomic-resolution STEM at low voltages by FIB. *Ultramicroscopy* **114**, 62-71 (2012).
- 6 Benoit, R. (CNRS Orléans, Orléans, France, 2016).
- 7 Patel, A. N., Collignon, M. G., Oconnell, M. A., Hung, W. O. Y., McKelvey, K., MacPherson, J. V. & Unwin, P. R. A new view of electrochemistry at highly oriented pyrolytic graphite. *Journal of the American Chemical Society* **134**, 20117-20130 (2012).
- 8 Velický, M., Bradley, D. F., Cooper, A. J., Hill, E. W., Kinloch, I. A., Mishchenko, A., Novoselov, K. S., Patten, H. V., Toth, P. S., Valota, A. T., Worrall, S. D. & Dryfe, R. A. W. Electron Transfer Kinetics on Mono- and Multilayer Graphene. *ACS Nano* **8**, 10089-10100 (2014).
- 9 Velický, M., Bissett, M. A., Toth, P. S., Patten, H. V., Worrall, S. D., Rodgers, A. N. J., Hill, E. W., Kinloch, I. A., Novoselov, K. S., Georgiou, T., Britnell, L. & Dryfe, R. A. W. Electron transfer kinetics on natural crystals of  $\text{MoS}_2$  and graphite. *Physical Chemistry Chemical Physics* **17**, 17844-17853 (2015).
- 10 Nioradze, N., Chen, R., Kurapati, N., Khvataeva-Domanov, A., Mabic, S. & Amemiya, S. Organic Contamination of Highly Oriented Pyrolytic Graphite As Studied by Scanning Electrochemical Microscopy. *Analytical Chemistry* **87**, 4836-4843 (2015).
- 11 Young, C. A., Taylor, P. R. & Anderson, C. G. *Hydrometallurgy 2008: Proceedings of the Sixth International Symposium*. (Society for Mining, Metallurgy, and Exploration, 2008).
- 12 Wang, R.-P., Zhou, G.-W., Liu, Y.-L., Pan, S.-H., Zhang, H.-Z., Yu, D.-P. & Zhang, Z. Raman spectral study of silicon nanowires: High-order scattering and phonon confinement effects. *Physical Review B: Condensed Matter and Materials Physics* **61**, 16827-16832 (2000).
- 13 Downs, B. (Department of Geosciences, University of Arizona, Tucson, AZ, USA, 2016).
- 14 Licht, S. Aqueous Solubilities, Solubility Products and Standard Oxidation-Reduction Potentials of the Metal Sulfides. *Journal of The Electrochemical Society* **135**, 2971-2975 (1988).
- 15 Bockrath, M., Markovic, N., Shepard, A., Tinkham, M., Gurevich, L., Kouwenhoven, L. P., Wu, M. W. & Sohn, L. L. Scanned Conductance Microscopy of Carbon Nanotubes and  $\lambda$ -DNA. *Nano letters* **2**, 187-190 (2002).
- 16 Datta, S. S., Strachan, D. R., Mele, E. J. & Johnson, A. T. C. Surface Potentials and Layer Charge Distributions in Few-Layer Graphene Films. *Nano letters* **9**, 7-11 (2009).

- 17 Kresse, G. & Furthmüller, J. Efficient iterative schemes for *ab initio* total-energy calculations using a plane-wave basis set. *Physical Review B: Condensed Matter and Materials Physics* **54**, 11169-11186 (1996).
- 18 Makovicky, E., Petricek, V., Dusek, M. & Topa, D. The crystal structure of franckeite,  $\text{Pb}_{21.7}\text{Sn}_{9.3}\text{Fe}_{4.0}\text{Sb}_{8.1}\text{S}_{56.9}$ . *American Mineralogist* **96**, 1686-1702 (2011).

## 5. Paper 2 – Isolation of 2D cylindrite as a naturally occurring van der Waals heterostructure

This chapter demonstrates the exfoliation of cylindrite ( $n,m=1$ ) to single unit cell thickness. Cylindrite possess the final stacking sequence which has yet to be exfoliated to the 2D limit. The successful exfoliation of cylindrite demonstrates that the exfoliation of MLCs is invariant to stacking sequence, and as such, all MLCs are realistic targets as 2D materials. The exfoliated specimens were characterised using analytical STEM, AFM and Raman spectroscopy. However, the exfoliation of cylindrite was noted to be quite poor, which hampered the fabrication of electrical transport devices. As such attempts to measure the expected in-plane anisotropy failed.

The mechanical exfoliation of many 2D materials is relatively easy. Typically adhesive tape is applied to an orientated source crystal and even pressure is applied with the pad of the thumb. Repeated bifurcation may be used to improve yield of thin flakes.<sup>1</sup> However the small size and cylindrical shape of the cylindrite source crystal made exfoliation challenging. In particular ensuring a good contact between the crystal and adhesive tape was difficult. Applying force using the thumb pad provided insufficient pressure, resulting in poor cleavage. It was found that if the tip of the thumb was used instead, more pressure could be applied, which yielded a better exfoliation.

Furthermore the small sizes of the exfoliated flakes made standard nanofabrication techniques more challenging. This was most apparent when searching the Si/SiO<sub>2</sub> substrate, where it was necessary to search using a 50x objective lens, in lieu of the more typical 10x or 20x lenses used for most other 2D materials. The use of colour filters and, heated substrates and polymer coated substrates were trialled and were found to have marginal benefit in improving the visibility and coverage of thin cylindrite flakes. The small lateral dimensions of flakes also hampered other cleanroom processes including the mechanical transfer of cylindrite flakes to SiN TEM grids, as adherence of the transferred flakes was poor.

In this paper, cross sectional STEM imaging is demonstrated to be an invaluable technique for the investigation of cylindrite's layered structure, unique curvature and previously unreported kink band structure. However, fabrication of suitably thin and damage free cylindrite cross sections for high quality STEM analysis was problematic. It

was found that lamellae which were sufficiently thin for high resolution imaging were mechanically unstable, resulting in catastrophic damage to the lamellae, either in the FIB instrument or in the transfer process to the STEM microscope. The damage of the lamellae took several different forms, including: the complete loss of the lamellae (i.e. lamellae fell off the copper grid), loss of the cylindrite region from lamellae, damage and delamination of the cylindrite region; and cylindrite region lifting off the substrate and swaying under the ion beam. Some examples of these problems are shown in Figure 5-1 a-d. Thicker specimens did not suffer from these mechanical instabilities, however they limited the imaging capabilities (Figure 5-1e,f). Consequently a new FIB procedure was designed to allow for the preparation of thin, but mechanically robust specimens. This new method utilised shallower TEM lamella (less silicon substrate), the deposition of a Pt strap parallel to the lamella-grid interface, and a larger border between the thinned region and lamella-grid interface. The full method is outlined in Figure 5-2.

#### **Contributions to work:**

Matthew Holwill and Dr. Gregory Auton assisted with the collection of the AFM data, Dr. Nicholas Clarke also assisted with the collection of AFM data and offered useful discussions for the processing of AFM data; Dr. David Perello and Matthew Holwill contributed to the fabrication of the electrical devices; Dr. Endre Tovari and Dr. David Perello conducted the electrical transport measurements and analysed the results. Dr. Nicholas Clarke assisted with the mechanical transfer of exfoliated cylindrite flakes to SiN TEM grids; Photoluminescence measurements were collected and analysed by Daniel Terry; EDX template matching was conducted by Yichi Wang; Matthew Hamer assisted with the thermal degradation studies of the exfoliated cylindrite flakes; Prof. Sarah Haigh and I co-wrote the manuscript.

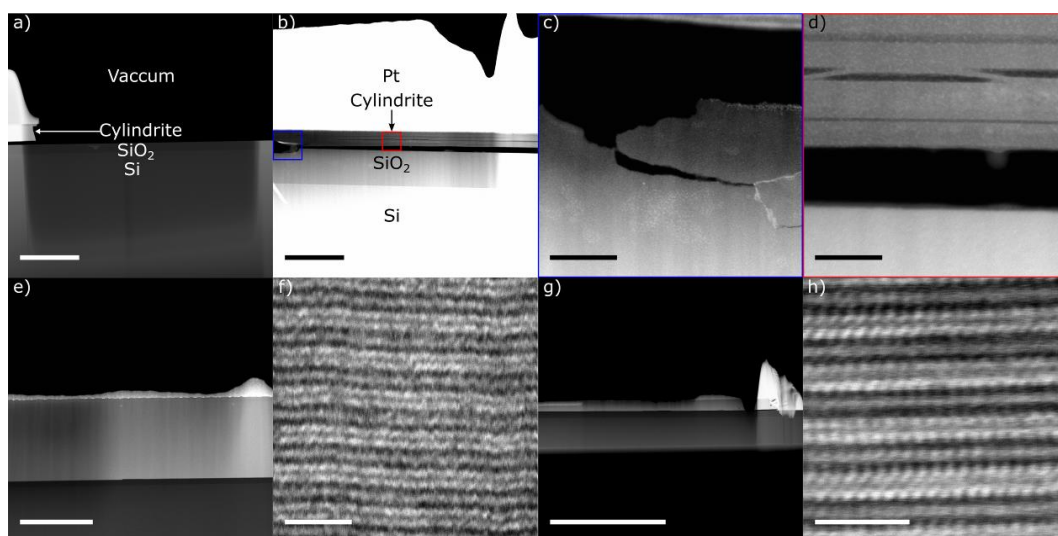


Figure 5-1 – HAADF STEM images of cylindrite cross sections prepared by FIB. (a) An example of failed FIB lamellae in which the region of interest has become removed from the substrate between FIB preparation and loading into the TEM. (b) Image of failed TEM lamellae. (c) Higher magnification image showing damaged cylindrite flake corresponding to blue box in (b). (d) Higher magnification image of delamination of cylindrite flake, corresponding to red box in (b). (e) Attempts to prepare more mechanically robust samples which resulted in insufficiently thinned lamellae. (f) Higher magnification image of (e), with poorly resolved atoms due to overly thick specimens. (g) Sufficiently thin and mechanically robust lamella, prepared by new method. (h) High magnification image of (g) with resolved atom columns. Scale bars correspond to (a) 2  $\mu\text{m}$ , (b) 500 nm, (c) 100 nm, (d) 50 nm, (e) 1  $\mu\text{m}$ , (f) 2 nm, (g) 10  $\mu\text{m}$  and (h) 2 nm.

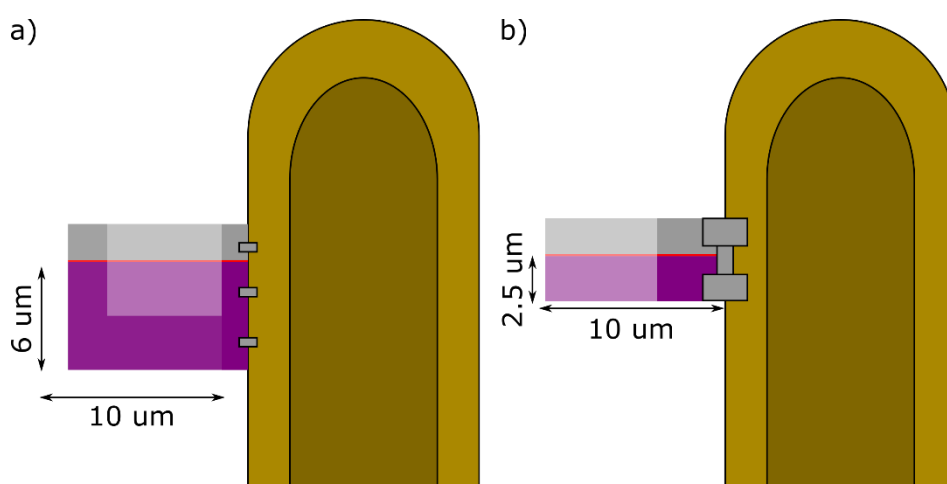


Figure 5-2 – Illustration of new FIB lamella preparation method (copper grid not to scale). (a) Original method where a relatively deep lamella ( $\sim 6 \mu\text{m}$ ) is transferred to copper half grid. The lamella is then welded with three small Pt straps, and the border between the thinned region and the copper post is approximately 1  $\mu\text{m}$ . (b) New method where a shallower lamella ( $\sim 2.5 \mu\text{m}$ ) is transferred to a copper half grid. The lamella is then welded using two perpendicular, and one parallel Pt strap. The parallel strap maximises the contact between the lamella and the copper grid. The border between the thinned region and copper half grid is larger ( $\sim 2 \mu\text{m}$ ).

# Isolation of 2D cylindrite as a naturally occurring van der Waals heterostructure

Alexander Rakowski<sup>1,3</sup>, David Perello<sup>2,3</sup>, Matthew Holwill<sup>2</sup>, Nicholas Clark<sup>2,3</sup>, Endre Tovari<sup>2,3</sup>, Yichi Wang<sup>1</sup>, Gregory Auton<sup>2,3</sup>, Daniel Terry<sup>2,3</sup>, Roman Gorbachev<sup>2,3</sup>, Andy Kretinin<sup>2,3</sup>, Kostya Novoselov<sup>2,3</sup>, Andre Geim<sup>2,3</sup> & Sarah Haigh<sup>1,3</sup>

1 - School of Materials, University of Manchester, Oxford Road, Manchester, M13 9PL, UK

2 - School of Physics and Astronomy, University of Manchester, Oxford Road, Manchester, M13 9PL, UK

3 - National Graphene Institute, University of Manchester, Oxford Road, Manchester, M13 9PL, UK

## Abstract

Misfit layer chalcogenides (MLCs) are a family of compounds formed from alternating 2D layers. They are able to incorporate a diverse range of elements into their structure, allowing for materials with a broad range of properties, and are readily synthesisable. The successful exfoliation of MLCs to single unit cell thickness has sparked interest in MLCs as an alternative route for the production of van der Waals heterostructures. Here we present the mechanical exfoliation of a naturally occurring MLC, cylindrite, to the single unit cell thickness. This is of particular importance as cylindrite possess the final stacking sequence which has yet to be successfully exfoliated to the 2D limit. We utilise cross sectional analytical STEM to investigate the chemical structure within the individual layers, examine cylindrite's unique curvature and investigate the previously unreported kink band structure. Finally we present electrical transport measurements and highlight the difficulties in the fabrication of cylindrite devices.

## Introduction

The field of two dimensional (2D) materials has expanded dramatically since graphene was first isolated in 2004<sup>2</sup>, and now includes a substantial library of 2D crystals spanning a broad range of electronic properties.<sup>3</sup> Such properties can be harnessed to realise new device architectures by stacking two or more different 2D crystals on top of each other, forming van der Waals heterostructures<sup>4</sup> with tailored properties.<sup>5</sup> However, synthesis of such heterostructures is currently only achievable via mechanical exfoliation and manual transfer of individual fragile layers, which is time consuming and difficult to scale up. There is therefore, significant interest in

alternative approaches for the synthesis of van der Waals heterostructures. Chemical vapour deposition and printed liquid exfoliated heterostructures offer routes to industrial scale fabrication, but the structures produced are generally highly defective, and hence only suitable for selected applications.<sup>6</sup>

A different approach to synthesising high quality van der Waals heterostructures is via exfoliation of bulk materials composed of alternating 2D layers. Misfit layer chalcogenides (MLCs) are one such family of materials where neighbouring atomic layers are only weakly bonded, and therefore possible to separate, using approaches similar to those used for exfoliation of graphene and transition metal dichalcogenides (TMDCs). MLCs are composed of alternating stacked pseudo-hexagonal (H)  $\text{TX}_2$  layers, where  $\text{T} = \text{Sn, Fe, V, Mo, Ta, Cr, Ti}$  and  $\text{Nb}$  and  $\text{X} = \text{S, Se}$  or  $\text{Te}$  and pseudo-tetragonal (T)  $\text{MX}$  layers, where  $\text{M} = \text{Pb, Sn, Sb, Bi}$  and rare earths.<sup>7-13</sup> Through contraction and expansion the T and H layers can match along the **b** axis, but are unable to do this along the **a** axis due to the differing unit cell sizes. The T and H unit cells therefore have an irrational relationship, and are incommensurate along the **a** axis. This unique crystallography has been of academic interest for several decades<sup>14,15</sup>, with a new mathematical framework required to describe the crystal structure<sup>16</sup>. MLCs are described by the general formula  $[(\text{MX})_n]_{1+x}[(\text{TX}_2)_m]$ , where  $n$  and  $m$  are integer values reflecting the stacking sequence of the layers, and  $x$  represents the mismatch between the T and H unit cells. Figure 5-3 provides schematic illustrations of the stacking for some example MLCs, franckeite where  $n=2, m=1$ ; cylindrite where  $n, m=1$ ; and  $[(\text{PbS})][(\text{NbS}_2)_2]$  where  $n=1, m=2$ .

MLCs are able to incorporate a wide range of metal and chalcogen elements in both T and H layers, and consequently a wide range of exotic properties are accessible in individual layers including metallic, semi-conducting, Mott insulating superconducting, topologically insulating and magnetic layers.<sup>17-20</sup> These compounds both exist naturally, and are readily synthesisable under mild reaction conditions.<sup>8-12</sup>

MLCs were first successfully exfoliated to the 2D limit in 1993, when synthetic MLCs,  $[(\text{PbS})][(\text{NbS}_2)_2]$  and  $[(\text{SmS})][(\text{NbS}_2)_2]$ , were liquid and electrochemically exfoliated to single unit cell thickness.<sup>21</sup> Both these compounds are  $n=1, m=2$  compounds, and exfoliation was shown to occur along the homogeneous interface between the two H

layers. Exfoliation between the two  $\text{TX}_2$  layers is readily understood as analogous to the exfoliation of TMDCs. More recently, franckeite has been exfoliated to the 2D limit<sup>22,23</sup> by mechanical and liquid phase exfoliation. Franckeite  $[(\text{Pb}_{1-x}\text{Sb}_x\text{S})_2][(\text{Sn}_{1-y}\text{Fe}_y\text{S}_2)]$  is a naturally occurring MLC with a  $n=2$ ,  $m=1$  stacking sequence and as such contains both homogeneous interfaces between the T layers and heterogeneous interfaces between the T and H layers (Figure 1c). Franckeite has been shown to exfoliate at both interfaces, although the heterogeneous interface is preferred.<sup>22</sup> Cylindrite and franckeite are formed from the same T ( $\text{Pb}_{1-x}\text{SbS}$ ) and H ( $\text{Sn}_{1-y}\text{Fe}_y\text{S}_2$ ) layers and possess a similar nominal chemical composition of  $(\text{Pb}_3\text{Sn})^{2+}\text{Fe}^{2+}\text{Sb}_2^{3+}\text{Sn}_3^{4+}\text{S}_{14}^{2-}$  and  $(\text{Pb}_5\text{Sn})^{2+}\text{Fe}^{2+}\text{Sb}_2^{3+}\text{Sn}_2^{4+}\text{S}_{14}^{2-}$  respectively. Despite these compositional and structural similarities, cylindrite and franckeite take remarkably different macroscopic crystal structures with franckeite forming flat tabular crystals, while cylindrite forms (eponymous) scrolled cylinders (Figure 5-3f,g). The  $n,m=1$  stacking of cylindrite results in only heterogeneous interfaces between layers, and to date no  $n,m=1$  compound has been successfully exfoliated to single unit cell thickness.

Here we demonstrate the successful exfoliation of cylindrite to the 2D single unit cell limit. As the final stacking sequence ( $n,m=1$ ) to be successfully exfoliated it demonstrates that the exfoliation of MLCs is invariant to stacking sequence. We demonstrate the use of atomic resolution scanning transmission electron microscopy (STEM), and energy dispersive X-ray (EDX) spectroscopy (EDXS) to study the crystal's structure and composition, and reveal the presence of rotational disorder between the layers and stacking sequence faults. We present the first characterisation of a kink band in cylindrite, and show the curvature to be complex. Finally, we examine the electronic properties of the 2D cylindrite.



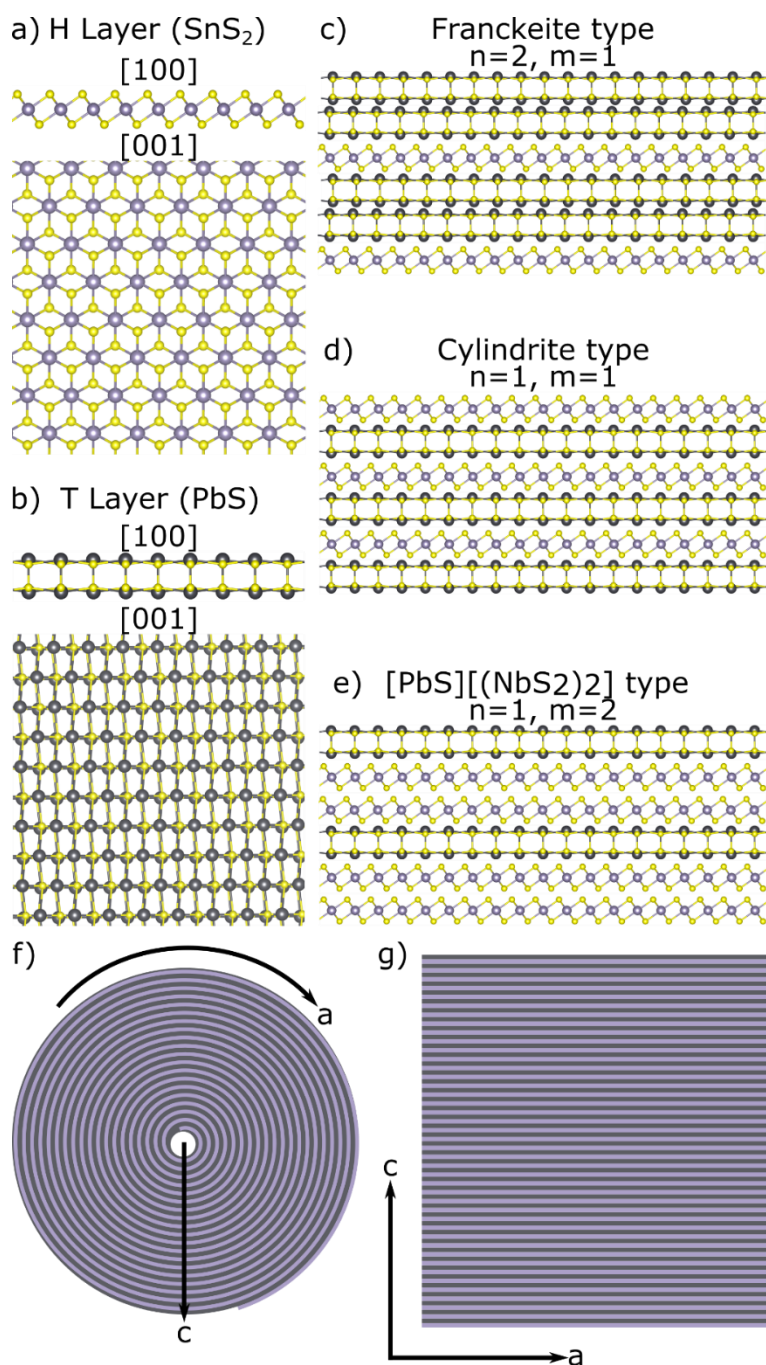


Figure 5-3 - Atomic models illustrating misfit layer compounds layering, (a) H layer viewed along the [100] and [001] directions, (b) T layer viewed along the [100] and [001] direction, (c) representing different stackings sequences possible for MLCs, franckeite where  $n=2, m=1$ ; (d) cyndrite where  $n,m=1$ ; and (e)  $[\text{PbS}][(\text{NbS}_2)_2]$  where  $n=1, m=2$ . Purple atoms represent Sn, Fe, V, Mo, Ta, Cr, Ti or Nb, yellow atoms S, Se or Te, and grey atoms Pb, Sn, Sb, Bi or rare earths. (f) Illustrative model of scrolled layering seen in cyndrite producing cylindrical geometry crystals, (g) illustrative model of flat layering producing planar crystals as seen in franckeite. Purple and grey slabs correspond to H layer and T layers respectively.

## Results and discussion

### Exfoliation

Using an identical approach to that applied to other 2D materials<sup>2</sup>, the bulk cylindrite crystals were successfully exfoliated to single unit cell thickness by mechanical exfoliation on to a Si/SiO<sub>2</sub> substrate. (Figure 5-4) It is noticeable that the cylindrite flakes were typically much smaller than is routinely achievable for graphene and TMDCs, with thin flakes having lateral dimensions up to 6  $\mu\text{m}$  wide, and up to 20  $\mu\text{m}$  long, although more typically 2-3 x 4-6  $\mu\text{m}$ . Furthermore the flakes often had high aspect ratios in-plane, with the largest dimension generally parallel to [010] direction. The generation of anisotropic flakes could either be attributed to (i) a limitation imposed by the scrolled cylinder structure, or (ii) an effect of the incommensurate layering in the [100] direction. While the effects of the cylindrical structure on flake exfoliation are in reasonable agreement with the typical flake sizes (SI Figure 5-10), the production of high aspect ratio flakes was also noted for franckeite<sup>22</sup>, suggesting that incommensurate layering is more likely to be responsible for this phenomena.

There were additional complications to the exfoliation process compared to the exfoliation of graphene from highly oriented pyrolytic graphite crystals. This was in part due to the small size of the cylindrite source crystal (radius  $\sim 500\ \mu\text{m}$ , length  $\sim 750\ \mu\text{m}$ ), limiting the amount of material which could be deposited on to substrates. Additionally, the cylindrical shape of the macroscopic crystal made handling and ensuring a good contact to the adhesive tape difficult. This resulted in a sparsely covered substrate, with very few regions of thin cylindrite flakes. Attempts to produce increased number/proportion of thin flakes by additional cleavage steps or repeated bifurcation resulted in disintegration of the flakes into a powder.

Atomic force microscopy (AFM) of a thin region of a representative cylindrite flake (Figure 5-4c,d) shows the presence of step heights of 1.82 and 1.32 nm. We assign these as single and two unit cell thick regions of cylindrite. We attribute the small difference in height compared to the unit cell dimension ( $\sim 1.17\text{-}1.18\ \text{nm}^{10,14,24}$ ) to the presence of a thin amorphous layer, impurities and changes in tip-sample interaction across the breadth of the substrate. The presence of impurities is supported by bubbles on the surface, visible in the height map, which are shown to be soft in the AFM deformation map (SI Figure 5-11). The AFM adhesion map shows the cylindrite tip

interaction is constant across the entirety of the flake (SI Figure 5-11). AFM analysis additionally reveals the presence of unusual crack defects; similar defects were also noted in cross-sectional HAADF STEM images of relatively thick flakes (SI Figure 5-12). Consequently these defects are suggested to be intrinsic to the source crystal, rather than induced by the exfoliation process.

Raman spectra for three and few unit cell (6-12) as well as bulk exfoliated cylindrite flakes (SI Figure 5-13) were collected using a 532 nm laser, with the contribution of the silicon background signal subtracted from the spectra (Figure 5-4e). The Raman signature shows a broad enhancement for the spectral region between 100 and 350  $\text{cm}^{-1}$ . In addition, the spectra have several distinct peaks at: 60, 75, 95, 164, 200, 245 and 315  $\text{cm}^{-1}$ . Raman spectra for cylindrite has not previously been reported but a tentative assignment may be achieved for the principal peaks by considering the individual Raman spectra of the constituent components: PbS (galena)<sup>25</sup>, SnS (herzenbergite)<sup>26,27</sup>, SnS<sub>2</sub> (berndtite)<sup>28</sup>, Sb<sub>2</sub>S<sub>3</sub> (stibnite)<sup>29</sup> and FeS<sub>2</sub> (pyrite)<sup>30</sup>. The peak at 60  $\text{cm}^{-1}$  is most likely the B<sub>1g</sub>/B<sub>3g</sub> of Sb<sub>2</sub>S<sub>3</sub>, but may also be assigned to the T<sub>1u</sub> of PbS. 75 and 95  $\text{cm}^{-1}$  may be assigned as the A<sub>g</sub> peak of Sb<sub>2</sub>S<sub>3</sub> and the A<sub>g</sub> peak of SnS respectively. 164  $\text{cm}^{-1}$  is assigned as the B<sub>3g</sub> peak of SnS. However, this peak is quite broad which we attribute to the overlap of peaks at 154 and 156  $\text{cm}^{-1}$  corresponding to the PbS  $\Sigma_{3g}/\Sigma_{3u}$  and Sb<sub>2</sub>S<sub>3</sub> A<sub>3g</sub> peaks. 200  $\text{cm}^{-1}$  is assigned to the E<sub>g</sub> peak of SnS<sub>2</sub>. Again this peak is quite broad which we believe is due to the overlap of PbS T<sub>1u</sub> and SnS B<sub>3u</sub> peaks at 210  $\text{cm}^{-1}$  and 220  $\text{cm}^{-1}$  respectively. While previously seen at 238  $\text{cm}^{-1}$ , we attribute the peak at 245  $\text{cm}^{-1}$  to a shifted B<sub>1g</sub>/B<sub>3g</sub> peak of Sb<sub>2</sub>S<sub>3</sub>. Finally we attribute the 315  $\text{cm}^{-1}$  to a combination of the A<sub>g</sub> Sb<sub>2</sub>S<sub>3</sub> (313  $\text{cm}^{-1}$ ), A<sub>1g</sub> SnS<sub>2</sub> (314  $\text{cm}^{-1}$ ) and the A<sub>1g</sub> of SnS<sub>2</sub> (317  $\text{cm}^{-1}$ ). The Raman spectra are dominated by the Sb<sub>2</sub>S<sub>3</sub>, SnS and SnS<sub>2</sub> with minimal contribution from PbS and FeS<sub>2</sub>. Sb<sub>2</sub>S<sub>3</sub> (1.72 eV), SnS (1.01 eV) and SnS<sub>2</sub> (2.10 eV) have larger bandgaps<sup>31</sup> than PbS (0.37 eV) and FeS<sub>2</sub> (0.95 eV), resulting in increased Raman scattering. The three unit cell thick flake gave the highest Raman signal and bulk flakes gave the lowest. Due to the small lateral sizes of the single unit cell thick flakes, it was not possible to collect Raman spectra. However we would expect a reduction in signal compared with three unit cell thick regions, following the trend observed in franckeite.<sup>22</sup> No photoluminescence signal was found between 1.2 and 2.2 eV, which is expected from the reported bandgap of bulk cylindrite (0.65 eV)<sup>32</sup>.

The cylindrite flakes were sensitive to laser damage with higher powers degrading the flake (SI Figure 5-14).

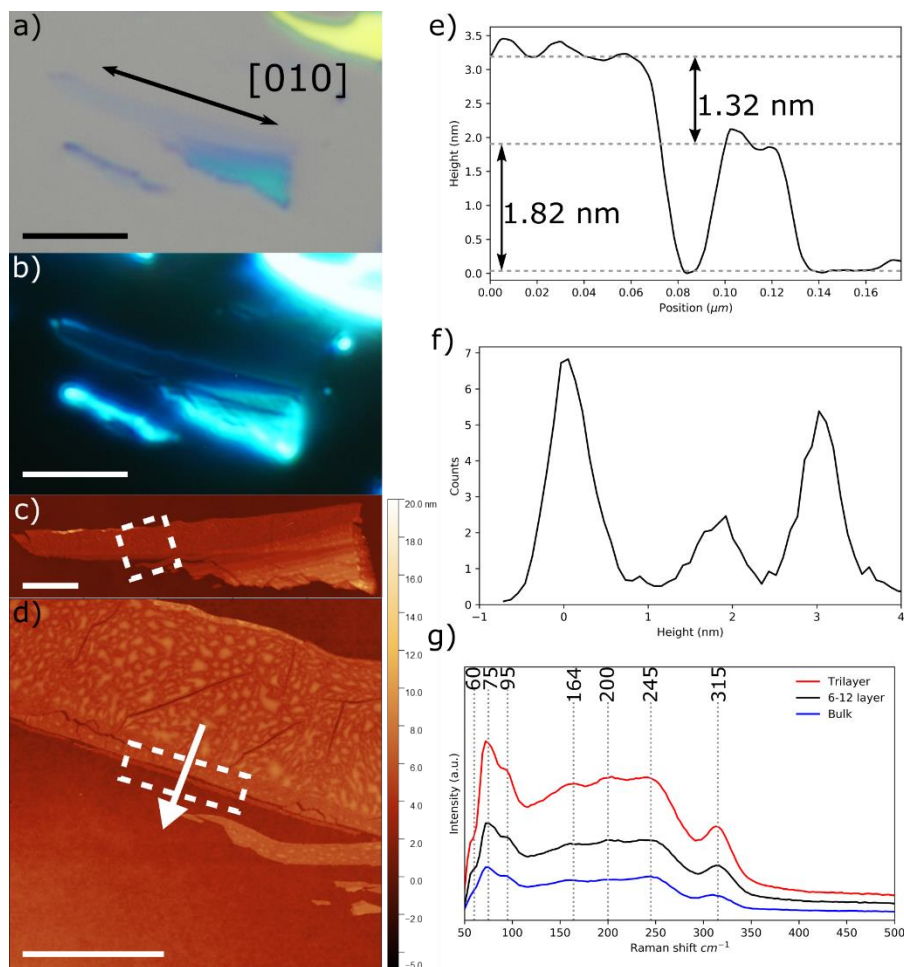


Figure 5-4 – Optical, AFM and Raman spectra of exfoliated a cylindrite flake. (a) Bright field optical image of exfoliated cylindrite flake on Si/SiO<sub>2</sub>, (b) dark field optical image, scale bar 5  $\mu$ m. (c) Low magnification AFM height map of cylindrite flake, scale bar 2  $\mu$ m. (d) High magnification AFM height map of white dashed box in (c), showing a small region of single unit cell thickness and extended two unit cell thick regions. Scale bar 1  $\mu$ m. (e) Line profile taken from SI Figure 5-11a, (f) histogram of height distributions taken from SI Figure 5-11a. (g) 532 nm Raman spectra of three, few unit cell and bulk cylindrite flakes with Si substrate background removed, peaks at 60, 75 95, 164, 200, 245 and 315  $\text{cm}^{-1}$ .

A well-known effect of reducing the dimensionality of the materials is a corresponding reduction in thermal stability (e.g. melting point of gold nanoparticles with size<sup>33</sup>).

Exfoliated cylindrite flakes were heated to 150°C under normal atmosphere (held for 1 hour) and 350°C in vacuum environments (ramped to 200°C, held for 1 hour then ramped to 350°C and held for 30 minutes), with no change in the appearance of the flakes in optical images. As such they appear to be thermally stable within temperature ranges useful for nanofabrication.

## Bulk characterisation

### Plan view characterisation

The composition of the cylindrite flakes was determined to be approximately  $(\text{Pb}_{3.5}\text{Sn})\text{FeSb}_2\text{Sn}_3\text{S}_{10}$  by STEM EDX of crushed cylindrite flakes (Table 5-1). This stoichiometry is not charge balanced, probably due to underestimation of the sulphur content caused by preferential absorption of low energy X-rays and overlap between the S K $\alpha$  and Pb M $\alpha$  X-ray peaks. A charge balanced crystal is recovered through the addition of sulphur yielding an approximate composition of  $(\text{Pb}_{3.5}\text{Sn})\text{FeSb}_2\text{Sn}_3\text{S}_{14.5}$ , in good agreement with the nominal stoichiometry. The elemental distribution within individual flakes was shown to be homogeneous (Figure 5-5), although there was some variation in the chemical composition between different flakes (SI Table 5-2). A variation in composition has been observed previously in literature, where it was found that the composition varies with distance from the core.<sup>10,14</sup>

<i>Element</i>	<i>Average concentration (Atomic w.t. %)</i>	<i>Approximate stoichiometry</i>	<i>Charge balanced stoichiometry</i>
<i>Tin<sup>2+/4+</sup></i>	20.03 ± 2.05	4.08	4.0 (1 <sup>2+</sup> ,3 <sup>4+</sup> )
<i>Lead<sup>2+</sup></i>	16.89 ± 1.72	3.44	3.5
<i>Iron<sup>2+</sup></i>	4.91 ± 0.23	1.00	1.0
<i>Antimony<sup>3+</sup></i>	9.97 ± 1.60	2.03	2.0
<i>Sulphur<sup>2-</sup></i>	48.20 ± 1.04	9.82	14.5

Table 5-1- EDXS quantification of 9 bulk cylindrite flake viewed along [001] direction. Uncertainty is one standard deviation in the measurements.

High angle annular dark field (HAADF) STEM imaging of cylindrite reveals the crystals' unusual structure. When viewed along the [001] direction (perpendicular to the layers) a Moiré pattern is visible with a period of ~3.4 nm. This is slightly smaller than previously reported values, (3.6 nm<sup>24</sup>, 3.8 nm<sup>15</sup>), but can be explained as the period is known to decrease with distance from the cylindrite core, and the exfoliated flakes sample the exterior of the crystal.<sup>14</sup> Moiré patterns are not usually observed for isolated single crystals but are common in MLCs due to the intrinsic incommensurate relationship between the T and H layers. Both cubic and hexagonal lattices can be observed for different locations of the same cylindrite flake. While the cubic can be confidently assigned to the T layer, the assignment of the hexagonal lattice is more

difficult. The hexagonal lattice was imaged close to a scroll in a cylindrite flake (SI Figure 5-16), and as HAADF STEM image contrast is roughly proportional to  $Z^2$ , the presence of Pb will provide a much larger intensity than Sn. Consequently the hexagonal lattice may be assigned to the cubic lattice tilted off the [001] zone axis (SI Figure 5-15). This assignment is supported by the lack of evidence of sub unit cell thickness in the AFM maps.

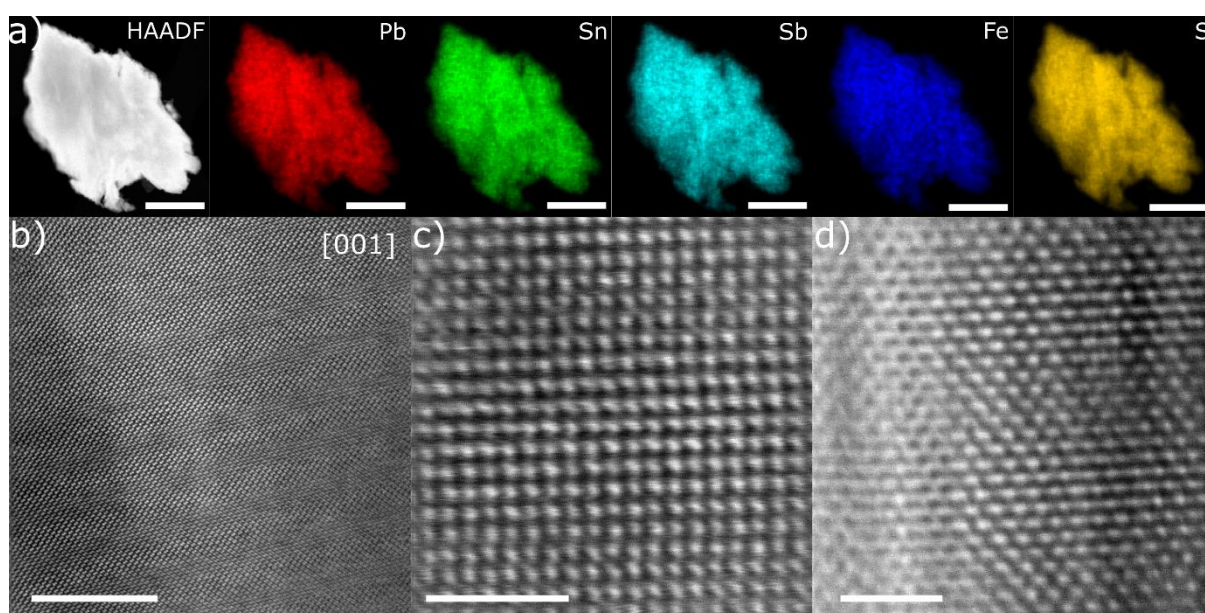


Figure 5-5 – Plan view characterisation of crushed and exfoliated cylindrite flakes. STEM characterisation along the [001] direction. (a) EDX maps for a crushed cylindrite flake. Scale bar 1 μm (b)-(d) Filtered HAADF STEM images of the cylindrite lattice. (b) Showing the Moiré pattern with a spacing of 3.4 nm. Scale bar 10 nm. (c) Cubic lattice corresponding to the PbS T layer, scale bar 2 nm. (d) Hexagonal lattice assigned a T layer tilted off the [001] direction. Scale bar 2 nm.

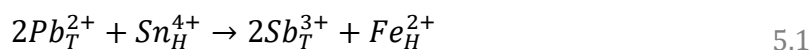
### Cross section characterisation

Cylindrite's layered structure is more clearly revealed by imaging exfoliated flakes parallel to the crystal layers along the [100] and [010] directions (Figure 5-6). The individual atomic layers are clearly visible in HAADF images, with the brighter planes corresponding to the T layer which has a higher mean atomic number. The unit cell dimension along the c axis ([001] direction) is determined experimentally from these images as 1.175 nm. This is in excellent agreement with previous X-ray diffraction and TEM studies.<sup>10,14,24</sup> There is a slight rotation between the T layers, when viewed along the [010] direction, which has previously been reported in synthetic MLCs (Figure 5-6e).<sup>34,35</sup> It is possible that this disorder may facilitate the exfoliation of these crystals and simultaneously limit the lateral size of the flakes yielded. The incommensurate



relationship between the T and H layers was examined, and the period between the two crystals becoming approximately aligned is 3.5 nm (SI Figure 5-20), similar to the period of the Moiré pattern (3.4 nm) visible when the crystal is viewed in the [001] direction. While it has been shown that in cylindrite scrolls the planes are curved along the [100] direction<sup>10</sup> the HAADF images show flat [100] planes. These samples were prepared by mechanical exfoliation from the outer most surface of the cylindrite source crystal. Consequently the curvature of the [100] planes is several micrometres and they therefore appear flat within the ~10 nm field of view visible in the HAADF images. The curvature of the cylinders has been proposed to be due to a lattice distortion of the T layers in the crystal. Such distortion is predicted to occur due to segregation of the larger cation species (Pb) to one side of the layer; inducing an expansion of the lattice and curvature of the layer. However due to the low curvature, efforts to investigate this expansion and contraction were unsuccessful (SI Figure 5-17). Further discussion on the curvature of cylindrite is presented later.

The elements are clearly segregated between the two distinct crystal layers with the distribution revealed by EDX elemental mapping (Figure 3c,f). The EDX maps clearly show that lead is segregated in the T layer, while the tin and iron are in the H layer. Sulphur and antimony are present in both T and H layers. The presence of antimony in both layers is likely to increase the stability of the structure; Sb<sup>3+</sup> ions sit at divalent lattice sites in the T layer inducing excess positive charge, while the same ions at tetravalent sites in the H layer induce excess negative charge. This leads to a charge transfer between the layers.<sup>17,36</sup> The presence of Fe<sup>2+</sup> in the H layers will also induce excess negative charge, which is likely to be balanced by excess Sb<sup>3+</sup> in the T layer, allowing for the crystal to remain charged balanced overall (Equation 2.1).<sup>15</sup>



Closer inspection of the elemental line profiles (SI Figure 5-18) shows that the sulphur signal peaks between the two lead atomic columns in the T layer whereas the structural model suggests that the sulphur signal should be most intense on the lead atomic columns. The discrepancy can be explained by a distortion of the layer's cubic structure, where the lead atoms are protruding outward and the sulphur atoms buckle inwards as seen in other MLCs.<sup>10,37</sup> The sulphur intensity profile in the H layer is

peaked either side of the tin atomic columns, in agreement with prior expectations of the crystal structure. However, we note that the potential for electron channelling along a low index crystal direction can cause distortions in the measured elemental distribution, making quantitative compositional analysis of individual atomic layers highly challenging.<sup>38</sup>

The most striking feature present in the high resolution STEM-HAADF images of cylindrite is the sinusoidal bending of the lattice planes when the structure is viewed along the [001] direction (Figure 5-6d). The wave has an amplitude of approximately 0.2nm and a period of ~3.4 nm, equal to the Moiré pattern along the [001], and close to the period along the [010] direction. This unusual transverse modulation has been previously described.<sup>10,14,24</sup> It was shown that the modulation allows for the semi-commensurate unit cells to become commensurate (SI Figure 5-19). Interestingly qualitative analysis of the STEM HAADF images reveals that the convex parts of the T layer appear brighter than the concave parts, suggesting a local increase in atomic number, most likely an increase in the Pb content. While this has been previously proposed to be the cause for the modulation<sup>10,15,24</sup>, it has not been seen prior to this study. A modulation of ion occupancy has been proposed theoretically as a means to reduce the strain of the lattice.<sup>10</sup> The larger Pb ions provide local lattice expansion which is favourable for atomic sites in the convex part of the wave, while the smaller Sb ions produce a slight lattice contraction, better suiting the concave sites. No HAADF intensity variation is visible in the H layer, but this is not unexpected due to the similarity in the atomic numbers of the cations Sb and Sn. Template matching of the STEM EDX spectrum images has been used to enhance the signal to noise ratio of the elemental maps; unfortunately the resolution remains too poor to distinguish the elemental segregation within the T layers suggested by the STEM HAADF. Ordering of Pb and Sb has also been seen in franckeite where the cations are found to create a chequer board pattern within the two innermost atomic planes of the T layer.<sup>22</sup> This difference in ordering behaviour is likely to be responsible for the drastically different macroscopic crystal structures observed for franckeite compared to cylindrite. The transverse modulation also appears to limit the resolution of atomic positions along the [010] direction, because the wave causes the atomic positions to be smeared out in the 2D projected image. HAADF STEM images from multiple cross sections taken



perpendicular to length of exfoliated flakes show the preferential cleavage direction is in the [100] direction, i.e. length of flake is parallel to the [010] direction.

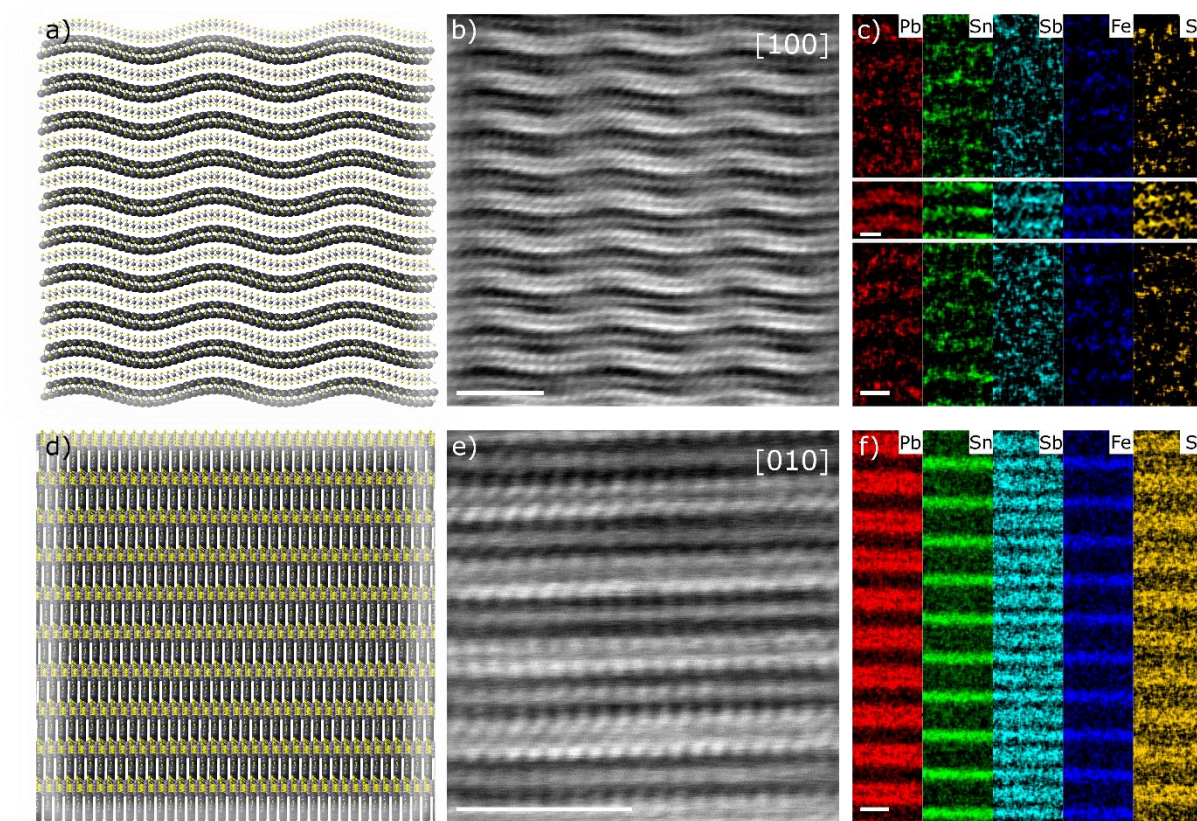


Figure 5-6 – Cross sectional characterisation of exfoliated cylindrite flakes. (a), (d) atomic models for cylindrite viewed along the [100] and [010] directions respectively, (b), (e) filtered HAADF STEM images of cylindrite viewed along [100] and [010] directions respectively. Scale bars 2.5 nm. (c), (f) EDX spectrum imaging showing elemental maps for cylindrite. Insert in c corresponds to template matched images used to improve contrast. Scale bars 1 nm.

### Curvature characterisation

While most of the exfoliated cylindrite flakes lie flat to the substrate, some flakes contained scrolled edges (Figure 5-7). Cross sections of these scrolled edges were prepared in an attempt to investigate the curvature of cylindrite. From these sections the curvature was confirmed to be along the [100] direction as previously reported.<sup>10,14,24</sup> The curvature was shown to be continuous, while the presence of circumferential bands were seen (Figure 5-7 f). These bands may correspond to a difference in local crystal tilts or a variation in elemental composition, and have not been previously reported. However, the vertical wedge like segmentation previously reported in literature for natural and synthetic cylindrite crystals was not observed (Si

Figure 5-21).<sup>10,14</sup> This is surprising as these vertical segments are found at the core and surface of cylindrite crystals, from which these flakes were exfoliated.

The core of the cylindrite source crystal was found to be highly defective and contain large voids which prevented representative high curvature regions from this region being prepared for cross sectional STEM examination. In order to investigate higher curvature regions, a cross section was prepared from a kink band in an exfoliated cylindrite flake (Figure 5-8a). These kink bands are previously unreported in literature, for cylindrite and MLCs generally. However, similar kink band defects have been previously identified in graphite and other layered structures, and are often observed in mechanically exfoliated crystals.<sup>39,40</sup> The kink band showed extensive and complex curvature, in which both regions of continuous curvature and abrupt tilt boundaries were present (Figure 5-8b). The low magnification image shows a clear difference in the contrast either side of the tilt boundary (indicated by white dashed line), which is likely to be due to an out-of-plane crystal tilt. Four distinct regions can be recognised in Figure 5-8 C: low curvature region with faceted features (indicated by white dashed line), high curvature region with faceted features (dashed blue box, Figure 5-8d), a nanotube-like region with continuous curvature (dashed purple box, Figure 5-8e), and sharp angled bends (dashed purple box, Figure 5-8e). While a change in curving mechanism as a function of radial distance from the core of cylindrite crystals has previously been reported<sup>14</sup>, the curvature that appears is more complex in the kink bands compared to that in bulk cylindrite. The atomically sharp bends have angles ranging from 70 to 88° (Figure 5-8e green dashed lines) and are present for curvature radii up to approximately 2.4 nm, with the bend angle decreasing as curvature radius increases. Curvature radii greater than 2.4 nm, can be formed with continuous or faceted features, contrary to literature which describes a curvature radius dependent transition between the two types<sup>14</sup>. Investigating the atomic positions in the high curvature region was challenging, probably due to the high level of local strain associated with such defects (Figure 5-8f-i). Defects in the stacking sequence (Figure 5-8j) were also observed to be present in close proximity to this fault. Here a H layer is missing from the structure leading to a T layer with double thickness (H-T-T-H layering). Similar stacking sequence fault defects have not been observed in cylindrite previously, but have been observed in synthetic MLCs.<sup>41,42</sup> These layering sequence

faults were not observed in other lamellae, but further work would be needed to determine whether these defects are important in the formation of kink bands.

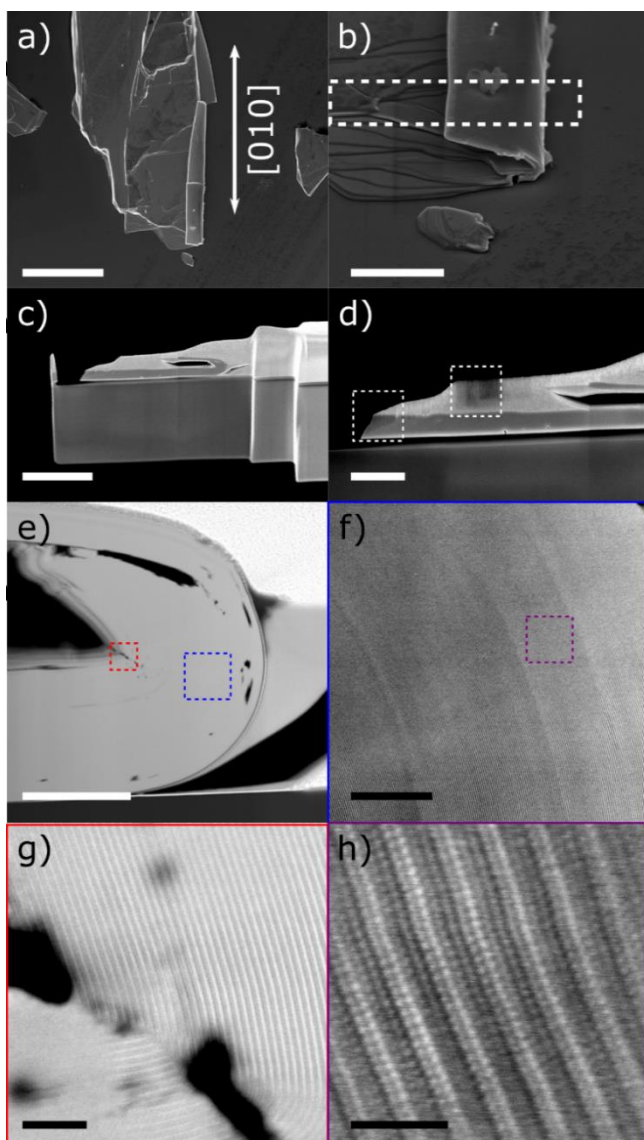


Figure 5-7 – Characterisation of scrolled cylindrite flake. (a)-(d) Secondary electron SEM images of, (a) cylindrite flake on a SiO<sub>2</sub> substrate viewed at 0° stage tilt, approximately parallel to [001], and (b) viewed at 52° stage tilt. (c) TEM lamella showing a FIB prepared cross section of the same cylindrite flake for the region of interest marked in (b). (d) Same lamella as (c) after further ion beam thinning. Further thinning caused the cylindrite to lift from the substrate and move under the ion beam leading to FIB induced damage (dashed white box). (e)-(h) HAADF STEM images, viewed along the [010] direction. (e) Low magnification cross section image of the cylindrite flake. (f) Low magnification image corresponding to blue box in (e), showing radial bands of different intensity. (g) High magnification image corresponding to red box in (e) showing the presence of voids, it is unclear if the voids are intrinsic or formed/exacerbated by FIB thinning. (h) Atomic resolution image corresponding to purple box in (f), showing curvature direction is in the incommensurate direction ([100]) as described by Kaden et.al.<sup>10</sup>. Scale bars correspond to (a) 10 μm, (b) 2 μm, (c) 3 μm, (d) 1 μm, (e) 100 nm, (f) 50 nm, (g) 10 nm and (h) 2 nm.



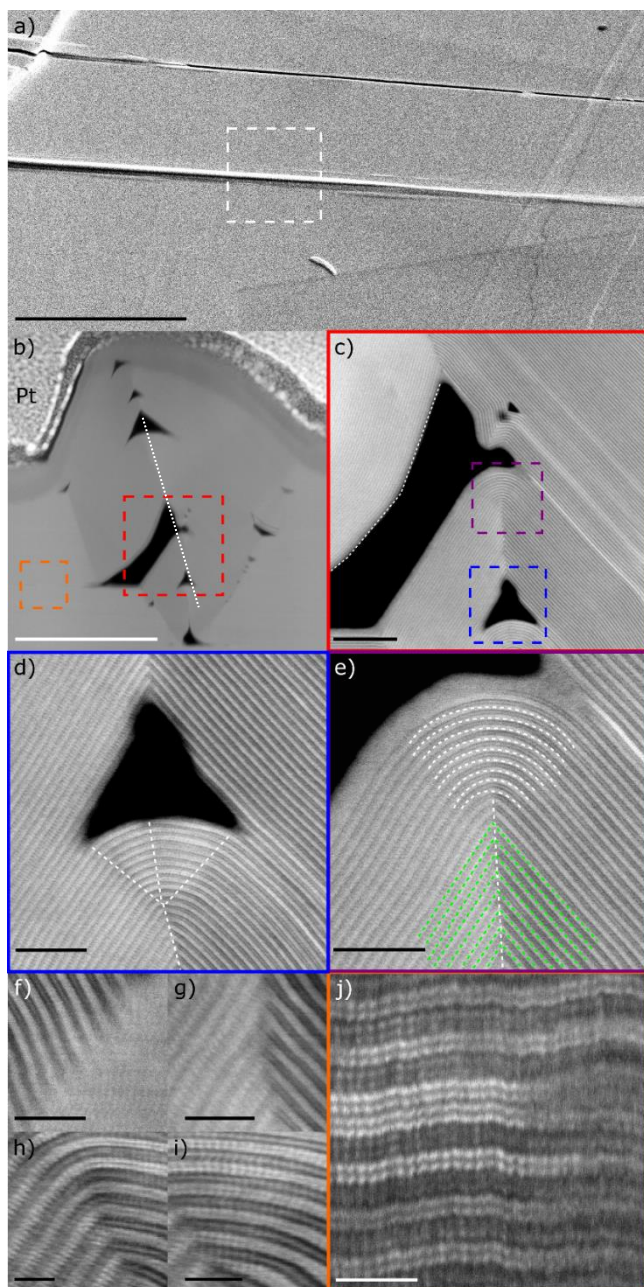


Figure 5-8 – Characterisation of kink band in exfoliated cylindrite flake. (a) SEM image of a kink band in cylindrite viewed at  $52^\circ$ . FIB cross section was extracted for the region highlighted. (b)-(j) HAADF STEM images. (b) Cross sectional image showing the variety and complexity of defects and curvature within the kink band. The differences in brightness are believed to be due to regions of the crystal having different local orientations. (c) Image containing multiple curvatures corresponding to the red box of (b). The left hand region with a large radius of curvature exhibits faceted surfaces, highlighted by the dashed white lines. (d) High magnification image of a region with a smaller radius of curvature corresponding to blue box in (c). Dashed white lines highlight abrupt tilt boundaries. (e) High magnification image corresponding to purple box in (c). Showing a transition from smooth curvature at the surface to an abrupt boundary deeper in the crystal. (f)-(i) examples of the atomic layer structure at the boundary. (j) Atomic resolution image corresponding to orange box in (b) showing stacking fault, in which cylindrite sample contains H-T-T-H layering. Scale bars correspond to (a)  $5\ \mu\text{m}$  (b)  $200\ \mu\text{m}$ , (c)  $25\ \text{nm}$ , (d)  $10\ \text{nm}$ , (e)  $10\ \text{nm}$ , (f)  $5\ \text{nm}$ , (g)  $5\ \text{nm}$ , (h)  $2\ \text{nm}$ , (i)  $2\ \text{nm}$  and (j)  $2\ \text{nm}$ .

## Device fabrication and transport measurements

In order to measure the electronic properties of the cylindrite flakes, a two terminal device was successfully fabricated, consisting of a 3-5 layer cylindrite flake encapsulated in h-BN, and contacted using few layer graphene (SI Figure 5-23). The cylindrite crystal was shown to be conductive, and demonstrated a temperature dependence indicative of a semiconductor (Figure 5-9a). The initial drop in resistance is attributed to the reduction in phonon scattering, and the subsequent increase to the reduction of charge carriers, suggestive of a thermally activated semiconductor. These findings are in good agreement with literature data on bulk crystals.<sup>32</sup>

Magnetoresistance studies were also conducted with a magnetic field sweep from 0 to 13.8 T and a back gate sweep of -100 to 50 V (achieved with two different sweeps, - 100 to - 40 V and - 50 to 50 V) (Figure 5-9b,c). However, the contribution of the few layer graphene contacts could not be deconvolved. Consequently, while there are distinguishable features interpretation is not possible. Nonetheless some of the weaker vertical features in Figure 5-9b are not typical of graphene, so are suggestive of a contribution from cylindrite.

The anisotropy in electrical properties between the in-plane vs out-of-plane for MLCs has been documented.<sup>20,37</sup> Additionally an in-plane anisotropy in electrical conductance has been observed for bulk MLCs<sup>43</sup>, including cylindrite crystals<sup>10</sup>. It has been proposed that this is due to the incommensurate structure results in a quasi-periodic 1D potential along the **a** axis, yielding different transport properties along the **a** and **b** axes.<sup>44</sup> It was hoped that the exfoliated cylindrite flakes would allow for further measurements of the in-plane anisotropy. However due to the small flake sizes, and cracks present in the exfoliated cylindrite flakes, the production of devices suitable for more detailed device measurements proved challenging. Multiple devices were made using different fabrication techniques all of which were unsuccessful. Some of these are presented in SI Figure 5-22. Improved electrical measurements will require higher quality source crystals.

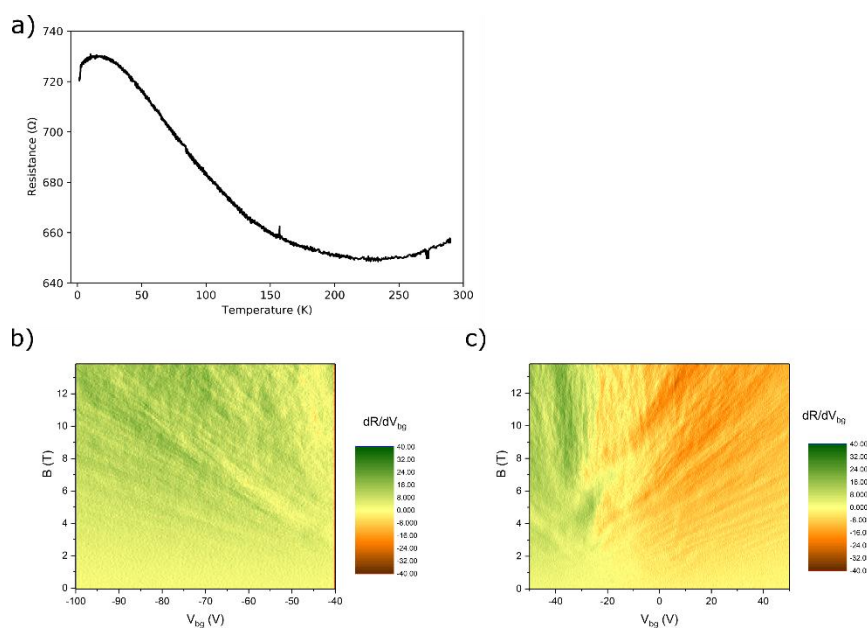


Figure 5-9 - Electrical transport measurements of cylindrite. (a) Resistance vs temperature sweep. (b) Magnetoresistance study, -100 to -40 V back gate sweep. (c) Magnetoresistance study, -50 to 50 V back gate sweep.

## Conclusion

In summary we successfully demonstrated the exfoliation of cylindrite (n,m=1) MLC to single unit cell thickness. As the final stacking sequence to be successfully exfoliated to the 2D limit, all MLCs may be considered as realistic candidates as 2D materials.

However, due to the poor quality of the source crystals, the exfoliation was poor and yielded highly faulted flakes. This hampered efforts for device fabrication and limited the ability to measure the expected in-plane anisotropy of the electronic properties.

We demonstrate the power of analytical cross sectional STEM for the characterisation of cylindrite and MLCs more generally. In particular it allowed for the observation of an occupational modulation along the transverse wave, and investigation of the curvature. We presented the first images of a kink band in cylindrite (or any MLC) which showed complex curvature. Both faceted segmentation and continuous curvature were observed for the same curvature radius.

## Methods

### Exfoliation and device fabrication

Natural cylindrite (Poopo, Bolivia) was exfoliated on to Si/SiO<sub>2</sub> (290 nm) substrates by mechanical exfoliation using the approach described in detail by Novoselov et.al.<sup>2</sup>

More force than is typical for exfoliation of other 2D materials was required to ensure good contact between the cylindrite crystal and the adhesive tape.

The heterostructure device was fabricated according to the method described by Frisenda et.al.<sup>5</sup> In brief, this consisted of using polydimethylsiloxane stamp transfer of mechanically exfoliated cylindrite, h-BN and graphene to create the heterostructure stack. Contacts were then added by electron beam lithography and sputtering of Ta/Pt (2/50 nm) contacts.

### **Transport measurements**

The samples were cooled in a VTI system dry refrigerator system helium atmosphere cryostat with a 14 T superconducting magnet. Magnetoresistance measurements were obtained by Low frequency AC lock-in technique (Stanford Research Systems SR830 DSP lock-in amplifier), 33.66 Hz and 300 ms integration time, 100 nA AC current (generated by a Stanford CS580 voltage controlled current source) with a -100 to 50 V back gate sweep and a 0 – 13.8 T magnetic field sweep.

### **STEM specimen preparation and imaging**

Plan view samples were prepared either by mechanical exfoliation of cylindrite on to a silicon wafer covered in a PMGI/PMMA bilayer, and subsequent dry transfer to a SiN TEM grid (prepared in house), or by crushing in agate pestle and mortar with liquid nitrogen and drop casted using minimal ethanol on to a copper Quantifoil TEM grid, depositing 10 mg of cylindrite material.

Cross section lamellae were prepared by focused ion beam. Cylindrite flakes were exfoliated on to a Si/SiO<sub>2</sub> substrate, and sputter coated with amorphous carbon and Au/Pd (60:40) protective layers *ex-situ*. The region of interest was then located and a 2  $\mu$ m thick protective Pt strap was deposited *in-situ*. Trenches were milled to shallow depths (4  $\mu$ m) and the lamella was milled free, then mounted on a copper half grid using an *in-situ* lift out method. The lamella was subsequently thinned using a series of progressively lower beam energies and currents until electron transparent.

STEM HAADF images were collected using a FEI Titan 80-200 X-FEG super twin fitted with a super-X EDX detector with a solid angle of  $\sim 0.8$  sr. Operated with a 200 keV acceleration potential, a 21 mrad convergence semi angle and a HAADF inner semi angle 54 mrad. High resolution HAADF images were collected with 90 pA beam current and EDX spectra collected with a 180 pA beam current. The specimens were aligned to the silicon Kikuchi pattern. HAADF images were filtered by average background

subtraction. The EDX spectra viewed down the [100] were processed by template matching. A repeated pattern in one HAADF image was chosen as the template image. This template image was cross correlated with 4 HAADF images acquired on different sample areas, which yielded four cross correlation coefficient value maps that the local intensity maxima corresponds to the centre of the best matched patterns. Subsequently each matched pattern was extracted and averaged. The pixel coordinates of extracted matched patterns on each HAADF original image have been recorded for the corresponding EDX map averaging due to the high signal-to-noise ratio nature of the HAADF image.

## **AFM**

A Bruker Dimeson Icon instrument, operating in PeakForce tapping mode with a frequency of 2 kHz, with a Scan Asyst-fluid plus tip, force constant  $0.7 \text{ Nm}^{-1}$ . The images were processed using WSxM<sup>45</sup> and Gwydeion. The 'Flatten plus'<sup>46</sup> algorithm was used to flatten the substrates, while background noise was removed with the application of median filtering and polynomial subtraction.

## **Raman spectroscopy**

Cylindrite samples were exfoliated on to a Si/SiO<sub>2</sub> substrate by mechanical exfoliation. Raman spectra were collected using a Horiba XploRA PLUS with a 532 nm laser excitation wavelength, operated with a power of 125  $\mu\text{W}$  and a 100x objective lens. The spectra were collected with a grating with 1200 grooves  $\text{mm}^{-1}$  with 60 second acquisitions and 20 accumulations. The effects of the silicon spectra were removed by normalisation of the Si 519  $\text{cm}^{-1}$  peak and subsequent subtraction of normalised Si spectra.

## **Optical microscopy**

A Nikon Eclipse LV100ND optical microscope and DS-Fi2 U3 CCD camera were used to image exfoliated cylindrite flakes in both bright and dark field modes.

## **Acknowledgments**

We would like to thank Dr Simon Howell for supplying the cylindrite source crystal, Adrian Ceferino for assistance in formalising the mathematical modelling of the exfoliated cylindrite flake widths and Dr Aidan Rooney for useful discussions.

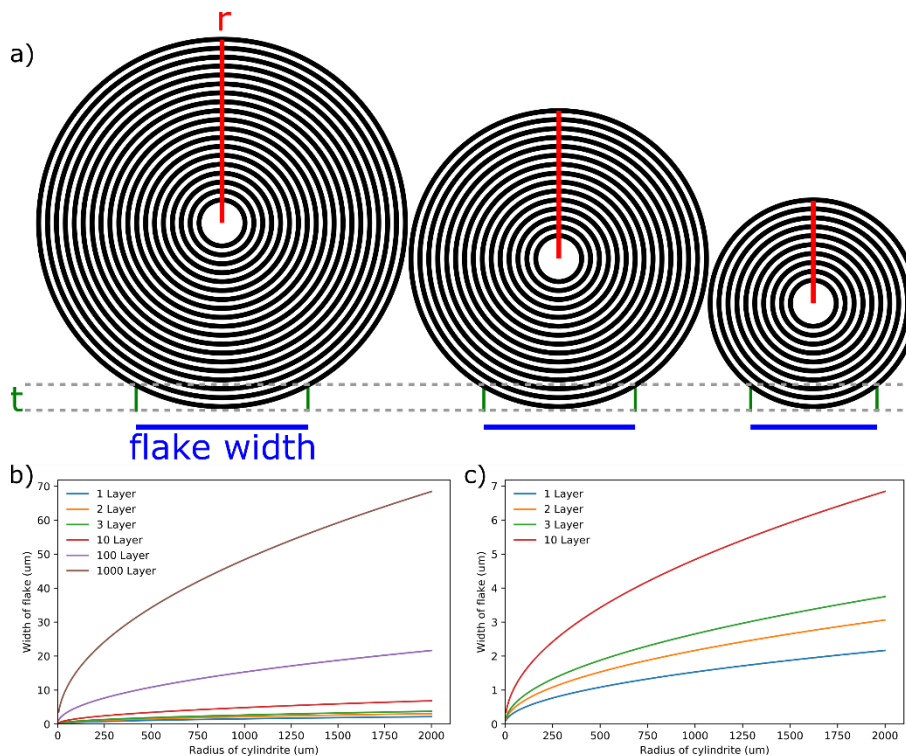


## 5.1. Supplementary information

### Effect of cylindrite's scrolled structure on exfoliation

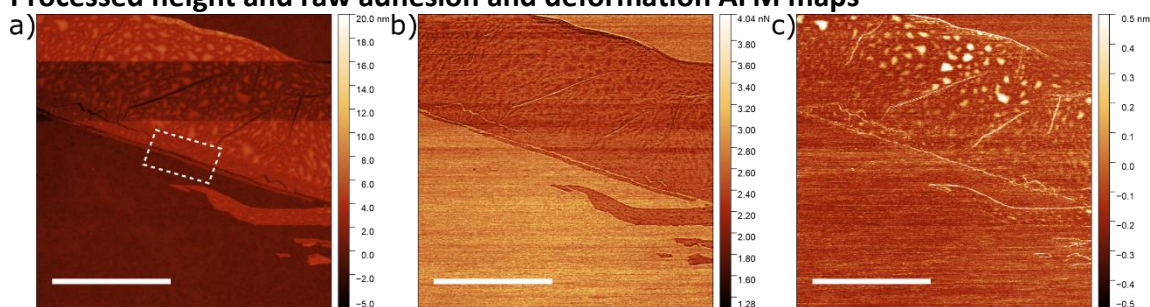
The effect of cylindrite's macroscopic crystal structure on exfoliation may be considered by the effective flatness of the cylindrite scroll. While a cylinder on a surface will touch at a single point, we can relax this criteria by allowing the surface of the cylinder to deviate from the plane by a distance. This yields an effective flat region, which is a function of the radius of the cylinder,  $r$ , and distance in which the cylinder may deviate from the surface,  $t$  (Equation 6-1). In the case of cylindrite,  $r$  corresponds to the physical radius of the cylindrite crystal, and  $t$  can be thought of number of single unit cells. The maximum widths of exfoliated flakes as function of cylindrite radius is plotted in SI Figure 5-10 for a number of different flake thickness. This model shows a reasonable agreement with the sizes of exfoliated flakes. However due to the production of high-aspect ratio flakes in franckeite<sup>22</sup>, we believe the incommensurate structure to be the primary reason.

$$\text{Flake width} \approx \text{Arc length} = \cos^{-1}\left(\frac{r}{t}\right)r \quad \text{SI 1}$$



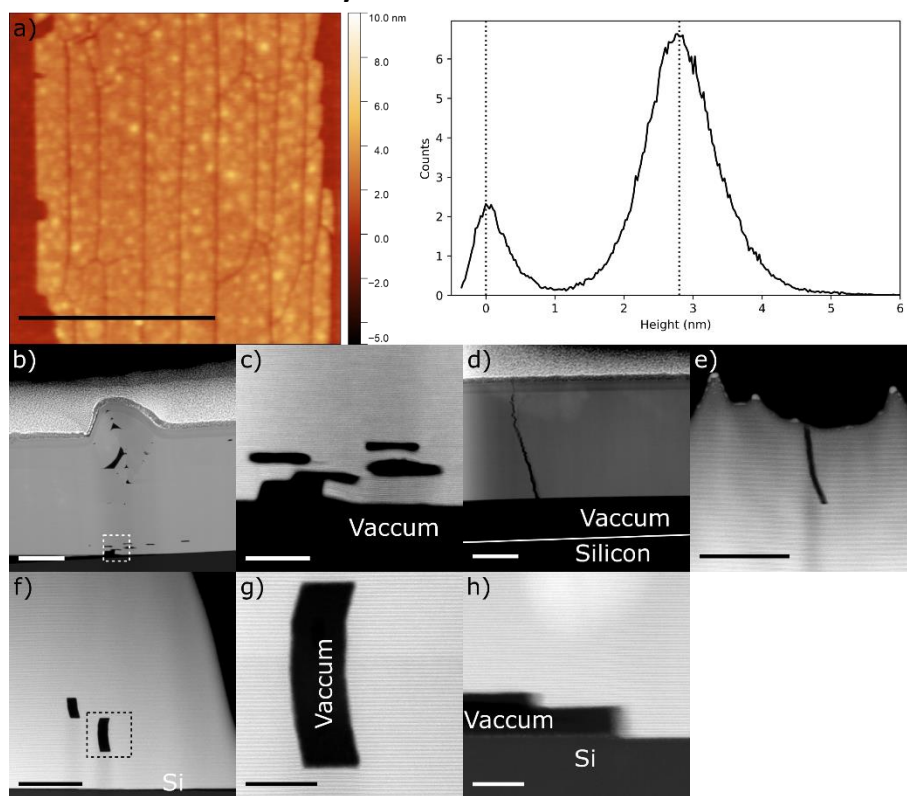
SI Figure 5-10 - Effects of the cylindrical shape of the cylindrite on its exfoliation. (a) An illustrative description of the exfoliation model. (b) Maximum exfoliated flake width as a function of cylindrite radius and number of exfoliated layers, 1-1000 layers (c) same as (b) but with 1- 10 layers

### Processed height and raw adhesion and deformation AFM maps



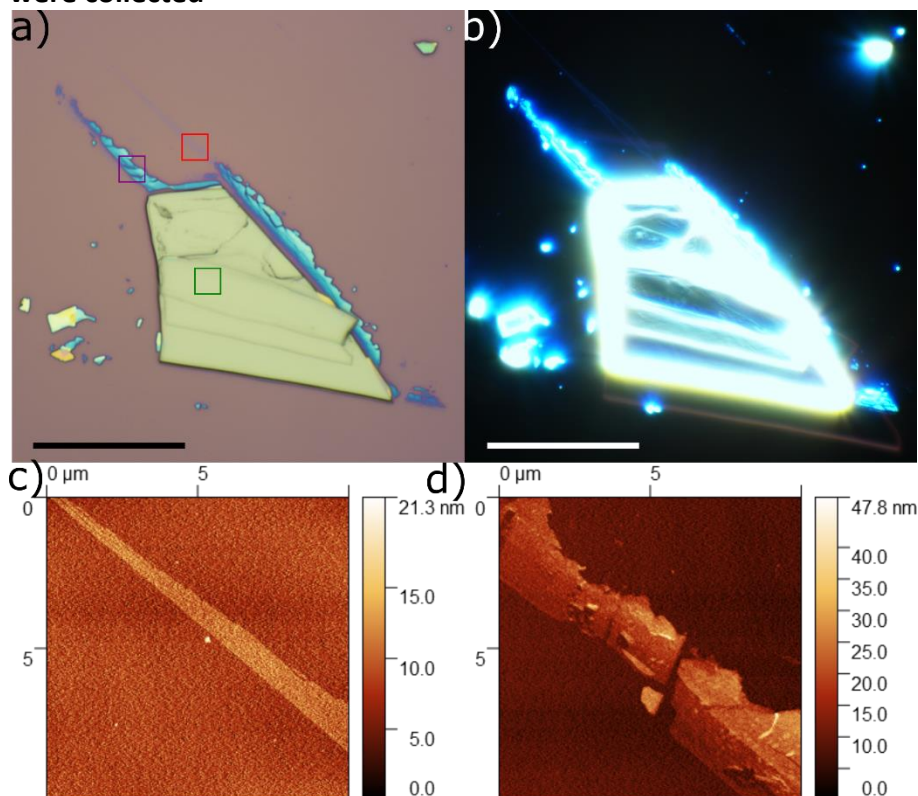
SI Figure 5-11 – Processed and raw Processed height and raw adhesion and deformation AFM maps of exfoliated cylindrite flake. (a) AFM height image after application of Flatten Plus algorithm, the white box corresponds to region where line profile and histogram shown in figure x. (b) Adhesion map of cylindrite flake, showing constant interaction across entirety of flake. (c) Deformation, showing cylindrite flake is of similar hardness to Si/SiO<sub>2</sub> substrate, and the presence of soft material on top of the flake, most likely hydrocarbon contamination. Scale bars correspond to 1 μm.

### Cracks in the exfoliated cylindrite flakes



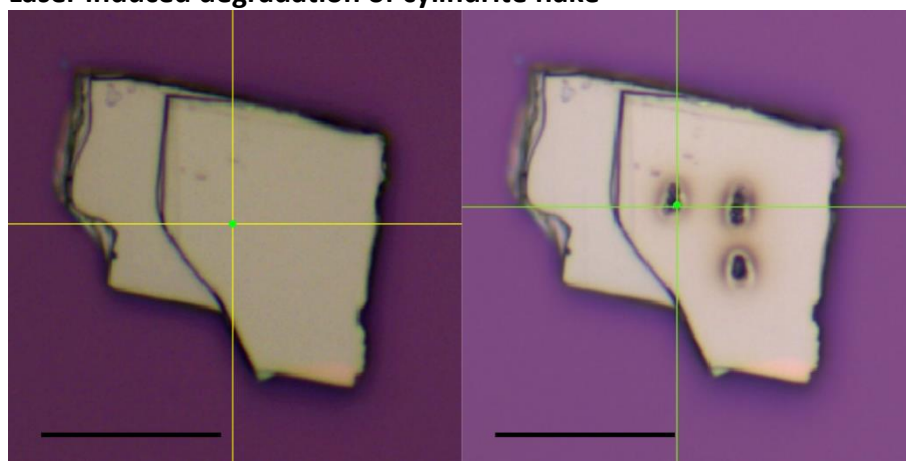
SI Figure 5-12 – AFM and HAADF STEM images of cracks and voids in exfoliated cylindrite flakes. (a) AFM height map and histogram of height distributions of a two unit cell thick (2.8 nm) cylindrite showing the presence of cracks estimated to be parallel to the [010] direction. It was not possible to ascertain whether they propagate through the entire height of the flake. (b)-(h) HAADF STEM images viewed along the [010] direction showing typical examples of defects seen in HAADF images. Scale bars (a) 1 μm, (b) 200 nm, (c) 50 nm, (d) 200 nm, (e) 100 nm, (f) 200 nm, (g) 20 nm and (h) 20 nm.

### Optical images and AFM height maps of the cylindrite flake from which Raman spectra were collected



SI Figure 5-13 – Optical images and AFM height map of cylindrite flake used in Raman spectroscopy characterisation. (a) Bright field and (b) dark field optical image of cylindrite flake on Si/SiO<sub>2</sub>, Red box corresponds to tri layer, purple corresponds to 6 -12 layers and green is bulk. Scale bars are 25 μm. (c) AFM height map of three unit cell thick cylindrite region corresponding to red box in (a), (d) AFM height map of 6-12 unit cell thick cylindrite region corresponding to purple box in (a).

### Laser induced degradation of cylindrite flake



SI Figure 5-14 - Demonstration of laser induced damage of exfoliated bulk cylindrite flake. (left) before, (right) after 2.15 mW 60 seconds per spot. Scale bars 20 μm.

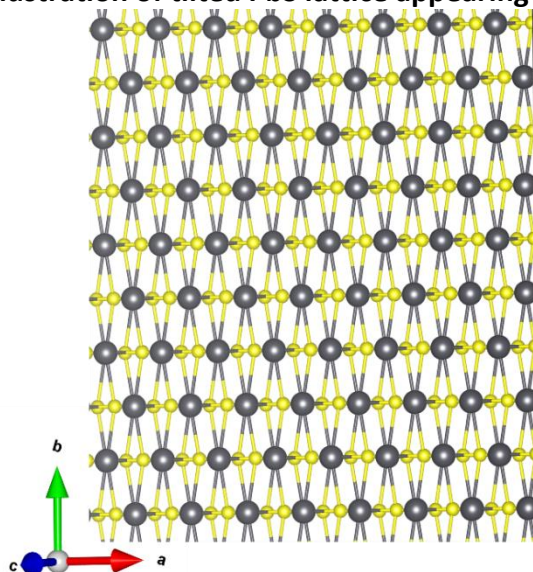
## EDXS quantification of cylindrite flakes

SI Table 5-2 – STEM EDX quantification of cylindrite flakes

Map	Element	Normalised Atomic %	Atomic % error (1 $\sigma$ )	Element	Normalised Atomic %	Atomic % error (1 $\sigma$ )
1	Tin	20.27	2.05	Lead	16.06	1.62
2	Tin	21.05	2.14	Lead	15.70	1.60
3	Tin	21.56	2.18	Lead	15.20	1.54
4	Tin	22.12	2.39	Lead	14.34	1.58
5	Tin	19.79	2.00	Lead	17.42	1.75
6	Tin	18.37	1.86	Lead	19.42	1.95
7	Tin	19.31	1.95	Lead	16.84	1.70
8	Tin	18.66	1.89	Lead	19.74	1.99
9	Tin	19.18	1.98	Lead	17.26	1.77
Average	Tin	20.03	2.05	Lead	16.89	1.72
Max	Tin	22.12	2.39	Lead	19.74	1.99
Min	Tin	18.37	1.86	Lead	14.34	1.54
Variation	Tin	3.74	0.53	Lead	5.39	0.45
Variation / 2	Tin	1.87	0.27	Lead	2.70	0.22
Map	Element	Normalised Atomic %	Atomic % error (1 $\sigma$ )	Element	Normalised Atomic %	Atomic % error (1 $\sigma$ )
1	Antimony	9.15	0.94	Iron	4.87	0.19
2	Antimony	8.79	0.92	Iron	4.81	0.23
3	Antimony	9.32	0.96	Iron	6.31	0.25
4	Antimony	12.19	1.39	Iron	4.52	0.42
5	Antimony	10.46	1.06	Iron	4.75	0.19
6	Antimony	10.02	1.02	Iron	5.00	0.19
7	Antimony	10.04	1.03	Iron	4.50	0.18
8	Antimony	10.10	1.03	Iron	5.06	0.19
9	Antimony	9.67	1.02	Iron	4.37	0.26
Average	Antimony	9.97	1.04	Iron	4.91	0.23
Max	Antimony	12.19	1.39	Iron	6.31	0.42
Min	Antimony	8.79	0.92	Iron	4.37	0.18
Variation	Antimony	3.39	0.48	Iron	1.94	0.24
Variation / 2	Antimony	1.70	0.24	Iron	0.97	0.12
Map	Element	Normalised Atomic %	Atomic % error (1 $\sigma$ )			
1	Sulphur	49.65	1.57			
2	Sulphur	49.66	1.62			
3	Sulphur	47.61	1.53			
4	Sulphur	46.83	1.99			
5	Sulphur	47.59	1.50			
6	Sulphur	47.19	1.49			
7	Sulphur	49.32	1.56			
8	Sulphur	46.44	1.47			
9	Sulphur	49.52	1.70			
Average	Sulphur	48.20	1.60			
Max	Sulphur	49.66	1.99			
Min	Sulphur	46.44	1.47			
Variation	Sulphur	3.22	0.52			
Variation / 2	Sulphur	1.61	0.26			

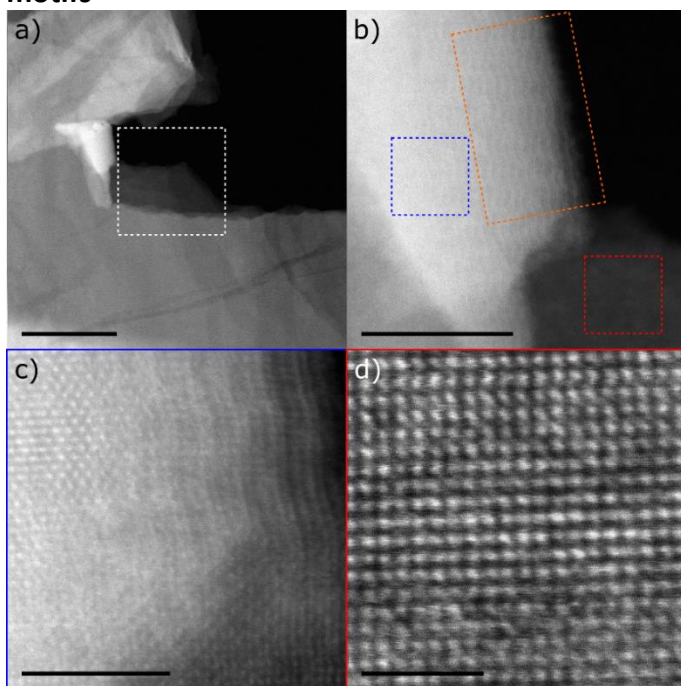


### Illustration of tilted PbS lattice appearing hexagonal



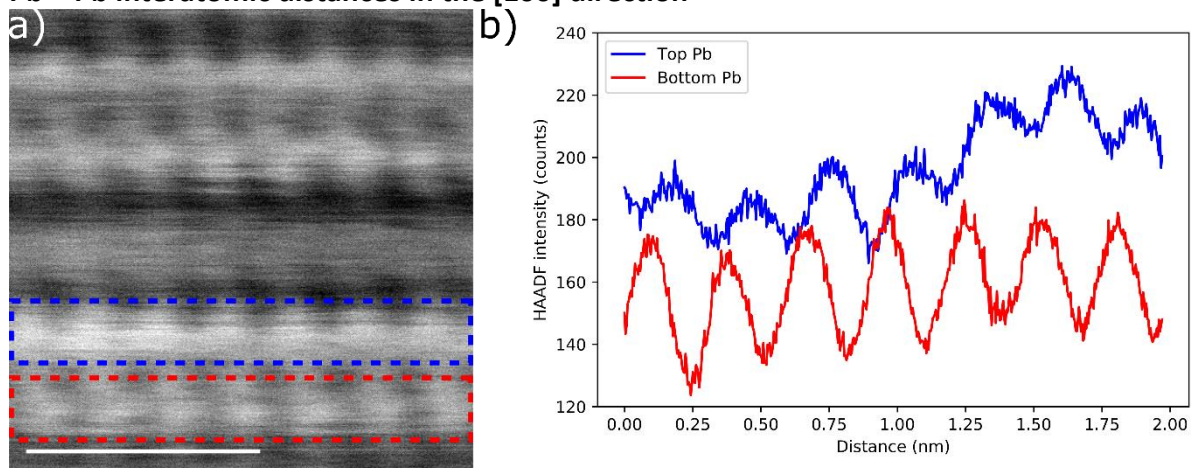
SI Figure 5-15 - Atomic model of the pseudo tetragonal (T) PbS layer tilted off the [001] axis resulting in the appearance of a hexagonal lattice.

### Plan view HAADF STEM images of cylindrite flake showing cubic and hexagonal lattice motifs



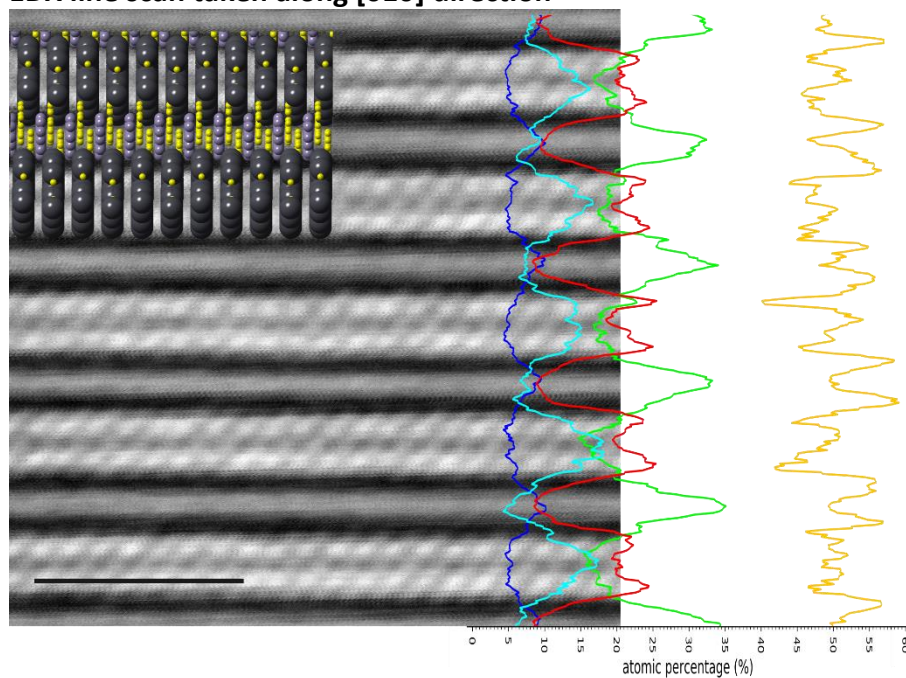
SI Figure 5-16 - HAADF STEM images of an exfoliated cylindrite flake viewed along the [001] direction which contains cubic and hexagonal motifs. (a) Low magnification STEM image of cylindrite flake. (b) Region corresponding to dashed white box in (a), which contains areas with hexagonal and cubic motifs, and a scroll in the flake in close proximity highlighted by blue, red and orange dashed boxes. (c) higher magnification image of (b). (d) Atomic resolution image corresponding to blue box in (b), showing the hexagonal lattice in close proximity to the fold in the flake. (d) Atomic resolution image corresponding to red box in (b), showing the cubic lattice. Scale bars (a) 100 nm, (b) 20 nm, (c) 5 nm and (d) 2 nm.

### Pb – Pb interatomic distances in the [100] direction



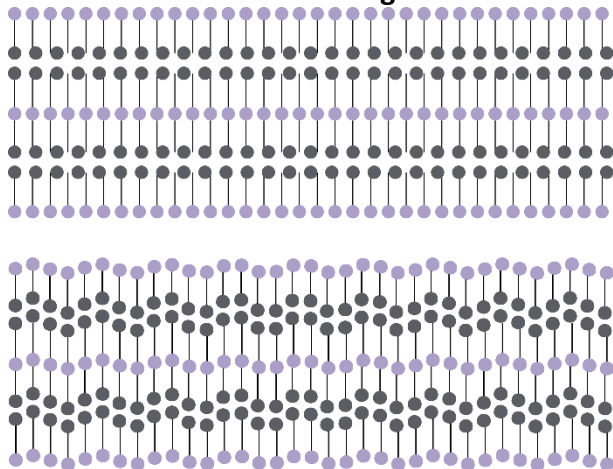
SI Figure 5-17 – Investigation of Pb-Pb interatomic distances for cylindrite flake with low curvature. (a) HAADF STEM image viewed along the [010] direction; scale bar corresponds to 1 nm. (b) Corresponding line profiles of HAADF intensity for top and bottom Pb rows. The Pb-Pb interatomic distance are approximately the same, with values of 0.293 and 0.286 nm for the upper and lower Pb rows respectively.

### EDX line scan taken along [010] direction



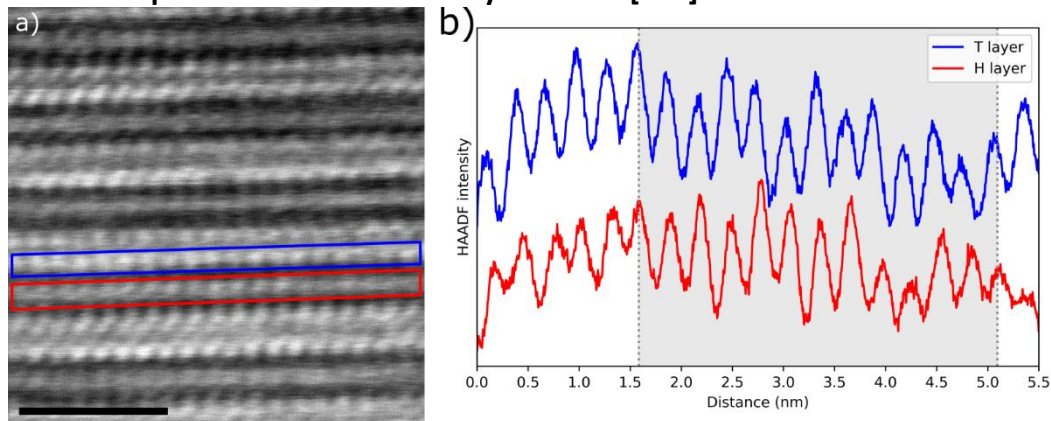
SI Figure 5-18 – EDX line scan taken along [010] direction. Filtered HAADF STEM image take from the [010] projection, with atomic model, and EDXS intensity profile overlaid. Yellow, green, red, light blue and dark blue correspond to sulphur, tin, lead, antimony and iron signals. Scale bar 2 nm.

### Transverse modulation along semi commensurate [010] direction



SI Figure 5-19 – Illustration of Transverse modulation along semi commensurate [010] direction. Atomic model viewed in the [100] direction (top) without and (bottom) with transverse modulation. Illustrating how the transverse modulation allows the semi-incommensurate layers to become commensurate along the [010] direction. The purple and grey spheres correspond to the atomic positions of the Sn cations in the H layer, and Pb cations in the T layers respectively. Not to scale.

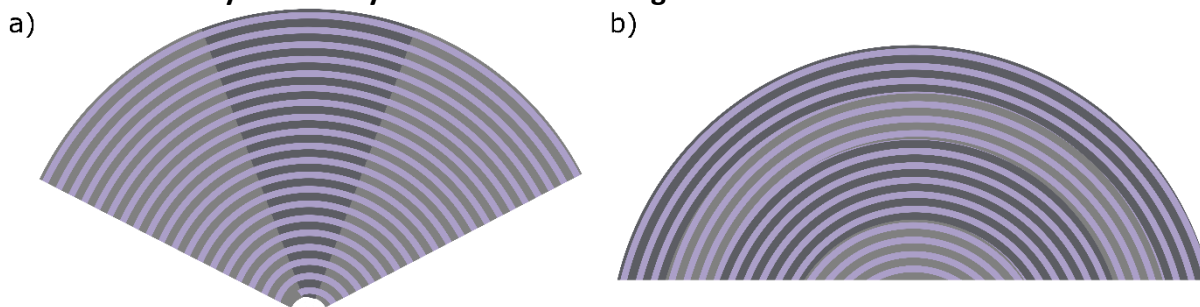
### HAADF STEM image viewed along the [010] direction showing an incommensurate relationship between the T and H layers in the [100] direction



SI Figure 5-20 - Incommensurate relationship along the [100] direction of exfoliated cylindrite flake. (a) HAADF STEM IMAGE viewed along the [010] direction, scale bar 2 nm, (b) line profiles corresponding to the T and H layers indicated in (a). The layers become approximately aligned with a period of 3.5 nm (highlighted by grey area).

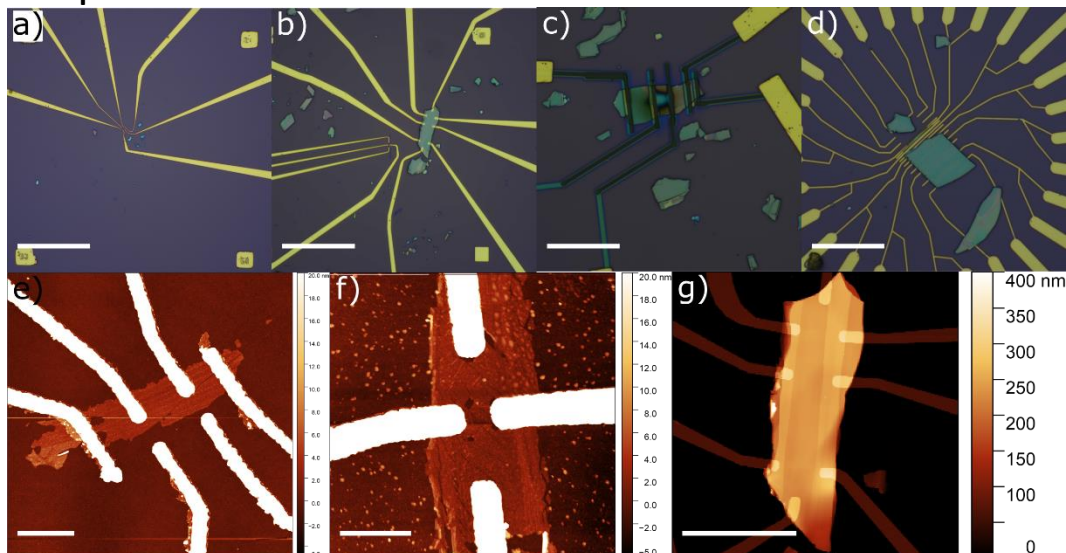


### Illustrations of cylindrite crystal tilts in curved regions



SI Figure 5-21 - Illustrative examples of crystal tilts observed in cylindrite crystals. (a) vertical segmentation as previously reported in references<sup>10,14</sup>, due to differences in crystal tilt. (b) Continuous circumferential segmentation seen in this work, likely a result of different crystal orientations or compositional variation. The different shades are reflective to HAADF intensities. Not to scale.

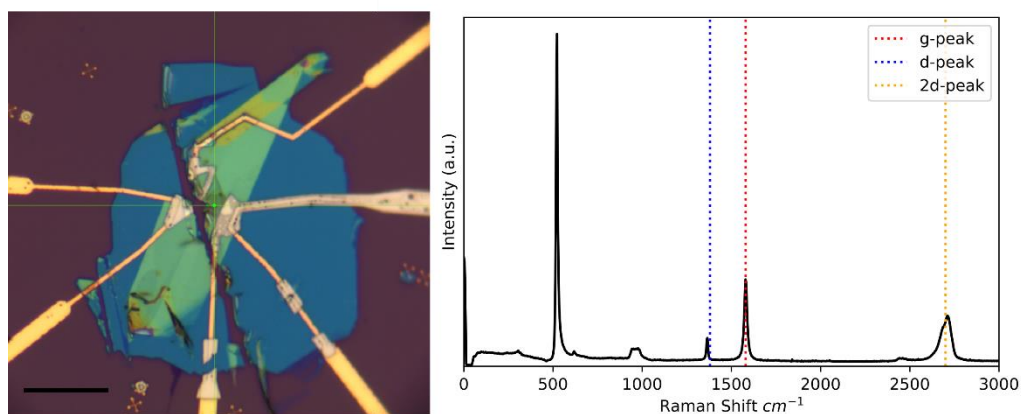
### Examples of failed electrical devices



SI Figure 5-22 - Optical and AFM images of failed cylindrite devices. (a)-(d) BF optical images. (a),(b) Au/Pd contacts deposited on top of flakes using electron beam lithography. (c) Pt contacts deposited by FIB, and extended out by photolithography. Note the flake appears to have been damaged during the Pt deposition. (d) Cylindrite flakes deposited on top of pre-deposited Au/Pd contacts. (e) AFM height image of device shown in (a). (f),(g) AFM height image of devices in (b). (e) and (f) show thin flakes, which are highly defective, which is likely the reason for device failure. (g) The height of the flake (~400 nm) made contacting the flake difficult, due to shadowing during the Au/Pd deposition. Scale bars (a)-(d) 15  $\mu\text{m}$ , (e), (f) 1  $\mu\text{m}$  and (g) 10  $\mu\text{m}$ .



## Raman spectrum of devices used in electronic measurement studies



SI Figure 5-23 - Optical image of electrical transport device and corresponding Raman spectrum showing the presence of graphene contacts. Scale bar is  $20\ \mu\text{m}$ .

## References

- 1 Yi, M. & Shen, Z. A review on mechanical exfoliation for the scalable production of graphene. *Journal of Materials Chemistry A* **3**, 11700-11715 (2015).
- 2 Novoselov, K. S., Geim, A. K., Morozov, S. V., Jiang, D., Zhang, Y., Dubonos, S. V., Grigorieva, I. V. & Firsov, A. A. Electric Field Effect in Atomically Thin Carbon Films. *Science* **306**, 666-669 (2004).
- 3 Xu, M., Liang, T., Shi, M. & Chen, H. Graphene-like two-dimensional materials. *Chem Rev* **113**, 3766-3798 (2013).
- 4 Geim, A. K. & Grigorieva, I. V. Van der Waals heterostructures. *Nature* **499**, 419-425 (2013).
- 5 Frisenda, R., Navarro-Moratalla, E., Gant, P., Pérez De Lara, D., Jarillo-Herrero, P., Gorbachev, R. V. & Castellanos-Gomez, A. Recent progress in the assembly of nanodevices and van der Waals heterostructures by deterministic placement of 2D materials. *Chemical Society reviews* **47**, 53-68 (2018).
- 6 Novoselov, K. S., Mishchenko, A., Carvalho, A. & Castro Neto, A. H. 2D materials and van der Waals heterostructures. *Science* **353** (2016).
- 7 Moore, D. B., Beekman, M., Disch, S. & Johnson, D. C. Telluride Misfit Layer Compounds:  $[(\text{PbTe})_{1.17}]_m(\text{TiTe}_2)_n$ . *Angewandte Chemie International Edition* **53**, 5672-5675 (2014).
- 8 Lin, Q., Heideman, C. L., Nguyen, N., Zschack, P., Chiritescu, C., Cahill, D. G. & Johnson, D. C. Designed Synthesis of Families of Misfit-Layered Compounds. *European Journal of Inorganic Chemistry* **2008**, 2382-2385 (2008).
- 9 Heideman, C., Nyugen, N., Hanni, J., Lin, Q., Duncombe, S., Johnson, D. C. & Zschack, P. The synthesis and characterization of new  $[(\text{BiSe})_{1.10}]_m[\text{NbSe}_2]_n$ ,  $[(\text{PbSe})_{1.10}]_m[\text{NbSe}_2]_n$ ,  $[(\text{CeSe})_{1.14}]_m[\text{NbSe}_2]_n$  and  $[(\text{PbSe})_{1.12}]_m[\text{TaSe}_2]_n$  misfit layered compounds. *Journal of Solid State Chemistry* **181**, 1701-1706 (2008).
- 10 Kaden, R., Wagner, G., Sturm, C., Schmidt-Grund, R., von Wenckstern, H., Prager, A., Bente, K. & Grundmann, M. Synthesis and physical properties of cylindrite micro tubes and lamellae. *physica status solidi (b)* **247**, 1335-1350 (2010).
- 11 Sachdev, S. C. & Chang, L. L. Y. Phase relations in the system tin-antimony-lead sulfides and the synthesis of cylindrite and franckeite. *Economic Geology* **70**, 1111-1122 (1975).
- 12 Lourdes, H., Julián, M., Jayasree, P. & L., T. J. Preparation and Characterization of New Misfit Layer Selenides  $\text{SnVSe}_3$  and  $\text{SnNb}_2\text{Se}_5$ . *Chemistry Letters* **20**, 1981-1984 (1991).
- 13 Rouxel, J., Meerschaut, A. & Wiegiers, G. A. Chalcogenide misfit layer compounds. *Journal of Alloys and Compounds* **229**, 144-157 (1995).
- 14 Su, W. & Buseck, P. R. Cylindrite: the relation between its cylindrical shape and modulated structure. *American Mineralogist* **77**, 758-764 (1992).
- 15 Wang, S. & Kuo, K. H. Crystal lattices and crystal chemistry of cylindrite and franckeite. *Acta Crystallographica Section A* **47**, 381-392 (1991).
- 16 Janner, A. & Janssen, T. Symmetry of incommensurate crystal phases. II. Incommensurate basic structure. *Acta Crystallographica Section A* **36**, 408-415 (1980).
- 17 Meerschaut, A., Moëlo, Y., Cario, L., Lafond, A. & Deudon, C. Charge Transfer in Misfit Layer Chalcogenides,  $[(\text{MX})_n]_{1+x}(\text{TX}_2)_m$ : a Key for Understanding their Stability and Properties. *Molecular Crystals and Liquid Crystals Science and Technology. Section A. Molecular Crystals and Liquid Crystals* **341**, 1-8 (2000).

- 18 Meerschaut, A. Misfit layer compounds. *Current Opinion in Solid State and Materials Science* **1**, 250-259 (1996).
- 19 Song, Y. J., Kim, M. J., Jung, W. G., Kim, B.-J. & Rhyee, J.-S. Superconducting properties of the misfit-layer compound  $(\text{SnSe})_{1.18}(\text{TiSe}_2)_2$ . *physica status solidi (b)* **253**, 1517-1522 (2016).
- 20 Wiegiers, G. A. Misfit layer compounds: Structures and physical properties. *Progress in Solid State Chemistry* **24**, 1-139 (1996).
- 21 Bonneau, P., Mansot, J. L. & Rouxel, J. Intercalation and exfoliation of misfit-layer compounds  $[\text{MNb}_2\text{S}_5 \text{ (M = Pb, Sm)}]$ . *Materials Research Bulletin* **28**, 757-766 (1993).
- 22 Velický, M., Toth, P. S., Rakowski, A. M., Rooney, A. P., Kozikov, A., Woods, C. R., Mishchenko, A., Fumagalli, L., Yin, J., Zólyomi, V., Georgiou, T., Haigh, S. J., Novoselov, K. S. & Dryfe, R. A. W. Exfoliation of natural van der Waals heterostructures to a single unit cell thickness. *Nature communications* **8**, 14410 (2017).
- 23 Molina-Mendoza, A. J., Giovanelli, E., Paz, W. S., Nino, M. A., Island, J. O., Evangeli, C., Aballe, L., Foerster, M., van der Zant, H. S., Rubio-Bollinger, G., Agrait, N., Palacios, J. J., Perez, E. M. & Castellanos-Gomez, A. Franckeite as a naturally occurring van der Waals heterostructure. *Nature communications* **8**, 14409 (2017).
- 24 Williams, T. B. & Hyde, B. G. Electron microscopy of cylindrite and franckeite. *Physics and Chemistry of Minerals* **15**, 521-544 (1988).
- 25 Smith, G. D., Firth, S., Clark, R. J. H. & Cardona, M. First- and second-order Raman spectra of galena (PbS). *Journal of Applied Physics* **92**, 4375-4380 (2002).
- 26 Chandrasekhar, H. R., Humphreys, R. G., Zwick, U. & Cardona, M. Infrared and Raman spectra of the IV-VI compounds SnS and SnSe. *Physical Review B* **15**, 2177-2183 (1977).
- 27 Brent, J. R., Lewis, D. J., Lorenz, T., Lewis, E. A., Savjani, N., Haigh, S. J., Seifert, G., Derby, B. & O'Brien, P. Tin(II) Sulfide (SnS) Nanosheets by Liquid-Phase Exfoliation of Herzenbergite: IV–VI Main Group Two-Dimensional Atomic Crystals. *Journal of the American Chemical Society* **137**, 12689-12696 (2015).
- 28 Mead, D. G. & Irwin, J. C. Raman spectra of SnS<sub>2</sub> and SnSe<sub>2</sub>. *Solid State Communications* **20**, 885-887 (1976).
- 29 Parize, R., Cossuet, T., Chaix-Pluchery, O., Roussel, H., Appert, E. & Consonni, V. In situ analysis of the crystallization process of Sb<sub>2</sub>S<sub>3</sub> thin films by Raman scattering and X-ray diffraction. *Materials & Design* **121**, 1-10 (2017).
- 30 Vogt, H., Chattopadhyay, T. & Stolz, H. J. Complete first-order Raman spectra of the pyrite structure compounds FeS<sub>2</sub>, MnS<sub>2</sub> AND SiP<sub>2</sub>. *Journal of Physics and Chemistry of Solids* **44**, 869-873 (1983).
- 31 Yong, X. & Schoonen, M. A. A. The absolute energy positions of conduction and valence bands of selected semiconducting minerals. *American Mineralogist* **85**, 543-556 (2000).
- 32 Boldish Steven, I. & White William, B. in *American Mineralogist* Vol. 83 865 (1998).
- 33 Schmid, G. & Corain, B. Nanoparticulated Gold: Syntheses, Structures, Electronics, and Reactivities. *European Journal of Inorganic Chemistry* **2003**, 3081-3098 (2003).
- 34 Lin, Q., Smeller, M., Heideman, C. L., Zschack, P., Koyano, M., Anderson, M. D., Kykyneshi, R., Keszler, D. A., Anderson, I. M. & Johnson, D. C. Rational Synthesis

- and Characterization of a New Family of Low Thermal Conductivity Misfit Layer Compounds  $[(\text{PbSe})_{0.99}]_m(\text{WSe}_2)_n$ . *Chemistry of Materials* **22**, 1002-1009 (2010).
- 35 Atkins, R., Wilson, J., Zschack, P., Grosse, C., Neumann, W. & Johnson, D. C. Synthesis of  $[(\text{SnSe})_{1.15}]_m(\text{TaSe}_2)_n$  Ferecrystals: Structurally Tunable Metallic Compounds. *Chemistry of Materials* **24**, 4594-4599 (2012).
- 36 Brandt, J., Kipp, L., Skibowski, M., Krasovskii, E. E., Schattke, W., Spiecker, E., Dieker, C. & Jäger, W. Charge transfer in misfit layered compounds. *Surface Science* **532-535**, 705-710 (2003).
- 37 Wiegers, G. A., Meetsma, A., van Smaalen, S., Haange, R. J., Wulff, J., Zeinstra, T., de Boer, J. L., Kuypers, S., Van Tendeloo, G., Van Landuyt, J., Amelinckx, S., Meerschaut, A., Rabu, P. & Rouxel, J. Misfit layer compounds  $(\text{MS})_n\text{TS}_2$  (M = Sn, Pb, Bi, rare earth elements; T = Nb, Ta ;  $n = 1.08 - 1.19$ ), a new class of layer compounds. *Solid State Communications* **70**, 409-413 (1989).
- 38 MacArthur, K. E., Brown, H. G., Findlay, S. D. & Allen, L. J. Probing the effect of electron channelling on atomic resolution energy dispersive X-ray quantification. *Ultramicroscopy* **182**, 264-275 (2017).
- 39 Rooney, A. P., Li, Z., Zhao, W., Gholinia, A., Kozikov, A., Auton, G., Ding, F., Gorbachev, R. V., Young, R. J. & Haigh, S. J. Anomalous twin boundaries in two dimensional materials. *Nature communications* **9**, 3597 (2018).
- 40 Tang, D.-M., Kvashnin, D. G., Najmaei, S., Bando, Y., Kimoto, K., Koskinen, P., Ajayan, P. M., Yakobson, B. I., Sorokin, P. B., Lou, J. & Golberg, D. Nanomechanical cleavage of molybdenum disulphide atomic layers. *Nature communications* **5**, 3631 (2014).
- 41 Heideman, C. L., Rostek, R., Anderson, M. D., Herzing, A. A., Anderson, I. M. & Johnson, D. C. Synthesis and Electronic Properties of the Misfit Layer Compound  $[(\text{PbSe})_{1.00}]_1[\text{MoSe}_2]_1$ . *Journal of Electronic Materials* **39**, 1476-1481 (2010).
- 42 Smeller, M. M., Heideman, C. L., Lin, Q., Beekman, M., Anderson, M. D., Zschack, P., Anderson, I. M. & Johnson, D. C. Structure of Turbostratically Disordered Misfit Layer Compounds  $[(\text{PbSe})_{0.99}]_1[\text{WSe}_2]_1$ ,  $[(\text{PbSe})_{1.00}]_1[\text{MoSe}_2]_1$ , and  $[(\text{SnSe})_{1.03}]_1[\text{MoSe}_2]_1$ . *Zeitschrift für anorganische und allgemeine Chemie* **638**, 2632-2639 (2012).
- 43 Ruscher, C. H., Haas, C., Smaalen, S. v. & Wiegers, G. A. Investigation of the optical reflectivity of misfit layer compounds:  $(\text{MS})_n\text{TS}_2$  (T=Ta, Nb; M=Sn, Pb, Sm, Tb, La;  $1.08 < n < 1.23$ ). *Journal of Physics: Condensed Matter* **6**, 2117 (1994).
- 44 Suzuki, K., Kondo, T., Enoki, T. & Bandow, S. Conduction mechanism and two-dimensional magnetism in incommensurate layered compounds  $(\text{RE})_x\text{MS}_2$  (RE=rare earth metal, M=Ta,V). *Synthetic Metals* **56**, 1741-1746 (1993).
- 45 Horcas, I., Fernández, R., Gómez-Rodríguez, J. M., Colchero, J., Gómez-Herrero, J. & Baro, A. M. WSXM: A software for scanning probe microscopy and a tool for nanotechnology. *Review of Scientific Instruments* **78**, 013705 (2007).
- 46 Gimeno, A., Ares, P., Horcas, I., Gil, A., Gómez-Rodríguez, J. M., Colchero, J. & Gómez-Herrero, J. 'Flatten plus': a recent implementation in WSxM for biological research. *Bioinformatics* **31**, 2918-2920 (2015).

## 6. Paper 3 – *In-situ* thickness determination of TEM lamellae prepared by focused ion beam

This chapter demonstrates two methods for the accurate *in-situ* measurement of TEM lamellae produced by FIB *in-situ*, overcoming the current shortcomings highlighted in section 2.1.2.4. The motivation for the project was to address the challenges in specimen preparation discussed in chapter 5 and those faced in the preparation of other samples, notably atomically thin suspended 2D crystals, during this PhD research project.

The first method describes an accurate calibration of a FIB-SEM instrument, by the production of a FIB lamellae and subsequent STEM EELS thickness measurement. The alignment of the SEM images and EELS thickness map required EELS thickness maps to be carefully aligned using cross-correlation and warp alignments within open source python packages. Within this section, we demonstrate that although both the ion conversion and electron (ICE) and the through lens detector (TLD) are able to estimate the thickness of the TEM lamellae, the ICE is more accurate for lamellae thicknesses in the range of 20-25 and 40-80 nm. Furthermore, we demonstrate that by exploiting the geometry of the detectors and the electrons detected, through considering the ratio of the ICE:TLD intensities, a more accurate and robust lamellae estimation may be achieved. The second method is an *a priori* method, requiring no prior calibration, and is suitable for all instruments with ICE and TLD detectors. Through novel and accurate Monte Carlo modelling the detector responses of the TLD and ICE for any material may be calculated. We subsequently propose a new workflow for thinning TEM lamellae which is well suited to automation.

### Contributions to work:

Dr. Aidan Rooney prepared the TEM lamellae, collected the EELS thickness map, aligned the EELS and SEM experimental data sets and extracted the TLD and ICE thickness vs signal intensity plots; Prof Sarah Haigh, Dr Aidan Rooney and I co-wrote the manuscript; Evan Tillotson and Jack Donoghue contributed to discussions on Monte Carlo modelling and SEM image formation respectively; Adrian Ceferino assisted with the formalisation of the mathematical framework for handling the calculations of errors.

# ***In-situ* thickness determination of TEM lamellae prepared by focused ion beam**

Alexander M Rakowski<sup>1,2</sup>, Aidan P Rooney<sup>1,3\*</sup>, Evan Tillotson<sup>1</sup> and Sarah J Haigh<sup>1,2\*</sup>

1 – School of Materials, University of Manchester, UK, M13 9PL

2 – National Graphene Institute, University of Manchester, UK, M13 9PL

3 – Department of Applied Physics, Aalto University, FI-00076 Aalto, Finland

\* Corresponding authors: sarah.haigh@manchester.ac.uk; aidan.rooney@aalto.fi

## **Keywords**

FIB, SEM, TEM lamellae preparation, Sample thickness, *In-situ* thickness measurement, Monte Carlo simulations

## **Abstract**

Focused ion beam (FIB) is routinely used to prepare thin lamellae of solid specimens in cross section for scanning/transmission electron microscopy (S/TEM) analysis. Despite recent advances in cross section specimen preparation, the quality of FIB lamellae, and the subsequent success of the procedure is ultimately dependent on the skill of the operator. Currently, the difficulty of accurately measuring sample thickness inside the FIB limits the preparation of high quality and damage free lamellae specimens for high resolution imaging. We demonstrate two methods to make a quantitative measurement of lamella thickness using the complementary scanning electron microscope (SEM) column, and associated detectors in a dual-beam instrument. First, we show this is possible by accurately calibrating greyscale values in SEM images for a lamella with a known thickness distribution. We demonstrate that the accuracy of the thickness determination may be improved by combining two detectors typically available on modern FIB systems. Secondly, we show that by accurately modelling the detectors, lamellae thickness can be determined *a priori*. This technique can be applied in any instrument, and to any thinned material. Finally, we propose a new workflow for the preparation of high quality lamellae, based on this improved thickness method and modelling. The workflow may be applied to any material, requires minimal previous experimental experience and is suitable for automation.

## Introduction

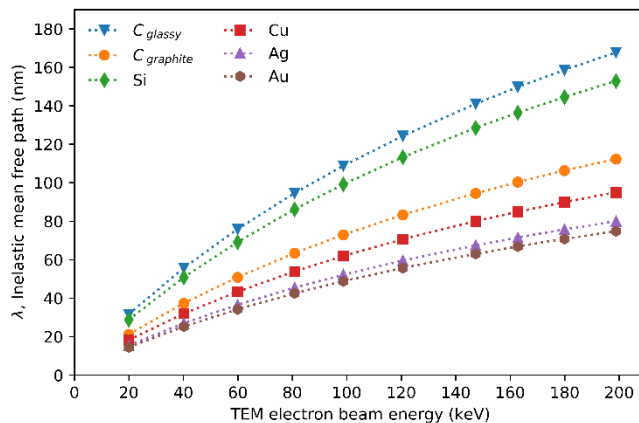


Figure 6-1–Calculated inelastic mean free path for an incident electron traversing a solid for a range of common materials and beam energies.<sup>1</sup> For high resolution TEM imaging, a lamella thickness in the range of 20 – 80 nm is usually required but is dependent on the density of the material and beam energy.

Despite producing cross section scanning/transmission electron microscope (S/TEM) lamellae for many different materials routinely for over 20 years<sup>2</sup>; determination of the final thickness of the lamella in the FIB-SEM is still largely a subjective judgement made by the microscope user, often based on the contrast enhancement in the secondary electron (SE) image. While some attempts have been made to quantify lamellae thickness *in-situ*, they are typically a combination of insufficiently accurate, prohibitively slow or requiring of additional equipment.

The S/TEM is a powerful tool for characterising the atomic structure of a wide range of materials.<sup>3</sup> Advances in instrumentation, including aberration correction and monochromators, have made 0.05 nm resolution readily achievable for sufficiently thin and clean specimens.<sup>4</sup> However in practice, both the imaging and spectroscopic capabilities of advanced S/TEMs are limited by microscopists' ability to produce specimens which are sufficiently thin, with minimal damage. Determining the thickness of a specimen before the S/TEM experiment ensures that the sample is the correct thickness for optimal imaging conditions. Furthermore it allows for accurate image simulations prior to imaging, aiding interpretation and allowing for improved data collection.

Most thickness measurements in the TEM rely on convergent-beam electron diffraction (CBED) or electron energy loss spectroscopy (EELS). CBED requires accurate

sample alignment and precise matching of the experimental data with simulations. It also generally requires a relatively thick homogeneous single crystal (50–500 nm).<sup>5</sup> In contrast, the EELS acquisition and thickness analysis method is quicker and easier. Additionally it does not require a crystalline specimen and is accurate over a large range of thicknesses<sup>6</sup> (15–500 nm). EELS measurements provide an estimate of the local  $t/\lambda$  ratio for the specimen, where  $t$  is sample thickness and  $\lambda$  is the inelastic mean free path (MFP), which describes the mean distance between inelastic collisions for the electron. The MFP of a specimen depends on its composition and density and thus, thickness constraints are particularly stringent for low kV S/TEM<sup>1</sup>(Figure 6-1). For atomic resolution TEM imaging and corresponding simulations, the weak phase object criterion requires no more than a single scattering event<sup>7</sup>. As such the specimen thickness needs to be much less than the elastic MFP (Si, 108 and 45 nm for 200 keV and 60 keV electron beam energies)<sup>8,9</sup>, while EELS requires  $t/\lambda < 1$ , and high quality EELS is best performed where  $t/\lambda < 0.2$ . Conversely, thicker samples offer more efficient collection of energy dispersive X-ray spectroscopy (EDXS), and are required for some diffraction based S/TEM techniques. Cross section specimens may be required to be as thin as 10 nm, or as thick as 100 nm<sup>10</sup>, but more typically between 20 and 80 nm<sup>11,12</sup>.

There are numerous specimen preparation methods to produce samples that are suitably thin for S/TEM imaging, including dimple grinding, wedge polishing, crushing, broad ion beam polishing, electropolishing and ultramicrotomy.<sup>13</sup> These mechanical or electrochemical polishing techniques typically rely on optical imaging or spectroscopy to monitor the specimen during thinning, and targeting a specimen's region of interest is extremely challenging (site specificity is typically  $\sim 1$  mm). In contrast, the focused ion beam (FIB) provides an essential tool for the site specific preparation of S/TEM specimen by ion bombardment and specimen sputtering.<sup>14</sup> The FIB is typically combined with a scanning electron microscope (SEM) in a single column and is an unrivalled tool for sculpting materials at the nano and micron scales using either gallium ions or, more recently, millimetre length scales using a Xe ion plasma FIB.<sup>15</sup> Integration of micromanipulator tools and sputtering deposition systems into the same chamber provide the FIB-SEM with the additional ability to locally deposit material and manipulate extracted material. There is a limitation on the minimum achievable thickness of a lamella, imposed by localised amorphisation of the lamella material and



implantation of gallium during ion thinning.<sup>16</sup> To reduce implantation and amorphisation it is vital to avoid exposing the specimen to unnecessary ion beam exposure and to change the beam energy and current as the sample is progressively thinned.

*In-situ* thickness measurements have been demonstrated using BSE images.<sup>17,18</sup> While offering thickness measurements at scanning rates, these methods are inaccurate and sensitive to detector geometry. Golla-Schindler<sup>19</sup> incorporated a specialised “STEM-UNIT” detector, allowing for thickness measurements from STEM images within the SEM chamber. However, this unit is currently incompatible with the continuous ion milling process. Another avenue for thickness determination is through integration of characteristic EDX peaks.<sup>20</sup> Van Mierlo et.al.<sup>17</sup> demonstrated the accurate measurement of ~40 nm thick GaN TEM lamellae, using the intensities of GaL $\alpha$  and GaL $\beta$  peaks. However this method is prohibitively slow (50-100 times slower than image based techniques), and exposes the lamella to many passes of the electron beam. This high electron dose makes it unsuitable for beam sensitive samples, and can lead to a build up of contamination. EDX based measurement is likely to be less accurate for thinner lamellae and/or those composed of lighter elements. Furthermore, the optimal working distance for EDX collection is typically not at the coincidence point of the ion and electron columns, further complicating sample preparation.

Here we demonstrate two methods for the accurate *in-situ* measurement of S/TEM lamellae. First we show how any FIB-SEM can be calibrated for *in-situ* thickness measurement for a specific material, through the precise alignment of SE SEM images with an EELS thickness map. Additionally we demonstrate how combining the SE images from the through lens detector (TLD), and the ion conversion and electron (ICE) detectors yields a more accurate thickness measurement than either individual detector. Secondly, we show an *a priori* method for accurate Monte Carlo modelling of the TLD and ICE detector intensities and subsequent *in-situ* thickness measurements of S/TEM lamellae. The models are reusable between instruments, and allow for accurate measurement in near real time. We apply our results to propose a new workflow for the preparation of high quality S/TEM lamellae with known thicknesses, which is suitable for automation.

## Theory of electron specimen interaction

When a high energy electron impacts on a solid, it will undergo elastic and inelastic collisions. These collisions are probabilistic and are formalised by elastic and inelastic MFPs, which describe the average distance the electron will travel within the specimen between scattering events. Inelastic collisions, in which energy is transferred from the primary electron to the specimen, limit the distance an electron can travel in a sample. The penetration depth of the electrons may be estimated using the linear energy transfer approximation.<sup>21</sup> However, due to the frequency of elastic collisions, the individual electrons travelling through the material have tortuous trajectories, leading to a distribution of implantation depths. The range of implantation locations describe an interaction volume in the shape of a teardrop, the size and density of which is dependent on a range of parameters including beam energy and specimen composition.<sup>22</sup>

SEMs are traditionally used as a surface characterisation method, where the entire interaction volume is contained within the specimen and no electrons are able to completely traverse the thickness of the material. SEM images are typically formed from two signals, either backscattered electrons (BSEs) or SEs. BSEs are primary electrons which have been scattered to sufficiently large angles by elastic collisions, so much so that they exit the top surface of the specimen (Figure 6-2a). These energetic electrons are collected by an electron detector inside the instrument, producing the image forming signal.

The depth at which the BSE are generated is probabilistic and can be described by a shallow interaction volume. The amount of BSEs generated is dependent on the BSE yield, a product of the number of incident probe electrons ( $N_{probe}$ ) and the BSE coefficient ( $\eta$ ) as shown in Equation 6-1.  $\eta$  describes the probability of the production of BSE per incident electron.

$$BSE\ yield = N_{probe} \eta \quad \text{Equation 6-1}$$

One of the mechanisms by which energy may be transferred from the probe electron to the specimen is through ionisation of the sample to create SEs. SEs are low energy, arbitrarily defined as possessing less than 50 eV<sup>22</sup>, and consequently may only travel a short distance. As such only SEs generated close to the surface may be detected and

contribute to the image signal.<sup>23</sup> The surface region in which SEs must be formed to be detectable outside of the sample is referred to as the escape depth (Figure 6-2) and was modelled by Kanaya and Ono.<sup>22</sup> Due to this limited escape depth, SEs are extremely sensitive to topological changes in the specimen, providing the SEM with its high surface imaging capabilities.

SEs may be classified by the method by which they were generated; those formed by the incident probe electrons entering the specimen are denoted SE<sub>1</sub> while those generated as BSE exit the sample are designated as SE<sub>2</sub> (Figure 6-2). SEs may also be formed by the BSEs interacting with the internal surfaces of the instrument, SE<sub>3</sub>, or by the electron probe impinging on a misaligned aperture, SE<sub>4</sub>.<sup>22</sup> The total SE yield is a function of the probability of SE generation by each separate process, the BSE yield and the number of incident probe electrons (Equation 6-2).

$$SE\ yield = N_{probe}(\delta_1 + \delta_4) + N_{probe}\ \eta(\delta_2 + \delta_3) \quad \text{Equation 6-2}$$

Where  $\delta_x$  are the coefficients for SE<sub>x</sub> (x=1-4) electron generation. These coefficients refer to SE signal generated above the specimen (probe side), and as such we will refer to these electrons as top surface produced (TSP) electrons. It has been shown that the majority of the detectable signal is generated by SE<sub>2</sub> and SE<sub>3</sub><sup>22</sup>; consequently we can ignore the first term in Equation 6-2 and use BSE yield alone to estimate the SE yield at the top surface (Equation 6-3).

$$SE\ yield \propto BSE\ yield = N_{probe}\ \eta \quad \text{Equation 6-3}$$

Unlike for a bulk specimen, as TEM lamellae are progressively thinned by an ion beam, the sample thickness approaches the depth of the electron interaction volume. As such it is possible that SEs may exit the bottom surface. If the sample is further thinned such that the specimen thickness is less than the interaction volume, many electrons will begin to transmit through the specimen. As these electrons transmit through the specimen, they may produce SEs within the bottom surface escape depth, which are emitted from the bottom surface (Figure 6-2b). This is analogous to the BSE generated TSP SEs. We will refer to SEs exiting the bottom side of the specimen as bottom surface produced (BSP) electrons. As the sample is progressively thinned, a higher percentage

of electrons will transmit and the yield of BSP electrons will increase. Conversely, as the sample is thinned the, BSE and primary electron interaction volumes are effectively sliced, reducing the probability of TSP and BSP SE production (Figure 6-2c). The differing response in TSP and BSP electron yields offers a route for accurate specimen thickness measurement. Due to the geometry of the detectors, the TLD may only collect the TSP electrons, whereas the oblique ICE detector can collect both TSP and BSP electrons (Figure 6-2d). The detection of these differing yields from different surfaces, forms the basis of two methods presented below, in which we show through consideration of both detectors, the thickness of TEM lamellae may be determined *in-situ* between ion milling steps.

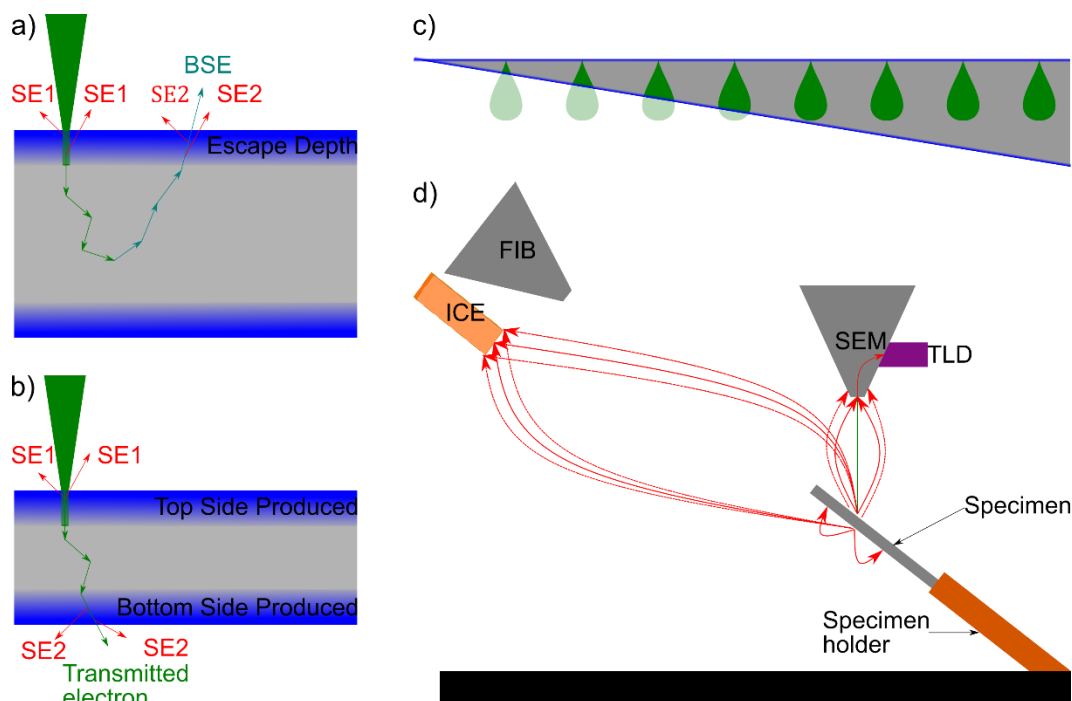


Figure 6-2 – Overview of electron generation in the FIB. (a) Illustration of secondary electron (SE) generation from a bulk specimen in which all electrons are top side produced (TSP). SE1 corresponds to secondary electrons produced from primary beam interactions and SE2 are those produced from BSE exiting the specimen. Note that only SEs generated within the escape depth may successfully exit the specimen to be detected. (b) Illustration of SE generation from a thinned specimen, such that primary electrons may exit the sample, leading to the production of electron back side produced (BSP) SEs. Note for clarity the BSE have been removed from the diagram but these may still be produced from a thinned specimen. (c) Illustration demonstrating how the electron interaction volume is effectively sliced as the specimen is thinned, compared to when it is bulk. (d) Illustration describing geometry of the FIB instrument. The FIB column is at 52° with respect to the SEM column, and is more distant. The TLD is very close to the TEM lamellae, and consequently is unable to collect BSP SEs. The ICE is more

distant, and better aligned for the collection of both TSP and BSP SEs. (All examples are for illustrative purposes only and are not to scale) **Methods**

### **General**

A silicon TEM cross section lamella was prepared and imaged using a dual-beam FIB-SEM instrument (FEI Helios 660). The silicon wafer was coated with protective layers of 3 nm Au/Pd and 5 nm Carbon, followed by a 20 x 1 x 1  $\mu\text{m}$  platinum strap deposited by electron and ion beam patterning. A lamella was milled from the silicon substrate parallel to a cleaved edge, to allow later TEM alignment down a high symmetry crystallographic direction. The lamella was extracted via the *in-situ* lift-out method<sup>24</sup>, transferred to an Omniprobe TEM grid, and thinned using 30 keV at 230 pA, 16 keV at 220 pA, 5 keV at 41 pA, and 2 keV at 23 pA gallium ions.<sup>14</sup> ICE and TLD SEM images were collected using 5 keV electron beam energy and 200 pA beam current, with tilt correction.

The distribution of thicknesses in the lamella was subsequently determined in a probe side aberration corrected FEI Titan 80-200 X-FEG with 200 keV beam energy, 180 pA beam current and 21 mrad convergence angle. The lamella was first tilted to the high symmetry zone axis normal to the cross section surface, using silicon Kikuchi bands. The  $t/\lambda$  map was acquired in a Gatan Imaging Filter (GIF) Quantum ER system with a 5 mm entrance aperture, a collection angle of 62 with an effective energy resolution of 1.8eV and a dispersion of 0.25eV/channel. The  $t/\lambda$  map was quantified using the log ratio method<sup>25</sup>, and converted to absolute thickness values using an inelastic MFP value of 142 nm.<sup>26</sup>

The SEM images and thickness map were aligned and analysed using the open source python packages scikit-image<sup>27</sup> and Hyperspy<sup>28</sup>. Monte Carlo simulations were run using the CASINO software package.<sup>29</sup> The electron implantation probability distribution functions (PDFs) for 2 – 20 keV beam energies were simulated using 100,000 electrons. Simulations to calculate the cumulative distribution functions (CDFs) for 5 and 10 keV electron beam energies used 5 million electrons.

### **Method 1: Alignment and ratio method by calibration of instrument.**

As discussed in the introduction section, the thickness of a prepared TEM lamellae can be accurately measured post ion milling by collecting a  $t/\lambda$  map using S/TEM EELS. By

correlating TLD and ICE SE SEM images with the EELS  $t/\lambda$  map, the TLD and ICE intensity values may be calibrated and assigned a corresponding thickness value for a material. Thickness estimation from  $t/\lambda$  maps is dominated by the accuracy of the inelastic MFP value,  $\lambda$ ; we chose silicon as a known standard to minimise this error (3%) ( $\lambda_{\text{Si}} = 142 \pm 5 \text{ nm}$ ).<sup>26</sup>

The distribution of lamella thickness was accurately measured using the log-ratio method on the zero loss and plasmon peak in the low loss region of a EELS spectrum image.<sup>25</sup> To calibrate each greyscale value of the TLD and ICE detectors to a corresponding thickness, the TLD, ICE and EELS thickness maps were carefully aligned using the cross-correlation and warp alignment tools in the scikit-image open source python library (Figure 6-3). Warping stretches different regions of the primary image (the EELS thickness map) such that the image subject adopts the shape of some target subject (TLD and ICE images). This essentially removes any scanning distortions induced during image acquisition and resizes the lamella to compensate for the tilt angle adopted for ion polishing. It should be noted that this method does not change the SEM greyscale values, actual or relative, for the different areas and thicknesses of the lamella. Cross correlation was used to align the images via translation. These methods were repeated iteratively until all three images were aligned.

As expected, the TLD and ICE detectors show different intensity responses,  $y$ , for lamella thickness,  $t$ , from the different detector positions. The TLD intensity is a monotonic function in which the signal decreases with decreasing lamella thickness. This behaviour results from the TLD only detecting TSP SEs, the yield of which will reduce as the number of BSEs generated decreases as the specimen is thinned. The ICE intensity variation is more complex as it is formed from both TSP and BSP SEs. The differing behaviour of the signals, in which TSP yield is reduced with thinner specimens while the BSP is simultaneously increased as more electrons transmit, allows specimen thickness to be estimated.

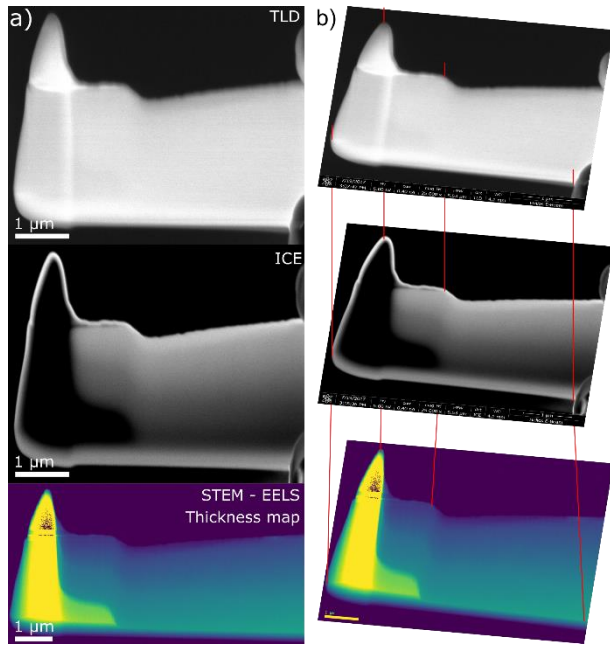


Figure 6-3– Alignment of SEM images (TLD and ICE detectors) to the STEM-EELS thickness map. The goal is to align the three images in (a) so that the greyscale values for each SEM detector can be matched to a corresponding lamella thickness. (b) The alignment method iterates between image warping and translation using cross correlation. The colour map in the STEM-EELS thickness map illustrates the range of thickness present in the lamellae, from  $\geq 2 t/\lambda$  (yellow) to  $\sim 0.2 t/\lambda$  (dark blue). All scale bars 1  $\mu\text{m}$ .

The TLD is simpler to interpret, with a decrease in signal corresponding to a thinner sample. In principal, a single TLD detector value will correspond to a single thickness measurement. The ICE trend contains a skewed peak, and so almost all of the ICE detector values correspond to two different specimen thicknesses, complicating interpretation. However, the spread in greyscale values for each detector, ( $\Delta y_{\text{TLD}}$  and  $\Delta y_{\text{ICE}}$  respectively), limits the accuracy of any reading, and introduces an uncertainty into the lamella thickness measurement.  $\Delta y_{\text{TLD}}$  and  $\Delta y_{\text{ICE}}$  correspond to one standard deviation in the SE detector values that were assigned the same nominal values of  $t/\lambda$ , and are represented by the vertical error bars in Figure 6-4a. The nature of ion thinning means that thickness changes gradually across the lamella. Therefore, the accuracy of our estimate can be improved by considering the rate of change of greyscale values with thickness, i.e. the gradient of the detector signal and the magnitude of the variation in detector intensity (Equation 6-4).  $\Delta t$  is the lamella thickness uncertainty,  $\Delta y$  is the variation of detector intensity for the each thickness, corresponding to one standard deviation and  $\left. \frac{dy}{dt} \right|_{t_0}$  is the gradient of the signal curve for a specific thickness of the lamella. These are plotted in Figure 6-4b. The detector signals were fitted with

4000 point 5<sup>th</sup> order polynomials. There is a large uncertainty in lamella thickness estimation for the TLD, for thick specimens (>70 nm). This is due to signal saturating in thicker samples, and consequently the gradient,  $\left. \frac{dy}{dt} \right|_{t_0}$  of the TLD signal is small, tending to zero. The ICE appears more robust, with the uncertainty remaining relatively constant regardless of specimen thickness. However this uncertainty approximation breaks down for the ICE at ~35 nm due to the skewed peak, where this model clearly over-estimates  $\Delta t$ , which tends to infinity at points where  $\frac{dy}{dt} = 0$ . While the error clearly cannot tend to infinity, simple inspection of the ICE signal clearly shows a marked increase in the spread of greyscale values. Consequently the ICE detector is less suited for estimating lamellae thickness between 25 and 40 nm. Discounting the effects of the spike in ICE intensity, the mean uncertainty within the region of interest (20-80 nm) for the ICE is superior to TLD, with an uncertainty of 8.73 nm and 19.32 nm respectively. The effect of the spike may be removed by only considering the uncertainties between 20-25 nm and 40-80 nm. As such the ICE detector generally outperforms the TLD in accuracy, although the TLD is preferred in the region of 25 – 40 nm.

$$\Delta t^2 = \frac{\Delta y^2}{\left( \left. \frac{dy}{dt} \right|_{x_0} \right)^2} \quad \text{Equation 6-4}$$

Traditionally, FIB samples are prepared using only one SEM image as a guide for specimen thickness, but as shown above, the uncertainties associated with the ICE and TLD are large with respect to the target thickness. However, by considering the ratio of the TLD and ICE signal intensities the uncertainty can be reduced. The ICE:TLD ratio is plotted in Figure 6-4a, and within the region of interest it is reasonably linear, with a single ratio value corresponding to a single specimen thickness. The variation in the ratio signal,  $\Delta y_{\text{RATIO}}$ , may be calculated by quadrature from the TLD and ICE. The ratio shows a smaller error than either individual detector. Also exhibiting a steeper gradient, the ratio method has a smaller uncertainty in lamellae thickness estimation. However due to the turning point in the ratio intensity at ~ 22 nm, a spike is present in the uncertainty. Nonetheless, as the turning point is sharper, the width of the spike is reduced. With a mean thickness uncertainty value of 4.12 nm excluding the effect of the spike (excluding 20 – 25 nm), which remains reasonably constant throughout.



Combining the benefits of both detectors and reducing the uncertainty, the ratio ICE:TLD is a superior method of estimating specimen thickness.

However, this method still requires detector calibration using a thin lamella of the same material, EELS thickness mapping and accurate data alignment. Additionally, calibration must be repeated for each FIB-SEM instrument and material. An alternative *a priori in-situ* thickness measurement method which is applicable to different specimens and transferable between instruments is therefore highly desirable.

## **Method 2: *In-situ* thickness determination using a model based approach**

As discussed above, optimal thickness determination during lamellae thinning within the FIB requires large changes in the SE detector signal as a function of thickness. Optimal imaging conditions will therefore be likely to correspond to a maximum change in the electron interaction volume as the sample is thinned. Electron interaction volumes may be described by probability distribution functions (PDFs) and cumulative distribution functions (CDFs). A PDF denotes the probability of an event at a certain depth, and a CDF the total number of events within a depth range. Here, the electron implantation and BSE generation PDFs are estimated from Monte Carlo simulations.

Figure 6-5a shows the PDF for electron implantation in silicon for beam energies typically available on commercial FIB instruments (2, 3, 5, 10, 20 keV). The 5 keV and 10 keV interaction volumes are shown to be the most favourable for the thickness range of interest (20-80 nm). Other beam energies shown are found to be non-optimal for various reasons: the 2 keV interaction volume does not span the full thickness range; the 3 keV PDF contains a turning point where the gradient will be minimal and the error in thickness estimation will become large; and the 20 keV interaction volume slowly varies in the required thickness range.

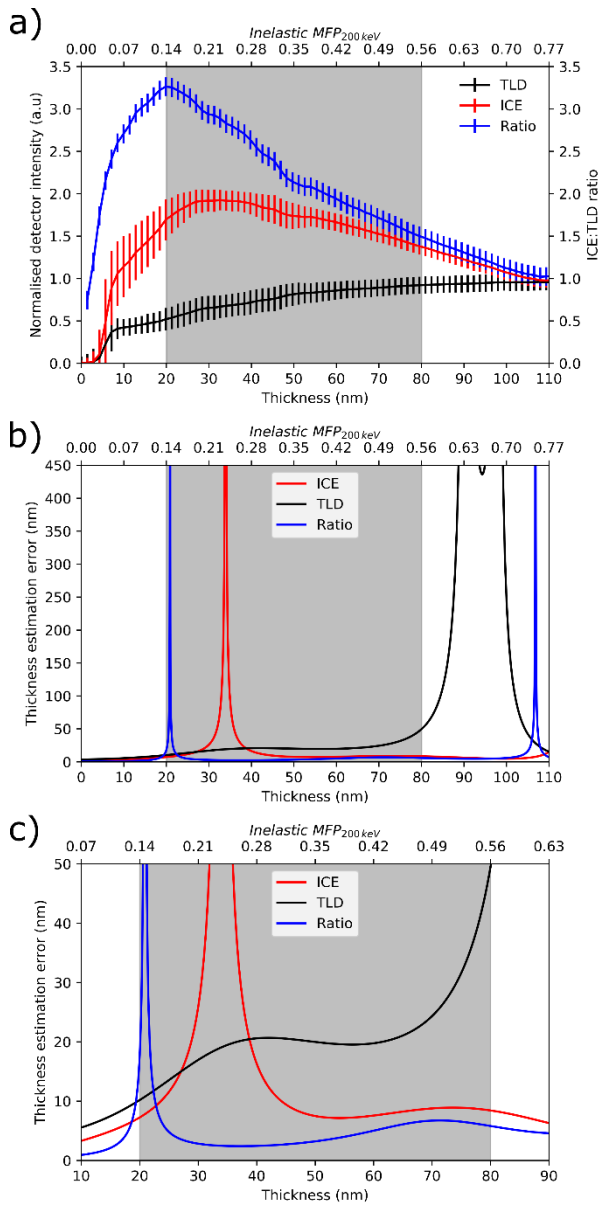


Figure 6-4 – Detector signals and associated errors in thickness estimation. (a) Shows normalised detector intensities against lamella thickness for TLD (black) and ICE (red) detectors, produced from the aligned ICE, TLD and EELS thickness maps. The TLD signal is a monoatomic function with a small gradient. Ratio and ICE have larger gradients than TLD, but contain turning points. Error bars correspond to one standard deviation in signal intensity. Also shown is the ratio of ICE and TLD intensities (blue), error bars calculated by quadrature from TLD and ICE errors. (b) Shows uncertainties in lamella thickness estimation for the ICE, TLD and Ratio signals, calculated from Equation 6-4 from signals fitted with 5<sup>th</sup> order polynomials. Due to the turning points in the ICE and Ratio signals there are spikes in the uncertainties estimation at 35 and 20 nm respectively. (c) Selected region of (b), showing the uncertainties are less for Ratio < ICE < TLD with uncertainties of 4.12, 8.73 and 19.32 nm respectively (if the effects of the spikes are excluded). The uncertainty in lamella thickness is smaller for Ratio < ICE < TLD within the region of interest, if the spikes are discounted. Region of interest (20-80 nm) shaded grey.

The CDF for BSE generation and electron implantation may be calculated from the respective PDFs. Assuming any electron not implanted in the material will be transmitted, the transmitted electron CDF may be calculated as (1 - implantation CDF).

As shown in Figure 6-5b & c, the BSE generation CDFs for 5 and 10 keV beam energies have a broadly similar behaviour in the thickness range of interest while the CDFs for the transmitted electrons are significantly different. The 5 keV transmitted electron CDF is found to be more steeply sloping for silicon samples between 20-80 nm in thickness, providing opportunities for more accurate thickness determination.

As demonstrated in the previous section, optimal thickness measurement is achieved through considering both the TSP and BSP secondary electrons. The ICE detector collects both TSP and BSP SEs, while the TLD detector collects only TSP SEs (Figure 6-2). The ICE signal can therefore be modelled by the sum of the BSE generation and transmission CDFs (Equation 6-5), while the TLD can be modelled using just the BSE generation CDF (Equation 6-6) (Figure 6-6a). Normalising these modelled curves to experimental images provides a good fit to the experimental ICE and TLD detector signals, (Figure 6-6b) as well as to the ICE:TLD ratio within the thickness range of interest (Figure 6-6c). It should be noted that for a specimen thickness of less than 20 nm the fit between theory and experiment is poor especially for the ICE:TLD ratio method. This is due to the model not considering the  $SE_1$  signal (generated by the primary beam) which is increasingly dominant over the  $SE_2$  signal (generated by the BSE signal) at very small lamella thicknesses. TSP SE yield is almost entirely dependent on BSE generation, and as sample thickness decreases, the CDF for BSE generation rapidly approaches zero, causing the ICE:TLD ratio to tend to infinity.

The good fit between theory and experiment for the SE detector response as a function of thickness (Figure 6-5b) suggests that even simple Monte Carlo modelling can provide powerful input for optimising electron imaging conditions, allowing for accurate determination of lamella thickness during ion milling.

The hypothesis of the TLD detector only collecting TSP, and ICE collecting TSP and BSP is validated by considering the difference in the two detector outputs, the behaviour of which gives a good match to the modelled BSP electron behaviour (Figure 6-6d). In these the difference between ICE and TLD signals is plotted for both experimental and modelled data. They show a reasonable match, confirming that the approximation is valid.

$$ICE_{model} = SE_{TSP} + SE_{BSP} \quad \text{Equation 6-5}$$

$$\approx BSE_{CDF} + Transmitted\ electrons_{CDF}$$

$$TLD_{model} = SE_{TSP} \approx BSE_{CDF} \quad \text{Equation 6-6}$$

The analysis presented here has concentrated on the final stage lamellae thinning. This is often the most critical step for optimal TEM imaging and spectroscopy, yet it is also important that earlier milling steps do not introduce through thickness ion beam damage that cannot be removed during later polishing stages. Details of ion currents and required thicknesses during progressive milling steps are provided in experimental methods, and SRIM<sup>30</sup> calculations can be employed to determine optimal lamellae thicknesses for different ion beam currents<sup>31,32</sup>.

Our model based thickness determination approach can therefore be extended to optimise earlier ion milling steps. For example, analysis of the interaction volumes presented in Figure 6-5a suggest that electron imaging at 20 keV would be the optimal beam energy for sample thickness from  $\geq 1 \mu m$  to  $\sim 500 \text{ nm}$ , corresponding to 30 and 16 keV ion beam energies. 10 keV electron beam energies would be suitable for thickness between  $\sim 500 \text{ nm}$  and  $\sim 100 \text{ nm}$ .

Furthermore, characterisation of the relationship between SE detector signals and thickness for the whole milling process would allow the thinning rate of the material to be accurately estimated, which would assist in automation of the FIB milling process.<sup>33</sup> Figure 6-7 shows a proposed workflow for such an optimised FIB milling procedure.

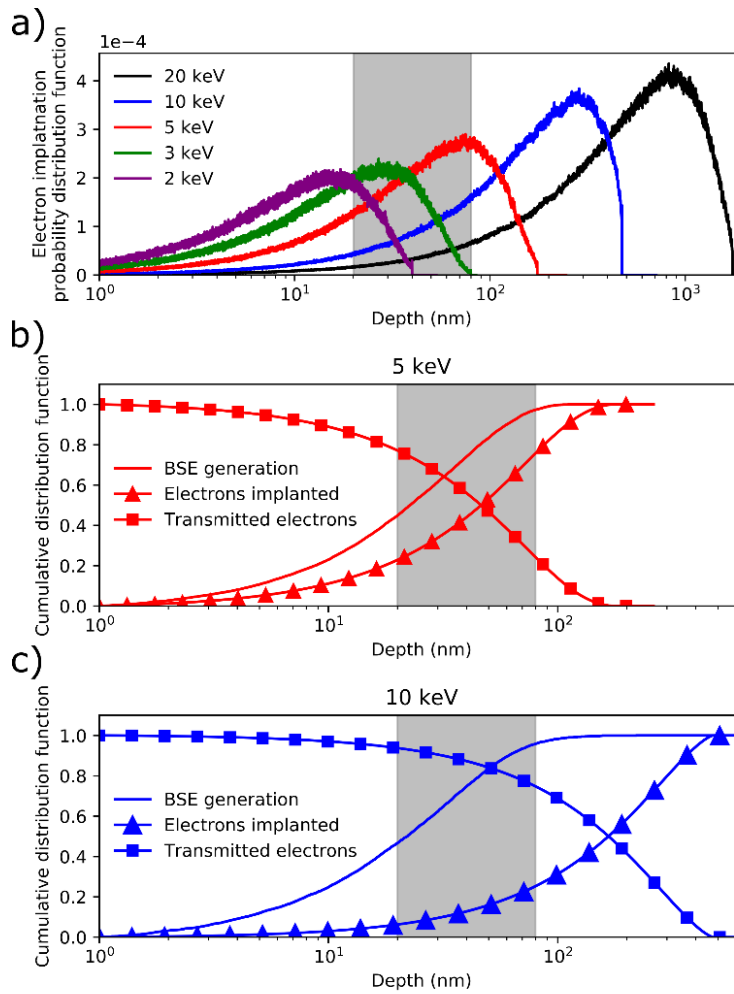


Figure 6-5- Probability and cumulative distribution functions for BSE generation, electron implantation and transmission in silicon. (a) Probability distribution functions for electron implantation in silicon for 2, 3, 5, 10 and 20 keV electron beam energies. Peaks correspond to 17, 27, 75, 286 and 824 nm. (b) Cumulative distribution functions (CDFs) of BSE generation, electron implantation and transmission for 5 keV electrons in silicon. (c) same as (b) but for 10 keV electrons. Data calculated using Monte Carlo package Casino<sup>29</sup> using 100,000 electrons for (a) and 10 million electrons for (b),(c). Region of interest (20- 80 nm) highlighted as shaded grey area.

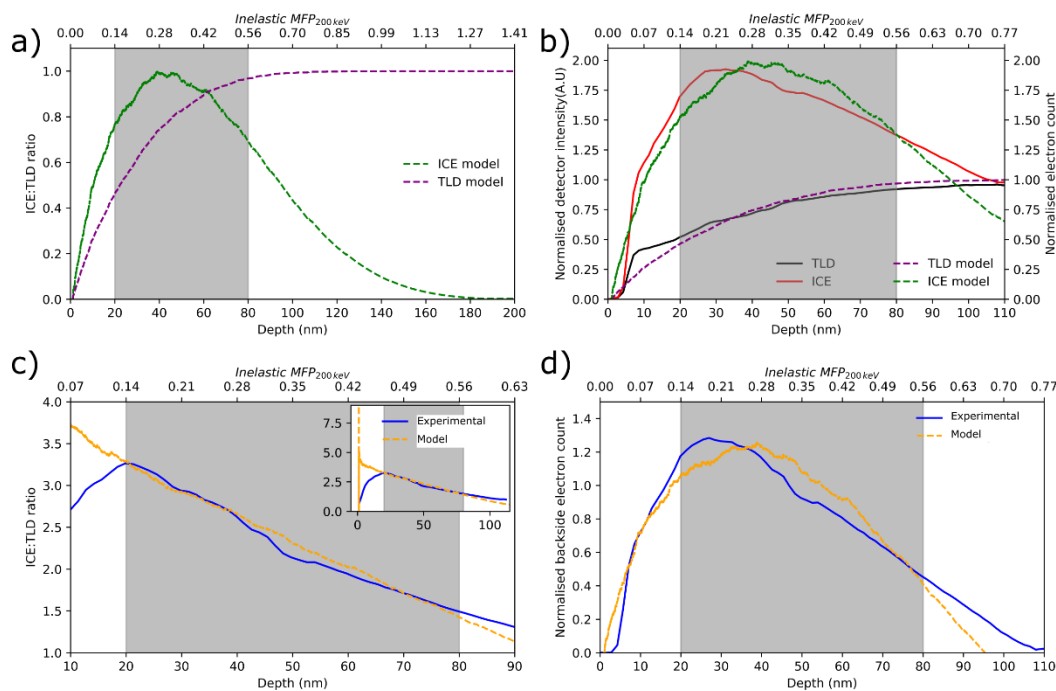


Figure 6-6 – Comparison of experimental and modelled detector responses. (a) Shows the uncalibrated models for TLD and ICE detector signals. The TLD is modelled as the BSE generation depth cumulative distribution function (CDF). The ICE is modelled as the sum of BSE generation CDF and transmitted electron CDF. (b) The modelled detector curves (green and purple dashed lines) are calibrated to the experimental detector signals (red and black solid lines), by normalisation. The fit between the experimental and modelled signals is in good agreement. (c) Shows the ratios of the ICE:TLD signals for the experimental (blue solid line) and modelled curves. Within the region of interest, both lines are reasonably linear and there is an excellent agreement between experimental and modelled data. (d) Shows the number of secondary electrons produced from the bottom side of the specimen, by plotting ICE-TLD intensities for both experimental and modelled data. There is a good agreement between modelled and experimental signals, validating the hypothesis of ICE collecting both top and bottom side produced secondary electrons, while TLD only collects top side produced secondary electrons. Region of interest (20- 80 nm) shaded in grey.

## Conclusions

In conclusion, we have demonstrated a method for the calibration of the FIB instrument for *in-situ* lamella thickness measurement. We show that thickness estimation can be achieved with an accuracy of ~5nm by considering the ratio of intensity values of two different SE detectors, where these detectors are positioned to collect both top and bottom surface emitted secondary electrons (ICE) and purely top surface emitted electrons (TLD). We demonstrate that Monte Carlo modelling of interaction volumes allows the imaging conditions to be optimised for thickness determination in a particular material and thickness range of interest. We propose that

this approach could be extended to improve thickness determination during automated thinning of TEM lamellae.

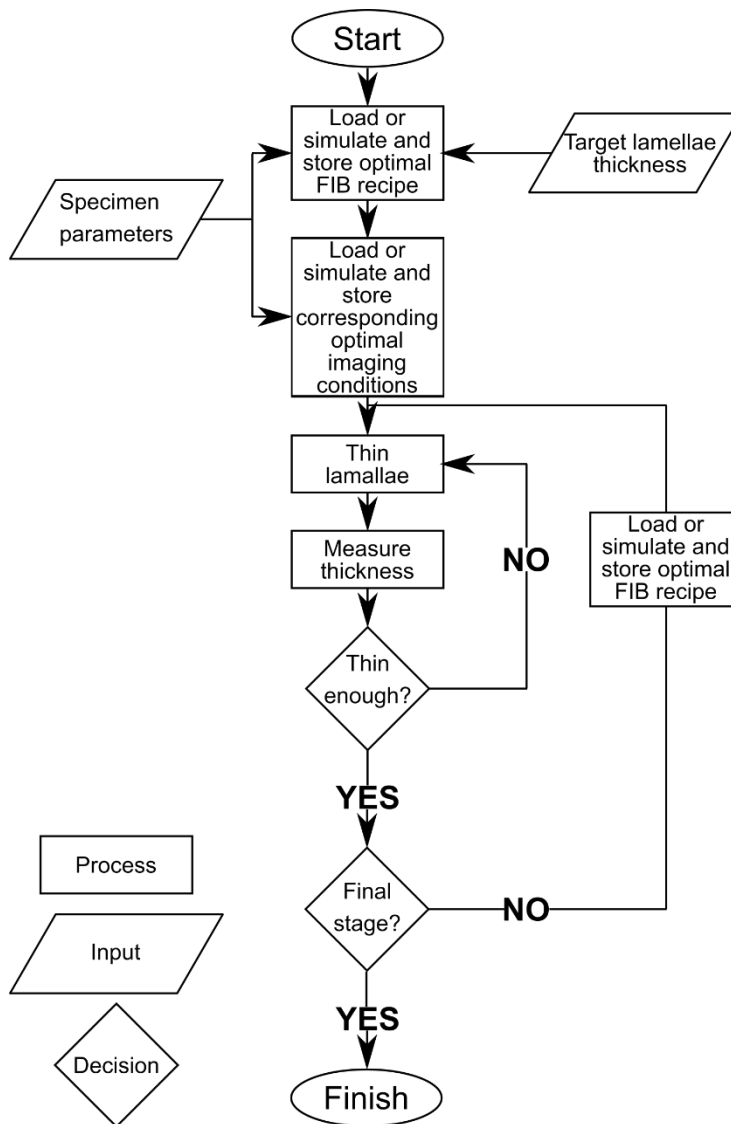


Figure 6-7 – Flowchart for the new proposed FIB thinning workflow

## Acknowledgements

We would like to thank Adrian Ceferino for assistance with providing the mathematical framework for handling the calculations of errors, and Jack Donoghue for useful discussions on SEM image formation.

## References

- 1 Shinotsuka, H., Tanuma, S., Powell, C. J. & Penn, D. R. Calculations of electron inelastic mean free paths. X. Data for 41 elemental solids over the 50 eV to 200 keV range with the relativistic full Penn algorithm. *Surface and Interface Analysis* **47**, 871-888 (2015).
- 2 Parmenter, C. D. J., Fay, M. W., Hartfield, C. & Eltaher, H. M. Making the practically impossible “Merely difficult” —Cryogenic FIB lift-out for “Damage free” soft matter imaging. *Microscopy Research and Technique* **79**, 298-303 (2016).
- 3 Pennycook, S. J. The impact of STEM aberration correction on materials science. *Ultramicroscopy* **180**, 22-33 (2017).
- 4 Erni, R., Rossell, M. D., Kisielowski, C. & Dahmen, U. Atomic-Resolution Imaging with a Sub-50-pm Electron Probe. *Physical Review Letters* **102**, 096101 (2009).
- 5 Kelly, P. M., Jostsons, A., Blake, R. G. & Napier, J. G. The determination of foil thickness by scanning transmission electron microscopy. *physica status solidi (a)* **31**, 771-780 (1975).
- 6 Mitchell, D. R. G. Determination of mean free path for energy loss and surface oxide film thickness using convergent beam electron diffraction and thickness mapping: a case study using Si and P91 steel. *Journal of microscopy* **224**, 187-196 (2006).
- 7 Cowley, J. M. *Electron diffraction techniques*. 135 (Oxford University Press, 1993).
- 8 Konstantin, I. & Kazutaka, M. Elastic scattering of 200 keV electrons in elemental solids: experimental observation of atomic-number-dependent oscillatory behavior. *Journal of Physics: Condensed Matter* **21**, 155402 (2009).
- 9 Jablonski, A., Salvat, F., Powell, C. J. & Y., L. A. in *NIST Standard Reference Database Number 64 Vol. 20899* (National Institute of Standards and Technology, Gaithersburg MD, 2016).
- 10 Spence, J. C. H. Absorption spectroscopy with sub-angstrom beams: ELS in STEM. *Reports on Progress in Physics* **69**, 725 (2006).
- 11 Krivanek, O. L., Lovejoy, T. C., Dellby, N. & Carpenter, R. W. Monochromated STEM with a 30 meV-wide, atom-sized electron probe. *Microscopy* **62**, 3-21 (2013).
- 12 Ondrej, L. K., Tracy, C. L., Matthew, F. M., Gwyn, S., Philip, E. B. & Niklas, D. Towards sub-10 meV energy resolution STEM-EELS. *Journal of Physics: Conference Series* **522**, 012023 (2014).
- 13 Ayache, J. (eds Luc Beaunier, Jacqueline Boumendil, Gabrielle Ehret, & Danièle Laub) (Springer Science+Business Media, LLC, New York, NY, 2010).
- 14 Schaffer, M., Schaffer, B. & Ramasse, Q. Sample preparation for atomic-resolution STEM at low voltages by FIB. *Ultramicroscopy* **114**, 62-71 (2012).
- 15 Burnett, T. L., Kelley, R., Winiarski, B., Contreras, L., Daly, M., Gholinia, A., Burke, M. G. & Withers, P. J. Large volume serial section tomography by Xe Plasma FIB dual beam microscopy. *Ultramicroscopy* **161**, 119-129 (2016).
- 16 Holmström, E., Kotakoski, J., Lechner, L., Kaiser, U. & Nordlund, K. Atomic-scale effects behind structural instabilities in Si lamellae during ion beam thinning. *AIP Advances* **2**, 012186 (2012).



- 17 van Mierlo, W., Geiger, D., Robins, A., Stumpf, M., Ray, M. L., Fischione, P. & Kaiser, U. Practical aspects of the use of the X<sup>2</sup> holder for HRTEM-quality TEM sample preparation by FIB. *Ultramicroscopy* **147**, 149-155 (2014).
- 18 Salzer, R., Graff, A., Simon, M. & Altmann, F. Standard Free Thickness Determination of Thin TEM Samples via Backscatter Electron Image Correlation. *Microscopy and Microanalysis* **15**, 340-341 (2009).
- 19 Golla-Schindler, U. in *EMC 2008 14th European Microscopy Congress 1–5 September 2008, Aachen, Germany: Volume 1: Instrumentation and Methods* (eds Martina Luysberg, Karsten Tillmann, & Thomas Weirich) 667-668 (Springer Berlin Heidelberg, 2008).
- 20 Hiscock, M., Dawson, M., Lang, C., Hartfield, C. & Statham, P. In-Situ Quantification of TEM Lamella Thickness and Ga Implantation in the FIB. *Microscopy and Microanalysis* **20**, 342-343 (2014).
- 21 Bethe, H. Zur Theorie des Durchgangs schneller Korpuskularstrahlen durch Materie. *Annalen der Physik* **397**, 325-400 (1930).
- 22 Goldstein, J., Newbury, D. E., Michael, J. R., Ritchie, N. W. M., Scott, J. H. J. & Joy, D. C. *Scanning electron microscopy and x-ray microanalysis*. Fourth edition. edn, (Springer, 2018).
- 23 Ding, Z.-J. & Shimizu, R. A Monte Carlo modeling of electron interaction with solids including cascade secondary electron production. *Scanning* **18**, 92-113 (1996).
- 24 Langford, R. M. & Clinton, C. In situ lift-out using a FIB-SEM system. *Micron* **35**, 607-611 (2004).
- 25 Malis, T., Cheng, S. C. & Egerton, R. F. EELS log-ratio technique for specimen-thickness measurement in the TEM. *J Electron Microscop Tech* **8**, 193-200 (1988).
- 26 Iakoubovskii, K., Mitsuishi, K., Nakayama, Y. & Furuya, K. Thickness measurements with electron energy loss spectroscopy. *Microscopy Research and Technique* **71**, 626-631 (2008).
- 27 Pedregosa, F., Varoquaux, G., Gramfort, A., Michel, V., Thirion, B., Grisel, O., Blondel, M., Prettenhofer, P., Weiss, R. & Dubourg, V. Scikit-learn: Machine learning in Python. *Journal of machine learning research* **12**, 2825-2830 (2011).
- 28 de la Pena, F., Ostasevicius, T., Tonaas Fauske, V., Burdet, P., Jokubauskas, P., Nord, M., Sarahan, M., Prestat, E., Johnstone, D. N., Taillon, J., Jan Caron, u., Furnival, T., MacArthur, K. E., Eljarrat, A., Mazzucco, S., Migunov, V., Aarholt, T., Walls, M., Winkler, F., Donval, G., Martineau, B., Garmannslund, A., Zagonel, L.-F. & Iyengar, I. Electron Microscopy (Big and Small) Data Analysis With the Open Source Software Package HyperSpy. *Microscopy and Microanalysis* **23**, 214-215 (2017).
- 29 Hovington, P., Drouin, D. & Gauvin, R. CASINO: A new monte carlo code in C language for electron beam interaction —part I: Description of the program. *Scanning* **19**, 1-14 (1997).
- 30 Ziegler, J. F., Ziegler, M. D. & Biersack, J. P. SRIM – The stopping and range of ions in matter (2010). *Nuclear Instruments and Methods in Physics Research Section B: Beam Interactions with Materials and Atoms* **268**, 1818-1823 (2010).
- 31 Mehrtens, T., Bley, S., Venkata Satyam, P. & Rosenauer, A. Optimization of the preparation of GaN-based specimens with low-energy ion milling for (S)TEM. *Micron* **43**, 902-909 (2012).
- 32 Giannuzzi, L. & Smith, N. TEM Specimen Preparation with Plasma FIB Xe+ Ions. *Microscopy and Microanalysis* **17**, 646-647 (2011).

- 33 Skalicky, J., Vystavel, T., Tuma, L. & Young, R. in *European Microscopy Congress: Proceedings* 346-347 (2016).

## 7. Summary and future work

This thesis presents the application of clean room fabrication techniques and analytical STEM for the exfoliation and characterisation of MLCs. It also presents the application of novel Monte Carlo modelling and image processing for accurate *in-situ* TEM lamellae thickness measurements. In the following section the work presented is summarised, after which three possible research routes are presented which build upon the work presented.

### 7.1. Summary of thesis

This thesis presents the exfoliation of the naturally occurring MLCs, franckeite ( $n=2$ ,  $m=1$ ) and cylindrite ( $n$ ,  $m=1$ ), to single unit cell thickness. These are the first examples of exfoliating MLCs without vdW to the 2D limit, and as the final stacking sequences to be exfoliated, demonstrates that the exfoliation of MLCs is invariant to stacking sequence. The power of analytical STEM, particularly when the specimen is viewed in cross section, is highlighted for the characterisation of these compounds. This has allowed for the direct investigation of the physical and chemical structure of the compounds difficult to characterise with other techniques. Difficulties faced in the preparation of lamellae discussed in this thesis and those in other work, provided motivation for the development of novel *in-situ* thickness measurement for specimens prepared by FIB.

In chapter 4, the paper *Exfoliation of natural van der Waals heterostructures to a single unit cell thickness*, demonstrated the exfoliation of franckeite to single unit cell thickness. This is the first example of a MLC not containing a vdW gap to be exfoliated to single unit cell thickness. In this paper, the role of analytical STEM, particularly viewed in cross section was crucial, in identifying the material as franckeite, and in understanding the cleavage of the material. Occupational modulations within the layers was discerned for the first time. The staggering and shielding by the outer lead columns, appears vital in minimising any curvature resulting in the tabular crystal. Furthermore liquid phase exfoliation was successfully demonstrated in franckeite. As the first MLC without a traditional vdW gap, offers hope for industrial scalability of these materials. Finally the electrochemical properties were found to be of particular

interest, and highly favourable compared to other 2D materials such as graphene and MoS<sub>2</sub>.

Chapter 5, presents the paper, *Isolation of 2D cylindrite as a naturally occurring van der Waals heterostructure*, in which the exfoliation of cylindrite to the 2D limit is demonstrated. As the final stacking sequence to be exfoliated, the success of this cleavage demonstrates that the exfoliation of MLCs is invariant to stacking sequence. However it was noted that the cleavage of these crystals by traditional mechanical exfoliation techniques was challenging. As such, an adaption of the standard technique was developed which increased the quantity of exfoliated flakes. This new technique is likely to be suitable for other crystals whose size or shape may hamper exfoliation. It was noted that due to the poor quality of the cylindrite source crystal, the exfoliated flakes were highly defective. Consequently the fabrication of devices suitable for the measurement of in-plane anisotropy of the electronic properties could not be attempted. The usefulness of analytical STEM viewed in cross section was again highlighted, allowing for the investigation of: positional and occupational modulations, unique curvature and the previously unreported kink bands in cylindrite. The occupational modulations are different from those seen in franckeite, highlighting the importance of these features on the resulting macroscopic crystal structure. While these modulations have been reported in literature, these are the first direct evidence of these features. The macroscopic curvature appears more complex than previously reported in literature. The structure of a kink band in a MLC was shown for the first time, which again demonstrated remarkable complexity with faceted and continuous curvature present. However the preparation of sufficiently high quality lamellae by FIB was found to be particularly challenging. As such, a new FIB protocol was developed which allowed for thin but mechanically robust lamellae to be prepared.

The penultimate chapter (6), contains the paper, *In-situ thickness determination of TEM lamellae prepared by focused ion beam*, which presented two novel methods for the accurate *in-situ* thickness measurement of TEM lamellae prepared by FIB. The first method describes the accurate calibration of a single FIB instrument, while the second demonstrates an *a priori* method, based on novel Monte Carlo modelling. The robust methodology for calibrating the FIB instrument, enables the accurate determination of lamellae thickness *in-situ* and may be applied to any FIB-SEM instrument. It is also

shown that the accuracy of this measurement may be increased through the combined use of multiple detectors. This method allows for higher quality lamellae to be produced with predetermined thicknesses. However, as a calibration method is limited by the requirement of a suitable calibration specimen, which may prove difficult for inexperienced users and/or those working on new specimens, and must be repeated for each instrument. However, the *a priori* method does not suffer from these drawbacks. It was shown that the SE signal responses for the TLD and ICE detectors, may be accurately modelled using Monte Carlo simulations. Finally, a new workflow suitable for automation, is proposed utilising the new *a priori* thickness measurement methods, in which an optimal FIB thinning procedure may be estimated prior to any experimental work. Successful implementation of this workflow would reduce both the requirement for an experienced FIB operator and instrument time; and yield more consistent lamellae of higher quality. This work was motivated by the challenges faced in the work presented in this thesis, and undertaken elsewhere, and to address a widely acknowledged issue in the field of FIB preparation of TEM specimens.

In conclusion, the successful exfoliation of franckeite and cylindrite highlights that all MLCs, regardless of stacking sequence, should be accessible as 2D materials. We show the power of analytical STEM, in particular when viewed in cross section, for the characterisation of MLCs. Finally we show two novel methods for the accurate *in-situ* thickness measurements of TEM lamellae prepared by FIB.

## **7.2. Future work**

### **7.2.1. Expanding the library of 2D misfit layer chalcogenides**

An outcome of chapters 4 and 5 was the demonstration of the successful exfoliation of two MLCs, showing that exfoliation is invariant to stacking sequence. As such, the most obvious extension of this work is to build upon this in expanding the library of exfoliated MLCs. The cylindrite-franckeite family contains several more minerals which can be inferred to successfully exfoliate. For example, provisional experiments into the exfoliation of coiraitite have appeared successful (Figure 7-1). Although it should be noted that further characterisation is required before the mineral may be confidently assigned as coiraitite.

While this family of minerals is reasonably diverse, issues associated with the small size and poor quality of crystals have hampered the nanofabrication of devices. What is perhaps most attractive about MLCs is the ability to readily synthesise crystals with specifically selected layers, creating crystals with tailored properties. It is plausible that with concerted effort, high quality crystals may be synthesised yielding a higher quality of exfoliation. MLCs formed with CrS<sub>2</sub> H layers would be of great interest if they were shown to exfoliate to the 2D limit, allowing for the examination of a TMDC which is otherwise inaccessible. CrS<sub>2</sub> is expected to be a direct semiconductor with technologically useful band gap of 1.4 eV.<sup>1</sup> Furthermore its magnetic properties would be of interest. MBE has been shown to be particularly adept at forming MLCs with complex stacking sequences, allowing for the formation of unique crystals. This flexibility in layering may be exploited for the exploration of novel physics phenomena. As discussed in section 2.3.4, Majorana fermions are theorised to exist at the interface between a topological insulator and a superconductor.<sup>2</sup> Magnetic insulating (e.g. GdS), topologically insulating (e.g. Bi<sub>2</sub>Se<sub>3</sub>) and superconducting layers (e.g. NbSe<sub>2</sub>) have been previously formed in MLCs. As such, it is possible that a MLC formed from a combination of these layers may be used in the search for these particles.

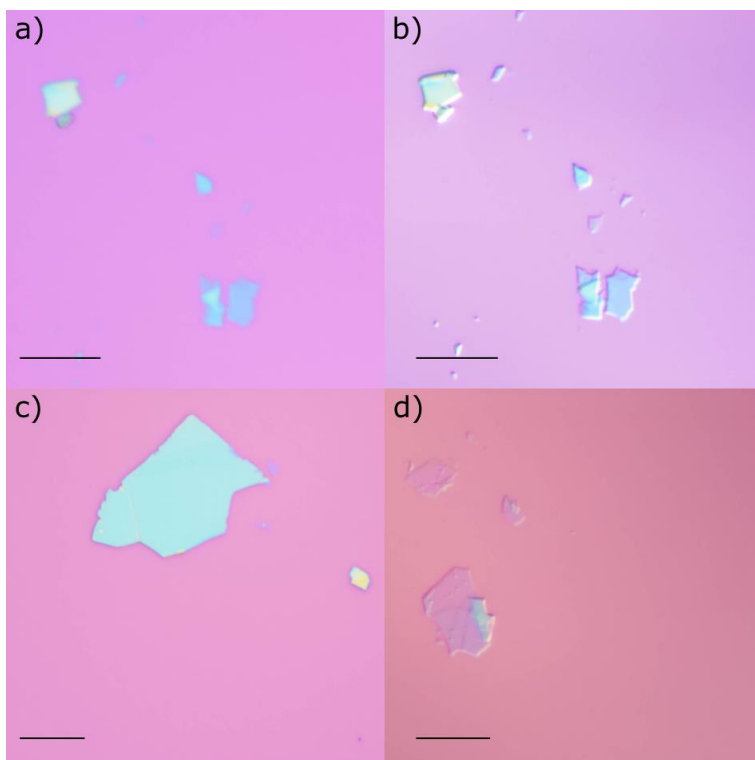


Figure 7-1 – Demonstration of the exfoliation of an MLC provided as ‘coiraite’, (a) bright field (BF) optical image of a few layer coiraite flake exfoliated on to Si/SiO<sub>2</sub> substrate, (b) corresponding differential image contrast (DIC) image of (a), (c) BF optical image of a many layer coiraite flake exfoliated on to Si/SiO<sub>2</sub> substrate, (d) DIC image of few layer coiraite flake exfoliated on to Si/SiO<sub>2</sub> substrate. All scale bars 10  $\mu$ m.

### 7.2.2. Exfoliation of non-layered crystals

The exfoliation of bulk materials to the 2D limit is reliant on an anisotropy between the in-plane and out-of-plane bond strengths.<sup>3</sup> Current efforts have primarily focused on the exfoliation of layered materials, such as vdW materials, and MLCs as presented in this work. However, it is plausible that provided a sufficiently large anisotropy exists, a non-layered crystal may exfoliate. This provides a possible route to a large number of new 2D materials, which have currently been overlooked. Again, turning to nature, the rare sulfosalt (non MLC) mineral vrbaite<sup>4</sup> was investigated. Composed of As<sub>2</sub>SbS<sub>5</sub> chains parallel to the **c** axis, and Hg<sub>3</sub>As<sub>4</sub>S<sub>10</sub> sheets perpendicular to the **b** axis, vrbaite is reported to cleave along the [010] plane.<sup>4</sup> Upon viewing the atomic structure (Figure 7-2) the structure does not appear layered, and the cleavage plane (highlighted in red) is not obvious. The cleavage appears to occur via breakage of sulphur bonds.

Figure 7-2 shows preliminary investigations into the exfoliation of vrbaite, and optical and AFM characterisation of the exfoliated flakes shows thin regions. The AFM shows

thinned areas corresponding to 2 and 2.5 unit cell thickness. These results are preliminary, and the presence of half unit cells may indicate that either the crystal is not vrbaite, or that the crystal contains multiple cleavage planes. A more extensive characterisation is required before confident assignment of the mineral as vrbaite can be made. The AFM data was collected and processed by Dr. Greg Auton.

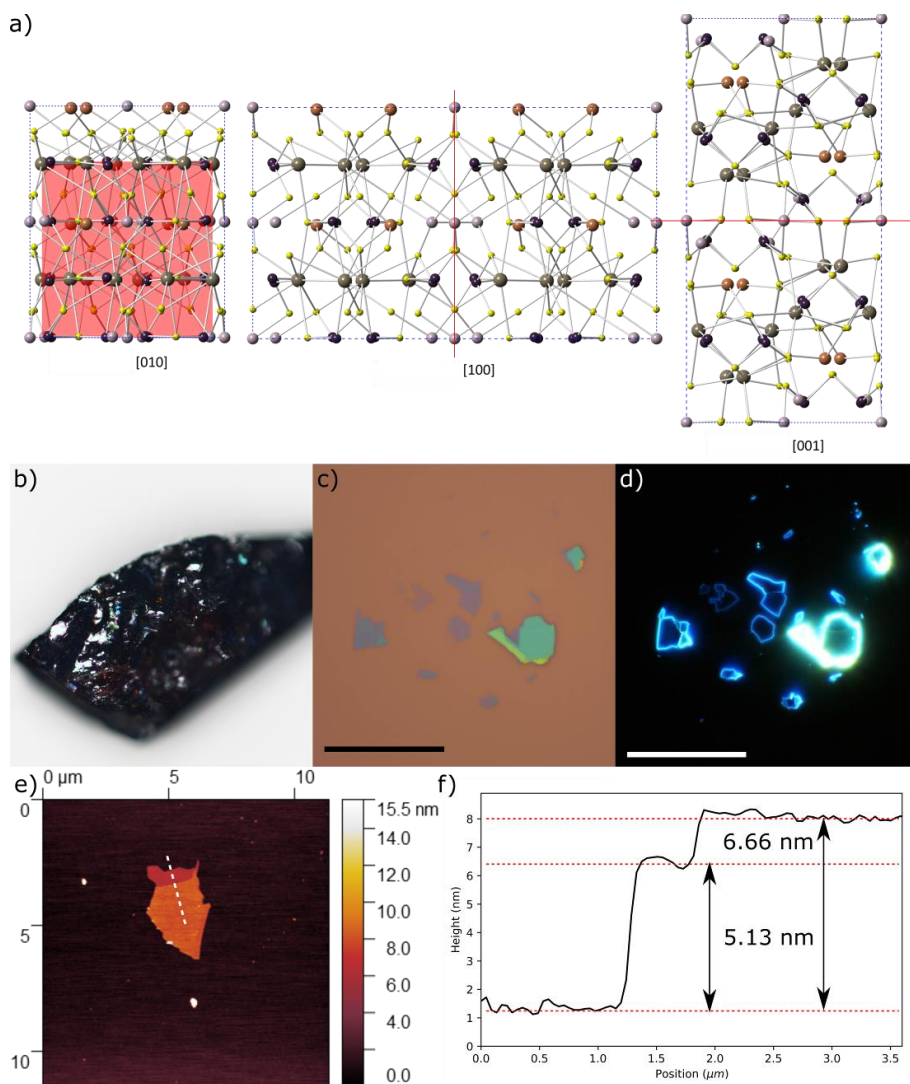


Figure 7-2 - Demonstration of the exfoliation of mineral 'vrbaite', a non-layered rare sulfosalt mineral. Composed of  $\text{As}_2\text{SbS}_5$  chains perpendicular to the **c** axis, and  $\text{Hg}_3\text{As}_4\text{S}_{10}$  sheets perpendicular to the **b** axis. (a) Atomic model of vrbaite, viewed along the [010], [100] and [001] directions. The reported cleavage plane, [010], is highlighted in red. (b) BF optical image of a ~5 x 2 mm vrbaite crystal. (c), (d) BF and DF optical images of exfoliated vrbaite flakes on a Si/SiO<sub>2</sub> substrate. Scale bars correspond to 25 μm, (d) AFM height map of exfoliated Vrbaite flake, (e) AFM height profile, with bilayer plateau and 2.5 unit cell layer.



### 7.2.3. Integration of *in-situ* thickness measurements with native FIB python interface

Chapter 6 demonstrated two methods for the *in-situ* thickness measurements for TEM lamellae by FIB. The second of which used Monte Carlo data generated using the Casino software package.<sup>5</sup> The subsequent data processing was conducted using python open source libraries. It was highlighted that the process should be readily automatable, particularly with the adaptation of python interfaces<sup>6</sup> on new FIB instruments. As such the logical extension would be to create a fully scripted version of this process using the FIB python interface, allowing the near real time analysis. This could be extended further as the Monte Carlo data may be generated using python libraries such as pymontecarlo.<sup>7</sup> The final step would be fully automated FIB thinning process, a process in which the user is only required to load the specimen, and to set the material parameters and ion beam thinning procedure. This will lead to more efficient use of machine and operator time, and yield more consistent FIB lamellae for STEM analysis. It is also possible that this *in-situ* measurement may be useful for other applications.

### 7.3. References

- 1 Zhuang, H. L., Johannes, M. D., Blonsky, M. N. & Hennig, R. G. Computational prediction and characterization of single-layer CrS<sub>2</sub>. *Appl Phys Lett* **104**, 022116 (2014).
- 2 Fu, L. & Kane, C. L. Superconducting Proximity Effect and Majorana Fermions at the Surface of a Topological Insulator. *Physical Review Letters* **100**, 096407 (2008).
- 3 Yi, M. & Shen, Z. A review on mechanical exfoliation for the scalable production of graphene. *Journal of Materials Chemistry A* **3**, 11700-11715 (2015).
- 4 Ohmura, M. & Nowacki, W. in *Zeitschrift für Kristallographie - Crystalline Materials* Vol. 134 360 (1971).
- 5 Hovington, P., Drouin, D. & Gauvin, R. CASINO: A new monte carlo code in C language for electron beam interaction —part I: Description of the program. *Scanning* **19**, 1-14 (1997).
- 6 Prokhodtseva, A. *Advanced DualBeam automation for every need* <<http://em-webinars.thermofisher.com/Advanced-DualBeam-Automation>> (2018),09/09/2018.
- 7 Pinard, P. T., Demers, H., Gauvin, R. & Richter, S. pyMonteCarlo: A Common Programming Interface for Running Identical Simulations using Different Monte Carlo Programs. *Microscopy and Microanalysis* **19**, 822-823 (2013).